Silesian University of Technology

Faculty of Electrical Engineering

Doctoral Thesis

Analysis and examination of selected methods of pulsed-field magnetization of high-temperature superconductors

Analiza i badania wybranych metod magnesowania nadprzewodników wysokotemperaturowych

Paweł Lasek MSc.

Supervisor: Mariusz Stępień, PhD, DSc, Prof. of SUT
Co-Supervisor: Janusz Hetmańczyk, PhD

Gliwice 2021

Contents

Nomenclature

Latin Symbols

Symbol	Unit	Description
A_{w1}	m^2	Cross-sectional area of a wire
A_{c}	m^2	Cross-sectional area of a ferromagnetic core
A_{g}	m^2	Cross-sectional area of an air gap
A_{m}	m^2	Equivalent cross-sectional area of a magnetic circuit
$\mathbf{A}$	Wb	Magnetic vector potential
$B_{\mathrm{s}}(t)$	T	Magnetic flux density as a function of time
$\mathbf{B}$	T	Magnetic flux density vector
B_{app}	T	Applied magnetic flux density
B_{c}	T	Critical magnetic flux density
B_{c0}	T	Critical magnetic flux density [1]
B_{c1}	T	First critical magnetic flux density
B_{c2}	T	Second critical magnetic flux density
B_{c1ab}	T	First critical magnetic flux density in a-b plane
B_{c2ab}	T	Second critical magnetic flux density in a-b plane
B_{c1c}	T	Second critical magnetic flux density along c-axis
B_{c2c}	T	Second critical magnetic flux density along c-axis
B_{max}	T	Maximum magnetic flux density
B_{trap}	T	Trapped magnetic flux density
B_{z}	T	Magnetic flux density component along z-axis
$\hat{B}$	T	Peak magnetic flux density
$\hat{B}_{\mathrm{z}}$	T	Peak magnetic flux density along z-axis
$B_{\parallel}$	T	Magnetic flux density parallel to a-b plane
$B_{\perp}$	T	Magnetic flux density perpendicular to a-b plane
$\Delta\mathbf{B}$	T	Finite difference of magnetic flux density
$\Delta\mathbf{B}_{\mathrm{ij}}$	T	Finite difference of magnetic flux density vector of a j-th segment of a i-th turn of a coil
C	F	Capacitance
$\mathbf{D}$	C/m^2	Displacement field
D_{w1}	m	Diameter of a wire
D_{in}	m	Inner diameter of a coil
D_{out}	m	Outer diameter of a coil
$D(s)$		Denominator's polynomial in s-domain
e	C	Elementary charge ($1.602176634 \cdot 10^{-19}$ C)
$e_{\mathrm{HTS}}(t)$	V	Voltage induced in HTS
E	V/m	Electric field intensity
$\mathbf{E}$	V/m	Electric field intensity vector
E_{c}	V/m	Critical electric field intensity
$\mathbf{F}$	N	Force vector

---

[1] Theoretical value calculated for $T = 0$ K and $\mathbf{J} = 0$ A/mm^2

Symbol	**Unit**	**Description**
H	m	Coil height
$\mathbf{H}$	A/m	Electric field density vector
H_{c}	A/m	Critical magnetic field intensity
H_{c1}	A/m	First critical magnetic field intensity
H_{c2}	A/m	Second critical magnetic field intensity
H_{t}	A/m	Thermodynamic magnetic field intensity
$i(t)$	A	Current
$i_1(t)$	A	Current during first stage
$i_2(t)$	A	Current during second stage
$I(s)$	A	Current in s-domain
I_{01}	A	Initial current value during the first stage
I_{02}	A	Initial current value during the second stage
$I_1(s)$	A	Current during the first stage in s-domain
$I_2(s)$	A	Current during the second stage in s-domain
$\hat{I}$	A	Peak current
I_{c}	A	Critical current
i_{L}	A	Current flowing through the coil
$\mathbf{J}$	A/m^2	Current density
J_{c}	A/m^2	Critical current density
J_{c0}	A/m^2	Critical magnetic flux density [1]
J_{max}	A/m^2	Maximum current density
k_{R}	Ω/turn	Coil resistance coefficient
k_{L}	Ω/turn^2	Coil inductance coefficient
K_{C}		Carter's coefficient
l_{avg}	m	Average turn length
l_{c}	m	Equivalent magnetic core length
l_{g}	m	Gap length
l_{m}	m	Equivalent magnetic circuit length
L	H	Inductance
$\Delta\mathbf{l}_{\mathrm{ij}}$		Finite length of j-th segment of a i-th turn of a coil
M		Number of segments in a loop approximated by a regular polygon
n		Power value in E-J power law
$N(s)$		Numerator's polynomial in s-domain
N		Number of turns
r	m	Radius
$\hat{\mathbf{r}}$		Unit vector of $\mathbf{r}$
$\mathbf{r}_{\mathrm{ij}}$	m	Distance from j-th segment of a i-th turn of a coil
$\hat{\mathbf{r}}_{\mathrm{ij}}$		Unit vector of $\mathbf{r}_{\mathrm{ij}}$
R	Ω	Resistance
R_{77}	Ω	Resistance @ 77 K
R_{300}	Ω	Resistance @ 300 K

---

[1] Theoretical value calculated for $T = 0$ K and $\mathbf{B} = 0$ T

Symbol	**Unit**	**Description**
R_c	Ω	Equivalent reluctance of magnetic core
R_C	Ω	Charging resistance
R_g	H^{-1}	Magnetic reluctance of air gap
R_m	H^{-1}	Equivalent magnetic reluctance of magnetic circuit
s	rad/s	Complex frequency
t	s	Time
t_C0	s	Capacitor discharge time
t_RL0	s	Current waveform period
T	K or °C	Temperature
T_c	K or °C	Critical temperature
U	V	Voltage
u_C or $u_\mathrm{C}(t)$	V	Capacitor's voltage
U_c	V	Critical voltage
$U_\mathrm{C}(s)$	V	Critical voltage in s-domain
U_C0	V	Capacitor's initial voltage during discharge
U_D1	V	Voltage drop on diode D_1
U_D2	V	Voltage drop on diode D_2
U_DC	V	DC voltage
$\mathbf{v}$	m/s	Velocity vector
V	m^3	Volume
W	J	Energy
$\hat{W}$	J	Peak energy
Y_{01}	S	Initial admittance (I_{01}/U_C0)

Greek Symbols

Symbol	**Unit**	**Description**
ρ	Ωm	Resistivity
τ	s	Time constant
δ	m	Skin depth
Δ		Discriminant of a polynomial
μ	H/m	Magnetic permeability
μ_0	H/m	Magnetic permeability of vacuum
μ_r		Relative magnetic permeability
$\phi_\mathrm{B}(t)$	Wb	Magnetic flux
ξ		Damping coefficient
ξ'		Adjusted damping coefficient
ω	rad/s	Frequency
ω'	rad/s	Adjusted frequency
ω_0	rad/s	Resonant frequency
ϱ_S	C/m^2	Surface charge density
ϱ_V	C/m^3	Volumetric charge density
ρ_V	kg/m^3	Material density
ϱ_S	C/m^2	Surface Charge density
ε	F/m	Electric permittivity
ε_0	F/m	Electric permittivity of vacuum
ε_r		Relative electric permittivity
χ_dia		Magnetic susceptibility of diamagnetic

Abbreviations

Symbol	Description
CMDC	Controlled Magnetic density Distribution Coil
CSM	Critical state model
FC	Field cooling
GS	Growth sector
GSB	Growth sector boundary
HTS	High-temperature superconductor
LTS	Low-temperature superconductor
MPSC	Multi-pulse sequential cooling
MMPSC	Modified multi-pulse sequential cooling
PFM	Pulsed-field magnetisation
TFM	Trapped-field magnet
TSMG	Top-seeded melt growth
ZFC	Zero-field cooling
RLC	Series connection of resistance (R), inductance (L) and capacitance (C)
ReBCO / ReBaCuO	Rare-earth Barium Copper Oxide
YBCO / YBaCuO	Yttrium Barium Copper Oxide
GdBCO / GdBaCuO	Gadolinium Barium Copper Oxide
BiSCCO / BiSrCaCuO	Bismuth Strontium Calcium Copper Oxide
Nb_3Sn	Niobium-Tin
NbTi	Niobium-Titanium

Mathematical symbols

Symbol	Description
$\lceil \cdot \rceil$	Ceiling of a number
$\lfloor \cdot \rfloor$	Floor of a number
$\approx$	Approximately
$\propto$	Proportional to
$\mathscr{L}^{-1}$	Inverse Laplace transform
$\mathbb{C}$	Set of complex numbers
$\mathbb{R}$	Set of real numbers
$\boldsymbol{\nabla}\varphi$	Gradient of φ
$\boldsymbol{\nabla} \cdot \mathbf{B}$	Divergence of $\mathbf{B}$
$\boldsymbol{\nabla} \times \mathbf{A}$	Curl of $\mathbf{A}$
j	Imaginary number $\sqrt{-1}$

Abstract

High-temperature superconducting (HTS) bulks can be used as a source of a strong magnetic field, exceeding that of permanent magnets. One of the techniques to magnetise superconducting bulks is the pulsed-field magnetisation (PFM) method, which utilises short pulses of current generated by flux pumps.

The research presented in the thesis focuses on the influence of the RLC flux pump system with emphasis on the description of current and magnetic field waveforms generated by the flux pump. The extensive literature review suggested minuscule exploration of magnetic field rate-of-change on the trapped magnetic field inside the HTS bulk; instead, most of the conducted research focused on applying stronger fields.

The developed methodology of designing a solenoidal coil for the PFM system is presented to achieve desired features of the flux pump, like a peak of magnetic field and its rate-of-change. A generalised mathematical description relevant for the single and multi-pulse operation of the RLC flux pump was derived. The analysed system has been designed and constructed to verify the influence of magnetic field gradient experimentally over time on the effectiveness of the PFM process for three designed coils. The trapped field inside the bulk cooled with liquid nitrogen was measured on the surface with seven linear-hall sensors in transient and steady states.

Numerical models based on the finite-element method (FEM) were created to verify and expand the results of the measurements. The mathematical description of the flux pump circuit was used to generate the current waveform in the FEM simulations. The numerical simulation provided an insight into otherwise unmeasurable values such as current density distribution within bulk and power losses during pulsed-field magnetisation.

Experimental and numerical results had confirmed that increasing applied field rate-of-change results in higher trapped fields at lower peak values in a consistent manner. As a consequence, the designed PFM system, especially coil, can be smaller and used inside devices such as electrical machines as a source of magnetic field replacing permanent magnets.

Streszczenie

Wysokotemperaturowe nadprzewodniki (ang. high-temperature superconductor, HTS) masywne (ang. bulks) mogą służyć jako źródło silnego pola magnetycznego wyższego niż wytwarzane przez magnesy trwałe. Jedną z metod magnesowania nadprzewodników masywnych jest magnesowanie pulsacyjne (pulsed-field magnetisation, PFM) wykorzystujące krótkie impulsy prądowe wygenerowane za pomocą pomp pola.

Badania przedstawione w niniejszej rozprawie doktorskiej skupiają się na analizie pompy pola typu RLC, w szczególności w zakresie wyznaczenia przebiegów zmian prądu i pola magnetycznego wytworzonego przez te pompy. Przeprowadzona analiza literatury przedmiotu wykazała niewielką liczbę badań wpływu szybkości zmian pola magnetycznego na pole magnetyczne zamknięte w nadprzewodniku masywnym, lecz większość badań skupiona jest na zadawaniu pól o większych wartościach.

Metodologia projektowania cewek solenoidalnych przeznaczonych do pomp pola magnetycznego została opracowana i opisana. Metodologia ta pozwala na osiągnięcie pożądanych parametrów pompy tj. wartości szczytowej oraz szybkości zmian wytworzonego pola magnetycznego. Dokonano opracowania uogólnionego opisu matematycznego pompy pola typu RLC przeznaczonej do pracy jedno- i wielo-pulsowej. Analizowany układ pompy został zaprojektowany i skonstruowany w celu weryfikacji eksperymentalnej wpływu gradientu pola w czasie na efektywność procesu magnesowania pulsacyjnego dla trzech zaprojektowanych cewek. Pomiar pola magnetycznego zachowanego w nadprzewodniku masywnym chłodzonym z wykorzystaniem ciekłego azotu w temperaturze 77 K został zrealizowany przy wykorzystaniu siedmiu czujników hallotronowych umieszczonych na powierzchni nadprzewodnika. Umożliwiło to zarejestrowanie zmian pola w stanach przejściowych i w stanie ustalonym.

Opracowany został model numeryczny bazujący na metodzie elementów skończonych (MES) w celu weryfikacji i rozszerzenia uzyskanych danych pomiarowych. Opracowany model matematyczny pompy pola został wykorzystany jako źródło prądu w przygotowanym modelu MES. Zastosowany model pozwolił na uzyskanie danych niedostępnych lub niemierzalnych tj. rozkład gęstości prądu wewnątrz nadprzewodnika, lub straty wytworzonych wewnątrz nadprzewodnika w stanach przejściowych podczas magnesowania.

Wyniki badań eksperymentalnych i numerycznych potwierdziły wzrost zachowanego pola magnetycznego wewnątrz nadprzewodnika wraz ze wzrostem szybkości zmian przyłożonego pola magnetycznego. Uzyskano większe wartości uwięzionego pola magnetycznego wewnątrz nadprzewodnika przy mniejszych wartościach szczytowych przyłożonego pola magnetycznego.

Przeprowadzona analiza umożliwia opracowanie mniejszych, kompaktowych pomp pola magnetycznego, w szczególności pozwala na zmniejszenie rozmiaru cewek magnesujących nadprzewodniki, które wykorzystywane są wewnątrz innych urządzeń jako źródła pola magnetycznego zamiast magnesów trwałych np. silniki elektryczne.

1

Introduction

1.1. Background and motivation

In recent years an increase of interest in superconductivity has been observed, especially in high-temperature superconductivity [1]. It can be attributed to the discoveries of new materials displaying superconducting properties at temperatures much closer to room temperature (20°C) than ever before [2]. A new family of ferrite compounds known as pnictides showing superconducting properties has been discovered in the last 15 years. Many of the compounds achieving superconductivity at higher temperatures usually also require high pressures measured in the range of gigapascals (GPa) [3]. The research groups continue the pursuit of room-temperature superconductivity.

There are few areas of commercial applications where high-temperature superconductors are used, which is due to possibility of using liquid nitrogen cooling. These applications are: power electric transformers [4, 5], superconducting fault current limiters (SFCL) [5], superconducting bearings [4, 6], superconducting magnetic energy storage (SMES) [4] or power cables [5]. Compared to the conventional materials used in electrical engineering - copper and aluminium; superconductors greatly reduce power losses. This allows for conducting high currents, which results in a high value of magnetic flux density.

Superconducting coils are used as a source of strong, DC, or low-frequency AC magnetic field, where achieving values of a couple of teslas is possible [7, 8], however high-frequency AC current of significant value can also pass through superconductors [9]. The coils are wounded using superconducting wires, consisting of multiple HTS tapes. To achieve higher values of magnetic fields, it is necessary to increase the size of the coil using the same wire. As the coil grows in size, the difficulty of cooling increases since the coolant has to be delivered to all parts equally, without creating hot-spots, which might result in quench.

Another way to create high magnetic fields is to utilise bulk superconductors instead of superconducting coils. The results published by [10, 11] had shown the possibility of achieving trapped fields over 17 T. This is possible due to the high cross-sectional area of superconducting material inside the bulks, compared to HTS tapes where current can flow. In order to trap the magnetic field inside the bulk superconductor, a flux pump is used, which job is to produce sufficiently high fields. There are three basic methods of trapping magnetic field inside the superconductor - field cooling (FC), zero-field cooling (ZFC) and pulsed-field magnetisation (PFM).

The main interest of the following research presented in the thesis is the pulsed-filed magnetisation, which differs from FC and ZFC in such a way that it relies on producing short pulses of a strong magnetic field rather than slowly applying a field to the superconductor (ZFC) or phase transition under the influence of magnetic field (FC). This allows for the minimisation of a coil used for magnetisation since the pulse lasts for a fraction of seconds. On top of that, the pulses can be applied multiple times to increase the total value of a trapped magnetic field.

Superconductors can replace some of the conventional materials used in power converting devices to increase their efficiency. Substituting neodymium magnets for HTS bulks producing magnetic fields of a few teslas would increase power and torque density of electric machines [12–14]. Such a feature could be beneficial for driving the propeller of an aircraft [15], where reduction in mass is desired. Another area of application could be in particle accelerators, and small, portable MRI or NMR apparatus, where currently large low-temperature superconducting coils are used, cooled with liquid helium, which could be replaced by HTS bulks [16, 17]. Last but not least, the high-field trapped-field magnets can be used in highly sensitive electromagnetic fluid velocimeters [18].

1.2. Pulsed-field magnetisation in the literature

To generate a current pulse, a pulse generator is used in the form of a capacitor bank, and a switch [19]. The circuit can be made as a quasi-sine wave or asymmetrical pulse-current generator [20]. The capacitor bank could be charged from the power supply or from an electrical grid via full-bridge rectifier [21]. An effect of different source voltage values has been investigated [22], and it has been shown that higher voltages result in higher peak currents, thus higher trapped fields. To further increase the voltage in the system, a voltage multiplayer can be used [23–25]. The analysis of the influence of flux pump parameters is presented in [26], but in a limited scenario for given values of R, L and C, as well as twofold change in values. The circuit has additional diodes to prevent current oscillation. Depending on the values of circuit components, the system can operate also as an oscillatory circuit [19], overdamped [27] or with critical damping [28, 29].

It is also possible to control pulses via a solid-state switch, i.e. transistor to modulate the pulses [30], which allows more precise control of the current waveform.

The pulses can be applied multiple times [31], to increase the value of stored flux, although there seems to be a limit to the amount of trapped field, depending on the number of pulses. The limit is related to the power losses and temperature diffusion within the bulk. There seems to be an optimal amount of pulses, which, if exceeded, results in a decrease of trapped flux [32]. It has been shown that the presence of a larger ferromagnetic core increases the stability of trapped field with consecutive pulses [33] with sufficient cooling.

In the multi-pulse methods, it has been noted that the shape of the trapped field after the first pulse should be M-shaped (along the bulk's diameter), rather than inverted V-shape, to achieve higher fluxes in consecutive pulses [34, 35].

An improvement to the multi-pulse method has been introduced in the form of a modified multi-pulse technique with stepwise cooling (MMPSC), where bulk is cooled to lower temperature with each pulse. Such an approach has shown greater stability of trapped field during magnetisation and increases it value significantly [36–38].

There are three commonly used types of coils for pulsed-field magnetisation - solenoid, split coils and controlled magnetic density distribution coil (CMDC) being a combination of multiple split coils [39]. It has been shown that solenoids generally provide lower magnetic flux density since the magnetic field penetrates from the sides. In the split-coil system, the magnetic field penetrates more from the top and bottom rather than the sides, resulting in higher trapped fields compared to the solenoid [40].

Devices used for magnetisation are called magnetisers, which could be with or without a ferromagnetic core. A ferromagnetic material creates a path of low reluctance for the magnetic field. The presence of core increases trapped field by focusing the flux acting on the bulk [41]. Although it has to be noted that values of the applied field presented in [41] are higher than 2 T at peak, which results in saturation of the core.
It has been shown that the system with two cores and split coil performs better than with a solenoid and core with only on one side of the bulk [28]. A good performance of the system with core has been proven for fields above 3 T [42] for both split and solenoid coils.
The shape of a ferromagnetic core in the magnetising circuit plays a role. The authors of [43] tested various shapes of the core in the vicinity of the bulk. The cylindrical core provides uniform magnetic flux density, whereas the ring-shaped core focuses the flux on the circumference rather than the center. The cross-shaped core was also used to match the location of growth-sector boundaries on the bulk.

The influence of the dimensions (outer/inner diameters and height) of the solenoid coil on the pulsed-field magnetisation has been analysed [44]. The coils presented by the authors [44] have similar performance, although a bit different time constants. The coil with a larger inner diameter tends to reach optimum flux density at lower values of the applied field, whereas the coil with smaller diameters reaches higher trapped fields but at higher applied flux densities. The split-coil is a derivative from axial-flux machine armature winding [45]. In the split coil system, the outer radius of the coil should be between values of bulk outer radius and half of it [46], which provides the highest values of the trapped field. The CMDC coil can be used to generate high magnetic flux densities locally [47–49]. In these systems, the peak of the trapped field creates a ring shape around the bulk, whereas in systems with solenoids, it is more uniform, reaching a peak value at the center.

Most widely researched high-temperature superconducting materials for pulsed-field magnetization are GdBaCuO (T_c = 95 K) [23, 24, 33, 38, 45, 48, 50–59], MgB$_2$ (T_c = 39 K) [28, 31, 60–75] and YBaCuO (T_c = 91 K) [20, 41, 76–81]. The popularity behind rare-earth high-temperature superconductors is the possibility of cooling with liquid nitrogen (77 K) due to high T_c and performance enhancement when cooled to lower temperatures with cryocoolers. The MgB$_2$ has a lower cost compared to already mentioned superconductors and low weight but requires much lower temperatures to achieve superconductivity. Besides bulk superconductors, HTS tape stacks with (RE)BaCuO superconductors are also utilised successfully [82–87].

The trapped fields created using pulsed-field magnetisation can be at values of a couple of teslas, way above 1.4 T [88] compared to the strongest neodymium magnets. Over the years, the trapped magnetic flux density increased consistently with a better understanding of the phenomenon occurring in the superconductors. The value of peak flux density of 4.5 T has

been reached for YBaCuO bulk at 77 K [89]. Over 5.2 T has been reached for GdBaCuO superconducting bulk by utilising the MMPSC method [90]. A bit lower field of 3 T, but with a different aim of making the PFM system as portable as possible, was achieved for the same superconductor [91]. A major leap in trapped fields was reached in 2003 by cooling the YBaCuO bulk to 29 K to achieve 17.24 T [10]. Much later, the GdBaCuO with shrink-fit steel ring and cooled to 26 K has trapped magnetic flux density of 17.6 T [11]. Another type of used bulk superconductors used for magnetisation are HTS tape stacks, one of which made out of SuperPower (RE)BaCuO tape with artificial pinning centers has reached 13.5 T at a temperature of 10 K [92], whereas a hybrid stack reached 17.7 T at 8 K [93].
An important observation from the pulsed-field magnetisation study was that the rate-of-change of applied magnetic field plays an important role in achieving flux jumps [91], which can be exploited to achieve higher values of trapped fields [94], although the literature on that topic is insufficient.

The comparison between bulks of different diameters has been made and shown that for larger diameters, the flux cannot intrude into the center of the bulk. Thus higher trapped fields are achieved for smaller diameters in a single pulse system [37]. Although, it has to be noted that a much higher field can be reached for bulks of larger diameters if the multi-pulse method is used [52]. Since the superconductors form crystals, the crystalline structure also plays a role. In places where the seed is used, there has been observed the highest values of flux densities [79, 95], regardless of the number of seeds [96]. Another common feature occurring in bulk superconductors is the presence of growth sectors (GS) separated by growth sector boundaries (GSB). Higher values of the trapped field have been measured on the GSB rather than GS, which is attributed to higher pinning force in those regions allowing for better flux penetration [53, 54, 97–99].

An important phenomenon occurring during pulsed-field magnetisation is a flux jump [94, 100, 101]. For low values of applied magnetic flux densities, the trapped field has a peak value forming a ring shape on the surface, close to the edges of the bulk, and a low value of flux density at the center of it (M-shape). The flux jump occurs after reaching a certain threshold value of an applied field, resulting in a sudden increase of trapped field at the center of the bulk [77]. One of the culprits behind this phenomenon pointed out could be the temperature increase at the center of the bulk due to heat conduction within [70].

In most cases, the HTS bulks are cooled via cryocooler or submerged directly in liquid nitrogen [22]. The former is rather used to achieve temperatures below 77 K, whereas the latter is used due to ease of usage. There are also other possibilities of cooling with cryogenic liquids such as neon [102], liquid helium [103] or liquid hydrogen [104], but those come at a much higher cost compared to liquid nitrogen.
The effect of temperature on trapped field is significant [105]. It has been shown that type of cryocooler affects the results of pulsed-field magnetisation [106] due to the heat removal capability during the magnetisation. To increase the thermal conductivity from the bulk to the coldhead, therefore increasing its thermal stability, a resin filler can be used [50].

The modelling of pulsed-field magnetisation usually aims to obtain the distribution of current density within the superconducting bulk and magnetic flux density at its surface. These fields are described in the form of partial differential equations, which can be solved by describing the problem in a finite-element method (FEM) solver. This method allows for finding a solution for complex geometries with different material properties.
To calculate the distribution of the aforementioned fields, different electromagnetic PDE formulations are used. Historically the $\mathbf{A}-$formulation was used the most [107–112],

T−formulation [113–117] and **E**−formulation [118–121]. Currently, the most popular formulation seems to be the **H**−formulation [122–133] since the application of nonlinear characteristics of the superconductors is the easiest. During the pulsed-field magnetisation, a significant amount of power losses and heat are generated, which results in a temperature rise within the bulk, especially at higher values of an applied field. This highly affects the critical current density and critical magnetic flux density of the superconductor; therefore, a thermal simulation should be performed [57, 70, 76, 134–137] to more accurately analyse the magnetisation process.

Another important factor taken into consideration is mechanical stress occurring in HTS bulk [29, 138, 139]. The forces inside the bulk are due to high values of currents within that interact with the crystalline structure of the bulk, which is prone to fracture [57]. In addition, the high magnetic fields generated by the bulk also result in high forces when interacting with other objects [136]. This requires a reinforcing ring around the bulk to improve both mechanical and thermal stability [140, 141].

1.3. Aim of the research

The literature review presented in the previous section has set a goal for the following thesis, which is the study of the circuit used for pulsed-field magnetisation and its components on the PFM process.

It has been noted that the RLC flux pump can be used as a pulse generator [19, 20]. The effect of the voltage of capacitance on the trapped field has been studied in a limited way [22, 142]. There has been a study describing the circuit with a nonlinear characteristic of the superconductor and influence of a number of coils turns on the peak value of current, and magnetic flux density [143]. There is also an analytical description of magnetic flux distribution produced by the coil, which was compared to the solution produced by finite-element method [144]. The study of coil dimensions on the effect of the trapped field has been made for particular cases of solenoid [44] and split coils [46]. There has not been a comprehensive guide for designing such flux pumps from an electric circuit point of view and the influence of coil construction on the current waveform. The influence of circuit parameters on the current rate-of-change and peak value has not been described in a consistent manner but has been mentioned as one of the deciding factors when it comes to pulsed-field magnetisation [91]. The presence of ferromagnetic core also plays a role in HTS bulk magnetisation [28, 41, 43] but its effect on the current waveform has not been described throughout.

In numerous publications [28, 29, 32, 41, 138, 139, 144–149] applied field is produced by current density source (1.1) or more commonly as magnetic flux density source (1.2), both described as waveforms resulting from a critically damped RLC oscillator, which is a special case of such a circuit [28, 29]. The RLC circuit for a pulsed-field magnetisation has been described as oscillatory [19] and overdamped [27], but in a limited way.

$$J_{\mathrm{s}}(t) = J_{\max}\frac{t}{\tau}\exp\left\{1-\frac{t}{\tau}\right\} \tag{1.1}$$

$$B_{\mathrm{s}}(t) = B_{\max}\frac{t}{\tau}\exp\left\{1-\frac{t}{\tau}\right\} \tag{1.2}$$

The research indicates the importance of applied field rate-of-change on flux jumps, resulting in higher trapped fields [91, 94], although the focus is usually on applying fields of higher magnitudes instead [94, 100, 101]. The partial-differential equations used for modelling superconductivity **T**−formulation (1.3) and **H**−formulation (1.4) use derivative of field as the source.

$$\nabla \times \rho\nabla \times \mathbf{T} = -\mu\frac{\partial\left(\mathbf{T}-\nabla\Phi\right)}{\partial t} - \frac{\partial \mathbf{B}_{\mathrm{s}}}{\partial t} \tag{1.3}$$

$$\nabla \times \rho\nabla \times \mathbf{H} = -\mu\frac{\partial \mathbf{H}}{\partial t} - \frac{\partial \mathbf{B}_{\mathrm{s}}}{\partial t} \tag{1.4}$$

The following research hypothesis can be formulated:

An influence of the circuit parameters, especially coil inductance in flux pump dedicated for pulsed-field magnetisation of superconductors, have an influence on the trapped magnetic field. The effectiveness of pulsed-field magnetisation of high-temperature superconducting bulks at 77 K can be enhanced by both the peak magnetic field and its gradient over time.

The effectiveness is the subject of an improvement and comparative analysis and can be expressed in terms of magnitude and distribution of trapped fields inside the bulk.

1.4. Object of the research

The objective of the thesis is to investigate the system for generating a standing wave of magnetic field - the flux pump dedicated for the pulsed-field magnetisation of superconducting bulks. The system is composed of the coil, represented in the schematic of the equivalent circuit model shown in Figure 1.1 as a series connection of resistance R and inductance L. The coil converts electrical energy to the magnetic field that is used for the magnetisation of superconducting bulk. The capacitor bank is represented in the lumped circuit model as single capacitance C and serves as a source of current pulses.

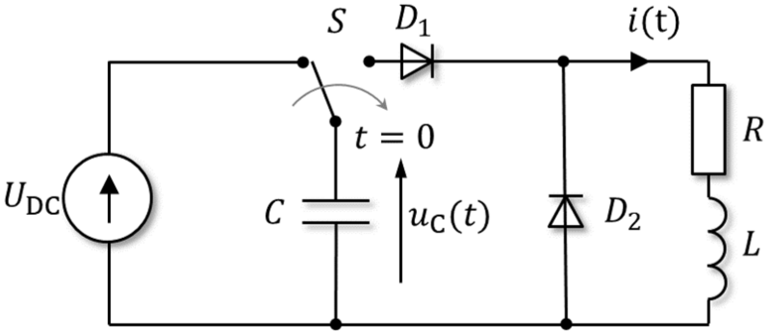

Figure 1.1. Flux pump lumped circuit model

The analysis focuses on the influence of circuit parameters R, L and C on the current waveform, as well as the design of the coil to achieve a magnetic field of required parameters - peak value and its rate-of-change. The research is narrowed to the examination of a solenoid-type coil. The effect of a different number of turns with the same wire and different wires with a different number of turns is studied. The magnetisation of superconductors is done for different voltages and capacitances. The investigation is conducted for one YBCO bulk shown in Figure 1.2 with a diameter $D_{\mathrm{HTS}} = 28$ mm and height $H_{\mathrm{HTS}} = 10$ mm that is cooled with liquid nitrogen, thus operating at 77 K.

Figure 1.2. YBCO bulk used for experimental investigation

Two coils using the same wire were primarily designed, constructed, and tested in the system with different capacitance and applied voltages to test the stated hypothesis. As a result of conducted measurements, the third coil has been designed and analysed experimentally in the setup, with the most promising outcomes derived from the previous analysis to conclude the hypothesis.

1.5. Thesis outline

The following thesis has been divided into eight chapters, each subdivided into sections and subsections for clearer division of discussed topics:

Chapter 1 is the current chapter, which contains the background and motivation behind the following thesis, a review of the literature related to the pulsed-field magnetisation and the hypothesis coming from the conducted survey.

Chapter 2 describes the fundamental properties of superconducting materials with an emphasis on the topics related to the HTS bulk magnetisation, but also a general overview of topics related to the superconductors, including history, discoveries and applications.

Chapter 3 aims to present a pulsed-field magnetisation in a broader view compared to what has been described in Chapter 1. An overview and description of magnetisation methods, systems and coils is presented.

Chapter 4 presents the design and modelling of the flux pump dedicated for pulsed-field magnetisation of bulk superconductors. The research is based on analysis of lumped circuit model of the flux pump and the influence of pump parameters - resistance, inductance and capacitance on the current waveform. The magnetic circuit of the coil for bulk magnetisation is designed and analysed to achieve design goals.

Chapter 5 describes experimental measurements of the PFM system. The results are compared with numerical models of the flux pump derived in the previous chapter. The analysis is carried out for different setups, where current waveforms are obtained and magnetic flux densities are measured. The measurements are made for different voltages and capacitance of the flux pump.

Chapter 6 contains information related to the modelling electromagnetic systems with a finite-element method. A general approach to solving partial differential equations is described as well as topics related directly to modelling superconducting materials. The chapter aims to present a numerical analysis using FEM to evaluate trapped magnetic flux densities inside the bulk superconductors during pulsed-field magnetisation achieved using the analysed circuit. The data is compared with the experimental results.

Chapter 7 is dedicated to the discussion and summary of the whole thesis, where conclusions are derived from obtained experimental and numerical data. Future research regarding flux pumps for HTS bulks is also proposed.

At the end of the thesis, the bibliography and attachments are located.

2

Fundamentals of superconductivity

The following chapter focuses on introducing and presenting basic information regarding superconductivity, mainly high-temperature superconductivity. Superconductivity is a relatively old branch of science that was first discovered at the beginning of the 20th century and has seen rapid growth since the discovery of high-temperature superconductivity in 1986. This phenomenon can be analysed from different perspectives - condensed-matter physics that lies in between quantum physics and material science, which can be named a microscopic point of view, and electrical engineering standpoint, which would be a macroscopic or engineering viewpoint. The low-temperature superconductivity has been successfully explained by London theory [150], Ginzburg-Landau theory [151], as well as BCS theory [152], the exact mechanism behind high-temperature superconductivity, is still debatable, not to say - mysterious [153].

In the first Section 2.1, a brief introduction to the history of superconductivity and how it compares to regular conductors is presented using electromagnetism to explain the occurring phenomenon. In the second Section 2.2 critical parameters are discussed for superconducting materials, which is followed by 3rd Section 2.3 discussing relations between those values. In the next Section 2.4 the line between LTS and HTS materials is drawn by comparing those materials from a material engineering point of view that results in anisotropic behaviour of HTS. Section 2.5 has been dedicated to the description of losses occurring in superconducting materials. The Critical State Model has been presented in Section 2.6 which describes the magnetisation of superconductors in a simplified way. Section 2.7 describes applications of the low-temperature superconductors briefly since these are widely used nowadays, whereas Section 2.8 is dedicated to showcasing the present and future applications of HTS materials.

2.1. Fundamental properties

The superconductivity phenomenon is a rapid decrease in resistivity of certain materials with a decrease in temperature. Although this phenomenon occurs at low, cryogenic temperatures, scientists still work on materials to achieve this phenomenon at room temperature without extremely high pressure.

Heike Kamerlingh Onnes first discovered superconductivity in 1911, which was done when he worked on achieving lower temperatures. The mercury sample was used to indirectly measure the temperature by measuring its resistivity. During the measurement, a sudden decrease of sample resistance was observed at around 4.2 K, which coincidentally is close to the boiling temperature of liquid helium. The measured value dropped to almost zero, thus hinting at the first observation of a new phenomenon for which Onnes won the Nobel Prize in physics in 1913 [154]. Superconductivity is a characteristic feature of many non-magnetic materials, yet it is not limited to these. Most superconductors in the normal state are often good conductors (i.e. aluminium), but not excellent conductors (i.e. copper or silver)[155, 156]. Below critical temperature T_c superconductors experience phase transition from normal to the superconducting state and fulfil both conditions:

1. the material lacks electrical resistivity ($\rho = 0$); currently measured values shows that it drops to values at the order of 10^{-26} Ωm [157];
2. the magnetic field is expulsed from inside of the material, which is known as the Meissner-Ochsenfeld effect or Meissner effect, where the material becomes a perfect diamagnetic;

Perfect conductivity is not equivalent to the existence of the superconducting state. According to Ohms law: $\mathbf{E} = \rho\mathbf{J}$ for a perfect conductor, there is no electric field inside $\mathbf{E} = 0$. When applying this condition to Faraday's law of induction (2.1), it states that the magnetic field inside the object is constant but not necessarily zero, thus making the second condition mandatory.

$$\begin{cases} \nabla \times \mathbf{E} = -\dfrac{\partial \mathbf{B}}{\partial t} \\ \mathbf{E} = 0 \end{cases} \implies \frac{\partial \mathbf{B}}{\partial t} = 0 \tag{2.1}$$

The Meissner effect - the total expulsion of the magnetic field from the superconductor - is a more fundamental feature of superconductors compared to lack of resistivity. This effect proves the existence of a new thermodynamic phase and phase transition [155]. In most of the materials, superconductivity and ferromagnetism are contradicting phenomenons. The existence of a local magnetic moment within the material is enough to destroy superconductivity. Although, recently, in 2008, a new family of iron-based superconductors was discovered, which occurs in iron pnictide compounds [158].

Above the critical temperature, the flux lines easily penetrate through the object as shown in Figure 2.1a. If the material will transition to a superconducting state without the presence of external sources of magnetic field and it will be applied afterwards, according to Faraday's law of induction (2.1) screening currents will be induced inside the material. These currents will prevent the magnetic field from penetrating the structure of the material, as presented in Figure 2.1b, resulting in zero magnetic fields inside the superconductor. By applying the superposition principle and subtracting the magnetic field shown in Figure 2.1a from 2.1b, the magnetic field created by screening currents will be as shown in Figure 2.1c.

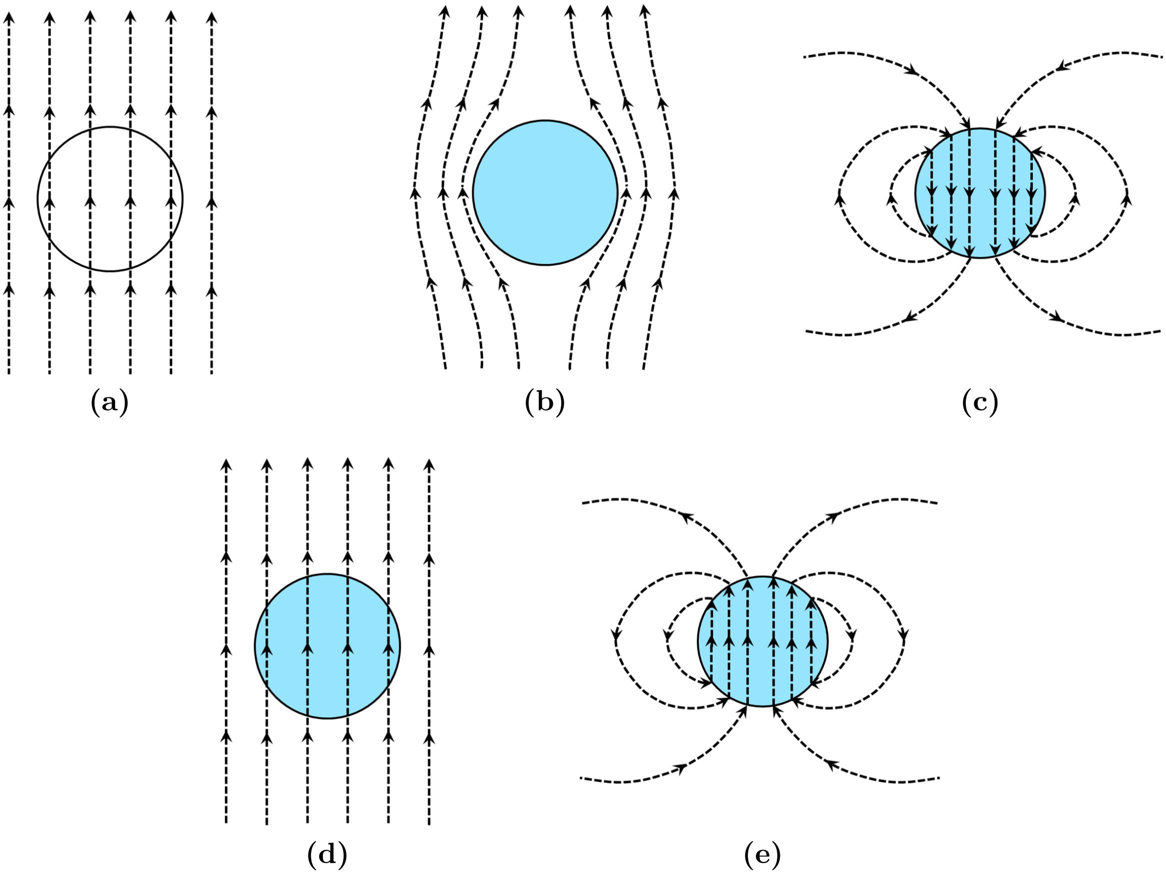

(a) **(b)** **(c)** **(d)** **(e)**

Figure 2.1. Distribution of magnetic field inside and around superconductor: (a) above critical temperature; (b) applying magnetic field after cooling superconductor below T_c; (c) after cooling superconductor below T_c with applied external magnetic field; (d) applying external magnetic field during phase transition from normal to superconducting state; (e) trapped field inside the superconductor

However, if the material will transition to a superconducting state in the presence of an external magnetic field and achieve perfect conductivity, as shown in Figure 2.1d, it will not expulse the magnetic field from the inside. Instead, however, it will become a source of the magnetic field itself. Thus, the magnetic field passing through the superconductor during phase transition will be "memorized" by the object as presented in Figure 2.1e. This is possible due to the existence of persistent current flowing through the material with no resistivity; therefore, losses [155, 159].

2.2. Critical parameters of superconductors

Every superconducting material can be described by three parameters related to its operational limits, at which the transition from superconducting to normal (resistive) state occurs [160, 161]. These are known as critical parameters, which are [162]:

- *critical temperature* T_c;
- *critical flux density* B_c or *critical field intensity* H_c;
- *critical current density* J_c;

When one of these parameters is exceeded, the transition between superconducting and normal state is known as *quench*, due to its rapid transition.

Critical temperature is the main factor determining whether the phase transition occurs in material. Below T_c, the material stays at a superconducting state and, at higher temperatures than that, reaches the normal (resistive) state. The value of critical temperature varies with material, purity, mechanical stress, pressure, or external magnetic field influence. The temperature dependence of resistivity is visualised in Figure 2.2.

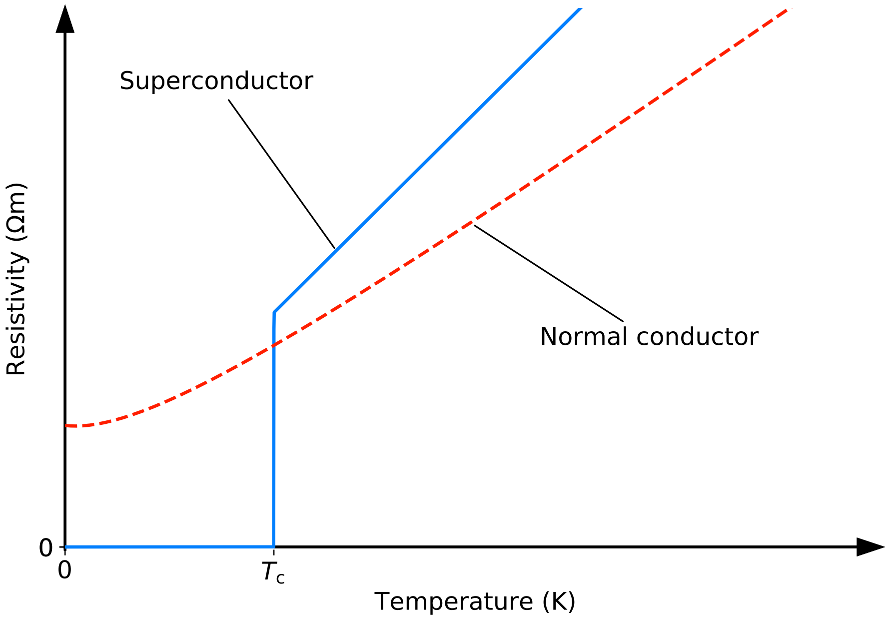

Figure 2.2. Change of resistivity with temperature in conductors and superconductors

Over the years, multiple research groups and institutions worldwide have been set on a conquest to find a material that will achieve superconductivity at room temperature and atmospheric pressure. Currently, only a handful of discovered superconducting materials are in use. Most commonly used are: Nb_3Sn, NbTi, BiSrCaCuO, YBaCuO, GdBaCuO and MgB_2 marked in Figure 2.3 [1, 2]. The first two compounds are mostly used in commercial and research applications such as particle accelerators, MRI, nuclear fusion due to ease of manufacturing and well-understood physics behind it, even though those require liquid helium for cooling. Other mentioned compounds are high-temperature superconductors. The magnesium diboride is a recent discovery that is promising due to ease of manufacturing [6].

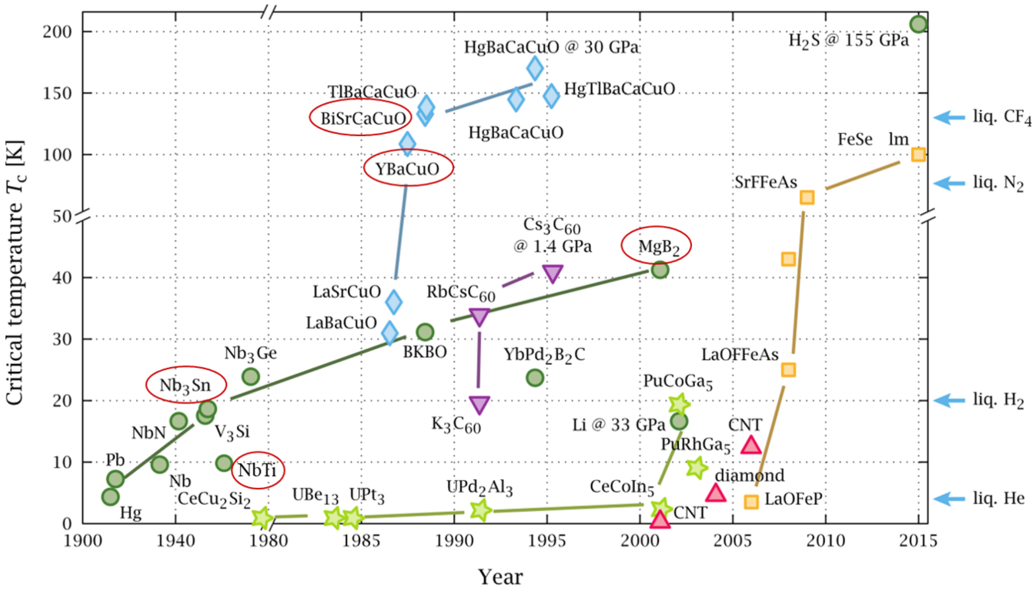

Figure 2.3. Graph of selected superconducting materials over time of their discovery with corresponding critical temperature [1, 2]

Critical magnetic field relates to either magnetic flux density B_c or field intensity H_c acting on a superconductor. It can either be a self-induced field due to current flow through the superconductor itself or applied from an external source. Therefore, the state of the superconductor is a superposition of the total magnetic field, both external and internal. A single value of critical field H_c in type-I superconductors describes the transition point from superconducting to the normal state. In type-II superconductors, there are two distinct values of the critical magnetic field due to the existence of three different states:

- below H_{c1} - superconducting state;
- between H_{c1} and H_{c2} - mixed (Meissner) state;
- above H_{c2} - normal state;

For type-II superconductors, usually, the value of the second critical field H_{c2} is used due to the fact that $H_{c1} \ll H_{c2}$. This means that in applications, type-II superconductors operate in a mixed state. The critical magnetic field can be estimated as in (2.2) [4]. The dependence between the magnetisation of a superconductor or the opposing field induced by the superconductor and the applied magnetic field has been shown in Figure 2.4.

$$H_c \approx \sqrt{H_{c1} H_{c2}} \tag{2.2}$$

In *Meissner state* or *mixed state*, some magnetic flux penetrates the structure of the superconductor [160]. This magnetic flux is quantized and has a value of [155]:

$$\phi_0 = \frac{h}{2e} = 2.0678 \cdot 10^{-15}\ \mathrm{Wb}$$

where: $h = 6.62607015 \cdot 10^{-34}$ J · s is the Plack's constant; $e = 1.602176634 \cdot 10^{-19}$ C is the elementary charge.

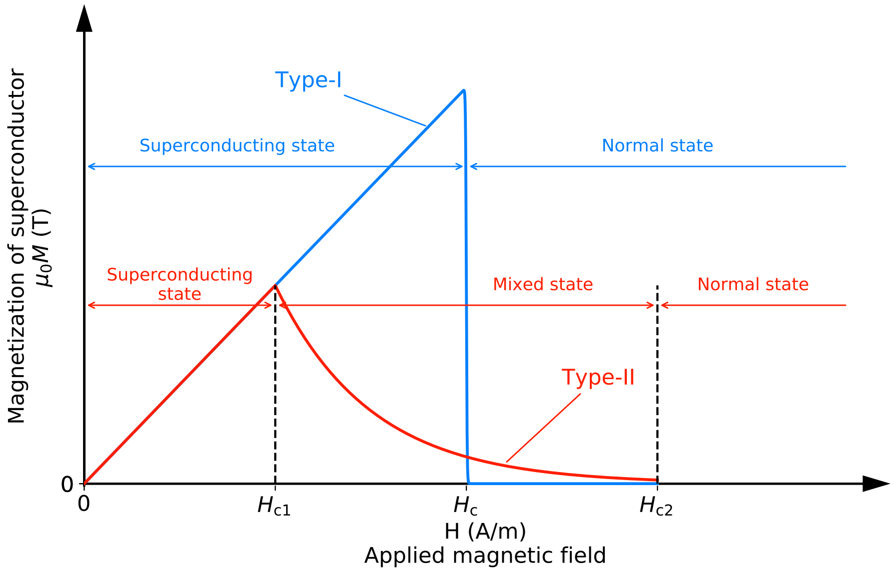

Figure 2.4. Magnetisation of type-I and type-II superconducting materials

The quantized magnetic flux penetrates regions where quantum vortexes are created, circulating currents within the superconductor structure. At the center of such a vortex, the material is in a normal state. The quantum vortex can flow through the material in the superconducting state. These currents flow in such a direction to sustain the flow of magnetic flux. Two parameters characterize quantum vortices: coherence length ξ_c and magnetic field penetration depth λ. The coherence length depends on temperature and tends to infinity when temperature increases to T_c. The vortex has a core diameter equal to $2\xi_c$. The magnetic field penetrates according to the structure of the superconductor according to (2.3) [156]:

$$B(x) = \hat{B}_{\mathrm{app}} \mathrm{e}^{-x/\lambda} \tag{2.3}$$

When the magnetic field increases, more flux penetrates through the material, and more vortexes are created. This happens up to reaching H_{c2} where there is no space to fit all vortexes on the superconductor's surface, thus destroying superconductivity and material transitions to the normal state. The mixed state of superconductivity from a thermodynamic point of view is also called *Abrokosov* or *Abrikosov-Schubnikov state*. In this state, the material can still lack resistivity but is not an ideal diamagnetic. The mixed state is a complex phenomenon in itself. For high enough magnetic fields and temperatures, the vortexes can create a *fluid vortex phase*. In this phase, the screening currents can be induced while the resistivity of the material is non-zero. When analysing the magnetic properties of superconductors, the object size and dimensions are essential. When an object has an uneven shape in some regions, the magnetic flux density **B** can be zero, whereas, in others, it could be non-zero. For type-I superconductors, some regions may reach B_c and be in a normal state, and others may still be superconducting, which changes the effective geometry (the part which is superconducting) of the object. In type-II superconductors, regions may be locally in one of the three phases [155]. To determine at which different phase regions of objects are, usually, the finite-element method is required.

In literature, there are two ways of approaching the superconducting phenomenon on the macroscopic level [159]:

1. The superconductor can be analysed as an object with properties of perfect diamagnetic ($\chi_{\mathrm{dia}} = -1$), which has a distribution of diamagnetic magnetic moment inside. The screening currents here are not considered explicitly. In this approach, the relation between magnetisation $\mathbf{M} = \chi_{\mathrm{dia}}\mathbf{H}$, applied magnetic field intensity $\mathbf{H}$, and the magnetic flux density $\mathbf{B}$ inside the object as shown in Figure 2.4 resulting in net-zero field inside the superconductor (2.4).

$$\mathbf{B} = \mu_0 \left(\mathbf{H} + \mathbf{M}\right) = 0 \tag{2.4}$$

2. The superconductor can be treated as a non-magnetic object with magnetic permittivity of vacuum ($\mu = \mu_0$) in which stationary currents are flowing.

Critical current density J_{c} is a parameter describing the maximum value of current density flowing through superconducting material. For type-I superconductors, the value of J_{c} is equal to transport current for which the self-field reaches the value of critical field intensity H_{c} within the superconductor [5]. In type-II superconductors, the definition of critical current density is much more complicated due to current vortexes in a mixed state. The value of J_{c} is higher than the current density responsible for magnetic field intensity of H_{c1}, yet lower than the current density creating H_{c2}. Therefore, the definition based on critical field intensity is not applicable [4].

Critical current density definition is thus based on *thermodynamic magnetic field intensity* H_t which is between 1st and 2nd critical field intensity $H_{\mathrm{c1}} < H_{\mathrm{t}} < H_{\mathrm{c2}}$ [5]. The critical current density J_{c} depends in reality on the mobility of quantum vortices in the superconductor. Every quantum vortex experience Lorentz force according to (2.5)[159].

$$\mathbf{F} = q \left(\mathbf{E} + \mathbf{v} \times \mathbf{B}\right) \tag{2.5}$$

With an increase of the magnetic field acting on the superconductor, the mobility of quantum vortices increases resulting in power losses, effectively causing a decrease of critical current. Impurities within the material structure can minimise the movement of those vortices in a superconducting material, which can be deliberately placed, thus creating localized potential wells for vortices to reside. The value of J_{c} in type-II superconductors correlates with the degree of defects in structure and can differ between samples of the same material.

Due to presented above difficulties, it is possible to define J_{c} based on the voltage drop criterion. *The critical current density* J_{c} *is a value of current density at which electric field inside the superconductor is equal to critical electric field* E_{c}. The value of E_{c} varies, but typically it ranges from 1 $^{\mathrm{\mu V}}/_{\mathrm{m}}$ to even 100 $^{\mathrm{\mu V}}/_{\mathrm{m}}$, depending on application and safety margin [4]. This definition of critical current density can be used as a comparative value describing features of superconducting materials in practical applications [155]. The relation between electric field and current density has been primarily described by Anderson-Kim model [163], but nowadays, the E-J power law is used, given by (2.6). The value of $\mathbf{E}$ is associated with the vector field. However, the lumped measurement results in voltage drop U across the sample of a given length when direct current I flows through as in (2.7). The U-I characteristics for different powers of n are shown in Figure 2.5.

$$\mathbf{E}(\mathbf{J},\mathbf{B},T) = \operatorname{sgn}(\mathbf{J}) E_\mathrm{c} \left(\frac{|\mathbf{J}|}{J_\mathrm{c}(\mathbf{B},T)} \right)^n \tag{2.6}$$

$$U(I,\mathbf{B},T) = U_\mathrm{c} \left(\frac{I}{I_\mathrm{c}(\mathbf{B},T)} \right)^n \tag{2.7}$$

Lower values of n mean stronger flux creep, and higher values represent stronger pinning. The critical state model (CSM) assumes that either absolute value of current density is equal to $|J_\mathrm{c}|$ or 0, which corresponds to $n \to \infty$. It has also been shown that values of power n depend on HTS operating conditions - magnetic field and temperature [164].

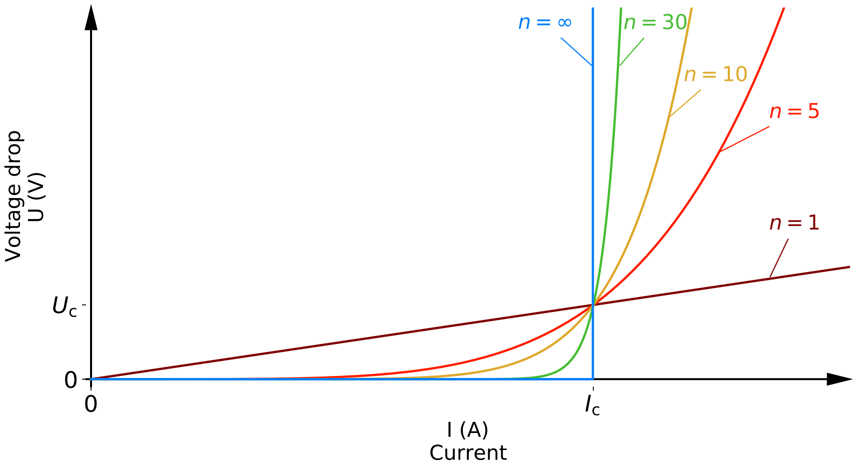

Figure 2.5. Voltage-current characteristics for different powers n

The critical parameters commonly used in superconducting materials have been listed in Table 2.1 [6]. Due to the crystalline structure of superconductors, there is a high anisotropy in principal axes in some materials, which mostly occurs in HTS. This results in different values of critical field acting perpendicular to a-b plane of crystalline structure denoted with subscript ab and perpendicular to c-axis denoted with subscript c. In both cases, there are two values of the critical magnetic field.

Table 2.1. Parameters of selected superconducting materials

Name	**Type**	**Critical temperature**	**Critical current**[1]	**Critical flux density**[2]	
NbTi	LTS	9.5 K	> 10 kA/mm^2	$B_\mathrm{c0} = 15$ T	
Nb$_3$Sn	LTS	18 K	> 100 kA/mm^2	$B_\mathrm{c0} = 32$ T	
MgB$_2$	LTS	39 K	≈ 10 kA/mm^2	$B_\mathrm{c0} = 74$ T	
YBCO – 123	HTS	92 K	≈ 200 kA/mm^2	$B_\mathrm{c1ab} = 520$ T $B_\mathrm{c1c} = 53$ T	$B_\mathrm{c2ab} = 650$ T $B_\mathrm{c2c} = 140$ T
BiSCCO – 2212	HTS	85 K	≈ 1 kA/mm^2	$B_\mathrm{c1ab} = 0.1$ mT $B_\mathrm{c1c} = 19 - 22$ mT	$B_\mathrm{c2ab} = 650$ T $B_\mathrm{c2c} = 140$ T
BiSCCO – 2223	HTS	110 K	≈ 2 kA/mm^2	$B_\mathrm{c1ab} = 0.1$ mT $B_\mathrm{c1c} = 13.5$ mT	$B_\mathrm{c2ab} = 1210$ T $B_\mathrm{c2c} = 39$ T

---

[1] Theoretical value calculated for $T = 0$ K and $\mathbf{B} = 0$ T

[2] Theoretical value calculated for $T = 0$ K and $\mathbf{J} = 0$ A/mm^2

2.3. Phase diagrams

The critical parameters: temperature T_c, magnetic flux density B_c and current density J_c are interdependent [159, 162]. The value of critical current density J_c0 should be given only for the temperature of 0 K, which is unachievable due to laws of thermodynamics; therefore, it is a theoretical value picked for purposes of modelling behaviour of superconductor is described by (2.8), when the temperature approaches T_c, the value of critical current decreases.

$$J_\mathrm{c}(T) = J_\mathrm{c0}\left[1 - \left(\frac{T}{T_\mathrm{c}}\right)^2\right]^{\frac{3}{2}} \tag{2.8}$$

The temperature also influences the value of critical magnetic induction B_c, which value decreases as temperature increases according to (2.9). The value of critical magnetic induction B_c0 is given at a temperature of 0 K and no applied current flowing through the superconductor.

$$B_\mathrm{c}(T) = B_\mathrm{c0}\left[1 - \left(\frac{T}{T_\mathrm{c}}\right)^2\right] \tag{2.9}$$

In the case of type-I superconductors, the diagram splits space into two states - superconducting (below the surface) and normal (above). As long as the operating point stays within the boundary given by the surface, the superconductor remains superconducting. For type-II superconductors, the phase diagram splits space into three states: superconducting, mixed and normal. Both values of critical magnetic flux density B_c1 and B_c2 are described by (2.9) with adequate subscripts. The dependence between temperature and magnetic flux given by (2.9) has been shown in Figure 2.6. The critical current density also depends on the applied magnetic field. The influence of magnetic field and temperature on critical current density is given by (2.10).

$$J_\mathrm{c}(\mathbf{B}, T) = J_\mathrm{c}(T)\left(1 + \frac{|\mathbf{B}|}{B_\mathrm{c}(T)}\right)^{-1} \tag{2.10}$$

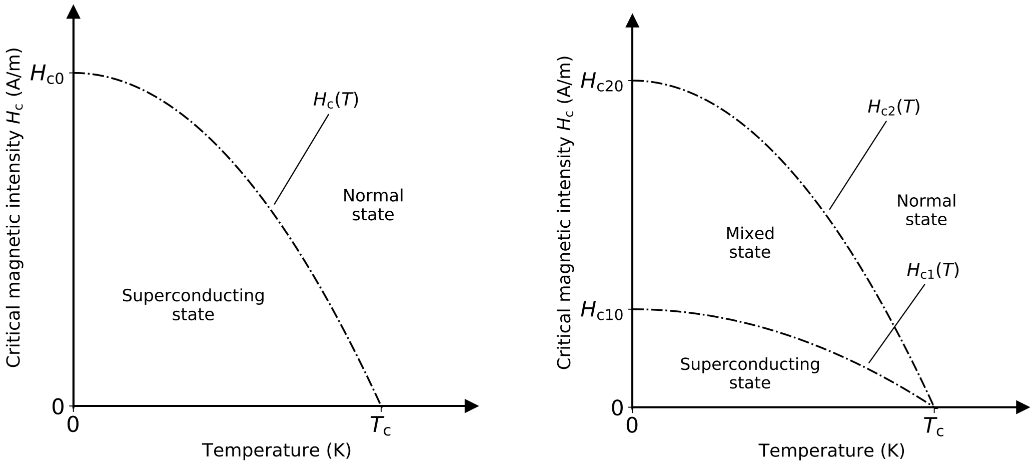

(a) **(b)**

Figure 2.6. Critical magnetic field intensity with respect to temperature for (a) type-I superconductors; (b) type-II superconductors

Equations (2.8), (2.9) and (2.10) all form a set of equations that are describing a general behavior of superconducting material when exposed to temperature and magnetic field of known value [155, 161]. These equations describe both type-I and type-II superconductors, and results can be represented as the three-dimensional surface of critical parameters Figure 2.7. Finally, the value of critical current density influences the value of electric field intensity E_c through (2.6). The influence of magnetic field and temperature on the E-J power law is shown below. From a practical point of view, where voltage and current are measured, the (2.6) can be expressed in terms of current I and voltage U across sample giving U-I power law described by (2.7) [159]. When critical current I_c decreases due to an increase of temperature or magnetic field, the U-I characteristics is presented in Figure 2.8.

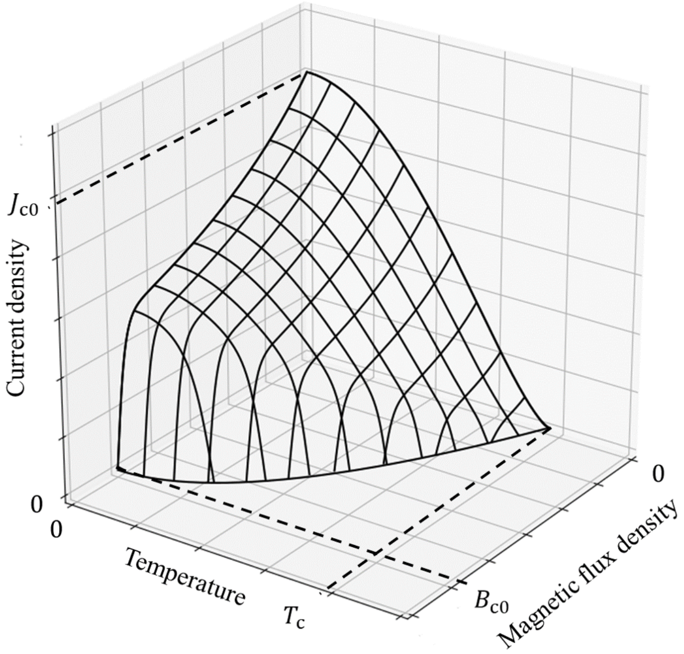

Figure 2.7. Boundary surface of critical parameters of superconducting materials

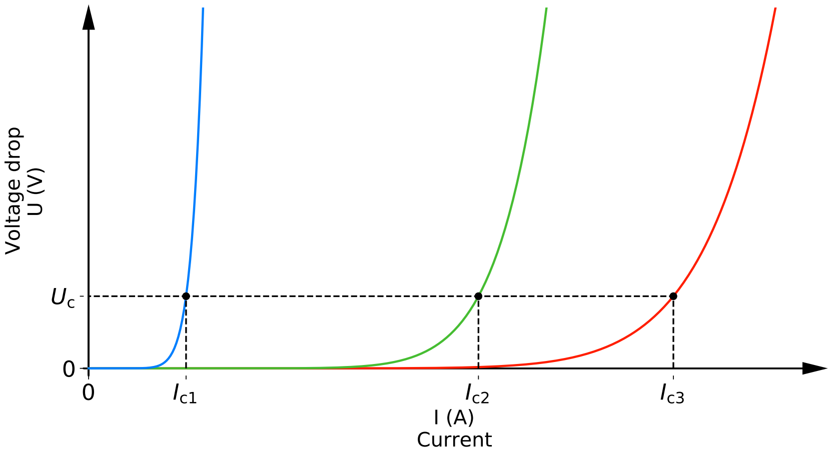

Figure 2.8. Voltage across superconductor with respect to current through superconductor for different critical currents

2.4. Anisotropy

Low-temperature superconductors usually are pure elements (i.e., lead, aluminum) or simple compounds (Nb_3Sn) shown in Figure 2.9a, which form a crystal lattice [162]. On the contrary, high-temperature superconductors are most likely ceramic materials formed by many different elements. High-temperature superconductivity was discovered in cuprate (copper-oxide compound) like LaBaCuO in 1986 [165]. It is worth mentioning that copper-oxide is not a superconductor itself. A characteristic feature of high-temperature superconductors at the atomic level is the existence of copper-oxide planes (a-b plane), which seems to be the key to the superconductivity phenomenon [166]. These planes are responsible for anisotropic properties in cuprate-based HTS and are also visible in other compounds such as YBCO and BSCCO shown in Figures 2.9b and 2.9c respectively [5, 155, 159, 161].

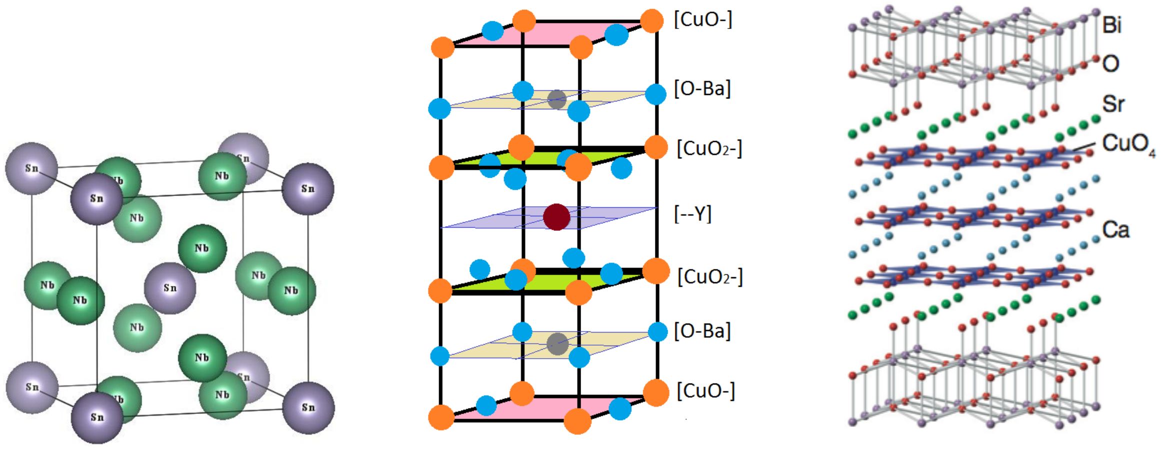

(a) **(b)** **(c)**

Figure 2.9. Crystalline structure of superconducting materials (a) Nb_3Sn; (b) YBCO; (c) BSCCO

In crystalline structure of presented HTS materials, there are three principal axes - a, b, c. The highest value of critical current occurs in the copper-oxide planes, which is the a-b plane. In the c-axis, perpendicular to copper-oxide planes, the critical current can be even tenfold smaller due to much lower conductivity [160, 167]. However, the magnetic field acting perpendicular to the a-b plane decreases the value of J_c the most [168]. This is due to the formation of quantum vortices on the plane in the mixed state, which increases local current density. However, the magnetic field acting perpendicular to the c-axis (parallel to a-b plane) has the smallest effect on critical current density [155]. The perpendicular and parallel components of the magnetic field acting on the structure are essential to the operation of HTS devices. Therefore, the values of these components (mostly perpendicular) are affecting critical current density. The effect of this anisotropy can be incorporated into (2.10), which results in the empirical formula known as Kim's equation (2.11) [159].

$$\begin{aligned} J_c(\mathbf{B},T) &= J_c(T)\left(1+\frac{\sqrt{(k\cdot B_{\|})^2+B_{\perp}^2}}{B_c(T)}\right)^{-b} \\ &= J_c(T)\left(1+\frac{\sqrt{(k\cdot|\mathbf{B}|\cos\theta)^2+(|\mathbf{B}|\sin\theta)^2}}{B_c(T)}\right)^{-b} \end{aligned} \tag{2.11}$$

The components of the magnetic flux density acting on the superconducting tape and the effect of the field acting at a different angle to the tape on its critical current have been presented in Figure 2.10.

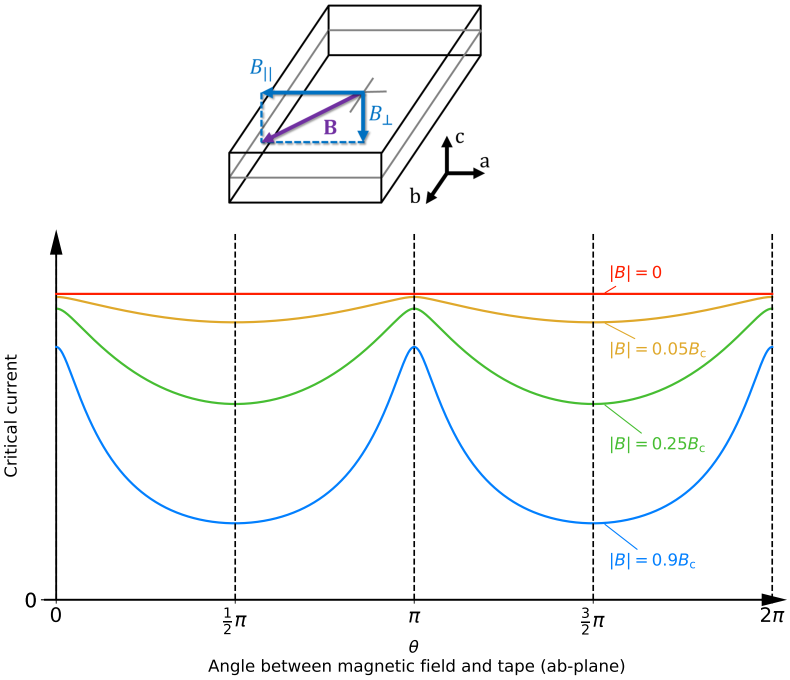

Figure 2.10. Effect of magnetic field on critical current depending on angle between ab-plane and magnitude of magnetic field

High-temperature superconductors mostly come in two forms - superconducting tapes or bulks. To deliver power from a source to a load, HTS tapes are used. Two main kinds of tapes were developed: 1st generation (1G) or 2nd generation (2G) tapes. The HTS material in 1G tapes forms thin strands (Figure 2.11a), whereas in 2G exists in the form of layered structure (Figure 2.11b) [5]. The manufacturing technology of 2G tapes requires additional layers for the orientation of the HTS structure in the desired direction. The layers of HTS material are oriented in such a way as to achieve the highest possible critical current density along the tape's length. The HTS material thickness inside the tape is in order of micrometers. The rest consists of other structures dedicated to HTS crystal alignment like substrate and buffer stacks or stabilisers to provide mechanical rigidity. For example, at the temperature of liquid nitrogen, the *American Superconductor* with 100 µm thickness and 4 mm width, where the thickness of superconductor is 1 µm can conduct up to 100 A of direct current [155, 160, 167].

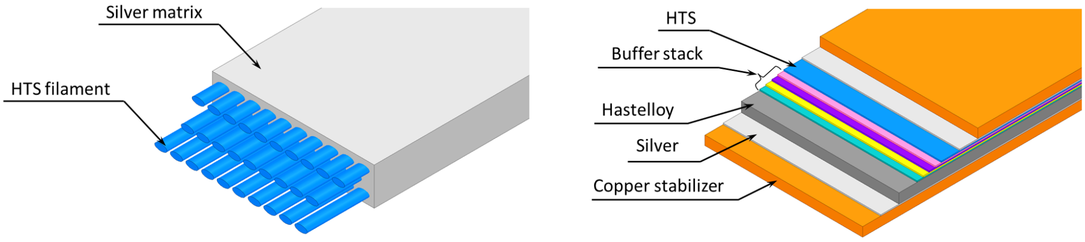

(a) **(b)**

Figure 2.11. Tape construction (a) 1st generation (1G); (b) 2nd generation (2G)

Another way to manufacture superconductors is to form bulk crystals. In most applications, the YBCO superconductor is used. A commonly used method for obtaining HTS bulks is the top-seeded melt growth (TSMG) process. During that process, Y-211 particles (green) are trapped inside the YBCO matrix. Those imperfections in the Y-123 matrix (black) could cause inhomogeneity of critical current in bulk and possibly in output magnetic flux [169]. These bulks have a place from which the crystal growth started. Both forms of YBCO can be seen in Figure 2.12a. The result of the TSMG process is a bulk crystal of superconducting material with an attached seed, which is removed in postprocessing [169]. The seed is a cube from which the growth starts - meaning that its structure becomes repeated. Since the cube facets are squares with two diagonals, these structures are also present in created bulk. These diagonals extend radially from the bulk's center and are called growth sector boundaries (GSB), whereas the area between these boundaries is called growth sectors (GS). The presence of both GS and GSB are presented in Figure 2.12. It has been shown that pinning in GSB is higher than in the GS region [39].

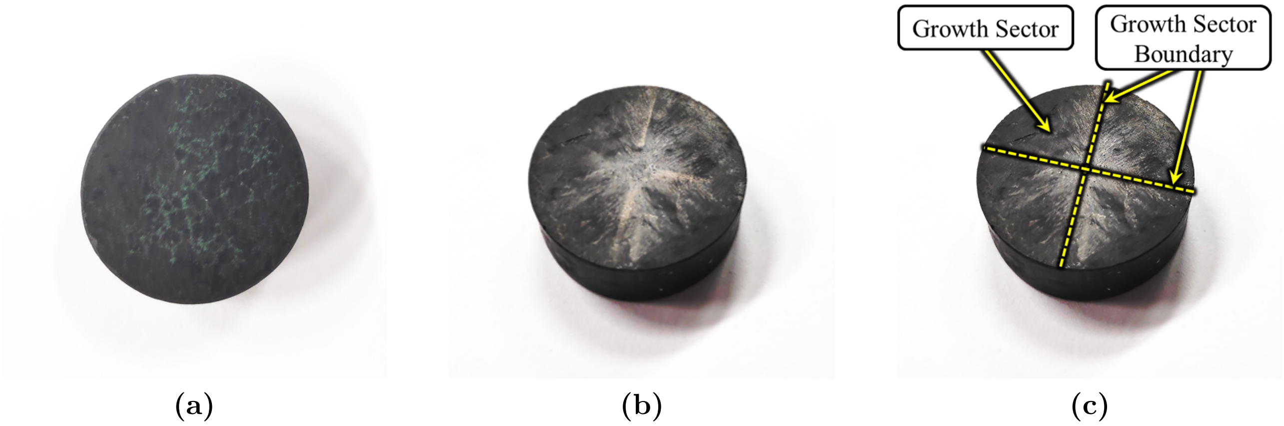

(a) **(b)** **(c)**

Figure 2.12. YBCO bulk with visible: (a) fractions of non-superconducting Y-211 (green) and superconducting Y-123 (black); (b and c) growth sectors (GS) and growth sector boundaries (GSB)

Bulks can be made into different shapes shown in Figure 2.13 and reach dimensions of a couple of millimeters; therefore, currents flowing through these structures are thousands of amperes and can be a source of the magnetic field of couple teslas [162].

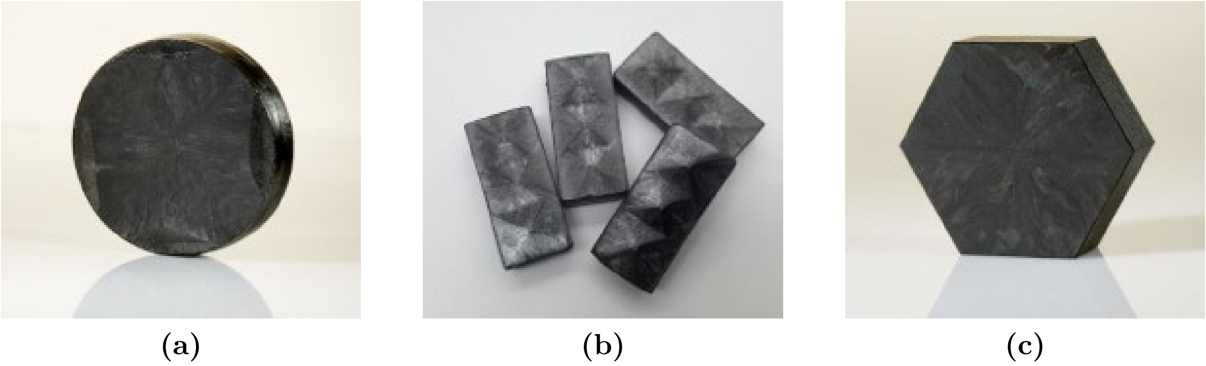

(a) **(b)** **(c)**

Figure 2.13. YBCO bulks: (a) round; (b) square; (c) hexagonal

2.5. Power losses

Resistance arises in ordinary type-II superconductors at low frequencies ($\leq$ 50 Hz) due to flux flow and flux creep. The interest in using type-II superconductors in various applications has increased due to outstanding critical current values and higher critical field values than type-I superconductors. However, the disadvantage of type-II superconductors lies in the mixed state, which leads to magnetic field penetration and fragility of the structure. The superconductors are rarely used independently; instead, they are used in tapes or cables. In other applications, superconducting bulks are used, sometimes with stainless rings around them, to provide mechanical stability in excess mechanical stress. Therefore, in some cases, there is a need to include losses occurring in or due to the existence of these structures. The AC losses in superconductors can be divided into the following categories [155, 159, 161, 162, 170]:

- *transport current losses*
    - flux flow losses;
    - hysteresis losses;
- *magnetisation losses*
    - hysteresis losses;
    - coupling losses;
    - eddy current losses;

2.5.1. Flux flow losses

The quantum vortices experience Lorentz force (2.5) and its value depends on the applied magnetic field and current density. When the value of force is not high enough, the movement of vortices is restricted by potential wells (pinning). On the other hand, with the increase of force or temperature, the potential well is not enough to keep vortices in place, which start to move if pinning is weak or jump in the direction of the applied force from one potential well to another if pinning is strong [171]. When a high-temperature superconductor is exposed to a magnetic field, either self-induced or external, the magnetic flux penetrates through the structure in the mixed state in places where quantum vortexes are forming. The superconductor material is not pure and has some defects in the crystalline structure on which these vortexes can reside due to the existence of potential wells. In pure superconductors, vortexes form an *Abrikosov vortex lattice* [172], where vortexes are arranged as hexagons. When there are randomly occurring defects in the superconductors, these vortexes are arranged randomly and form a *glass vortex state*. The degree of imperfections, therefore, the depth of potential wells, dictates the mobility of vortexes. In order to restrict the movement of fluxons, this means - increases potential barrier for their movement, some imperfections are introduced intro superconductors structure deliberately. These places are called *pinning centers*, which can be created by mixing a ratio of superconducting and non-superconducting compounds. For example, during the production of the YBCO superconductor, there could occur Y-123 (superconducting) and Y-211 (non-superconducting) compounds mixed together during the manufacturing process [173]. Other ways include adding caesium or zirconium in the form of oxides or other compounds [174]. The pinning centers can also be created as small holes in thin films using a laser [175].

2.5.2. Hysteresis losses

The hysteresis losses are created during the demagnetisation of superconductors. When the magnetic field is applied to a superconductor, there is an induced screening current flowing inside the superconductor and has such value that it opposes this magnetic field [159]. This current results in the apparent magnetisation of superconductors. When applied magnetic field changes, this implies that the value or even direction of this current has to change. During this period, losses occur [171] or can be calculated as an area encapsulated by hysteresis loop shown in Figure 2.14. Similarly, hysteresis losses occur when AC current flows through the superconductor and induced self-field opposing change of the current direction and depends on the frequency [161]. Hysteresis losses are dominating part of AC losses in HTS wires, and value depends on frequency [170]. The value of AC losses related to the flow of current through superconductor [171].

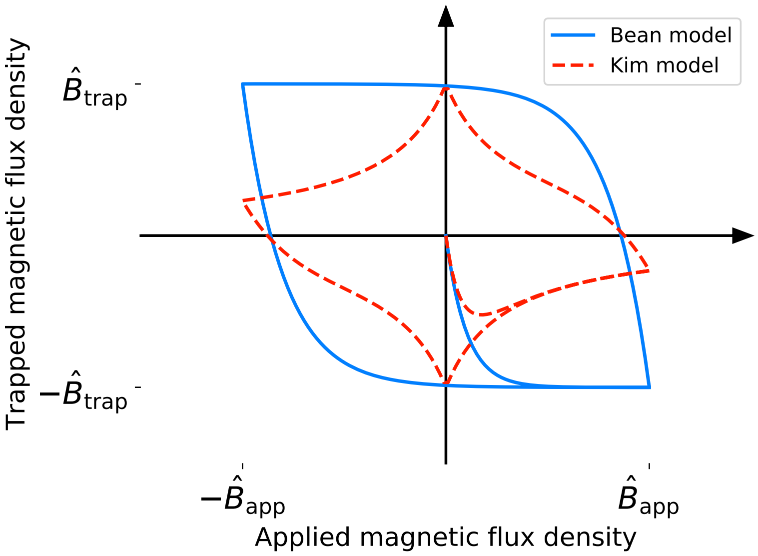

Figure 2.14. Example magnetisation hysteresis of a superconductor obtained numerically with E-J power law using Bean's model ($n \to \infty$), and with applied Kim's model

2.5.3. Coupling losses

The coupling losses may occur in either multifilamentary tapes, wires, or superconducting coils, where turns are not insulated. The losses occur in the stabilizer matrix of wire, which is usually made of copper or silver. The losses are due to current flow through those structures, causing ohmic losses. In order to cause coupling losses to occur, an external magnetic field is required, which forces electrical coupling between neighbouring strands of the superconductor to couple as shown in Figure 2.15. The external AC magnetic field creates eddy currents in every strand of the superconductor and induces voltage potential differences between those. At low frequencies, the currents flow only through superconductors since those have much lower resistivity than the surrounding matrix, which at this point has much higher electrical resistance (Figure 2.15a). For higher frequencies, the potential difference is high enough to force current flow through the matrix between strands. This causes a multifilamentary wire to behave as a single-strand wire, significantly reducing critical current due to increased hysteresis losses (Figure 2.15b). These losses can be minimised by intertwining or twisting strands as for example, in Roebel cable. This technique reduces the effective length of the wire and limits the electric field, significantly reducing coupling between strands. Another way is to introduce a material with high resistivity into the matrix, usually around every strand, which increases the required potential difference for currents to flow between strands [170].

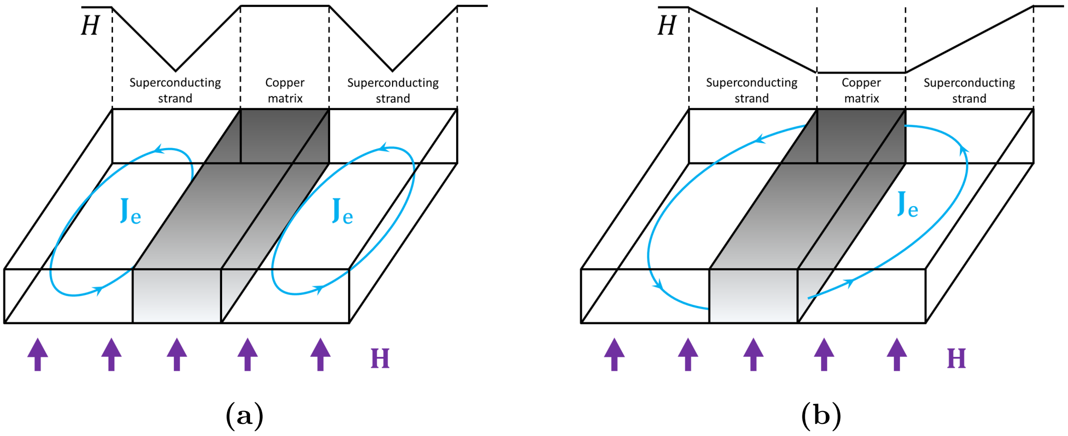

Figure 2.15. Effect of external magnetic field on multifilamentary superconducting wire: (a) no coupling between strands at low field; (b) coupling between strands at high field

2.5.4. Eddy current losses

The eddy current losses are related to the skin effect and occur in the matrix of superconducting wire. Those currents are created when a wire is exposed to the AC magnetic field, which induces an electric field inside the matrix, forcing the current to flow. The current density inside conducting material is not distributed evenly. It decreases with the distance, which strictly depends on material properties such as resistivity ρ, magnetic permeability μ, and frequency f of the magnetic field. The current density decreases exponentially with distance, and the rate of current density change is given by a characteristic parameter known as *skin depth* which can be calculated by (2.12) [176].

$$\delta = \sqrt{\frac{\rho}{\pi f \mu}} \tag{2.12}$$

At low frequencies, the skin depth is negligible, and eddy currents flow through the whole cross-section of the matrix. With an increase of frequency, the current density of eddies starts to be uneven in some places leading to an increase of current density and decrease in others. This decreases effective cross-section of matrix A_{eff} leading to increased Joule losses given by (2.13). For high enough frequencies, eddy currents start to flow only on the surface of the matrix. These losses are proportional to the square of frequency, and the amplitude of the magnetic field $\hat{H}$ [176].

$$\Delta P = \rho |\mathbf{J}|^2 \propto \frac{\rho}{A_{\mathrm{eff}}} f^2 \hat{H}^2 \tag{2.13}$$

To minimise these losses, it is recommended to have a matrix with dimension perpendicular to the magnetic field at most of the size equal to skin depth given by (2.12) for a given frequency. This ensures that current density through this cross-section will be uniform and not cause excessive losses if induced.

2.5.5. Flux creep

During magnetisation, a relaxation of the magnetic field inside the superconductors has been observed. This phenomenon has been named flux creep due to a change of magnetic field gradient. It has been observed in different superconductors, both LTS and HTS. The determining factors seem to be low pinning due to relatively high temperature and strong magnetic field. The relaxation is connected to the vortex movement, leading to power losses due to flux flow. The flux creep is thus responsible for the vanishing of the trapped magnetic field in bulk superconductors [86, 177].

The flux creep is a type of diffusion of vortices within the superconductor and leads to power dissipation over time. Only for low enough current density, where the magnetic field does not exceed H_{c1} the losses do not appear, but such small values for high-temperature superconductors are not sufficient for many applications. Therefore, trapped-field magnets (TFM) will lose stored magnetic fields over time and require periodic magnetisation [86, 177]. With further increase of force or temperature beyond flux creep, which leads to a state *flux flow*.

2.6. Critical state models

The *critical state model* (CSM) is also known as the *Bean's model* and is based on the assumption that the superconductor behaves as an ideal conductor. The CSM can be represented in three key points [178, 179]:

1. The current density can be either equal to critical current density $|J_c|$ in the critical region or 0 in flux free region.

2. When an external magnetic field induces a current in a superconductor, the critical region appears from the object's edges.

3. The distribution of critical current always prevents changes in the magnetic field inside the superconductor.

The magnetisation process begins with a non-magnetised sample. The magnetic field starts penetrating the superconductor from the edges, which results in induced current density equal to J_c (Figure 2.16-1). As the value of the applied magnetic field continues to rise, the magnetic flux penetrates through the superconductor due to quantum vortices (Figures 2.16-2 and 2.16-3). At this point, the magnetic field starts decreasing, which leads to decreasing the value of flux starting from the edges. The gradient of flux density changes locally, thus the direction of current flow (Figure 2.16-4). While decreasing the flux density, the induced net-zero current through superconductor is zero (Figure 2.16-5). As flux continues to decrease (Figures 2.16-6 and 2.16-7), a more pronounced peak magnetic flux density is seen in the center of the superconductor, and the distribution of flux is V-shaped (Figure 2.16-8), but is inverted compared to what is seen in Figure 2.16-2. When magnetic flux is applied further in the same direction, the flux generated by the superconductor shifts, and the current density stay the same (Figure 2.16-9). The process leads to a hysteresis loop since from the first step (Figure 2.16-1) onwards since the magnetic fluxes are adding up, which causes shifting or gradual change in the slope of the field starting from the edges, and the direction of current changes instantaneously.

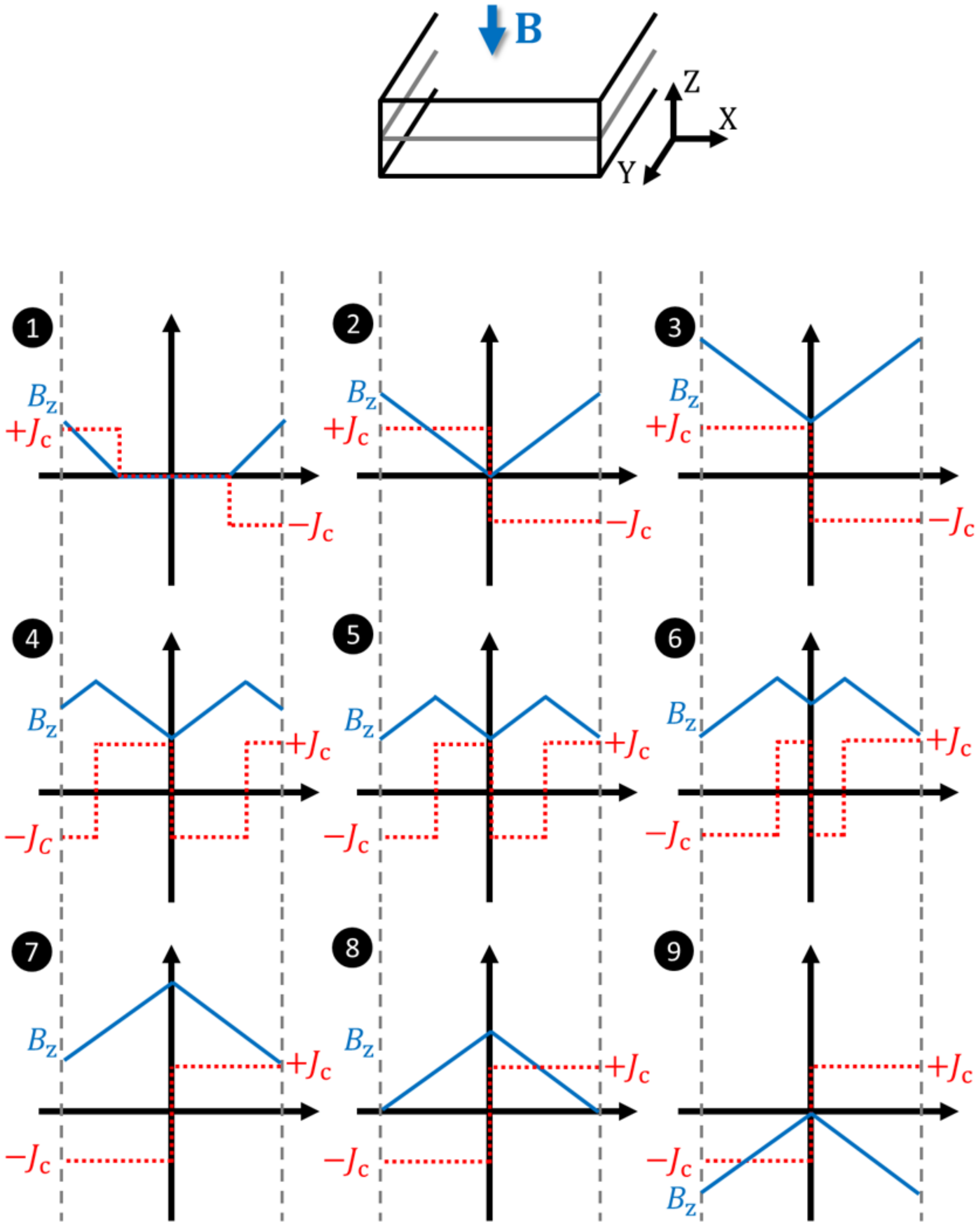

Figure 2.16. Magnetisation of superconductor in steps under critical state model

2.7. Applications of type-I superconductors

The main utilised feature of superconductors is the capability to conduct high current density with little to no losses. The superconductors are manufactured in two primary forms - cables or bulks. Depending on the application, one or the other is used. In most of the applications, low-temperature superconductors are present since those are well examined, with predictable behaviour, and backed up with the well-established theoretical background. This is why cables made of LTS materials are used in medicine, particle accelerators, or fusion reactors. The manufacturing process of LTS cables is simple and is based on repetitive drawings of copper tubes filled with superconducting material to achieve multi-strand wires. The main downside of using LTS is the necessity of cooling with liquid helium (LHe) at the temperature of at most 4.2 K, which is expensive and requires special handling. Although other cryogenic liquids can be used, like neon or argon, the LHe is mostly used due to its safety, relative abundance (compared to neon or xenon), and unique state - superfluidity. Though, high-temperature superconductors are gaining more interest in recent years in some areas [159].

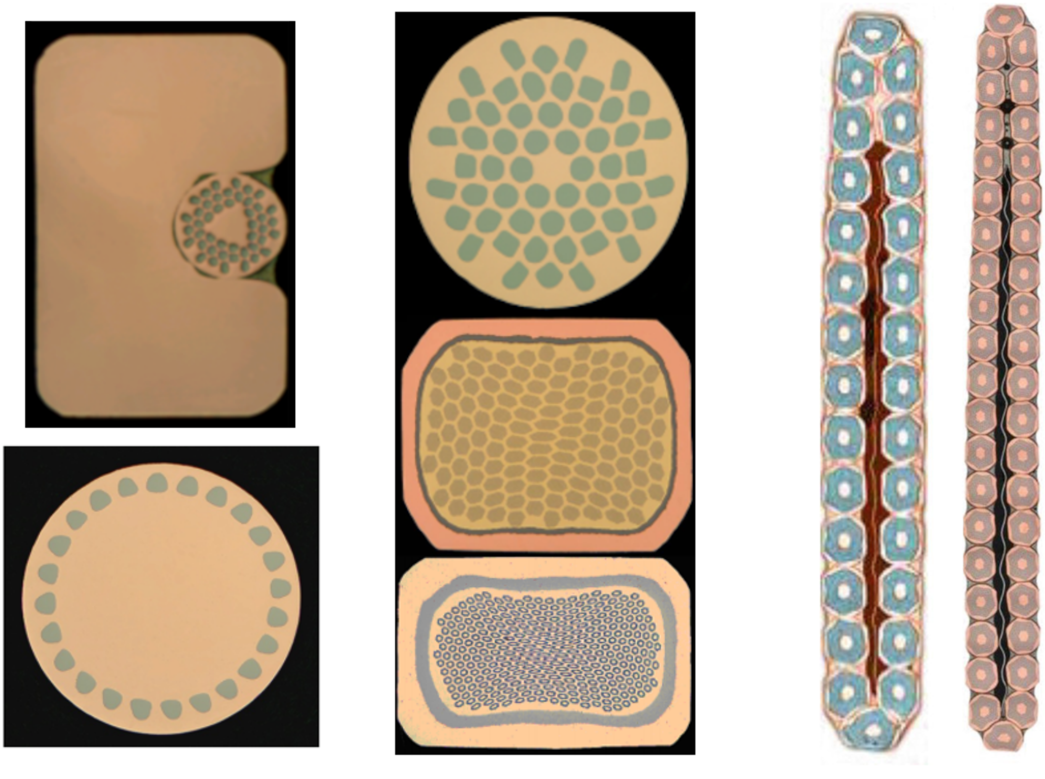

Figure 2.17. Types of LTS cables in systems: (a) MRI; (b) NMR; (c) CERN magnets

The main area of application for superconductors is medicine, where it is used in magnetic resonance imaging (MRI) or nuclear magnetic resonance (NMR). Superconducting cables are used to create a magnetic field of flux densities reaching a couple of teslas. In MRI machines, mainly NbTi low-temperature superconductors are used [161]. For NMR, either NbTi or Nb_3Sn are used [161, 180]. It can be seen that in MRI cables, copper occupies a huge percentage of the cross-sectional area (Figure 2.17a) of the cable in order to increase its thermal stability. In the NMR, such a safety margin for stability is not as important, and the matrix can occupy a lower volume (Figure 2.17b), thus resulting in an overall smaller device. In these machines, coils are usually energized at the manufacturing facility to the nominal value and seldom require boosts of current due to losses occurring on contacts and during operation. The machine also consists of gradient coils that require power supply during operation [162]. LTS are widely used in the field of particle physics, where coils produce high values of magnetic flux density to control the direction of charged particles. In CERN (fr. *Conseil Européen pour la Recherche Nucléaire*), for example, coils are manufactured as Rutherford cables seen in Figure 2.17c, which is different in construction from MRI or NMR multi-strand cables [1, 8]. Here, individual strands are braided and interlaced. The copper matrix consists of much lower volume than in other cables mentioned above to lower cost and wound coils as compactly as possible due to high strain and stress occurring during operation. Besides particle physics, the LTS are used in the new generation of fusion reactors, which supposedly should produce more energy that is required to feed into the system. The coils are also made of Nb_3Sn, and NbTi cables with the cooling channel inside, which are known as cable-in-conduit conductors (CICC) [4, 5, 181].

2.8. Applications of type-II superconductors

So far, high-temperature superconductors will not replace LTS in applications mentioned above, even due to higher critical parameters, with even higher safety margins when cooled with LHe. However, the high-temperature superconductors so far are used in various power electric applications. This is attributed due to liquid nitrogen (LN) that could be used to cool HTS, which is easier to handle and cheaper than liquid helium. The LN also has good insulating properties and has a higher breakdown voltage than SF_6 [4, 170, 181] making it suitable for high-voltage applications.

2.8.1. Cables

Single tape is rarely used to transfer power but rather is combined with multiple tapes to form cables to increase current capacity since cooling and construction of a cable remain similar wheater there is a single strand or multiple. By replacing conventional power lines with superconducting cables, it is possible to increase power density and decrease power losses. Superconducting power cables can be divided into two main categories: with *warm dielectric* and with *cold dielectric*. In cables with warm dielectric only superconductors are cooled, and dielectric operates at its normal temperature, whereas in cables with cold dielectric, the insulation is also exposed to the coolant.

HTS tapes are not used in power cables as parallel straight strands stacked together due to high mutual inductance and high magnetic flux densities acting on tapes, resulting in non-uniform current density shared between tapes, but rather are interlaced in some way. One of the ways to interlace individual tapes is by continuous transposition, also known as Roebell cable, which consists of tapes cut into a shape allowing for intertwining [170] shown in Figure 2.18a. This reduces coupling losses and increases overall current capacity compared to single tape with the same amount of superconducting material inside. Another type of cable is Conductor on Round Core (CORC) cable, where tapes are wounded in a helix on the round core as shown in Figure 2.18b. Both have their advantages and disadvantages - the cross-section of the Roebell cable is smaller compared to CORC, but half of the material is wasted since the tape is cut to obtain a specific shape from a wider tape. On the other hand, the current capacity of CORC cable is lower compared to Roebell, with the same amount of material used. Finally, there are a couple of places where superconducting cables were used to deliver electricity, like, for example, an HTS cable in Essen [5].

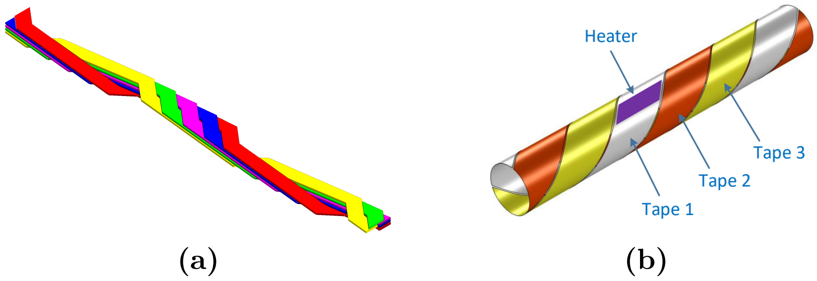

Figure 2.18. Types of HTS cables (a) Roebell; (b) CORC

2.8.2. Superconducting fault current limiters

Superconducting fault current limiters (SFCL) are gaining popularity in recent years due to their astounding properties of rapid current limiting properties and success. In conventional current limiters, the time delay required for opening the circuit is at least equal to half period current waveform in the grid. In SFCL, the current is limited when reaching critical current, which is within the quarter of the waveform cycle and acts instantly as shown in Figure 2.19 [182]. In the nominal operating state, the SFCL has a minimal impedance value, and with an increase of current, the impedance rises due to the transition from superconducting to the normal state of the used superconductor. Another advantage of SFCL is the capability of returning to the normal state on its own when cooled. The principle of operation of superconducting fault current limiters is based on the nonlinear resistivity of superconductors given by E-J power law - when current is low, the superconductor has little to no resistance. With the increase of current, the resistance rises steeply. There are two basic types of SFCL: resistive and inductive.

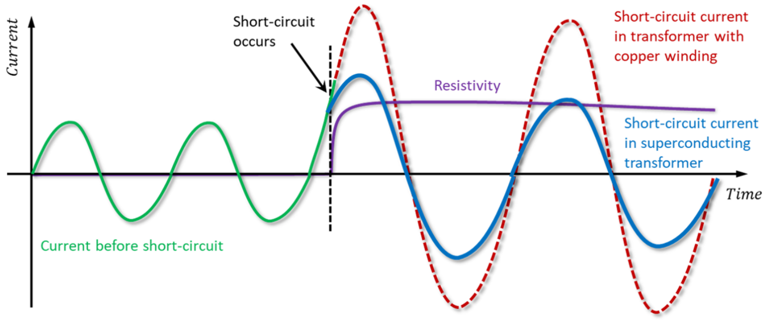

Figure 2.19. Current behavior during fault in system with SFCL (blue) and without (red)

The resistive type is connected in series with a circuit as presented in Figure 2.20a, and when the current exceeds the critical value, the superconductor limits the current due to the increase of resistance. The inductive type SFCL has a similar construction to transformers, as shown in Figure 2.20b. The primary circuit is connected in series with the circuit and usually is made of copper or aluminium. The secondary winding is made of a superconductor, which is shorted. During nominal operation, the magnetic fluxes created by primary and secondary windings counteract each other in the magnetic core, leading to very low impedance. When the current rises in the primary winding, the current flowing through the secondary will exceed critical value and no longer be superconducting. Then, fluxes will not be counteracting, and impedance measured from primary terminals will increase, limiting the current rise. In both types of SFCL, either HTS cables or superconducting bulks are used [5, 182].

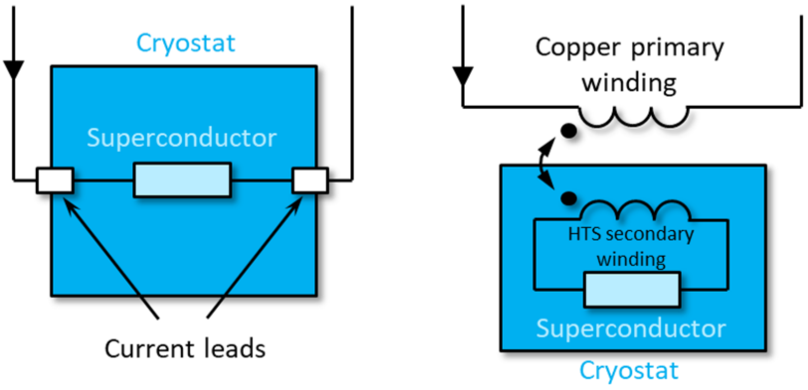

(a) **(b)**

Figure 2.20. Superconducting fault current limiters (a) resistive; (b) inductive

2.8.3. Superconducting transformers

In superconducting transformers, one or both windings are replaced with a superconductor, but usually, it is the low voltage winding replaced with HTS due to high currents. There are two types of superconducting transformers - with warm-core (Figure 2.21a) or cold-core (Figure 2.21b). The *warm core* means that ferromagnetic core is not exposed to cryogenic fluid, whereas in *cold core* it is. Superconducting transformers can serve two functions simultaneously - firstly, transform voltage and current, just as regular transformers; secondly, as current limiters on the same basis as SFCL described above. Since liquid nitrogen has good electrical insulating properties, it is possible to bring windings closer together, decreasing leakage reactance. This decreases the shunt voltage of a transformer; therefore, voltage drop during operation and peak current during short circuit state [4, 5, 182].

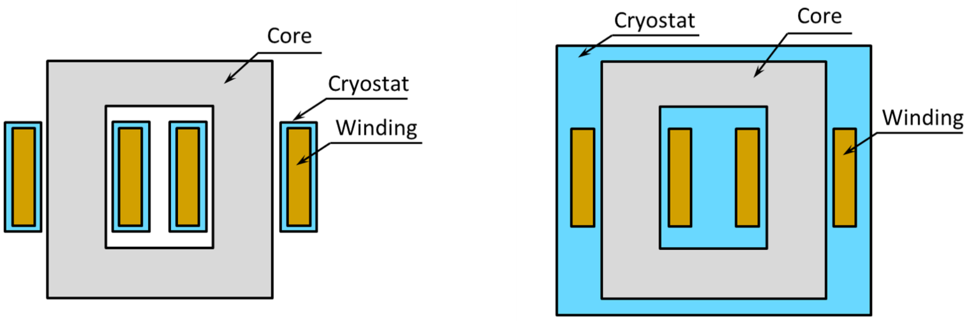

(a) **(b)**

Figure 2.21. Superconducting transformer with (a) warm core; (b) cold core

2.8.4. Superconducting magnetic energy storage

Superconducting magnetic energy storage (SMES) systems store energy in a magnetic field and are designed for rapid bursts of energy to be stored or deployed on demand. The value of energy stored in a magnetic field of a coil can be calculated as $W = \frac{1}{2}Li^2$, which clearly depicts the main advantage of superconductors - high current density. The inductance of SMES coils is in order of magnitude of a few henries. A typical operating circuit for connecting SMES coil to the grid has been shown in Figure 2.22. The primary sources of losses are semiconductors and connections [4, 161].

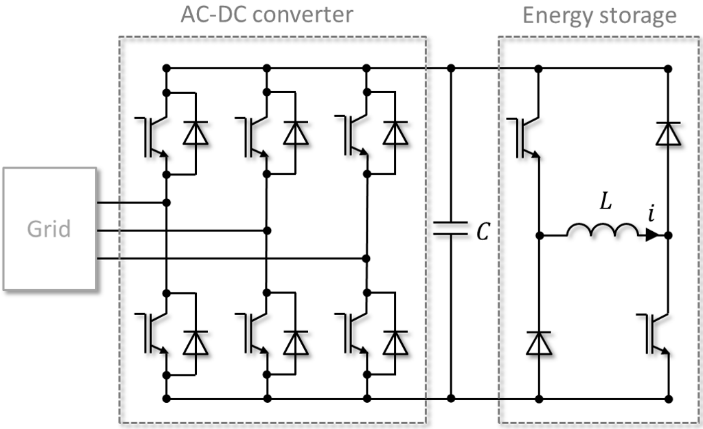

Figure 2.22. Power electronic system with SMES coil

2.8.5. Superconducting machines

Superconductors can also be used in rotating electrical machines like generators and motors. The spectrum of applications is wide. Superconducting coils can be used as armature windings [183] shown in Figure 2.23a, excitation winding [184] or rotor squirrel-cages in induction machines [185]. The design process of superconducting machines require special treatment due to the influence of magnetic field on superconductors [186, 187]. HTS bulks can be used on the rotor, which, when magnetised, can replace permanent magnets in synchronous machines [26] or if not magnetised, the machine can operate as a hysteresis motor, which can be seen in Figure 2.23b. The great advantage of using superconductors in electric machines, or transformers, is the possibility of increasing power density [4, 170].

(a) stator **(b)** rotor

Figure 2.23. Utilisation of superconductors in electric motors as: (a) stator coils [184]; (b) superconducting bulks on rotor [26]

2.8.6. Superconducting levitation

Due to the capability of becoming a source of the magnetic field, the HTS bulks can also serve as bearings in machines, either linear or rotating, as presented in Figure 2.24a [6]. The superconducting bearings provide excellent stability and no mechanical friction during operation. This principle is also explored in superconducting trains such as Maglev or Rapidtrans shown in Figure 2.24b [4, 6].

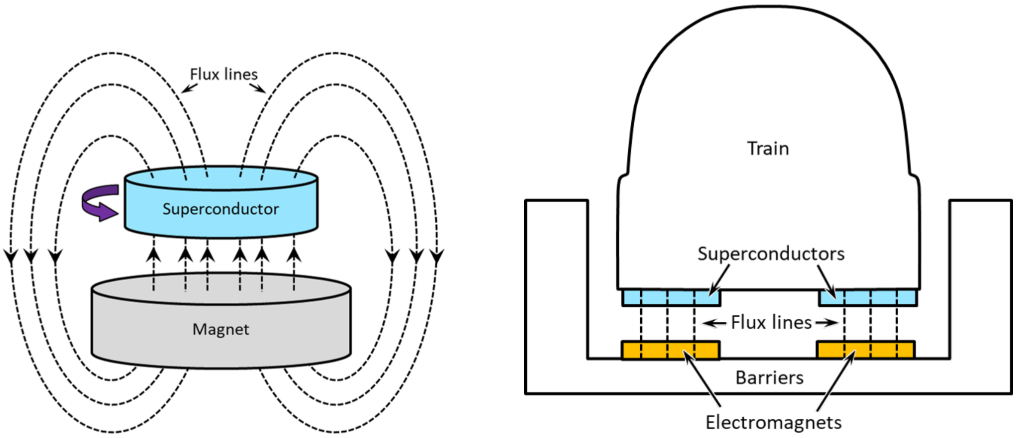

(a) bearing

(b) Maglev

Figure 2.24. Utilisation of superconducting levitation (a) bearing; (b) Maglev

2.8.7. Magnetic cloaking

When an object has relative magnetic permeability significantly different than $\mu_\mathrm{r} \neq 1$, the magnetic field will be disturbed. Magnetic cloaking is a way to cover the surroundings of that object with such a combination of materials or geometry where the external magnetic field is not disturbed [4]. The cloaking can be achieved by combining materials with magnetic permeabilities on two opposing ends of the spectrum - ferromagnetics and superconductors [170]. The superconductor will screen an object placed within the superconducting shell from the magnetic flux (Figure 2.25a), whereas ferromagnetic material will attract it (Figure 2.25b). When combined, the magnetic cloak is formed, which does not disturb the magnetic field on the outside and shields from the magnetic field inside the structure as shown in Figure 2.25c.

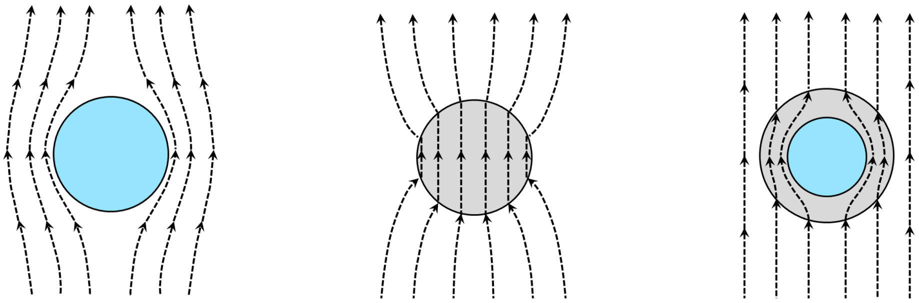

(a) **(b)** **(c)**

Figure 2.25. Magnetic flux lines in different material: (a) superconductor; (b) ferromagnetic; (c) superconductor surrounded with ferromagnetic

2.9. Summary

Although superconductivity is a quite old phenomenon, it still holds many mysteries, especially high-temperature superconductivity. Superconductor applications can be analysed from the engineering point of view in certain systems, where one of the three critical parameters are important: temperature, magnetic field and current density.
These parameters influence one another, and the exact operating point can be pinpointed on or within the critical parameter surface. The fundamental relations used to analyse superconductors from an electrical engineering point of view are a result of empirical data rather than theoretical study. The high-temperature superconductors belong to type-II superconductors where there are three possible regimes of operation: superconducting (Meissner) state, mixed state and normal state. The range of operation in the Meissner state is quite narrow since the first critical field value H_{c1} is much smaller compared to the second critical field value H_{c2}. In the mixed state, the magnetic flux lines penetrate the superconductor structure depending on the value of the magnetic field, which results in quantum vortices. The movement of these vortices is associated with flux creep losses, and to limit this behaviour, some form of pinning is required, usually in the form of impurities either introduced deliberately or due to the manufacturing process. Other forms of losses like hysteresis losses are related to forcing current in the opposite direction than the electric field. The existence of hysteresis can be explained in simple terms by the critical state model, which states that a magnetic field penetrates through the superconductor starting from the outer edges, and the gradient of that field determinates the current direction.

The high-temperature superconductors are anisotropic, which results in different critical values along different principal axes. The highest values of critical current are observed for the *a*-*b* plane, but the magnetic field acting perpendicular to that plane also has the strongest effect. The most significant advantage of HTS like YBCO or BiSCCO is the ease of achieving superconductivity by utilising liquid nitrogen for cooling. The liquid nitrogen is easy to handle, does not require cryostats, is easily accessible and cheap. Although HTS materials have outstanding parameters, especially when cooled way below critical temperature are not replacing LTS in its current applications. Though, high-temperature superconductors may shine in other areas in future, like electric power systems, electrical machines or transportation.

3

Magnetisation of superconductors

This chapter is dedicated to the magnetisation of high-temperature superconductors, underlying phenomenon, flux pumps and results found in literature so far regarding the process of magnetisation. The chapter starts with a brief introduction to the magnetisation of superconductors (Section 3.1) that results in creating trapped-field magnets (TFM). The second section contains information about two basic methods behind creating TFMs (Section 3.2) that gives a context for the third Section 3.3. Section 3.3 describes a pulsed-field magnetisation (PFM) method, which is the main subject of interest of this thesis. Next, Section 3.4 contains a state-of-the-art systematic review of flux pumps dedicated to PFM for trapped-field magnets made out of tapes or superconducting bulks. Various constructions of flux pumps are described and ordered, depending on purpose and properties. The chapter continues with Section 3.5 with a broad review of research on pulsed-field magnetisation. The section includes a description of different magnetisation techniques and topologies of magnetisation circuits, the role of pinning and anisotropy, as well as mathematical description and theoretical limits of pulsed-field magnetisation.

3.1. Trapped-field magnets

Superconductors dominate mainly power transmission applications, such as cables or current-conducting parts of other devices. In the narrow field of applications, superconductors can serve as a magnetic field source, similarly to permanent magnets (PM). The superconductor-based magnets are also known as trapped-field magnets (TFM) [188–190], indicating that magnetic field is produced via different means than remanent flux density in PMs via an arrangement of magnetic domains.

In permanent magnets, the magnetic domains of ferromagnetic materials are responsible for generating the magnetic field, such as neodymium magnets. At some point during the manufacturing process, the magnets are placed inside a strong and uniform magnetic field to align all magnetic domains inside the object, thus strengthening and orienting the output magnetic field of PMs [4].

Storing magnetic field inside superconductors is based on a zero-resistance phenomenon, whereby the magnetic field is created by inducing persisting superconducting current inside the element. Without resistance, currents can flow for a long time. The methods of inducing such current inside the superconducting structure can be divided into two distinctive techniques:

- static - field cooling (FC) and zero-field cooling (ZFC);
- dynamic - pulsed-field magnetisation (PFM);

3.2. Field cooling and zero-field cooling

In the field cooling (FC) method, previously mentioned in Section 2.1, the superconducting material is exposed to an external magnetic field in a normal state as shown in Figure 2.1d. During cooling below critical temperature T_c of material, the magnetic field is "remembered," thus the object will act as a source of the magnetic field as seen in Figure 2.1e. This "memorization" of the field passing through the superconductor during cooling can be explained on the basis of achieving the lowest energy state. On the fundamental level, the formation of Cooper pairs can explain this phenomenon during phase transition. In essence, the electrons want to occupy the lowest energy state, and that is done by allowing the magnetic field to pass through superconducting material without disturbing the field itself. In order to pass that magnetic field, the superconducting current is formed, such that the magnetic field does not change. After removing the external field, the currents persist inside the structure, which results in the creation of a magnetic field; thus, the superconductor acts as a source [178, 179].

In contrast, in the zero-field cooling (ZFC) method, as the name implies, the superconductor is cooled below T_c without the presence of an external magnetic field (hence the "zero field"). The magnetic field is applied to superconductors in the already superconducting state. Applying a magnetic field to the superconductor will induce an electric field inside the structure, resulting in a current flow. On the one hand, the magnetic flux can penetrate the superconductor at the London's penetration depth [150] when in the superconducting state. On the other hand, due to the low H_{c1}, the superconductor easily transitions to a mixed state; thus, some magnetic flux penetrates the material's structure. This method resembles forcing a magnetic field to the superconductor by applying a stronger field gradually and building up the superconducting current inside. The effect of applying an external magnetic field can be seen on the hysteresis loop Figure 2.14. The main difference between FC and ZFC is that the magnetic field will be "remembered" inside the structure as it was during cooling below the critical temperature.

For ZFC, the final distribution of the magnetic field depends on the value and change of the magnetic field over space and time. It has to be noted that changes in the magnetic field over time are assumed to be much lower compared to the PFM method; therefore, it is categorized as a static method [32].

In both methods, the applied magnetic flux has been removed (FC) or introduced (ZFC) in some way, but it is assumed that the change of magnetic flux over time is negligible and will not cause additional eddy currents, leading to sufficient power losses or temperature rise.

3.3. Pulsed-field magnetisation

The PFM method is based on the same principle as ZFC and is sometimes referred to as pulsed-ZFC [191]. Compared to ZFC, in pulsed-field magnetisation, the change of magnetic flux over time can not be neglected. The process of pulsed magnetisation, also known as flux pumping relays on subjecting superconducting materials to pulses of the magnetic field. Due to the zero-resistance phenomenon in superconductors, by exposing them to a varying magnetic field, superconducting currents are induced, which results in the generation of the magnetic field. The induced currents have the additive property that may cause an increase of current density with consecutive pulses, therefore increase of the magnetic field. The magnetic field produced by bulk superconductors is a DC field – meaning that applying varying magnetic fields leads to the flow of DC current in superconductors without using any rectification circuit. The complexity of pulsed-field magnetisation makes it difficult to create a generalised model of flux pumping due to simultaneous phenomenon occurring during the process - the flux jumping [94, 100, 101], power losses and temperature increase [57, 70, 76, 105, 134–137], the system geometry as well as used materials, which influence magnetic field distribution [44, 45, 47–49].

3.4. Flux pumps

A source of the magnetic field is required to create trapped-field magnets (TFM). The TFM comes in two forms - bulk superconductors and coils, also called superconducting magnets. Starting from the latter - HTS coils are typically wound in a closed-loop as spirals or vortex coils, where the superconducting current is induced. With a large number of turns, these can serve as powerful magnets. The former type of TFM is based on superconducting bulks that can either be made of solid crystal pieces of superconducting material or stacks made out of HTS tapes. Every type of TFM requires a dedicated flux pump [192]. Generally, standing wave systems are used for bulk superconductors, whereas travelling wave systems are rather utilised for HTS coils. The travelling wave system requires space, through which the wave of magnetic flux can travel. On the contrary, bulk superconductors or HTS stacks occupy a small space; thus, applying standing wave can be more effective [22, 142] compared to thermally actuated systems [193, 194]. The PFM process can also consist of multiple pulses to build up the current in the superconductor, resulting in higher values of the magnetic field than applied in a single pulse [31, 85]. This phenomenon has been explained quite recently [192] and is attributed to the nonlinear resistivity of superconductors.

Similarly, HTS bulks can be magnetised using multiple pulses, but the dynamics of the whole process is more complicated and will be discussed further below. A broader overview of such pumps has been presented in [195]. The PFM systems can be categorised in different ways, depending on specific features, which has been presented in Figure 3.1.

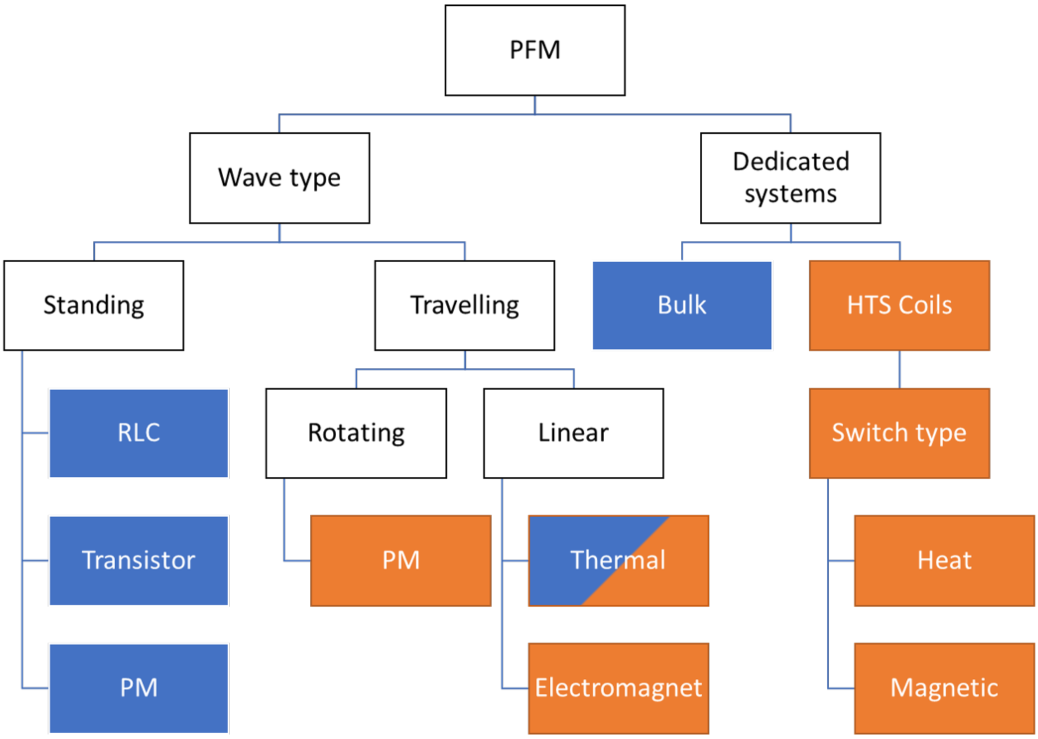

Figure 3.1. Categories of flux-pumping systems for HTS

A significant DC current can be induced in superconducting tapes by applying AC magnetic field. This phenomenon has been attributed to nonlinear characteristics of superconductors [192], which is utilised mainly to magnetise HTS tapes, typically in coils with multiple turns. It has a possibility of achieving high electric loading due to significant current. These systems use two types of flux pumps that are based either on switches or waves. In switch-based pumps, the systems have two loops - one containing a coil and another with source and switch. The switching is carried out on the part of HTS tape by operating it between superconducting/mixed and normal states. This can be achieved by exceeding one of three critical values, but the critical field is at tens or hundreds of teslas for most high-temperature superconductors. Therefore the magnetic field is not typically used as a switching mechanism. Usually, either current or thermal switches are used, whereas, in the case of the current switch, the magnetic field can be applied to lower the threshold of the switch [189]. The superconducting switch acts as a relay that directs the current to the coil. Generally, the transformer is used as a source of current for such pumps, therefore are called *Switched Transformer-Rectifier Pumps* [189, 196, 197].

On the other hand, the magnetic wave systems do not require any switching. To induce a current in tapes, some system generating travelling wave is used that usually resembles parts of electric machines, i.e. stator of a linear motor. The *Linear Electromagnets-Based on Traveling Wave Flux Pump* consists of a set of electromagnets operating in consecutive order to generate a linearly travelling magnetic wave [198]. The advantage of such a system is the possibility of precisely controlling the wave's shape (amplitude and frequency), but that comes with the disadvantage of a very bulky system generating a lot of heat in the process. Another more compact version with high promises is an HTS dynamo, conventionally named as *Rotating Magnet-Based Traveling Wave Flux Pump* [199, 200]. The travelling magnetic wave is generated by rotating magnets. The influence of magnet shapes has been investigated [201]. It has been shown that DC current can be induced in HTS coils by applying standing or travelling waves [202]. The possibility of inducing DC current in coils might allow creating HTS DC generators

or motors with DC excitation without rectifiers or commutators, therefore resulting in higher efficiency [185, 189].
The idea behind using pulsed-field magnetisation is to exploit the highly nonlinear resistive characteristics combined with nearly zero resistance to induce DC current in superconductors. PFM systems based on electromagnetic coils are usually used for magnetisation of bulks [142, 143], whereas flux pumps utilising magnets are used for magnetisation of tapes [200].

The simplest of flux pumps utilises electromagnet, which generates standing wave and therefore is called *Electromagnet Based Standing Wave Flux Pump* [22]. The shape of the coil and core may vary, but the principle stays the same, which is exposing a superconductor to the applied magnetic field. The applied magnetic field is unipolar, thus has a DC component, but the shape current waveform could be different. The current waveform can be generated in various ways. One such pump is based on a capacitor bank, which can store energy and deliver a high current quickly. To avoid oscillations and thus to alternate current, diodes are used. Such a system can be called a *LC Flux Pump*.

The *Electronic Switches-Based Transformer-Rectifier Flux Pumps* [30] is another type of flux pump, where a set of diodes and capacitor bank are replaced by a power supply and controllable power electronic switches like transistors. The current waveform can be shaped using the PWM method and has high dynamics in such a system.
It is rather uncommon to use thermally generated standing waves, but few have been built and researched. In these systems, a material with temperature-dependent magnetic permeability is used, such as Prussian blue [194] or gadolinium [193, 203] are ferromagnetics at 77 K, but when heated up become weak paramagnetic. Thus, when immersed in liquid nitrogen, the part of the magnetic circuit made of these materials diverges flux lines away from the superconductor, but when heated up, allows the magnetic field to reach the bulk.

3.5. Features of pulsed-field magnetisation

According to the CSM, model [178, 179], the superconductor's trapped magnetic field using the PFM method can not exceed the trapped field using the FC method. That is due to the heating of superconductors during the magnetisation process with alternating fields. Therefore, the field cooling can serve as a baseline for magnetisation with a given system. However, there are some advantages compared to field cooling. Firstly it is the size of the magnetisation system, which for PFM, it can be smaller. Secondly, the time of magnetisation of a single pulse lasts milliseconds. To achieve a high magnetic field, a decent number of ampere-turns is generally required; therefore, most of the systems based on FC/ZFC rely on superconducting magnets to minimise the impact of excessive losses in the system. In the PFM method, even copper coils are sufficient because of the low duration of pulses; higher current values are achievable without stressing the cryogenic system. The PFM systems can fit into the motor, or even armature winding can magnetise bulks located on the rotor [142].

The HTS materials have a crystalline structure, and to grow superconducting bulks, a top-seeded melt growth (TSMG) process is used where HTS crystal grows from seed. During that process, Y-211 particles are trapped inside YBCO matrix [204]. Those imperfections in the Y-123 matrix could cause inhomogeneity of critical current in bulk but form a pinning center where the magnetic field can be anchored, preventing flux flow and increasing critical current density. This results in notable growth sectors (GS) and growth sector boundaries (GSB) visible on one side of the bulk. There is a notable difference in pinning on GSB compared to GS. This results in non-axisymmetric current distribution on the a-b plane [39]. The influence of multi-grain HTS bulks reveals slight anisotropy in trapped magnetic field [205].

The PFM method is also referenced as the pulsed-ZFC method since the magnetic field is applied when the bulk is already at a superconducting state. The theoretical limit of ZFC is $B_{\text{trap}} \leq \ ^1\!/_2 B_{\text{app}}$, therefore similar behavior has been expected from PFM. Although CSM has predicted this limit for ZFC, it does not hold for all conditions since it does not consider phenomena taking place in superconductors like flux-creep, flux-flow, or flux-jump. It has been shown that it is indeed possible to achieve $B_{\text{trap}} \approx B_{\text{app}}$ [191]. Although the PFM method has high promises of achieving substantial trapped magnetic fields, besides having a theoretical limit [190], there has been observed a limit coming from coupled multi-physical phenomenon during PFM - mechanical, thermal and electromagnetic. It is expected that by applying the magnetic field of higher peak values, the trapped magnetic field will also rise. That happens up to some point where the maximum trapped field is achieved, and applying a field of higher magnitudes results only in further decrease. This value has been named the optimum trapped field [91] attributed to an excessive increase of temperature within superconductors, with higher applied magnetic fields leading to a decrease of trapped field [91, 188].

The general limits of bulk magnetisation have been derived and compared in [206]. In more general, the trapped field on the surface of bulk in the center can be calculated using (3.1) which is bounded by J_{c}, bulk diameter D_{HTS} and thickness H_{HTS}. The correction factor k is due to finite thickness and shape of bulk and can be calculated from (3.2) [112].

$$B_{\text{trap}} = k\mu_0 J_{\text{c}} \frac{D_{\text{HTS}}}{2} \tag{3.1}$$

$$k = \frac{H_{\text{HTS}}}{D_{\text{HTS}}} \ln\left(\frac{D_{\text{HTS}}}{2H_{\text{HTS}}} + \sqrt{1 + \frac{D_{\text{HTS}}^2}{4H_{\text{HTS}}^2}}\right) \tag{3.2}$$

The magnetic field at some distance from magnetised HTS bulk can be calculated given the (3.3) [112]. This is a result of applying Biot-Savart law to axisymmetric disc with uniform current density within.

$$\begin{aligned} B_{\text{trap}}(z) = \frac{\mu_0 J_{\text{c}}}{2} \Bigg[(z + H_{\text{HTS}}) \ln\left(\frac{\frac{D_{\text{HTS}}}{2} + \sqrt{\frac{D_{\text{HTS}}^2}{4} + (z + H_{\text{HTS}})^2}}{z + H_{\text{HTS}}}\right) \\ - z \cdot \ln\left(\frac{\frac{D_{\text{HTS}}}{2} + \sqrt{\frac{D_{\text{HTS}}^2}{4} + z^2}}{z}\right)\Bigg] \end{aligned} \tag{3.3}$$

For magnetic fields lower than the optimum value, the HTS bulk operates in the flux flow region. In contrast, at a state of increased temperature, the resistivity rises due to flux creep, which for sufficiently higher fields may lead to runaway effect decreasing trapped field substantially [127, 188]. To prevent such effects, there have been attempts to increase pinning inside bulk superconductors, which have been done by introducing pinning centers via neutron bombardment of the crystalline structure to introduce defects or even placing ferromagnetic rods within bulk [127]. Stronger pinning leads to a steeper E-J curve (2.6) (Figure 2.5), which corresponds to higher values of power $n > 20$ and possibly even 2 or 3 times higher values of J_{c}. During the PFM process, the trapped field might have relatively low values up to the point where a sufficiently high field results in flux jump leading to a trapped field of a magnitude similar to the applied field. For lower values of B_{app} the peak of trapped field forms a ring shape, whereas, for sufficiently high applied fields, it reaches peak values at the center [205]. The flux jumps lead to a rapid increase in temperature [127, 207].

The HTS stacks made of superconducting tapes have been magnetised successfully, achieving trapped fields of a few teslas. The major drawback is the active superconducting cross-section area in such stacks where superconductor comprises a small percentage of total cross-sectional area, but this also results in higher thermal capacity of the entire stack improving its stability [82, 84, 208]. At cryogenic temperatures below 100 K, it is important to take the influence of the temperature into account, especially when materials are exposed to wide temperature changes. Besides considering the influence of temperature on superconductivity itself and critical parameters, the temperature influences the thermal capacity of materials such as copper or stainless steel. Most of these characteristics are nonlinear but also not monotonic functions of the temperature [127]. (Re)BCO superconductors have a low thermal conductivity which does not favour PFM, and the thermal capacitance decreases at lower temperatures [112]. Both effects result in a rapid increase of temperature during PFM but also delay restoring superconducting/mixed state within the superconductor [127]. The arrangement of HTS tapes in the stack can affect the gradient of the trapped magnetic field. The angled stack of HTS tape pieces has been shown to achieve significant uniformity of trapped magnetic field [209] but of low value due to the small cross-sectional area of individual tapes limiting the current.

Instead of using the single-pulse PFM method, the superconductors can be magnetised by multiple pulses one after the other. The simplest multi-pulse technique relies on applying identical pulses multiple times in a row. The pulses cause the magnetic field to penetrate the superconductor structure and result in a build-up of subsequent pulses of magnetic flux. As a result, the current density distribution within the structure is not uniform. The current density regions created by every applied pulse can be distinguished from one another due to zero current or zero magnetic flux regions, which are interleaving [208]. Another more complicated variation is multi-pulse sequential cooling (MPSC), in which the main feature is decreasing superconductor temperature after applying a number of pulses and continuing at a lower temperature. The applied magnetic field also increases with every pulse since the magnetised samples can handle higher magnetic fluxes, and heat can be removed easily at lower temperatures without destroying superconductivity [82]. The modified MPSC (MMPSC) requires additional temperate decrease with every pulse and has proven to be more effective [36–38].

In electromagnet-based flux pumps, various coils are used: *solenoid* (Figure 3.2a), *split* (Figure 3.2b), *vortex* (Figure 3.2c), or *controlled magnetic density distribution coil* (CMDC). Each has its unique features related to PFM. Solenoid coils can be used as part of a larger system with or without ferromagnetic core [40]. The ferromagnetic material can either be small and placed in the vicinity of the bulk or form a magnetic core like in inductors with an air gap, where instead bulk is located. The core focuses the magnetic field onto the bulk, which increases the trapped field [40, 205, 210]. The bulk should be located in the center of a solenoid, where magnetic flux has the highest value to achieve good performance. During the PFM process, the magnetic field penetrates HTS bulk from its edges to the center [40, 127, 210].

Split or pancake coils are another commonly used type of coil in electromagnetic PFM systems. Coils are formed as spirals or pairs of solenoids. The coils are called *pancake coils* when the whole cross-sectional area is populated by the wire, whereas *split coils* refer to a double solenoid system. The key difference between the split and the single solenoid coil is

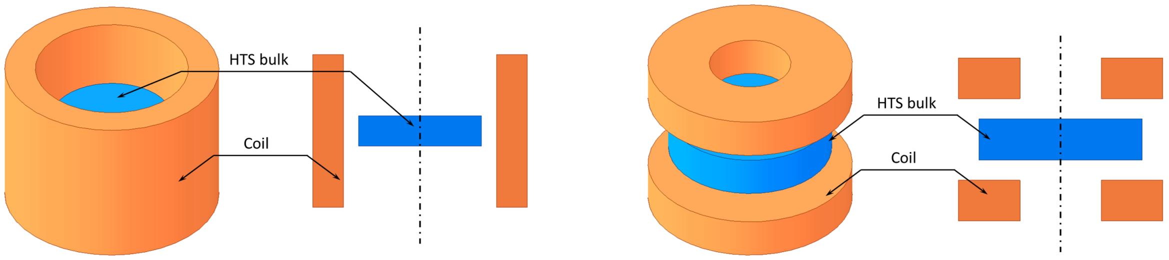

(a) solenoid coil **(b)** split coil

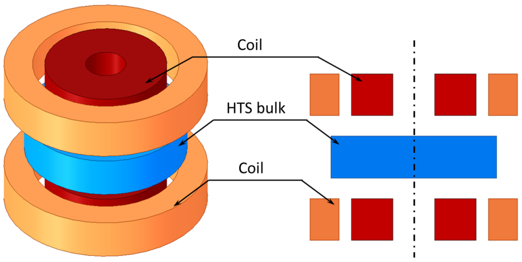

(c) CMDC coil

Figure 3.2. Types of coils used in PFM systems with 3D view (left) and 2D cross-section (right): (a) solenoid coil; (b) split coil; (c) CMDC coil

that usually, in the former, the bulk is located in between coils. When using split or pancake coils for PFM, it has been observed that the magnetic field penetrates HTS bulk from top and bottom instead of edges. This results in a higher magnetic field than in single-solenoid systems [39, 40, 207, 210]. Similarly to solenoid coils, the presence of iron yoke increases the trapped field [205]. It has been observed that a higher magnetic field is achieved on GSB compared to GS [39]. Spiral coils can be found in axial-flux machines with HTS bulks mounted on the rotor; therefore, they can be magnetised in place [211].

A CMDC coil is similar in build to the split-coil, but instead of placing all turns uniformly in the axial direction in the same radius, the radius of some turns may vary; the direction of turns (or current flow direction) may also change. Such construction allows for the adjustment of magnetic field distribution. The magnetic field created by the single-solenoid system is relatively uniform but results in a higher temperature rise within HTS, especially on edges and non-uniform current distribution. On the contrary, it has been shown that by increasing the gradient of the applied magnetic field either by using split or CMDC coils, the heating can be substantially suppressed and could result in a more uniform current density distribution within HTS bulk [84, 212].

3.6. Summary

The precise definition of the operating point in the PFM method is complicated due to many unknowns, resulting from the difficulty in determining the temperature distribution inside the bulk structure, local magnetic field distribution and current densities in the superconducting material. Exceeding the critical values even locally can lead to a destructive positive feedback loop and loss of superconductivity in the whole sample. With increased current density in superconductors, significant mechanical stress that adversely affects the brittle crystal structure of superconductors is created inside. There is also the interaction between the magnetised object and the excitation system. Including these phenomena in the analysis is not without significance. It is also possible to replace bulk superconductors with compact stacks of HTS tapes, which provides better mechanical support. To improve the mechanical strength of HTS bulks, a stainless steel ring can be placed around the bulks to support the structure by compression or penetrating resins can be used as well [191].

The challenge of the research is, therefore, to develop appropriate mathematical models of flux pumps. Above all, the processes during pumping are multi-criteria and interdisciplinary, requiring accounting for a number of electromagnetic, thermal, and mechanical phenomena. For example, bulk superconducting structures or bulks can function as a source of strong magnetic fields, exceeding 2 T - unattainable for currently manufactured permanent magnets. Therefore, bulks could successfully replace permanent magnets and even provide more favourable operating conditions resulting in higher power density. Methods developed for trapping the magnetic field in superconductors - Field Cooling (FC) and Zero-Field Cooling (ZFC) are usually used as *ex-situ* methods. However, the usage *in-situ* requires costly and large-sized systems for magnetisation that might become inadequate economically for the application.

The use of pulsed-field magnetisation could have significant economic viability in producing strong magnetic field sources. The costs of purchase, maintenance, and use of magnetising devices can be reduced due to the low power consumption required for generating a strong magnetic field lasting for a fraction of seconds. During PFM, the superconducting material is usually continuously in the superconducting state, which is a considerable advantage compared to FC, requiring phase transition under the influence of an external field. In contrast to the capabilities of permanent magnets, currently, one of the highest achieved magnetic fields stored in the superconducting bulk magnet is over 17 T [93].

The magnetic field transfer in PFM is contactless, and in short bursts, the magnetic excitation circuit could be potentially placed outside the cryostat, eliminating the need for expensive current leads. Furthermore, the magnetised object can be fully isolated, eliminating the formation of thermal bridges and additional losses in the place of energy transfer. This allows for achieving greater cryogenic efficiency and overall lower system costs. It is assumed that results obtained in the following research will complement what was described above, as well as research carried out in other scientific institutes. This will enable the application of mathematical description of generalised pump structures for the synthesis of such devices and indicate potential areas for improving the efficiency of the PFM process in order to obtain the desired distribution and value of the magnetic field stored in a superconductor. These models can also be used as part of the excitation circuit of high-efficiency electric machines with high power densities to drive planes, water vessels, or renewable energy sources.

4

Design of PFM standing wave system

The following chapter describes an electric circuit dedicated to generating pulses of a magnetic field - the flux pump. To select proper components for the circuit, it is necessary to analyse its behaviour under various conditions and predict the operation of the circuit. It is assumed that the coil will serve as a source of the pulsed-field; therefore, a sufficiently high current must be applied to achieve significant magnetic flux density values. The chapter has been divided into three main sections. The first Section 4.1 has been dedicated to the description of the flux pump from the lumped circuit model perspective, where the analytical solution can be derived. The circuit is described in the *s*-domain using Laplace Transform. This results in a mathematical formula for current and voltage waveforms. The solution is analysed for various conditions, depending on components values. The influence of voltage drop on power electronic components and its influence on power losses is analysed. The second Section 4.2 has been dedicated generally to the description of a magnetic circuit and focuses on the influence of a number of turns on the resistance and inductance. In the third Section 4.3 the results of the performed analysis are presented. Under various conditions, the influence of circuit parameters on current waveforms and its characteristic parameters (i.e., peak value, rate-of-change) is analysed. The fourth Section 4.4 focuses on designing the solenoid coil used specifically for magnetisation of HTS bulks. The methodology of designing a solenoid coil with specific parameters and dimensions is presented. The last, fifth Section 4.5 summarises and concludes the whole chapter.

4.1. Lumped circuit model of the pulse-generating circuit

The analysed flux pump system generates a standing wave of magnetic field, and has two parts: supply circuit shown in Figure 4.1a with an electromagnetic coil, either with a ferromagnetic core (Figure 4.1b) or without (Figure 4.1c). The electric circuit of the flux pump consists of a power supply U_{DC} that delivers energy to the system by charging the capacitor bank C that acts as a pulse current source when the switch S is turned clockwise (close). The capacitor bank is composed of capacitors connected in series or parallel or a combination of both, but from the lumped circuit model perspective is seen as a single capacitance C. From the terminal point of view, the circuit can be represented by a lumped circuit model as a series connection of resistance R and inductance L. These parameters might change with time or the current value, but for analysis of equivalent circuits, the model can be set as constant values. The advantage of using capacitors as an energy source is fast charging and discharging time, resulting in high current, compared to other energy sources. The applied magnetic field ought to be unipolar; therefore, the current should flow in one direction, and oscillations of current between coil and capacitor bank are undesirable since it might damage electrolytic capacitors. The diode D_1 prevents current from flowing from RL circuit back to capacitor bank, whereas the diode D_2 creates a pathway for current to flow through the coil when the capacitor bank is discharged. If the current flow through the coil is interrupted, it will result in overvoltage damaging other components.

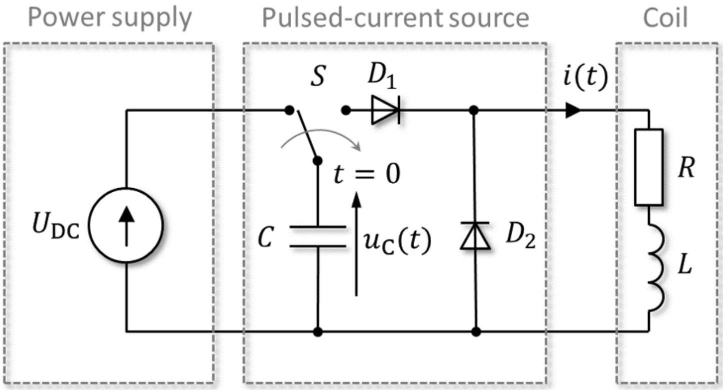

(a) lumped circuit model of a flux pump

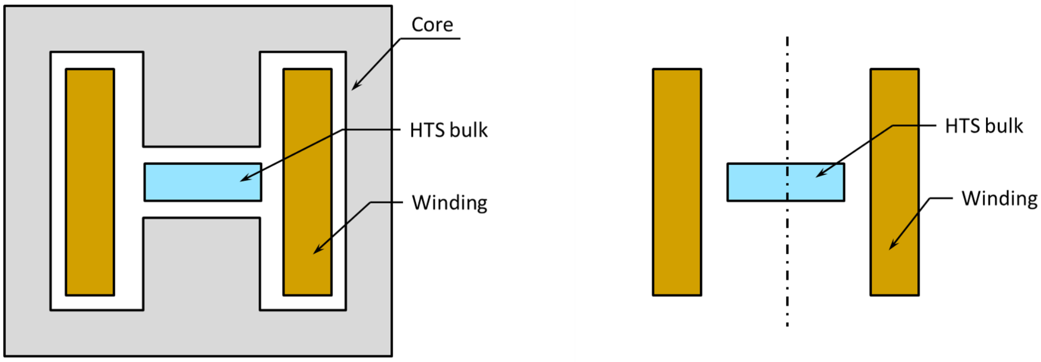

(b) magnetiser with core

(c) coreless magnetiser

Figure 4.1. RLC flux pump system for magnetisation of superconducting bulks: (a) lumped circuit model; (b) magnetiser with core; (c) coreless magnetiser

The operation of the circuit presented in Figure 4.1a can be split into two sub-circuits presented in Figure 4.2. The process of charging the capacitance C is out of interest in the analysis. The circuit can be analysed in the time domain with ordinary-differential equations (ODE). However, its parameters influence on the current waveform will not be clear at first glance. The Laplace Transform allows for analysis of circuits and obtaining the solution in the complex domain $\mathbb{C}$ electric networks. In the most general case, the circuit can operate in two states. The Figure 4.2a represents the state of the circuit during capacitor bank discharge that begin at $t = 0$ s, where only diode D_1 conducts current. After discharging the capacitor bank, the current flow continues through the diode D_2 as shown in Figure 4.2b and decays to zero due to losses. When the capacitor bank is discharged, the switch S can be moved counterclockwise to charge the bank and the cycle repeats. Both solutions can be combined using the superposition principle. The first state is the default, whereas the transition to the second depends on circuit parameters. At this stage of analysis, the forward voltage drop on diodes D_1 and D_2 are neglected.

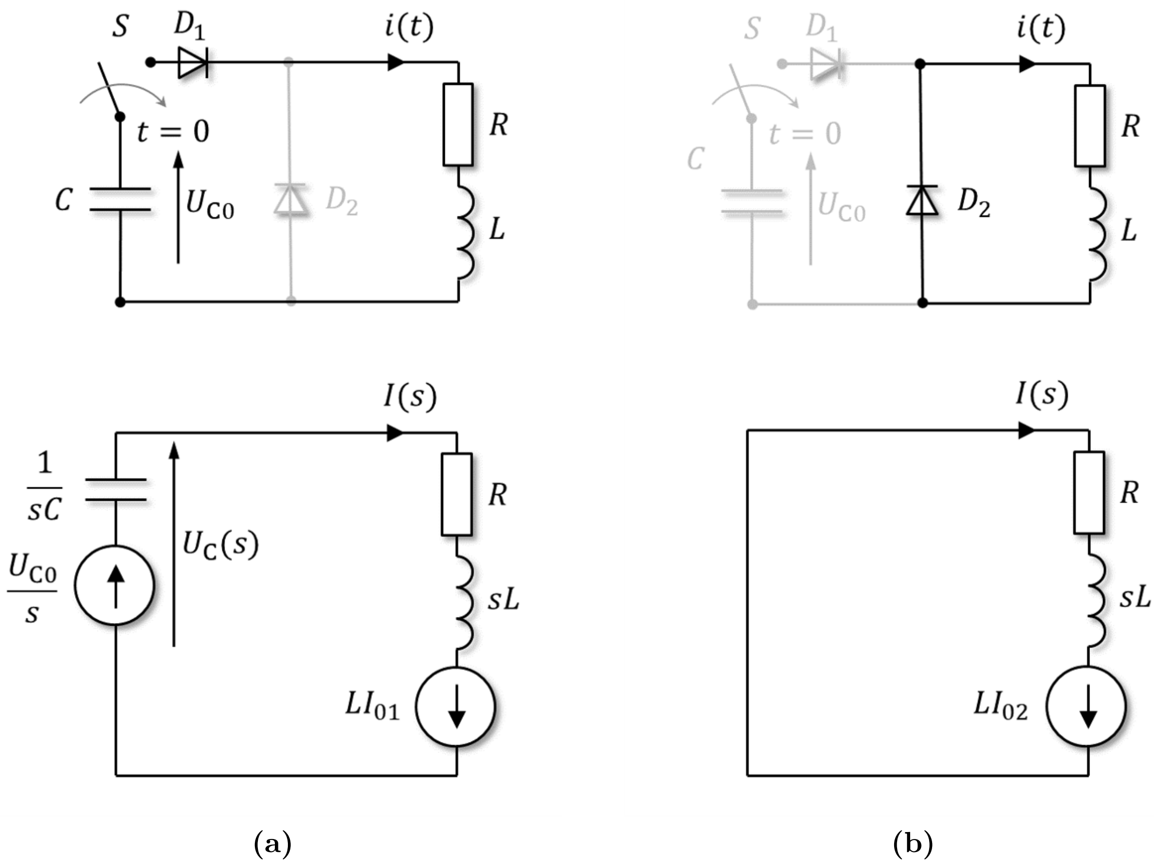

Figure 4.2. Equivalent circuit model in s-domain of the RLC flux pump: (a) current loop during capacitor discharge; (b) current loop during current decay

The U_{C0} is the capacitor's voltage at $t = 0$ s; $U_{\mathrm{C}}(s)$ is the capacitor's voltage in s-domain; I_{01} - is the initial current flowing through the coil, which might occur in multi-pulse operation and is a residual from the second state to the first; I_{02} is the residual current flowing through the coil at a point of transition from the first to the second state of the circuit.

In more general - the operation of the flux pump is a multi-pulse operation. Consequently, the current pulses can be applied at different periods and of different magnitude; thus, when deriving equations, it is helpful to include an initial condition in the form of residual currents flowing through the coil: I_{01} and I_{02}.

4.1.1. Flux pump operation during capacitor discharge

The capacitor bank is charged, up to initial voltage U_{C0} and starts to discharge at $t = 0$ s. At this phase, the equivalent circuit shown in Figure 4.2a applies. The current is given by the (4.1).

$$I(s) = \frac{\frac{U_{\mathrm{C0}}}{s} + LI_{01}}{R + sL + \frac{1}{sC}} = \frac{U_{\mathrm{C0}}}{L} \frac{1 + sL\frac{I_{01}}{U_{\mathrm{C0}}}}{s^2 + s\frac{R}{L} + \frac{1}{LC}} = \frac{U_{\mathrm{C0}}}{L} \frac{1 + sLY_{01}}{s^2 + 2\xi\omega_0 s + \omega_0^2} \tag{4.1}$$

Characteristic parameters typical for this kind of 2$^{\mathrm{nd}}$-order oscillatory systems are: natural frequency ω_0 (4.2) and damping coefficient ξ (4.3) that relate to parameters of a resonant circuits. The ratio of initial current and initial voltage can be represented as initial admittance Y_{01} (4.4).

$$\omega_0 = \frac{1}{\sqrt{LC}} \tag{4.2}$$

$$\xi = \frac{R}{2}\sqrt{\frac{C}{L}} \tag{4.3}$$

$$Y_{01} = \frac{I_{01}}{U_{\mathrm{C0}}} \tag{4.4}$$

The current is described as the second-order system by the (4.1), and depending on the value of poles of the transmittance $I(s)$ (4.5), the system can operate in three states: overdamped, critically damped or oscillatory damped circuit.

$$I(s) = \frac{U_{\mathrm{C0}}}{L} \frac{1 + sLY_0}{(s - s_1)(s - s_2)} = \frac{U_{\mathrm{C0}}}{L} \frac{N(s)}{D(s)} \tag{4.5}$$

To analyse the operation of the circuit and find poles of the denominator $D(s)$, the discriminant Δ can be calculated using (4.6).

$$\Delta = 4\omega_0^2 \left(\xi^2 - 1\right) \tag{4.6}$$

There are three possible cases to be analysed:

$$\begin{gathered} \{\Delta > 0 : s_1 \neq s_2; s_1, s_2 \in \mathbb{R}\} \\ \{\Delta < 0 : s_1 \neq s_2; s_1, s_2 \in \mathbb{C}\} \\ \{\Delta = 0 : s_1 = s_2; s_1, s_2 \in \mathbb{R}\} \end{gathered}$$

The system described by (4.5) has two poles s_1 and s_2 that can be factored out. The current in time domain $i(t)$ is calculated by performing an *Inverse Laplace Transform* $\mathscr{L}^{-1}\left[I(s)\right] = i(t)$, which can be done by using *Cauchy Residue Theorem*. As a result, there are two general solutions to (4.5) depending on the case listed above, which can be written as (4.7).

$$i(t) = \begin{cases} \dfrac{U_{\mathrm{C0}}}{L}\left(\dfrac{1+s_1LY_{01}}{s_1-s_2}\mathrm{e}^{s_1t} - \dfrac{1+s_2LY_{01}}{s_1-s_2}\mathrm{e}^{s_2t}\right) & \text{if } s_1 \neq s_2 \\ \dfrac{U_{\mathrm{C0}}}{L}(1+s_0LY_{01})t\mathrm{e}^{s_0t} & \text{if } s_1 = s_2 = s_0 \end{cases} \tag{4.7}$$

The capacitor's voltage can be calculated by calculating voltage drop across capacitance in s-domain (4.8).

$$U_{\mathrm{C}}(s) = \frac{1}{sC}I(s) = \frac{U_{\mathrm{C0}}}{LC}\frac{1+sLY_{01}}{s(s-s_1)(s-s_2)} = \frac{U_{\mathrm{C0}}}{LC}\frac{N(s)}{sD(s)} \tag{4.8}$$

Similarly to the current waveform (4.7), the voltage is described with an (4.9).

$$u_{\mathrm{C}}(t) = \begin{cases} \dfrac{U_{\mathrm{C0}}}{LC}\left(\dfrac{1+s_1LY_{01}}{s_1(s_1-s_2)}\mathrm{e}^{s_1t} - \dfrac{1+s_2LY_{01}}{s_2(s_1-s_2)}\mathrm{e}^{s_2t} + \dfrac{1}{s_1s_2}\right) - U_{\mathrm{C0}} & \text{if } s_1 \neq s_2 \text{ and } s_3 = 0 \\ \dfrac{U_{\mathrm{C0}}}{s_0^2LC}\left[1-\mathrm{e}^{s_0t} + s_0(1+s_0LY_{01})t\mathrm{e}^{s_0t}\right] - U_{\mathrm{C0}} & \text{if } s_1 = s_2 = s_0 \text{ and } s_3 = 0 \end{cases} \tag{4.9}$$

4.1.2. Overdamped circuit

The circuit of the PFM system is overdamped when $\Delta > 0$, thus resulting in poles equal to (4.10), and both are real numbers.

$$s_{1,2} = -\omega_0\left(\xi \pm \sqrt{\xi^2-1}\right) = -(A \pm B) \tag{4.10}$$

where: $A = \omega_0\xi$ and $B = \omega_0\sqrt{\xi^2-1}$.

The solution takes a form of (4.11) for coil's current, and (4.12) for capacitor's voltage.

$$i(t) = i_1(t) = \frac{U_{\mathrm{C0}}}{L}\left[\frac{1-ALY_{01}}{B}\sinh(Bt) + LY_{01}\cosh(Bt)\right]\mathrm{e}^{-At} \tag{4.11}$$

$$u_{\mathrm{C}}(t) = -U_{\mathrm{C0}}\left[\frac{A-w_0^2LY_{01}}{B}\sinh(Bt) + \cosh(Bt)\right]\mathrm{e}^{-At} \tag{4.12}$$

4.1.3. Critically damped circuit

The critical damping of the circuit happens when $\Delta = 0$, which means that damping factor $\xi = 1$, therefore there is a single solution s_0 expressed by (4.13).

$$s_0 = -\omega_0\xi = -A \tag{4.13}$$

where: $A = \omega_0$ for consistency of description, and the current waveform is described by the (4.14). The voltage on the capacitor bank discharges according to the (4.15).

$$i(t) = i_1(t) = \frac{U_{\mathrm{C0}}}{L}\left[(1-ALY_{01})t + LY_{01}\right]\mathrm{e}^{-At} \tag{4.14}$$

$$u_{\mathrm{C}}(t) = -U_{\mathrm{C0}}\left[(A - w_0^2 L Y_{01})t + 1\right]\mathrm{e}^{-At} \tag{4.15}$$

4.1.4. Oscillatory damped circuit

The circuit becomes oscillatory damped if the $\Delta < 0$ thus value of damping factor $\xi < 1$. The poles of the system are pairs of complex numbers that are conjugated to one another (4.16).

$$s_{1,2} = -\omega_0\left(\xi \pm \mathrm{j}\sqrt{1-\xi^2}\right) = -(A \pm \mathrm{j}B) \tag{4.16}$$

where: $A = \omega_0\xi$ and $B = \omega_0\sqrt{1-\xi^2}$.
The solution takes the form of (4.17) for current and (4.18) for capacitor's voltage.

$$i_1(t) = \frac{U_{\mathrm{C0}}}{L}\left[\frac{1 - ALY_{01}}{B}\sin(Bt) + LY_{01}\cos(Bt)\right]\mathrm{e}^{-At} \tag{4.17}$$

$$u_{\mathrm{C}}(t) = -U_{\mathrm{C0}}\left[\frac{A - w_0^2 LY_{01}}{B}\sin(Bt) + \cos(Bt)\right]\mathrm{e}^{-At} \tag{4.18}$$

When the voltage drops to zero, the diode, D_1 stops conducting current and the current loop is formed through D_2. The voltage drops to zero at time t_{C0} (4.19).

$$t_{\mathrm{C0}} = \frac{1}{B}\,\mathrm{atan}\left(\frac{-B}{A - w_0^2 LY_{01}}\right) + n\frac{\pi}{B} \tag{4.19}$$

since the circuit is oscillatory, there are multiple zero-crossings every multiple of π/B, but the first one occurs for $n = 1$. At that stage, the diode D_2 starts conducting and the voltage $u_{\mathrm{C}}(t > t_{\mathrm{C0}}) = 0$ V.

The current decays to zero regardless of system type. However, the decay only happens through D_2 when the circuit becomes oscillatory damped since the voltage of the capacitor's drops to zero in finite time and does not discharge asymptotically to 0 like in other cases. The system is described by the schematic shown in Figure 4.2b, and the current flow is described by (4.20).

$$I_2(s) = I_{02}\frac{1}{s + \frac{R}{L}} \tag{4.20}$$

which has a pole $s_0 = -\frac{R}{L} = -1/\tau$, thus resulting in current waveform described by (4.21).

$$i_2(t) = i_1(t_{\mathrm{C0}})\mathrm{e}^{-\frac{t - t_{\mathrm{C0}}}{\tau}} \tag{4.21}$$

where: t_{C0} is the time at which transition between subcircuits Figure 4.2a and Figure 4.2b occurs, and gives arise to initial condition $I_{02} = i_1(t_{\mathrm{C0}})$. The current decays with a time constant $\tau = \frac{L}{R}$ that depends only on a coil. The superposition of currents in both states in oscillatory-type circuit yields (4.22).

$$i(t) = \begin{cases} i_1(t) = \dfrac{U_{\mathrm{C0}}}{L}\left[\dfrac{1 - ALY_{01}}{B}\sin(Bt) + LY_{01}\cos(Bt)\right]\mathrm{e}^{-At} & \text{if } t \in [0; t_{\mathrm{C0}}) \\ i_2(t) = i_1(t_{\mathrm{C0}})\mathrm{e}^{-\frac{t - t_{\mathrm{C0}}}{\tau}} & \text{if } t \geq t_{\mathrm{C0}} \end{cases} \tag{4.22}$$

4.1.5. Forward voltage drop on diodes and effective series resistance

In the previous subsections of the current chapter, the circuit of a flux pump has been analysed with an assumption of ideal components, besides coil, which has been analysed as a series connection of resistance R and inductance L. In practice, the electric components have parasitic parameters - resistance, inductance and capacitance, although only selected might be considered depending on application and type of operation. Furthermore, the analysed circuit is not a fast-switching converter; instead, it operates at a duty cycle of at least a couple of milliseconds or even slower. Therefore, considering parasitic parameters of components is not necessary. Nevertheless, the main factors that ought to be considered are effective series resistance (ESR) of the capacitor bank and forward voltage drop on the diodes. The ESR is at the order of a couple of milliohms [213], whereas the diodes can be treated as constant voltage sources representing forward voltage drop across, regardless of current value flowing through.

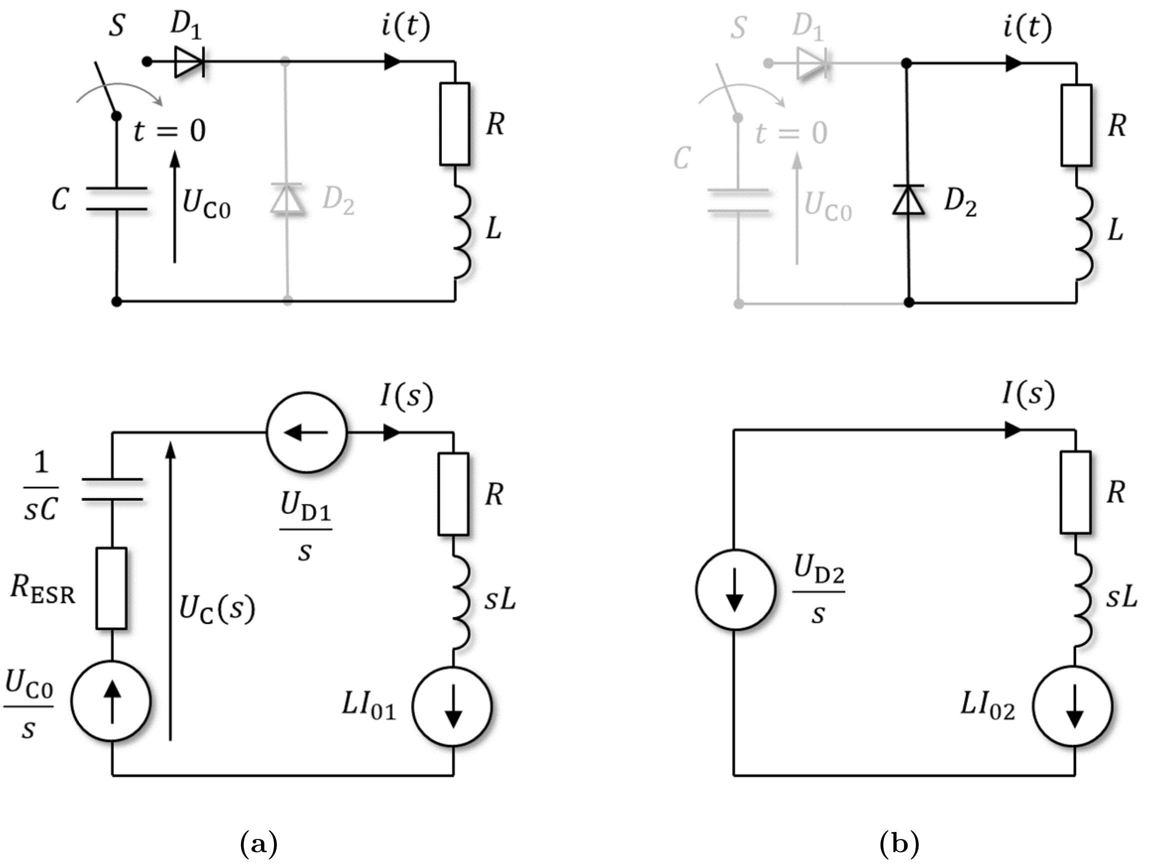

Figure 4.3. Equivalent circuit model in s-domain of the RLC flux pump with forward voltage drop on diodes: (a) current loop during capacitor discharge; (b) current loop during current decay

The equivalent series resistance R_{ESR} of the capacitor bank is connected in series with coil's resistance; therefore, it can be combined into one $R' = R + R_{\mathrm{ESR}}$ in the first circuit shown in Figure 4.3a, which influences damping coefficient $\xi \rightarrow \xi'$ in (4.3) and related coefficients $A \rightarrow A'$, $B \rightarrow B'$. During the second stage (Figure 4.3b) only coil resistance plays a role in calculating time constant.

When the capacitor bank is being discharged, the voltage applied to the coil is lower by the value of forward voltage drop across the diode D_1 (4.23).

$$U'_{\mathrm{C0}} = U_{\mathrm{C0}} - U_{\mathrm{D1}} \tag{4.23}$$

The initial admittance can also be corrected for that forward voltage drop as shown in (4.24).

$$Y'_{01} = \frac{I_{01}}{U'_{\mathrm{C0}}} = \frac{I_{01}}{U_{\mathrm{C0}} - U_{\mathrm{D1}}} \tag{4.24}$$

Both (4.23) and (4.24) can be incorporated into current equations, by substitution $U_{\mathrm{C0}} \to U'_{\mathrm{C0}}$ and $Y_{\mathrm{C0}} \to Y'_{\mathrm{C0}}$ describing circuit in different cases: (4.11), (4.14), and (4.17), (4.21). The example equation in oscillatory case is shown in (4.25).

$$i(t) = \begin{cases} i_1(t) = \dfrac{U'_{\mathrm{C0}}}{L}\left[\dfrac{1 - A'LY'_{01}}{B'}\sin(B't) + LY'_{01}\cos(B't)\right]\mathrm{e}^{-A't} & \text{if } t \in [0; t_{\mathrm{C0}}) \\ i_2(t) = -\dfrac{U_{\mathrm{D2}}}{R} + \left[i_1(t_{\mathrm{C0}}) + \dfrac{U_{\mathrm{D2}}}{R}\right]\mathrm{e}^{-\frac{t-t_{\mathrm{C0}}}{\tau}} & \text{if } t \in [t_{\mathrm{C0}}; t_{\mathrm{RL0}}) \\ 0 & \text{if } t \geq t_{\mathrm{RL0}} \end{cases} \tag{4.25}$$

where time t_{RL0}, at which coil current reaches zero is given by the (4.26), which results from solving for time in circuit during current dissipation state Figure 4.3.

$$t_{\mathrm{RL0}} = \tau \cdot \ln\left(\frac{U_{\mathrm{D2}}}{Ri_1(t_{\mathrm{C0}}) + U_{\mathrm{D2}}}\right) + t_{\mathrm{C0}} \tag{4.26}$$

The influence of forward voltage drop across diodes becomes significant at low currents, where it becomes equal or higher than voltage drop in the equivalent coil resistance. The forward voltage drop does not change significantly the equation describing current during capacitor discharge in (4.25), except already mentioned damping coefficients ξ', A' and B', but significantly affects the equation describing current during decay. Comparing (4.22) and (4.25) a constant negative bias of current equal to $-U_{\mathrm{D2}}/R$ is introduced, therefore current does not decay asymptotically to zero, but rather, current time period is limited to value t_{RL0}.

4.2. Magnetic circuit

An important component of the flux pump is a magnetiser, through which a magnetic flux is applied to HTS bulk. As mentioned at the beginning of the following chapter, the magnetiser can be equipped with a ferromagnetic core (Figure 4.1a) or without (Figure 4.1b). The magnetic circuit can be analysed using the lumped circuit model in the more general case regardless of the system [214]. The magnetic flux source is given by the product of a number of turns N and current at a given point in time $i(t)$. The reluctance (magnetic resistance) of core R_c depends on the core's geometry and its magnetic permeability μ. The air gap can be treated as part of the circuit with magnetic permeability equal to vacuums magnetic permeability $\mu = \mu_0$. Usually, the magnetic permeability of the core is nonlinear. For complex geometries, especially with much larger air gaps or coreless systems, other methods for calculating magnetic flux can be used, i.e. finite-element method. Nevertheless, assuming that system is linear, it can be solved using methods known from electric circuit theory. An example of the magnetic circuit with a single coil is shown in Figure 4.4.

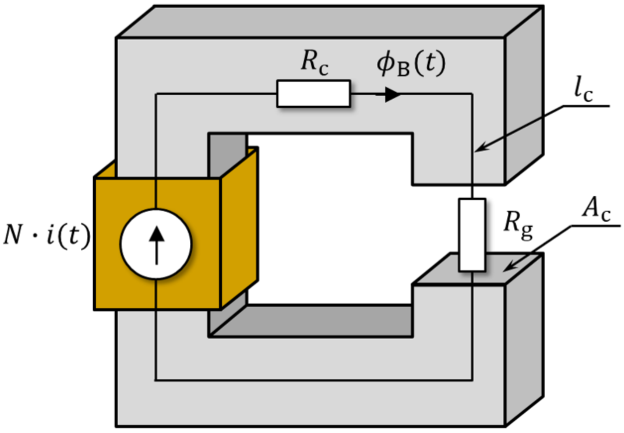

Figure 4.4. Example of a magnetic circuit of a single coil

The magnetic flux $\phi_\mathrm{B}(t)$ produced by the current $i(t)$ flowing through a coil with N turns is given by (4.27).

$$\phi_\mathrm{B}(t) = \frac{Ni(t)}{R_\mathrm{c} + R_\mathrm{g}} \tag{4.27}$$

The magnetic flux density inside the core can be calculated by dividing the magnetic flux by cross-sectional area through which it flows (4.28), whereas the peak magnetic flux density $\hat{B}$ is achieved when the current reaches peak value $\hat{I}$ (4.29).

$$B(t) = \frac{\phi_\mathrm{B}(t)}{A_\mathrm{c}} \tag{4.28}$$

$$\hat{B} = \frac{\hat{\phi}_\mathrm{B}}{A_\mathrm{c}} = \frac{1}{A_\mathrm{c}} \frac{N\hat{I}}{R_\mathrm{c} + R_\mathrm{g}} \tag{4.29}$$

where reluctance of magnetic core is given by (4.30) and the reluctance of the air gap R_g by (4.31). The K_C factor corrects for the fringing effect occurring in the vicinity of the air gap [214]. The length and cross-section of each part of the circuit can be different. In general, the relative magnetic permeability μ_r varies for ferromagnetic material due to the B-H curve. As for the air gap, if air or any other non-magnetic material is placed there, the relative magnetic permeability $\mu_\mathrm{r} = 1$. In the case of placing a superconductor in the air gap, the relative permeability is lower than 1 in the superconducting state and equal to 1 in the normal state.

$$R_\mathrm{c} = \frac{l_\mathrm{c}}{\mu_\mathrm{r}\mu_0 A_\mathrm{c}} \tag{4.30}$$

$$R_\mathrm{g} = K_\mathrm{C}\frac{l_\mathrm{g}}{\mu_\mathrm{r}\mu_0 A_\mathrm{g}} \tag{4.31}$$

During pulsed-field magnetisation, there are two ways of inducing current inside superconductors. One is by applying extremely slow-changing or "DC" field as in FC and ZFC methods (Section 3.2), the peak magnetic field $\hat{B}$ applied to HTS occurs at peak current $\hat{I}$ in (4.32).

$$\hat{B} = \frac{N}{A_\mathrm{HTS}(R_\mathrm{c} + R_\mathrm{g})}\hat{I} \tag{4.32}$$

The second way is via inducing an electric field inside the superconductor, which can be written by (4.33). This indicates that the slope of a current and magnetic field, for that matter, could play a role in magnetising HTS.

$$e_\mathrm{HTS}(t) = -\frac{\mathrm{d}\phi_\mathrm{B}(t)}{\mathrm{d}t} = -\frac{N}{R_\mathrm{c} + R_\mathrm{g}}\frac{\mathrm{d}i(t)}{\mathrm{d}t} \tag{4.33}$$

Both ways occur during PFM (Section 3.3) since applied fields are of significantly high values, and current waveforms have significantly high rates of change. The inductance L of the flux pump viewed from the terminals is related to flux linkage associated with the coil.
As first approximation, assuming that magnetic permeability $\mu = const$ stays constant, the inductance is independent from current value (4.34), where equivalent reluctance of the magnetic circuit can be expressed as $R_\mathrm{m} = l_\mathrm{m}/(\mu_\mathrm{r}\mu_0 A_\mathrm{m})$.

$$L = \frac{N\phi_\mathrm{B}(t)}{i(t)} = \frac{N^2}{R_\mathrm{c} + R_\mathrm{g}} = \frac{N^2}{R_\mathrm{m}} \tag{4.34}$$

Therefore, the resistance (4.35) is proportional to the number of turns by constant k_R, whereas inductance (4.36) is proportional to number of turns squared by a different constant k_L.

$$R = \rho\frac{l_\mathrm{avg}}{A_1}N = k_\mathrm{R}N \tag{4.35}$$

$$L = \mu_\mathrm{r}\mu_0\frac{A_\mathrm{m}}{l_\mathrm{m}}N^2 = k_\mathrm{L}N^2 \tag{4.36}$$

The constants k_R and k_L depend on the type of system, wire and magnetic circuit, including its linearity. The nonlinearity and other factors of the system have to be considered when choosing a specific flux pump system. However, they serve as an anchor point for reducing the number of parameters influencing the flux pump system, which can be analysed simpler.

4.3. Influence of circuit parameters on current waveforms

The derived equations in proceeding sections for current and capacitor bank voltage allow for generating waveforms, extracting parameters and examining circuit behavior. As an example, the PFM circuit with parameters: $R = 1\ \Omega$, $L = 1$ mH, $U_{C0} = 100$ V in a single-pulse operation will be examined, thus initial current is equal to $I_{01} = 0$ A. The forward voltage drop on diodes will be neglected $U_{D1} = 0$ V, $U_{D2} = 0$ V. The current and voltage waveforms are shown in Figure 4.5a and Figure 4.5b respectively, and have been generated for three values of capacitance 2 mF, 4 mF, 6 mF. It is assumed that the parameters of the flux pump are constant and independent from other factors, thus $R = const$ and $L = const$. The system with critical damping is a special case that is less likely to occur due to uncertainty measurement of the components and potential change of their parameters for different current and voltage values. As stated in Section 4.1, the diode D_2 conducts in an oscillatory system, which can be seen on the capacitor's voltage waveform (Figure 4.5b), where only for oscillatory system, the voltage reaches zero, but the current continues to flow through the coil, whereas in other systems the $u_C(t)$ goes to zero asymptotically. To determine in which state the system will operate, checking the sign of $(\xi^2 - 1)$ in the equation for evaluating the discriminant Δ (4.6) is sufficient. By rearranging the formula and substituting for damping coefficient (4.3), resistance (4.35) and inductance (4.36) results in relation independent from number of turns as shown in (4.37).

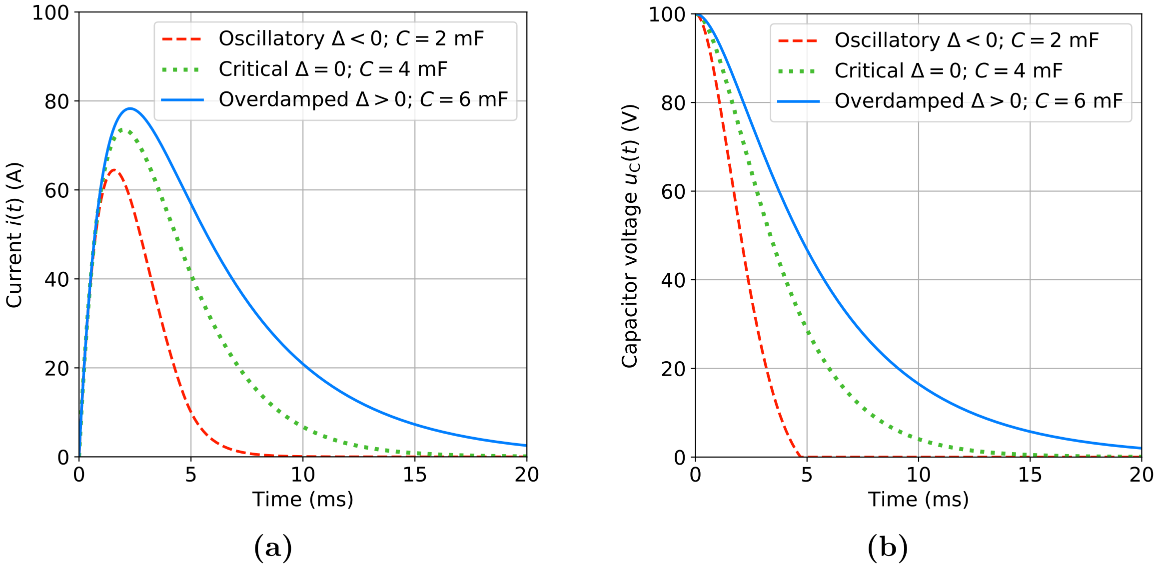

Figure 4.5. (a) Current $i(t)$ and (b) voltage $u_c(t)$ waveforms of the RLC flux pump

$$\begin{cases} \text{critical damping} & \text{if } \xi = 1 \Rightarrow C = 4k_L/k_R^2 \\ \text{overdamped} & \text{if } \xi > 1 \Rightarrow C > 4k_L/k_R^2 \\ \text{oscillatory} & \text{if } \xi < 1 \Rightarrow C < 4k_L/k_R^2 \end{cases} \tag{4.37}$$

The relations in (4.37) indicate that less important is selecting a number of turns, but rather than choosing appropriate components (i.e. conductor's material, a cross-section of wire) and geometry - dimensions of the magnetic circuit. Thus, the ratio between k_L and k_R^2, as well as the choice of capacitance, dictates the type of the system.

As mentioned in Section 4.2, the magnetic flux density is proportional to product of number of turns N and current flowing through coil $i(t)$ 4.38. The product $N \cdot i(t)$ is also called ampere-turns.

$$B(t) \propto N \cdot i(t) \tag{4.38}$$

The peak magnetic flux density and magnetic field rate-of-change, both can be written as in (4.39) and (4.40) respectively. Since the derivative of the current changes over time, for the analysis, the time $t = 0$ s has been chosen.

$$\hat{B} \propto N \cdot \hat{I} \tag{4.39}$$

$$\left.\frac{\mathrm{d}B(t)}{\mathrm{d}t}\right|_{t=0} \propto N \left.\frac{\mathrm{d}i(t)}{\mathrm{d}t}\right|_{t=0} \tag{4.40}$$

From the design perspective, all of the parameters mentioned above have to be chosen to achieve sufficient value of applied magnetic flux density - at the end, the coil has to be wounded with some number of turns, and the system has to have some dimensions. The current is influenced by three parameters R, L and C besides time t being an independent variable. The visualisation and analysis effect of change of these parameters required four-dimensional space. Since resistance and inductance are both related to number of turns by (4.35) and (4.36) respectively it is possible to represent current waveform as a function of only two variables (N and C) and one independent variable t (4.41) and extract essential parameters.

$$i(t) \rightarrow i(t, R, L, C) = i(t, N, C) \tag{4.41}$$

For purpose of preliminary analysis the parameters $k_{\mathrm{R}} = 10^{-2}\ {}^{\Omega}\!/_{\mathrm{turn}}$ and $k_{\mathrm{L}} = 100\ {}^{\mathrm{nH}}\!/_{\mathrm{turn}^2}$ have been chosen. The current waveforms will be analysed for capacitance $C = 0.5 \ldots 5.5$ mF and $N = 40 \ldots 190$ turns, and since all derived equations (4.11), (4.14) and (4.17) are directly proportional to the voltage U_{C0}, the values can be examined per applied voltage (A/V). Three characteristic parameters of the flux pump have been chosen: peak current $\hat{I}$, current rate of change $\left.\frac{\mathrm{d}i(t)}{\mathrm{d}t}\right|_{t=0}$ and peak ampere-turns $N\hat{I}$ as shown in Figure 4.6. The main conclusions from performed analysis are:

- The peak current (4.42) depends on both capacitance and the number of turns. Increasing capacitance increases stored charge, which then will be delivered to the coil, resulting in higher $\hat{I}$. On the other hand, lowering the number of turns results in lower resistance and inductance, which are opposing current rise, therefore decreasing those values is beneficial for achieving higher peak currents as shown in Figures 4.6a and 4.6b.

$$\hat{I} = \max\{i(t)\} \tag{4.42}$$

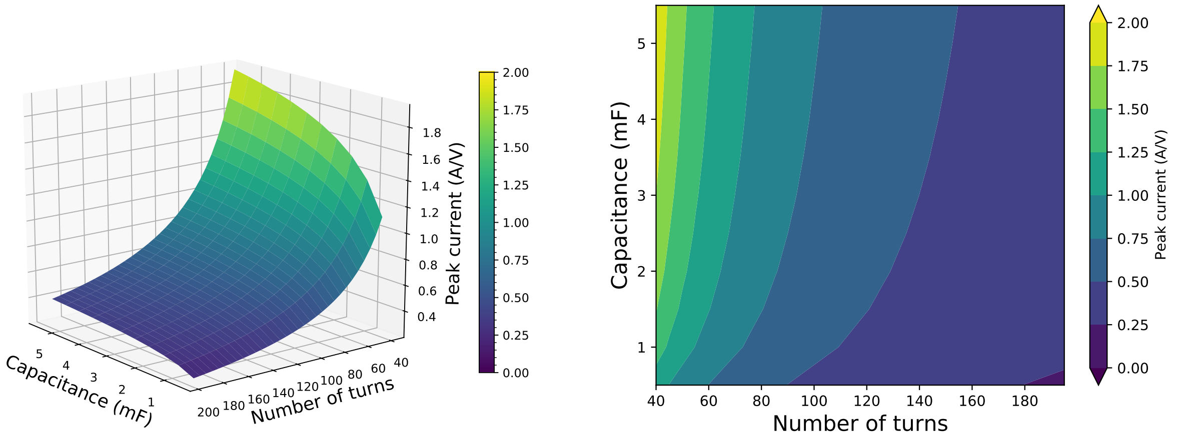

(a) peak current - contour plot

(b) peak current - surface plot

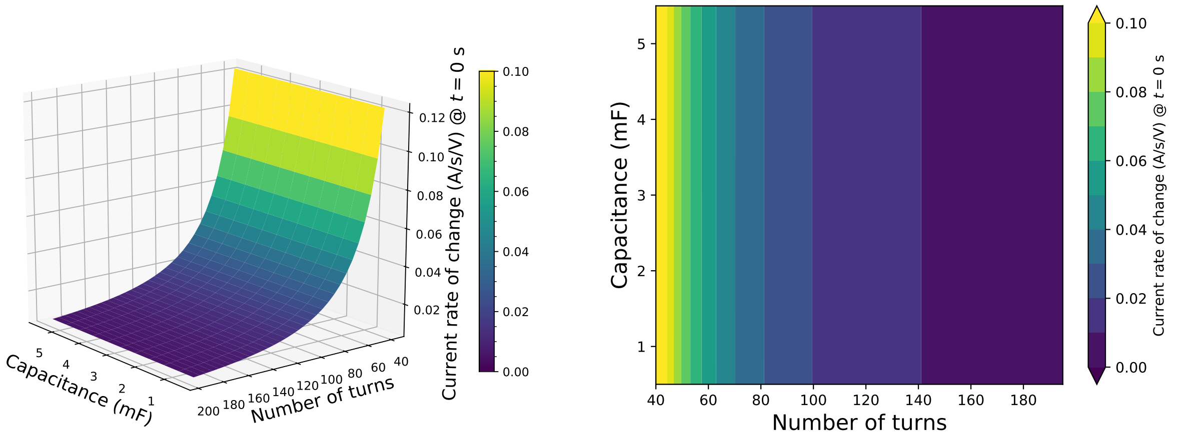

(c) current rate-of-change ($t = 0$ s) - - surface plot

(d) current rate-of-change ($t = 0$ s) - - contour plot

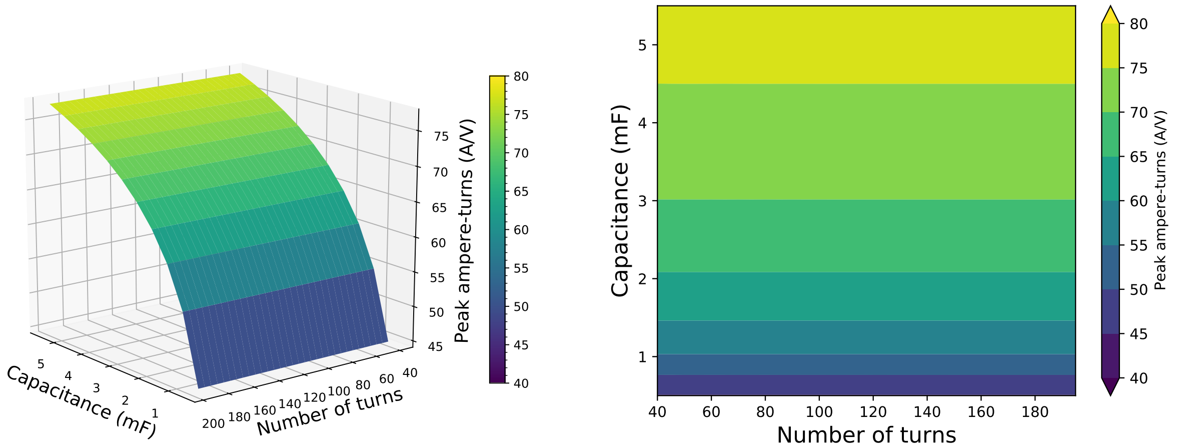

(e) peak ampere-turns - surface plot

(f) peak ampere-turns - contour plot

Figure 4.6. RLC flux pump circuit parameters (number of turns N and capacitance C) influence on: (a and b) peak current; (c and d) current derivative at $t = 0$ s; (e and f) peak value of ampere-turns

- The Figures 4.6c and 4.6d show that the current rate-of-change at $t = 0$ s is also higher for a lower number of turns due to lower inductance, being the main limiting factor. The current rate-of-change is independent of the capacitance value C, which can be seen by calculating its derivative (4.43).

$$\left.\frac{\mathrm{d}i(t)}{\mathrm{d}t}\right|_{t=0} = \frac{U_{\mathrm{C0}}}{L} \tag{4.43}$$

- The peak ampere-turns and consequently peak magnetic flux density (4.39) is independent from number of turns and depends only on the value of capacitance (Figures 4.6e and 4.6f). As explained in the first point, higher capacitance results in a higher total value of delivered charge to the coil, resulting in a higher peak value. This means that peak ampere-turns should be affected by k_{R} and k_{L} instead, and in the conducted analysis were constants, which is not always true, especially when a number of conductors changes, since it will affect coil dimensions; therefore flux leakage.

The peak current $\hat{I}$ influences mainly on a choice of elements such as diodes D_1 and D_2 in the system network (Figure 4.1) and potentially capacitors. On the other hand, the current rate of change and peak magnetic flux density is related to the pulsed-field magnetisation process, and at least one of those is desired to be a high value. Therefore, the limiting factor of the system seems to be the peak and average current that the diodes can conduct.

The number of turns N and value of capacitance C are common factors on the above plots (Figure 4.6); therefore, it is possible to relate all above parameters to one another and can be placed on a single plot as presented in Figure 4.7. The parameter surface in Figure 4.7 shows that increasing the current rate-of-change also increases peak current, which is congruent to what already has been mentioned above with regards to R and L as limiting factors of the circuit. On the other hand, high peak ampere-turns and the high current rate-of-change are mutually exclusive, although the relation is nonlinear.

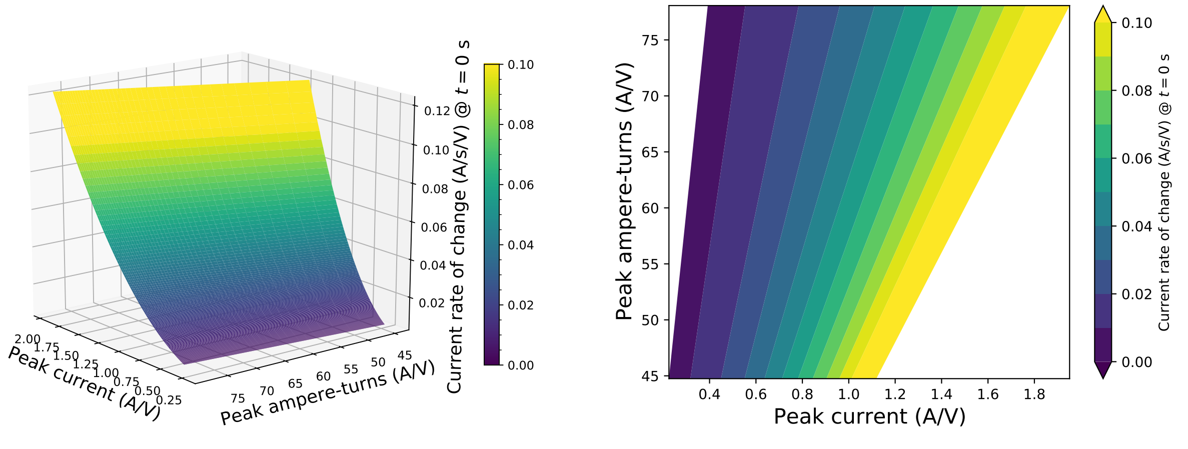

(a) **(b)**

Figure 4.7. Relation between peak current, peak ampere-turns and current rate-of-change at $t = 0$ s: (a) surface plot; (b) contour plot

In the next step, to analyse influence of resistance (4.35) and inductance (4.36) coefficients, the number of turns has been fixed ($N = 100$) and capacitance set to $C = 1$ mF. The values of analysed parameters are set for ranges $k_\mathrm{R} = 0.01 \ldots 0.1$ Ω/turn and $k_\mathrm{L} = 1 \ldots 10$ nH/turn^2. The surfaces representing influence of those parameters on peak current $\hat{I}$ and current rate of change $\left.\frac{\mathrm{d}i(t)}{\mathrm{d}t}\right|_{t=0}$ are shown in Figure 4.8. Since the value of N is constant, there is no need to analyse product $N \cdot \hat{I}$. The analysis shows that resistance R is the main factor influencing peak current, whereas inductance L mainly influences the current rate-of-change, with minor influence from the resistance. Furthermore, the smaller the values of coefficients, the larger the peak field and its derivative are.

To conclude conducted analysis, the parameters of resistance and inductance k_R and k_L should be at the lower side of the spectrum to achieve high peak current and high magnetic flux density. This approach will also result in higher current derivatives and lower rising time. Furthermore, the peak magnetic flux density $\hat{B}$ can be further improved by increasing capacitance value, whereas all parameters can be scaled accordingly by controlling the voltage of the capacitor bank.

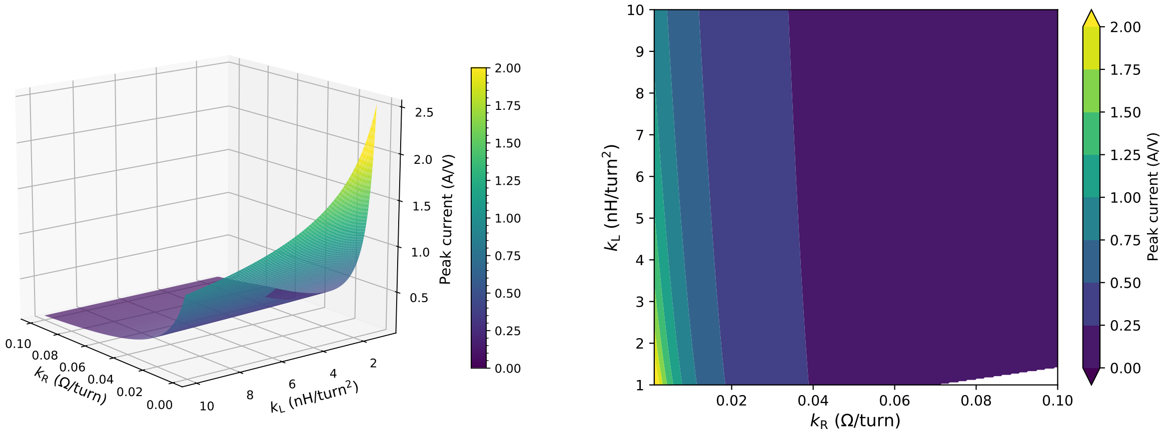

(a) peak current - surface plot

(b) peak current - contour plot

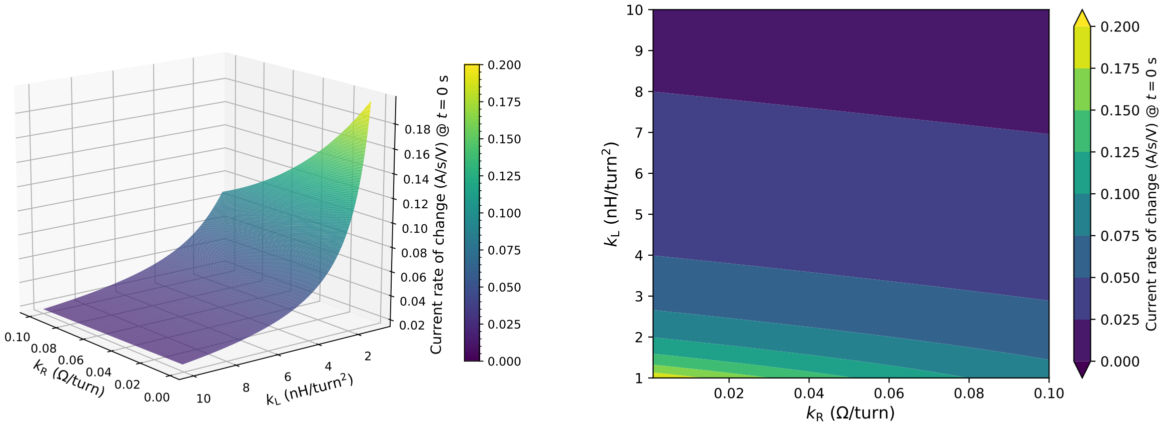

(c) current rate-of-change ($t = 0$ s) - - surface plot

(d) current rate-of-change ($t = 0$ s) - - contour plot

Figure 4.8. Influence of coil's k_R and k_L parameters on: (a and b) peak current; (c and d) current rate-of-change at $t = 0$ s

4.4. Flux pump circuit design

The goal of the following thesis is to examine the influence of a peak magnetic flux density $\hat{B}$, and its derivative $\frac{\mathrm{d}B(t)}{\mathrm{d}t}$ on the trapped field inside the HTS bulk. Therefore, the design should take into account systems that are comparable, i.e. should have similar dimensions but a different number of turns. As previously described in Section 3.5, the magnetiser circuit with a ferromagnetic core has its benefits in higher trapped field [40, 205, 210] but also introduces additional nonlinearity in the system. The nonlinearity comes from the B-H curve of the material, which has a saturation typically at around 1.8 T (for electrical steel). Having a whole magnetic circuit made of electrical steel as in Figure 4.1a with a large air gap and superconductor located in the air gap would possibly result in saturation of parts in the vicinity of the gap, resulting in magnetic flux flowing from the center column directly to side columns. The advantage is the possibility of achieving high inductance L for the relatively low number of turns, but only until reaching saturation of the core. If the core becomes saturated, the relative magnetic permeability approaches permeability of the free space $\mu \rightarrow \mu_0$. This nonlinearity would result in different current waveforms compared to Figure 4.5a. Therefore, to eliminate those effects, a linear system would be appropriate, such as the core-less system.
From the three coil types: CMDC, split-coils and solenoid (Figure 3.2), the last would be preferred since it is a single-coil making it easy to manufacture and use in other systems. However, the CMDC and split-coils are located on top and bottom of the bulk, making it difficult to use as a part of other systems, i.e. in electric motors, whereas the solenoid coil is wounded around the bulk and does not interfere with trapped magnetic flux. Therefore, a solenoid coil has been chosen as a coil for the PFM system.

For the capacitor bank, the electrolytic capacitors provide high energy to size ratio and are readily available for voltages 400 V or 650 V, which are dedicated for DC bus in power converters. The capacitor bank can then be charged using mains voltage with a rectifier or a laboratory power supply. The capacitance of a single unit easily ranges from couple microfarads to millifarads and can withstand short circuit state on terminals with currents reaching up to 1 kA momentarily.

The starting point of the design is the HTS bulk which will be used for pulsed-field magnetisation with a dimensions of: diameter $D_{\mathrm{HTS}} = 28$ mm and height
$H_{\mathrm{HTS}} = 10$ mm. The bulk diameter limits the minimum inner diameter of the solenoid, which should be larger than the bulk's diameter $D_{\mathrm{HTS}} < D_{\mathrm{in}}$. The inner diameter D_{in} should also account for additional space due to tolerance issues and space required for sensor wiring. Too large inner diameter would diminish the field; therefore, the coil should be as close as possible to the bulk.

The magnetic flux density in the axial direction B_{z} acting on the HTS bulk should also be as uniform as possible. The magnetic field produced by the solenoid flowing through the bulk of thickness H_{HTS}, should have a similar value at both ends of the bulk at $|z| = {}^{H_{\mathrm{HTS}}}/_{2}$ as the field value at the center at $z = 0$; therefore, the peak magnetic flux density at the axis of symmetry of a finite solenoid can be calculated using (4.44) [215], where H is the total height of the solenoid coil. Equation (4.44) is an approximation and does not take into account the solenoid thickness but instead assumes infinitely small thickness.

$$\hat{B}_{\mathrm{z}}(z) \approx \mu_0 \frac{N\hat{I}}{2} \left[\frac{{}^{H}/_{2} - z}{H\sqrt{{}^{D_{\mathrm{in}}^2}/_{4} + ({}^{H}/_{2} - z)^2}} + \frac{{}^{H}/_{2} + z}{H\sqrt{{}^{D_{\mathrm{in}}^2}/_{4} + ({}^{H}/_{2} + z)^2}} \right] \tag{4.44}$$

The number of turns and value of the current are proportionality constants which do not influence flux distribution, but only its value. For different values of solenoid height $H = 1 \ldots 100$ mm a ratio of magnetic flux densities at $z = 5$ mm and $z = 0$ mm has been calculated $\hat{B}_\mathrm{z}(z = 5)/\hat{B}_\mathrm{z}(z = 0)$ for different inner diameters D_in and plotted as shown in Figure 4.9.

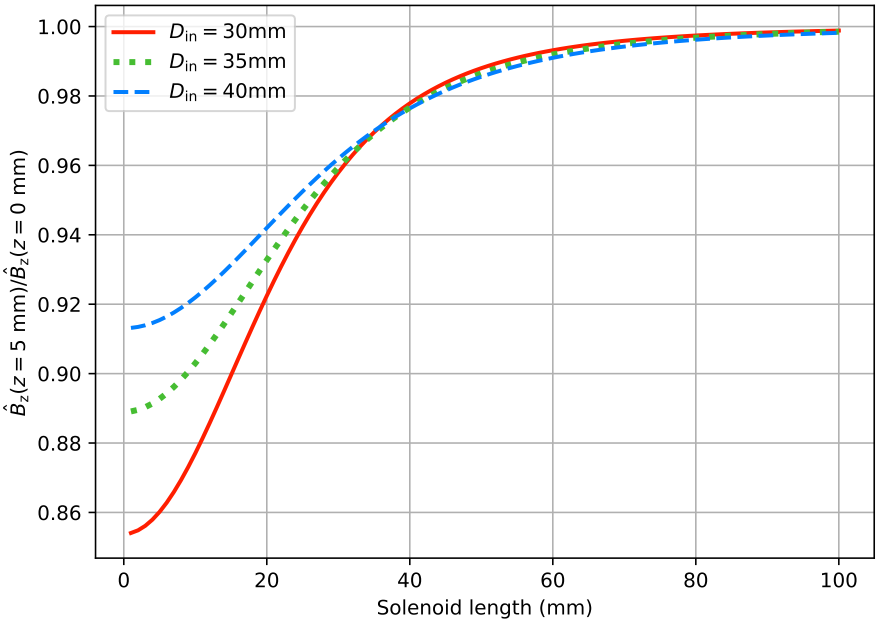

Figure 4.9. Magnetic field uniformity for solenoids of different length and inner diameters

The analysis shows that for solenoids of length $L \approx 40$ mm there is no difference in field uniformity between solenoids of analysed diameters, with diminishing returns for lengths over 60 mm. The field becomes more uniform as solenoid length becomes longer.

To test the hypothesis stated in the thesis relating to the influence of the derivative over time of applied field on the trapped field, two coils with similar peak field $\hat{B}$ capabilities ought to be designed, where minor adjustments can be made by applying different voltages. Therefore, the value shown in (4.45) has been set as a goal for designing the system. Thus, two coils for comparison will be designed primarily.

$$\frac{\hat{B}_\mathrm{z}(z = 0)}{\hat{I}} = \frac{1\ \mathrm{T}}{100\ \mathrm{A}} \tag{4.45}$$

As has been shown in previous Section 4.3 and shown in Figure 4.6, the number of turns influences the current (and magnetic field) rate-of-change; therefore, resistance and inductance coefficients of the designed coils should be constant and as similar as possible for a fair comparison. This means that in order to $k_\mathrm{R} = const$, the same kind of wire should be used, meaning it should have the same cross-sectional area A_1 and be made out of the same material. The average length of turn l_avg should also be the same, but this might differ depending on the total number of turns in the solenoid coil. The inductance k_L would also be the same for both coils if those solenoids had similar dimensions.

The coils are designed to be submerged in the liquid nitrogen at the temperature of 77 K, which would significantly reduce wire resistance; it has been assumed that the designed circuit would most likely operate as oscillatory (4.37), and the current is described by the (4.25). The peak current occurs at the first stage, and assuming there is no initial current; hence $Y_{01} = 0$ S, the peak current is given by the (4.46).

$$\hat{I} = \frac{U_{\mathrm{C0}}}{L}\frac{1}{B} = \frac{2U_{\mathrm{C0}}}{N}\sqrt{\frac{C}{4k_{\mathrm{L}} - k_{\mathrm{R}}^2 C}} \tag{4.46}$$

The design point for coil would be to achieve $\hat{B}_{\mathrm{z}} = 2$ T at voltage $U_{\mathrm{C0}} = 300$ V, which is limited by power supply and leaves room for adjustment, the maximum capacitance would be $C = 5$ mF, and coil dimensions $D_{\mathrm{in}} = 35$ mm, $H = 60$ mm. Two coils with a corresponding flux density to current ratios are designed to be 1 T/100 A. The peak energy stored in the magnetic field $\hat{W}$ in the volume V (4.47) can be used to estimate inductance L of coil required to achieve given parameters as shown in (4.48). As the thickness of both coils is still unknown, it can be assumed that the majority of the energy is stored in the inner volume of the solenoid $V \approx V_{\mathrm{in}}$.

$$\begin{cases} \hat{W} = \dfrac{1}{2}\hat{B}\hat{H}V_{\mathrm{in}} = \dfrac{1}{2}\dfrac{\hat{B}^2}{\mu_0}V_{\mathrm{in}} \\ \hat{W} = \dfrac{1}{2}L\hat{I}^2 \end{cases} \tag{4.47}$$

$$L \approx 2\frac{V_{\mathrm{in}}}{\mu_0}\left(\frac{\hat{B}_{\mathrm{z}}}{\hat{I}}\right)^2 = \frac{HD_{\mathrm{in}}^2}{2\mu_0}\left(\frac{\hat{B}_{\mathrm{z}}}{\hat{I}}\right)^2 \tag{4.48}$$

$$L = \frac{60 \cdot 10^{-3} \cdot (35 \cdot 10^{-3})^2}{2\mu_0}\left(\frac{1}{100}\right)^2 = 9.185 \text{ mH}$$

The current rate-of-change per voltage is an inverse of the inductance as shown in (4.49), which for this coil would be ≈ 110 A/s/V.

$$\frac{1}{U_{\mathrm{C0}}}\left.\frac{\mathrm{d}i(t)}{\mathrm{d}t}\right|_{t=0} = \frac{1}{L} \tag{4.49}$$

The second coil has been designed such that its inductance will be one-third of the first one, therefore $L = 3$ mH with similar dimensions D_{in} and H, resulting in a ratio of magnetic flux density to current equal to ≈ 0.6 T/100 A and current rate-of-change being ≈ 330 A/s/V. Equation (4.44) is an approximation for an infinitely thin solenoid but rearranged can serve as a boundary for calculating the minimum required number of conductors required to achieve set parameters $N \geq N_{\mathrm{min}}$ as shown in (4.50) for $z = 0$, where $\lceil\cdot\rceil$ is a ceiling of a number. The total number of conductors N will be greater, as with the number of turns, the thickness of coil increases, the influence of outermost turns will become lower.

$$\begin{cases} N \geq N_{\mathrm{min}} \\ N_{\mathrm{min}} = \left\lceil \dfrac{\hat{B}}{\mu_0\hat{I}}\sqrt{D_{\mathrm{in}}^2 + H^2} \right\rceil \end{cases} \tag{4.50}$$

For the 9 mH coil, the minimum required number of conductors $N_{\mathrm{min}} = 553$, whereas for 3 mH coil it is equal to $N_{\mathrm{min}} = 387$. The coil can be wounded with wires being stacked on one-another (Figure 4.10a) or with an offset (Figure 4.10b). The number of wires with diameter D_{w1} that will fit into the window with dimensions $W \times H$ for pattern in Figure 4.10a can be calculated using set of equations (4.51), whereas for pattern with translated wires in Figure 4.10b, the set of equations (4.52) is valid. The symbol $\lfloor\cdot\rfloor$ is a floor of a number. The second pattern is usually easier to manufacture, especially for wires with smaller diameters where controlling position of placed turns becomes difficult.

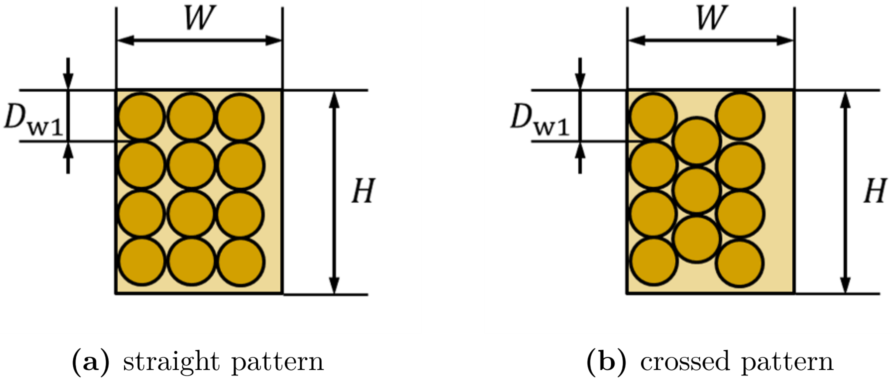

(a) straight pattern **(b)** crossed pattern

Figure 4.10. Coil turn patterns: (a) straight; (b) crossed

$$\begin{cases} N_{\mathrm{w}} = \left\lfloor \dfrac{W}{D_{\mathrm{w1}}} \right\rfloor \\ N_{\mathrm{h}} = \left\lfloor \dfrac{H}{D_{\mathrm{w1}}} \right\rfloor \\ N = N_{\mathrm{w}} N_{\mathrm{h}} \end{cases} \tag{4.51}$$

$$\begin{cases} N_{\mathrm{w}} = \left\lfloor 2\dfrac{\sqrt{3}}{3}\left(\dfrac{W}{D_{\mathrm{w1}}} - 1\right) \right\rfloor + 1 \\ N_{\mathrm{h\ max}} = \left\lfloor \dfrac{H}{D_{\mathrm{w1}}} \right\rfloor \\ N = \dfrac{N_{\mathrm{w}} + (N_{\mathrm{w}} \bmod 2)}{2} N_{\mathrm{h\ max}} + \dfrac{N_{\mathrm{w}} - (N_{\mathrm{w}} \bmod 2)}{2} (N_{\mathrm{h\ max}} - 1) \end{cases} \tag{4.52}$$

Assuming the coil thickness $W > 0$, the (4.44) in that form no longer holds. Nonetheless, the magnetic flux density can be calculated for a solenoid coil with an equivalent diameter D_{eq} that is in between inner and outer diameters as stated in (4.53).

$$D_{\mathrm{in}} \leq D_{\mathrm{eq}} \leq D_{\mathrm{out}} \tag{4.53}$$

Combining (4.46) and (4.44) and assuming $z = 0$, the peak magnetic flux density $\hat{B}_{\mathrm{z}}$ can be calculated as (4.54) in terms of equivalent diameter D_{eq}.

$$\hat{B}_{\mathrm{z}} = \mu_0 U_{\mathrm{C0}} \sqrt{\frac{4C}{(4k_{\mathrm{L}} - k_{\mathrm{R}}^2 C)(D_{\mathrm{eq}}^2 + H^2)}} \tag{4.54}$$

By rearranging the (4.54), the formula relating resistance coefficient k_R with inductance coefficient k_L and other parameters is given as (4.55).

$$k_\mathrm{R} = 2\sqrt{\frac{k_\mathrm{L}}{C} - \frac{1}{D_\mathrm{eq}^2 + H^2}\left(\frac{\mu_0 U_\mathrm{C0}}{\hat{B}_\mathrm{z}}\right)^2} \tag{4.55}$$

The (4.55) is satisfied if number under the square root is positive, meaning, that condition (4.56) is satisfied.

$$k_\mathrm{L} > \frac{C}{D_\mathrm{eq}^2 + H^2}\left(\frac{\mu_0 U_\mathrm{C0}}{\hat{B}_\mathrm{z}}\right)^2 \tag{4.56}$$

It can also be pointed out that for minimum value of inductance coefficient k_L, the resistance coefficient k_R also reaches minimum $k_\mathrm{L\ min} \implies k_\mathrm{R\ min}$; therefore, it should result in minimum coil dimensions since the k_R is proportional to the average length of turn l_avg. In coreless systems, there is no clear path for magnetic flux to take, unlike in systems with a magnetic core, the equivalent reluctance of it can be assumed to have some equivalent cross-sectional area A_m and length l_m as in (4.36). Since the equivalent diameter of the solenoid with thickness is between inner and outer diameters (4.53), the inductance coefficient k_L should also fall in between parameters $k_\mathrm{L\ in}$ and $k_\mathrm{L\ out}$ calculated for both diameters respectively. The length of the magnetic circuit is assumed to be H according to (4.57).

$$\mu_0 \frac{D_\mathrm{in}^2}{4H} \leq k_\mathrm{L} \leq \mu_0 \frac{D_\mathrm{out}^2}{4H} \tag{4.57}$$

The inductance coefficient as an unknown can be calculated for known inductance L and square of a number of turns $N(D_\mathrm{w1}, W)$ given as a function of a wire diameter D_w1 and coil thickness W as shown in (4.58).

$$\mu_0 \frac{D_\mathrm{in}^2}{4H} \leq \frac{L}{N^2(D_\mathrm{w1}, W)} \leq \mu_0 \frac{(2W + D_\mathrm{in})^2}{4H} \tag{4.58}$$

The inequalities (4.57) and (4.58), could be expressed in terms of D_out instead of W, but operating on coil thickness is easier from the design perspective and calculating the number of turns N with set of equations (4.51) or (4.52). Therefore, the limits for selecting a number of turns depending on the coil thickness W and wire diameter D_w1 are given a set of equations (4.59), whereas the second set is given as set of equations (4.50), which is a global lower boundary. Additionally, the number of turns should be selected such that condition (4.56) is satisfied with a possibly minimal value of k_L to achieve the lowest k_R. This would be possible if equivalent coil diameter D_eq would be as high as possible so that $k_\mathrm{R} \to 0$; therefore, D_out or W should be maximised.

$$\begin{cases} N_\mathrm{max} \geq N(D_\mathrm{w1}, W) \geq N_\mathrm{min}(W) \\ N_\mathrm{max} = \left\lfloor \sqrt{\frac{4HL}{\mu_0}} \frac{1}{D_\mathrm{in}} \right\rfloor \\ N_\mathrm{min}(W) = \left\lceil \sqrt{\frac{4HL}{\mu_0}} \frac{1}{2W + D_\mathrm{in}} \right\rceil \end{cases} \tag{4.59}$$

The minimum number of turns depending on coil width $N_{\text{min}}(W)$ has been shown in Figure 4.11 with a global lower boundary according to (4.50). The upper boundary for choosing number of turns $N_{\text{max}} = \lfloor \sqrt{\frac{4HL}{\mu_0}} \frac{1}{D_{\text{in}}} \rfloor$ for 9 mH coil is equal to $N_{\text{max}} = 1184$ and for 3 mH solenoid is $N_{\text{max}} = 683$ turns.

From performed analysis, coil thickness for 9 mH coil has been chosen as $W = 20$ mm, whereas for 3 mH coil is $W = 13.5$ mm. Picking the highest value possible would allow using wires of higher diameter resulting in the lowest total resistance of the coil, improving its performance. The same wire diameter D_{w1} will be chosen for both designed coils. This narrows down the choice of wire diameters to 1.1 mm $\leq D_{\text{w1}} \leq$ 1.5 mm as shown in Figure 4.12 with solid black lines. As highest value as possible is desired to reduce resistance, thus $D_{\text{w1}} = 1.445$ mm (dashed vertical black line) has been chosen to leave some room for possible adjustments, which resulted in $N = 609$ turns for 9 mH coil, and $N = 421$ turns for 3 mH coil.

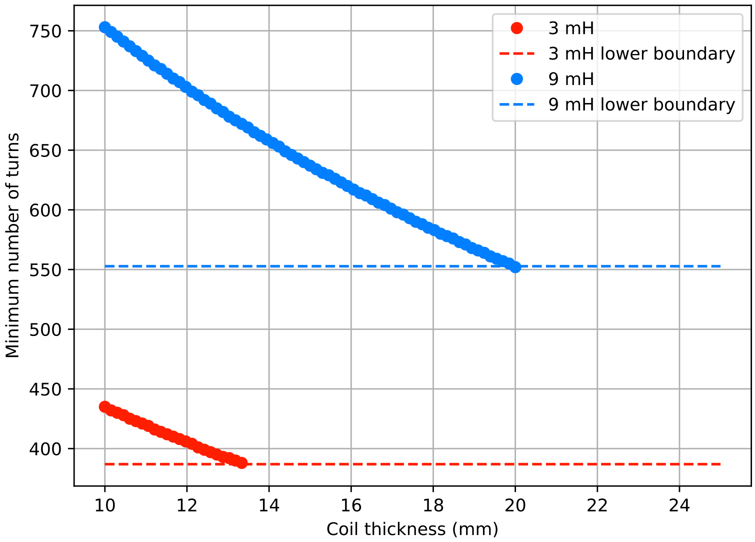

Figure 4.11. Minimum number of turns N_{min} required to achieve design point of solenoid coils L_1 and L_2 depending on coil thickness

To test further the hypothesis on influence of current rate-of-change a third coil has been designed using the same procedure described above, that will have inductance $L \approx 1$ mH and 0.3 T/100 A for $U_{\text{C0}} = 300$ V and $C = 5$ mF. The coil will have the same inner diameter $D_{\text{in}} = 35$ mm and height $H = 60$ mm as previous two coils, but will be made using wire with diameter $D_{\text{w1}} = 2$ mm to reduce resistance. This resulted in values: $W = 17$ mm and $N = 219$.

A series of simulations were performed to estimate the flux pump's behaviour for each coil connected to the system. The simulations were based on equations derived in Section 4.1. The resistance of the coil in LN2 can be calculated using (4.60), where R_{T0} is the resistance in reference temperature T_0 in Kelvins. The resistance R_{T} can be calculated for a given temperature T, which in this case is $T = 77$ K.

$$R_{\text{T}} = R_{\text{T0}} \frac{T - 38.15}{T_0 - 38.15} \tag{4.60}$$

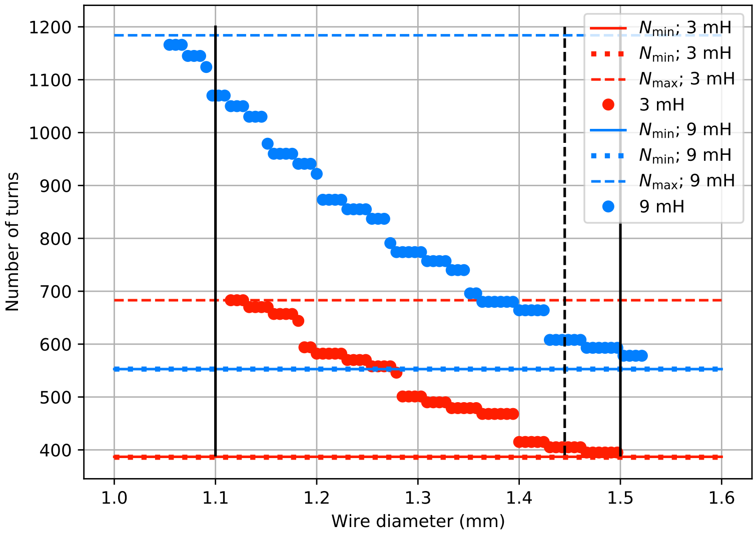

Figure 4.12. Number of turns N and wire diameter D_{w1} required to achieve design parameters of coils L_1 and L_2

For all designed coils, measurements of inductance and resistance have been performed, which resulted in values shown in Table 4.1. The slight deviation from planned design values results from gaps between wires, effectively decreasing coil inductance. The difference in values of k_{R} or ampere-turns per volt is due to different coil thicknesses. To keep k_{R} and k_{L} values constant, the distance between turns in the coil would need to be increased uniformly to achieve the same thickness for both L_1 and L_2 coils, making it difficult to manufacture.

Table 4.1. Parameters of designed coils

Name	**Value**	**Unit**	L_1	L_2	L_3
Number of turns	N	(-)	609	421	219
Inductance	L	(mH)	9.147	3.015	0.927
Resistance @ 300 K	R_{300}	(Ω)	1.1	0.64	0.27
Resistance @ 77 K	R_{77}	(mΩ)	166.3	96.7	40.8
Wire diameter	D_{w1}	(mm)	1.45	1.45	2.0
Coil inner diameter	D_{in}	(mm)	35	35	35
Coil height	H	(mm)	60	60	60
Coil thickness	W	(mm)	20.0	13.5	17.0
Magnetic flux density to current ratio (gain)	$\hat{B}/\hat{I}$	(T/100 A)	0.9	0.6	0.3
Peak ampere-turns per volt @ 5 mF	$N\hat{I}/U_{\mathrm{C0}}$	A/V	454.8	544.6	489.9
Inductance coeff.	k_{L}	(nH/turn^2)	24.66	17.01	19.33
Resistance coeff. @ 300 K	k_{R300}	(mΩ/turn)	1.806	1.520	1.233
Resistance coeff. @ 77 K	k_{R77}	(mΩ/turn)	0.273	0.230	0.186
Time constant @ 77 K	τ	(ms)	55.0	31.2	22.7
Capacitor discharge time @ 77 K[1]	t_{C0}	(ms)	11.0	6.3	3.6
Time of reaching $\hat{I}$ @ 77 K[1]	t_{max}	(ms)	6.7	3.9	2.2
Total pulse time @ 77 K[1]	t_{RL0}	(ms)	200	115	78

---

[1] Under conditions: $U_{\mathrm{D1}} = U_{\mathrm{D2}} = 1$ V, $U_{\mathrm{C0}} = 300$ V and $C = 5$ mF

At this point, the values associated with components of the flux pump circuit are known and listed in Table 4.1. For those components a series of simulations was performed to evaluate behavior of the circuit under various conditions. Firstly, a comparison between models without including forward voltage drop on diodes ($U_{\mathrm{D1}} = U_{\mathrm{D2}} = 0$ V) described with (4.22) and with included forward voltage drop ($U_{\mathrm{D1}} = U_{\mathrm{D2}} = 1$ V) given by (4.25) for $C = 5$ mF and $U_{\mathrm{C0}} = 300$ V is shown in Figure 4.13. The results show slight difference between waveforms, mainly during descending phase. The highest current and therefore highest power losses occur for coil with $L = 1$ mH. Secondly, power losses are evaluated in components of the system with the coil ($L = 1$ mH) and included forward voltage drop on both diodes equal to 1 V are presented in Figure 4.14. The instantaneous power losses in resistance are calculated using (4.61) and diodes with forward voltage drop U_{D} with (4.62). The total power losses in coil are estimated by integrating instantaneous losses over pulse time period t_{RL0}, wheres losses in diode D_1 occurs over time $[0; t_{\mathrm{C0}}]$ and in D_2 over time $(t_{\mathrm{C0}}; t_{\mathrm{RL0}}]$. The power losses in capacitor's equivalent series resistance R_{ESR} are neglected. It can be seen that the majority of power losses is generated in coil (2.5 kW), whereas conduction power losses in diodes are equal to 9 W and 190 W on series diode D_1 and parallel diode D_2 respectively. Power losses generated in the coil are large in value, but the coil is planned for operation in liquid nitrogen, which mass will be substantial, providing high thermal inertia of the system, compared to the pulse duration.

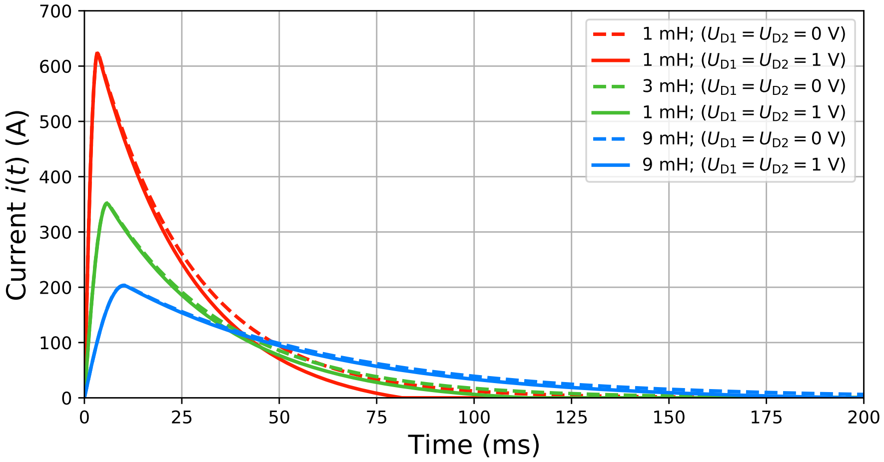

Figure 4.13. Comparison of derived current waveform models generated by flux pump with and without included forward voltage drop on diodes in system with $C = 5$ mF and $U_{\mathrm{C0}} = 300$ V

$$\Delta p_{\mathrm{R}}(t) = R_{77} \cdot i^2(t) \tag{4.61}$$

$$\Delta p_{\mathrm{D}}(t) = U_{\mathrm{D}} \cdot i(t) \tag{4.62}$$

Since the magnetic flux density to current ratio of each coil ($\hat{B}/\hat{I}$) is known (Tab. 4.1), the peak applied fields $\hat{B}_{\mathrm{app}}$ generated by flux pump system can be estimated. Peak field increases with value of capacitance, thus systems with highest value of used capacitance $C = 5$ mF are plotted for different voltages $U_{\mathrm{C0}} = 50 \ldots 300$ V. The coils differ in values $\hat{B}/\hat{I}$; therefore for comparison of coils from an electric point of view the waveforms presented in Figure 4.15 have the same scale on current axis $i(t)$ (left), but differ on magnetic flux density axis $B(t)$ (right). All analysed coils are capable of achieving similar peak fields $\hat{B}_{\mathrm{app}} \approx 2$ T, but require different peak currents $\hat{I}$. The coils differ in the current rate-of-change as intended by design, both on ascending and descending phases of the current pulse.

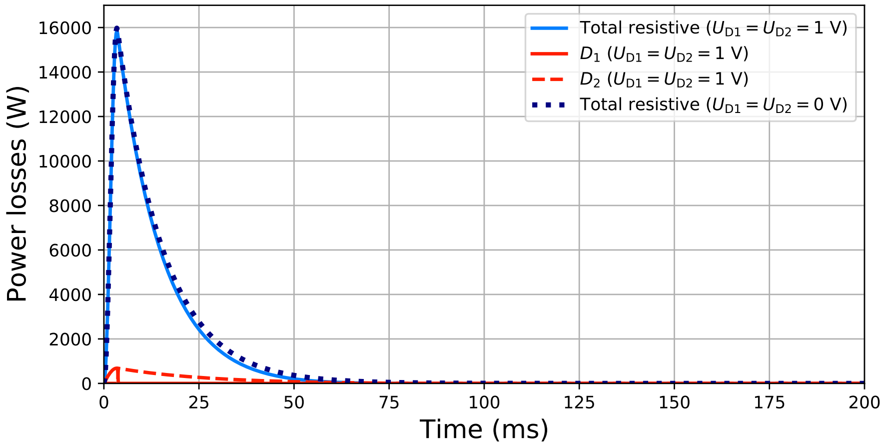

Figure 4.14. Power losses generated in coil and diodes in flux pump system with $L_3 = 1$ mH coil, $C = 5$ mF and $U_{C0} = 300$ V

The diodes (or other power electronic switches) should handle such voltages and currents without breaking. One of the parameters describing the diode is a *diode forward average current* I_{FAV} which is limited by the maximum junction temperature T_{vjmax}. That current is given for a pulsed current lasting for time $t_{\mathrm{p}} = 10$ ms, which typically is equal to half of grid voltage period (in 50 Hz grid system) in which time the current would raise the junction temperature to T_{vjmax}. Based on the current waveforms in Figure 4.5a for the majority of the time, the current decays; therefore, it can be assumed that in the worst-case scenario, the diode conducts the whole current for time t_{RL0} (4.26). The allowed pulsed current can be then evaluated using (4.63) assuming that the energy required for achieving the maximum allowed junction temperature are the same but last for a different amount of time. Judging by the current shape generated for all designed coils shown in Figure 4.15, the current approximately has a triangular shape; thus, the average diode current can be approximated as half of the peak current value.

$$I_{\mathrm{Fmax}} \approx I_{\mathrm{FAV}} \sqrt{\frac{t_{\mathrm{RL0}}}{t_{\mathrm{p}}}} \approx \frac{1}{2} \hat{I} \sqrt{\frac{t_{\mathrm{RL0}}}{t_{\mathrm{p}}}} \tag{4.63}$$

In worst case-scenario, the peak current value is expected to be $\hat{I} \approx 630$ A and lasts for $t_{\mathrm{RL0}} \approx 78$ ms; therefore:

$$I_{\mathrm{Fmax}} = \frac{1}{2} 630 \sqrt{\frac{78}{10}} \approx 900 \text{ A}$$

Similarly, the diode D_1 conducts current only when the capacitor bank is discharged, therefore up to reaching time $t = t_{\mathrm{C0}}$, the same approach can be used:

$$I_{\mathrm{Fmax}} = \frac{1}{2} 630 \sqrt{\frac{3.6}{10}} \approx 110 \text{ A}$$

The forward current of a parallel diode D_2 should be rated up to at least 900 A. The manufacturers provide *maximum surge current* (or *peak impulse current*) I_{SM} parameter in datasheets, which should suffice the condition $I_{\mathrm{SM}} \geq I_{\mathrm{Fmax}}$.

However, the frequency of operation of the system would suggest, that it would be operating closer to room temperature $T = 20°\mathrm{C}$. The diode should also withstand *maximum repetitive reverse blocking voltages* of at least 300 V nominally; however, a similar voltage rating should be applied to all components.

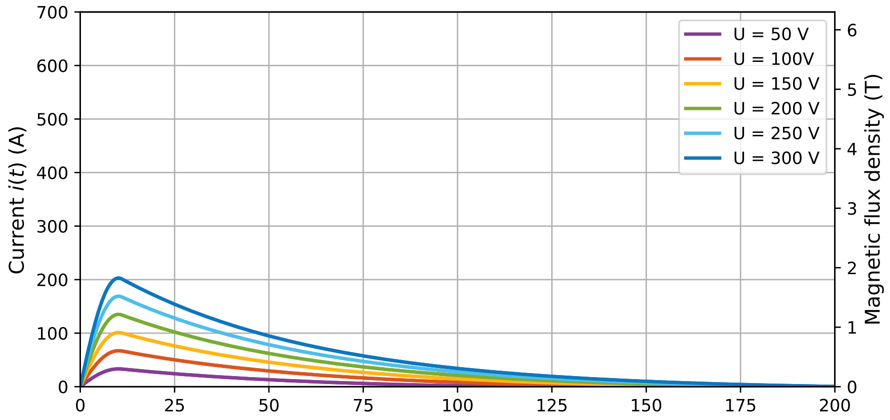

(a) $L_1 = 9$ mH

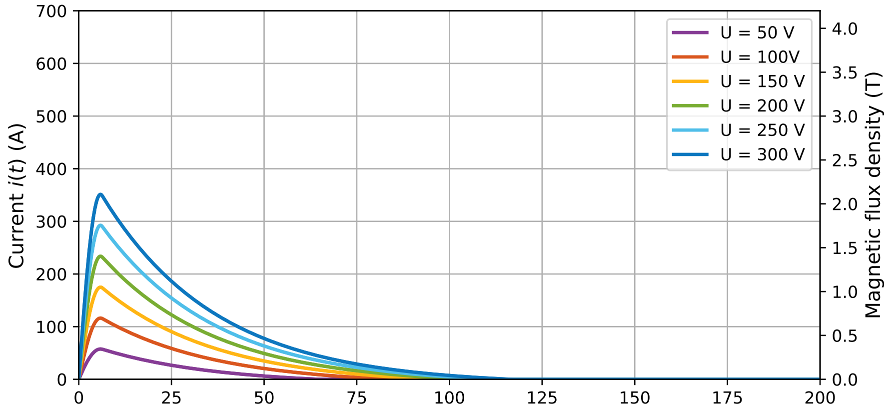

(b) $L_2 = 3$ mH

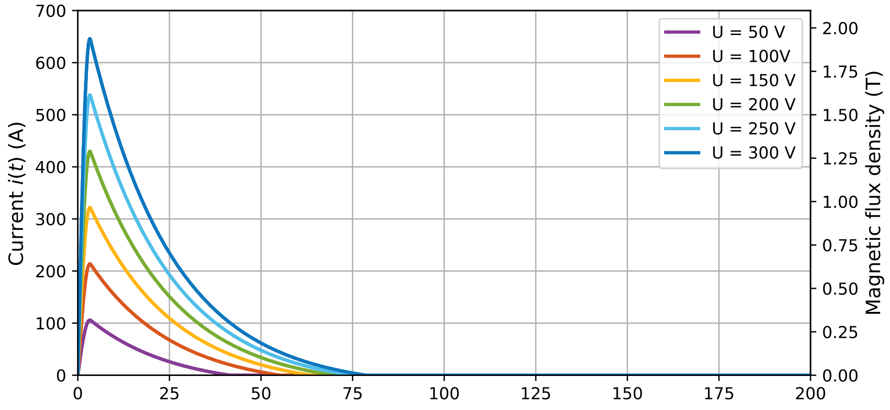

(c) $L_3 = 1$ mH

Figure 4.15. Current and applied magnetic flux density waveforms in flux pump systems with designed coils, $C = 5$ mF and $U_{\mathrm{C0}} = 300$ V

4.5. Summary

The flux pump designed for a pulsed-field magnetisation has to fulfil the requirements of achieving the given magnetic flux density applied to the HTS bulk. A mathematical model has been derived and analysed for a proposed topology of an electric circuit for the flux pump. The model allows for analysis of the influence of circuit parameters on current waveforms in the designed circuit. The data obtained from current waveforms can be used for choosing other components of the flux pump. The analysis revealed that $\hat{B}_{\mathrm{app}}$ depends mostly on capacitance C and voltage of capacitor bank U_{C0} with minor influence from the number of turns N for a given wire diameter D_1. The current rate-of-change depends mainly on the coil inductance. A procedure for designing coil with given parameters such as peak magnetic flux density $\hat{B}_{\mathrm{app}}$, peak current $\hat{I}$ as well as current rate-of-change $1/L$ (or inductance L) has been developed. This resulted in designing three coils without a ferromagnetic core to reduce nonlinearity in the system that will also be used for experimental verification of the influence of current rate-of-change on trapped magnetic flux density in the HTS bulk.

Three coils were designed in total, whereas the third (L_3) as a result of measurements presented in the next chapter (Chapter 5). The coils differ in current rising and falling time due to different inductances $L_1 = 9$ mH, $L_2 = 3$ mH and $L_3 = 1$ mH. The peak flux density can be adjusted by charging capacitor bank to different voltages U_{C0}, and all coils are capable of achieving ≈ 2 T field at $U_{\mathrm{C0}} = 300$ V. The derived current waveforms for systems with and without included forward voltage drop on diodes show significant differences at the descending phase. The analysis also showed that most power losses are generated in the coil, whereas a tenth of that is generated in diodes in total. The losses in coil reach 16 kW at peak, and 2.5 kW mean power losses during pulse time, although only for a few milliseconds, which does not result in high-temperature increase due to thermal inertia of both coil and liquid nitrogen surrounding it. Circuit components, especially diodes, should also be able to withstand generated power losses; however, due to the short pulse duration and single-pulse operation of the flux pump, the temperature is not expected to increase. Nevertheless, cooling, i.e. radiator providing both temperature dissipation and additional thermal inertia, should suffice.

5

Experimental verification

The current, 5th chapter has been dedicated to presenting experimental results of the pulsed-field magnetisation of superconducting bulks using the designed RLC flux pump system. The magnetisation of the HTS bulk has been conducted using a flux pump system with different setups to verify operation and derived models of the flux pump and coils described in the previous chapter (4). The following chapter has been divided into three main sections. The first Section 5.1 describes the topology of the flux pump and its components. The methodology of the measurements is presented with a corresponding system setup. Next, Section 5.2 aims to present obtained data from the conducted experimental investigation in a consistent manner with corresponding explanation and has been divided into three subsections. The first Subsection 5.2.1 presents the data collected in transient states during pulsed-field magnetisation. The waveforms of current and measured magnetic flux density on the surface of the bulk have been plotted. The second Subsection 5.2.2 presents the data plotted as a function of the distance on the bulk's surface with respect to applied peak magnetic flux density $\hat{B}_{\text{app}}$ at both GS and GSB. Additionally, the values of peak magnetic flux densities recorded by the sensors are plotted similarly for comparison. The third Subsection 5.2.3 presents the data of trapped field, and peak field with respect to peak applied magnetic flux density $\hat{B}_{\text{app}}$ at points where sensors were located. Lastly, Section 5.3 summarises the conducted experimental research.

5.1. Flux pump setup

5.1.1. System topology

The final circuit topology presented in Figure 5.1a differs from the previously shown circuit in Figure 4.1a, due to practical and safety reasons. The photo of the assembled system is presented in Figure 5.1b. The circuit is powered from the DC supply with a given voltage U_{DC} and is turned off when the capacitor bank is charged-up. In such a power supply, there could be switches to short-circuit output when it is turned off, or the output capacitors could resonate with an external circuit. The diode D_3 prevents reverse current flow from the capacitor bank to the power supply. The series resistance R_{C} has two purposes - firstly, it reduces rush current in case of applying high voltage U_{DC}; secondly, it serves as a discharge resistor in case of emergency, when switch S_2 is closed. The switch S_1 is the main switch, which allows for discharging the capacitor bank through the coil (RL circuit). The diode D_1 prevents from oscillations and reverse current flow through capacitor bank C, being composed of electrolytic capacitors. In that case, to avoid immediate current decrease, thus high $^{di}/_{dt}$, the current slowly discharges through parallel diode D_2. The capacitor bank can be composed of up to five capacitors connected in parallel.

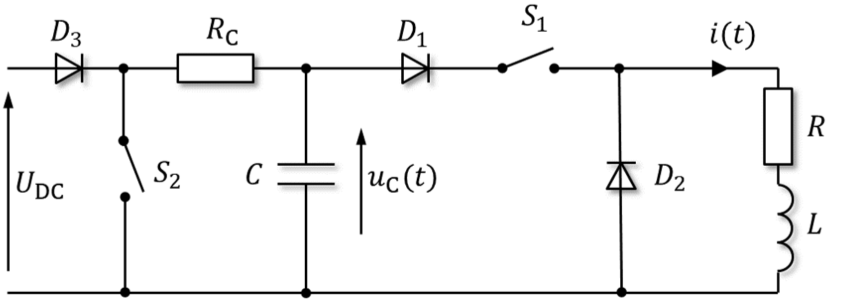

(a) schematic

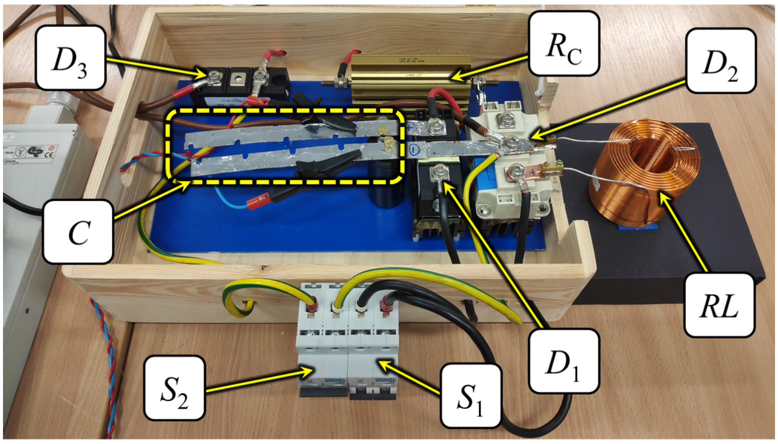

(b) assembled system

Figure 5.1. The RLC flux pump system: (a) schematic; (b) assembled system

To assemble the circuit a thyristor/diode modules VS-VSK 162 [216] were used for diodes D_2 and D_3. The diode D_1 is a parallel diode in IGBT module SKM 200GB173D [217]. For switches, S_1 and S_2, the DC manual circuit breakers of nominal current 64 A were used. The capacitor bank C is composed of electrolytic capacitors KEMET ALS70A120DE400 [213] rated up to 400 VDC and 1 mF each with nominal deviation of ±20%. The measured capacitance of each capacitor is at around 0.88 mF, which is within specification. Despite the deviation from the nominal capacitance value, the cases will be named in the following sections: 1 mF, 2 mF, and so on - for simplicity. The coils designed in Chapter 4 are presented in Figure 5.2. The coil L_3 differs in colour from the other two coils L_1 and L_2 since it was made out of different wires with a different coating.

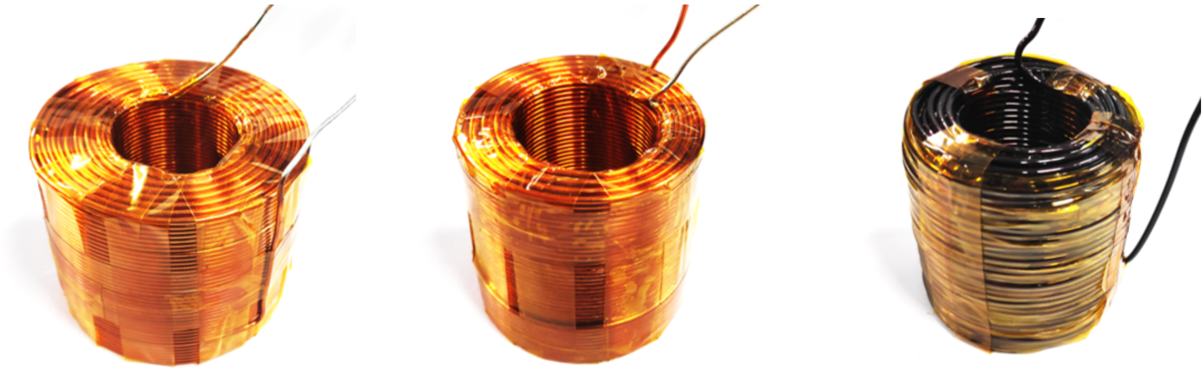

(a) L_1 coil **(b)** L_2 coil **(c)** L_3 coil

Figure 5.2. Coils used for magnetisation of HTS bulk: (a) L_1; (b) L_2; (c) L_3

5.1.2. Sensor placement

For magnetisation, the melt-textured HTS bulk CSYL-28 manufactured by CAN Superconductors [218] with a diameter of 28 mm and height 10 mm has been used. Seven magnetic flux sensors CYSJ362A [219] have been used. The calibration and uncertainty calculation of the sensors is described in detail in Appendix A. The sensors were placed and secured in the 3D printed sleeve: three along GSB (B1, B2, B3), through the GS along the radius at an angle of 45° from GSB (B5, B6, B7) and one in the center (B4). The Kapton tape insulated the sensors to prevent any short circuits through the superconductor or between connections as shown in Figure 5.3a. The HTS bulk fits tightly into the sleeve, but it has been secured with additional Kapton tape to restrict movement once exposed to the magnetic field (Figure 5.3b). The sensors are wired using $\phi 100$ µm wire, soldered to each pin and twisted along to reduce mutual inductance and reduce possible induced voltage.

The HTS bulk with sensors has been placed on a 3D printed stand Figure 5.3c, which locates the bulk at the center of the coil's height, and is pressed in place by another cylindrical piece from the top, with an additional, non-magnetic weight on top. The 3D printed parts were printed using polylactic acid (PLA), an organic compound and non-magnetic, therefore does not disturb the magnetic field. Additionally, the PLA has a negligible change in dimensions when exposed to liquid nitrogen. To reduce temperature gradient, which might induce excess mechanical stress inside the 3D printed part, those with significant thickness have been printed with a low infill, where LN2 can flow through imperfections in the walls.

To test the hypothesis of influence peak magnetic flux density ($\hat{B}$) or its rate-of-change ($^{dB}/_{dt}$) on the trapped magnetic field inside the bulk, two coils have been constructed. Both coils were made of $\phi 1.445$ mm wire with the same inner diameter $D_{\text{in}} = 35$ mm and same height $H = 60$ mm. The coils differ by the number of turns and external diameter and thickness to compact every turn as close as possible to the inner diameter. The data of both coils is presented in Table 4.1. The third coil with $L_3 = 1$ mH has been constructed additionally as a result of measurements conducted for 9 mH and 3 mH coils. The coil with the lowest inductance was tested only 5 mF, since data obtained for 2 mF system did not show significant enough values of the trapped field.

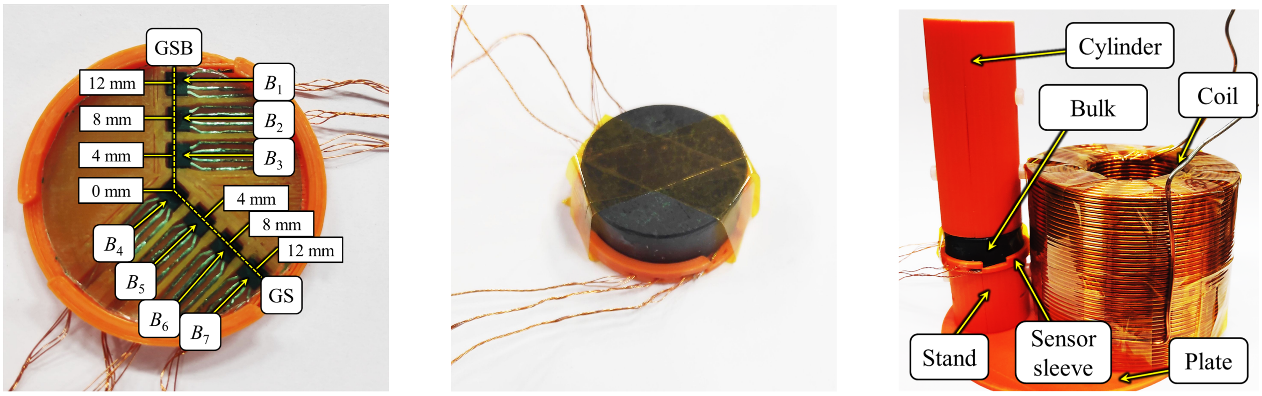

(a) **(b)** **(c)**

Figure 5.3. 3D printed sleeve with sensors for mounting the HTS bulk: (a) mounted sensors; (b) with attached bulk; (c) mounting pieces

5.1.3. Measurement description

The measurements were taken in two stages: in the first stage, during the transient-state stage where the current pulse is applied and peak values are captured, and in the second stage, at the steady-state, the trapped magnetic field distribution is measured with sensors.

According to provided circuit analysis in Section 4.3 peak flux density depends on capacitance C; therefore, the measurements were conducted for two capacitances - 2 mF (two capacitors in parallel) and 5 mF (five capacitors in parallel). The peak current, and consequently, peak magnetic flux density, does not change proportionally to capacitance and using two capacitors instead of a single allowed for lower current drawn from each, avoiding excess heating and potential damage. The main factor influencing peak magnetic flux density is voltage U_{C0} of the capacitor bank (Section 4.3); therefore, the measurements were conducted for different voltages ranging from 50 V to 300 V.

The *applied magnetic flux density* $\hat{B}_{\mathrm{app}}$ referred in the following thesis *is the magnetic flux density induced in the system without superconducting bulk in the very center of space, where that bulk would be located.* In the case of the solenoid coil, the magnetic flux density increases along the radius as getting closer to the windings. In different systems, i.e. with a ferromagnetic core, the magnetic field could be uniform in the air gap where the superconductor would be located. Nevertheless, defining $\hat{B}_{\mathrm{app}}$ as such reduces ambiguity and provides a precise definition, regardless of field distribution. For analysis, it is necessary to present data in a more general fashion, independent of the system where voltage and current may differ; thus, measurements in steady-state are presented in terms of $\hat{B}_{\mathrm{app}}$ instead of voltage or peak current since these are setup-dependent. The peak applied field is evaluated by using measured linear characteristics for each coil (A.1) and extrapolating data to a given current value as shown in Figure A.2.

The measured values were captured and displayed on the oscilloscopes (Agilent Technologies DSO-X 2004A [220] and Keysight DSO-X 2014A [221]) triggered simultaneously. The voltage readings from all sensors were obtained via oscilloscope probes Rigol PVP2150 [222]. The voltage to the sensors was delivered from AIM-TTI QPX600DP [223] power supply set to a constant voltage of 10 V. The current has been measured using Chauvin Arnoux PAC 12 [224] current probe, and the power supply used for powering the flux pump system was the TKD-Lambda Americas GEN300-5 [225].

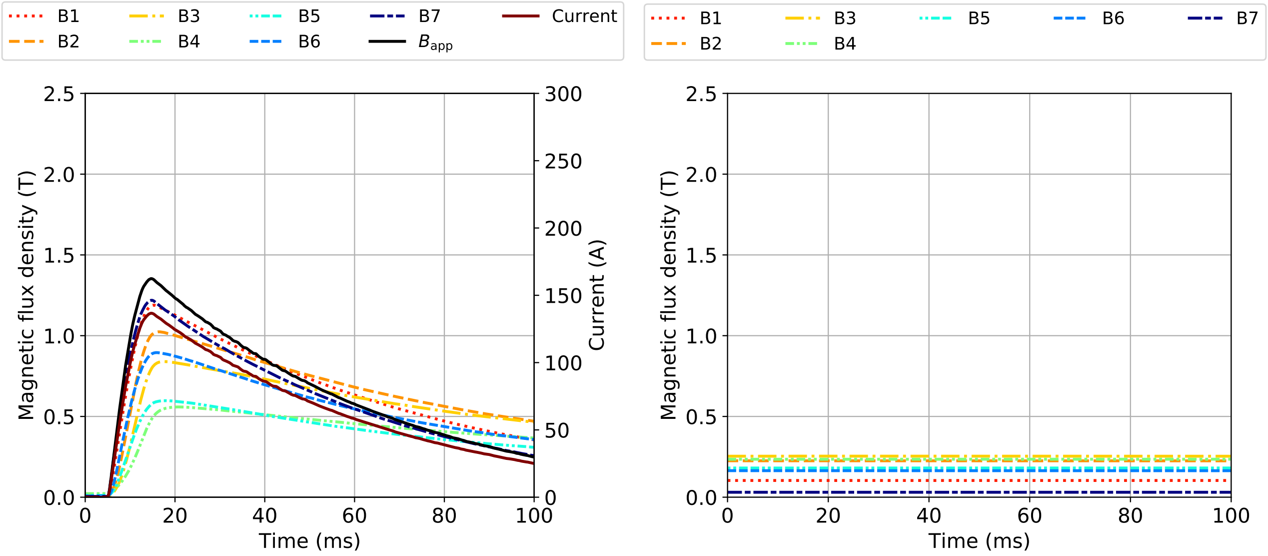

(a) transient-state **(b)** Steady-state

Figure 5.4. Waveforms of measured magnetic flux density and current for system L1/5mF/200 V

Figure 5.4a shows waveforms of current, applied and measured magnetic flux density at various points on the surface of HTS bulk. Firstly, the current rises rapidly when capacitor bank C is being discharged. The peak value is achieved after a few milliseconds, and then the current decays with a time constant. The power is dissipated on the resistance and parallel diode D_1 (Figure 5.1). It can be seen that the magnetic flux density has some inertia at different points on the bulk's surface. The highest inertia is at the center of the bulk (B4), whereas the lowest is at the edge at the bulk (B7). The highest values of the magnetic field are trapped on the GSB, which is consistent with what has been explained in Section 2.4 - the GSB region has higher pinning compared to GS.

5.2. Results

5.2.1. Transient-state results

To make a fair comparison between coils, the cases with similar peak applied magnetic flux density have been chosen but have to differ by applied voltage since it is the main factor that controls the current value. The data to present in this subsection in the transient state were picked for highest voltages U_{C0} due to significant influence on the trapped field and most interesting dynamics of the PFM process. Comparing systems with 2 mF and 5 mF capacitance shows that indeed, the system with lower capacitance results in lower peak values of current and, therefore, flux densities as shown in Figure 5.5. Also, as seen in previous chapter (Figures 4.6e and 4.6f), the peak current is nonlinearly dependent on the capacitance value. In the following system the 2.5 increase of capacitance (from 2 mF to 5 mF) resulted in 1.5 increase of peak applied field (i.e. for coil L_1 from 1.3 T to 1.9 T). Therefore, increasing the number of capacitors in parallel can be justified mainly by decreasing the total current drawn from each. Sensors B1 and B7, which are closest to the edges and exposed to the strongest applied field, show the highest field readings. These regions also have the lowest inertia for field penetration, whereas the regions closer to the center have higher inertia (Figures 5.5 and 5.6). The influence of inductance on the current rate-of-change has been confirmed for all coils (Figure 5.6). The readings from GS (B5, B6, B7) show higher inertia than GSB (B1, B2, B3) due to lower pinning resulting in slower penetration of the field. The highest inertia occurs at the center of the bulk (B4). This shows that the inertia of magnetisation increases as getting closer to the center of the bulk. This manifests in two ways - firstly, it delays magnetic field rising time, and secondly, it delays also falling time of the field. Additionally, it results in lower peak magnetic flux density values at points where sensors were located (B3, B4 and B5) closest to the center. The delay in the magnetic field measured at the center results from induced eddy current in the HTS bulk during magnetisation that opposes the applied field. However, probably due to losses, the strength of the applied magnetic field and its duration during rising higher readings are achieved closest to the center.

Power losses generated inside the bulk could contribute to temperature rise inside the bulk and a temperature wave propagating through the bulk from the edges to the center resulting in higher field penetration. During the time when the current decays, the counter-current starts being induced inside the bulk. That newly induced current flows in the opposite direction to current induced during ascending phase and sums up over a much longer time period during descending phase. Due to the superconducting phenomenon and corresponding near-zero resistivity of the material, the induced current has a significantly higher value, possibly close to its critical value.

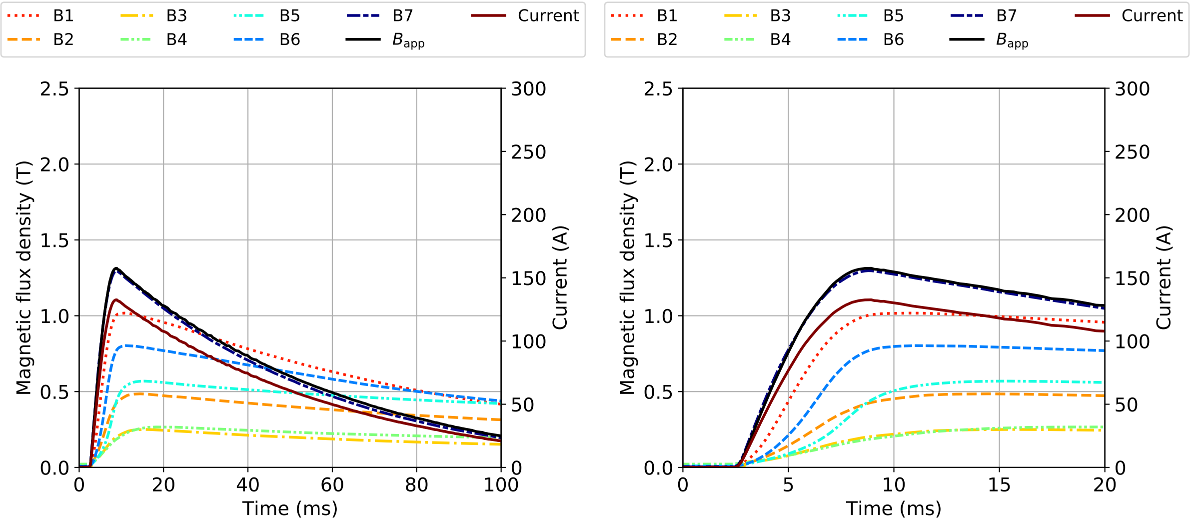

(a) L_1/2 mF/300 V **(b)** L_1/2 mF/300 V

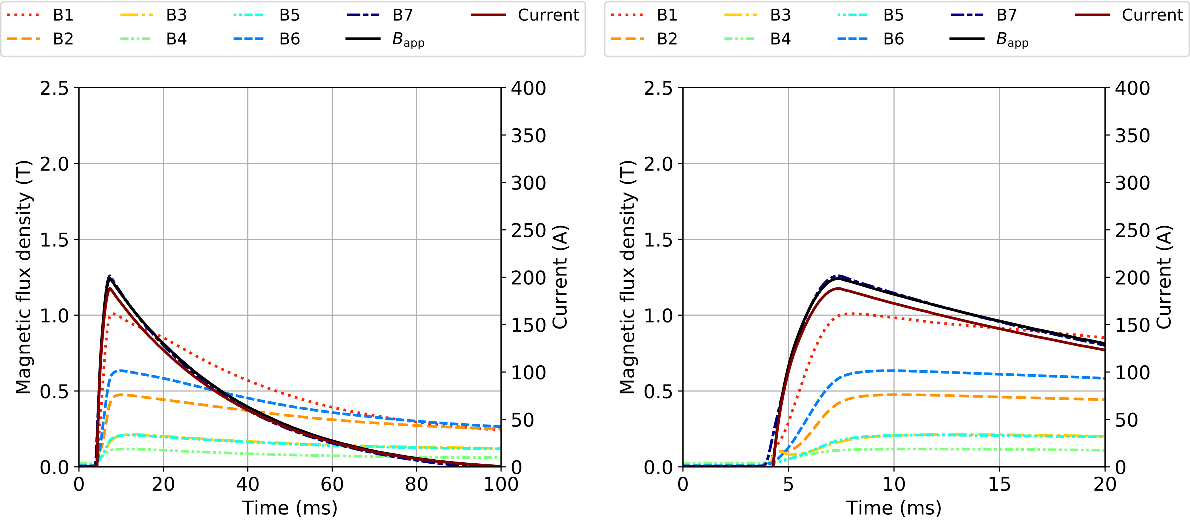

(c) L_2/2 mF/250 V **(d)** L_2/2 mF/250 V

Figure 5.5. Current and magnetic flux density waveforms during magnetisation in $C = 2$ mF system

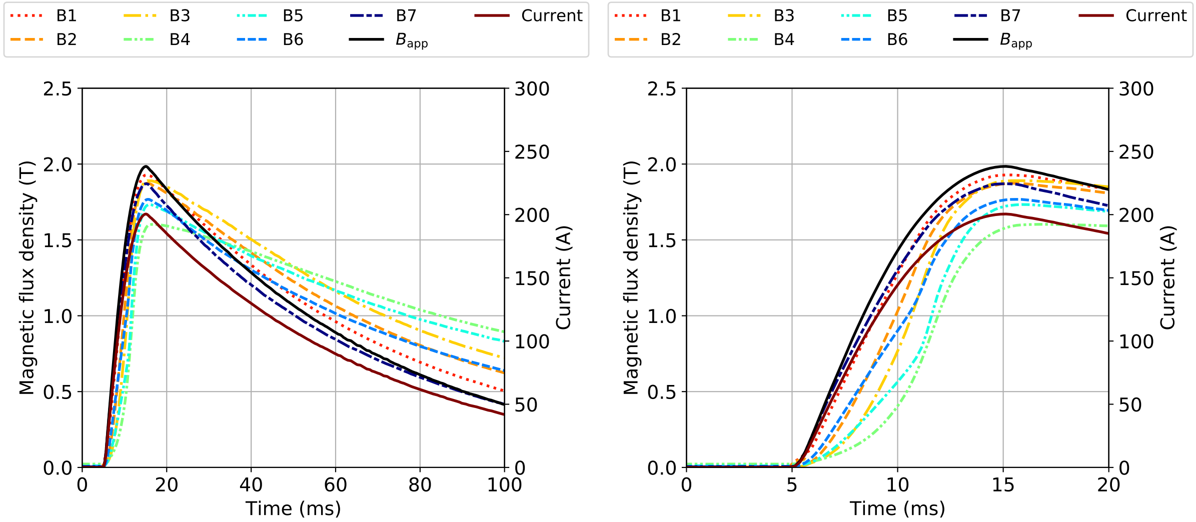

(a) $L_1/5$ mF/300 V **(b)** $L_1/5$ mF/300 V

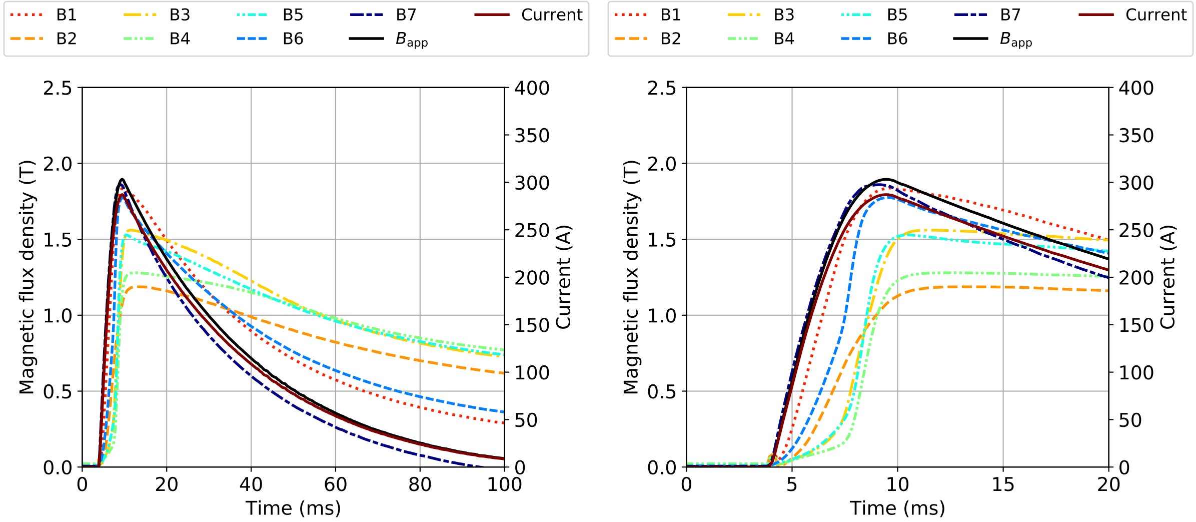

(c) $L_2/5$ mF/250 V **(d)** $L_2/5$ mF/250 V

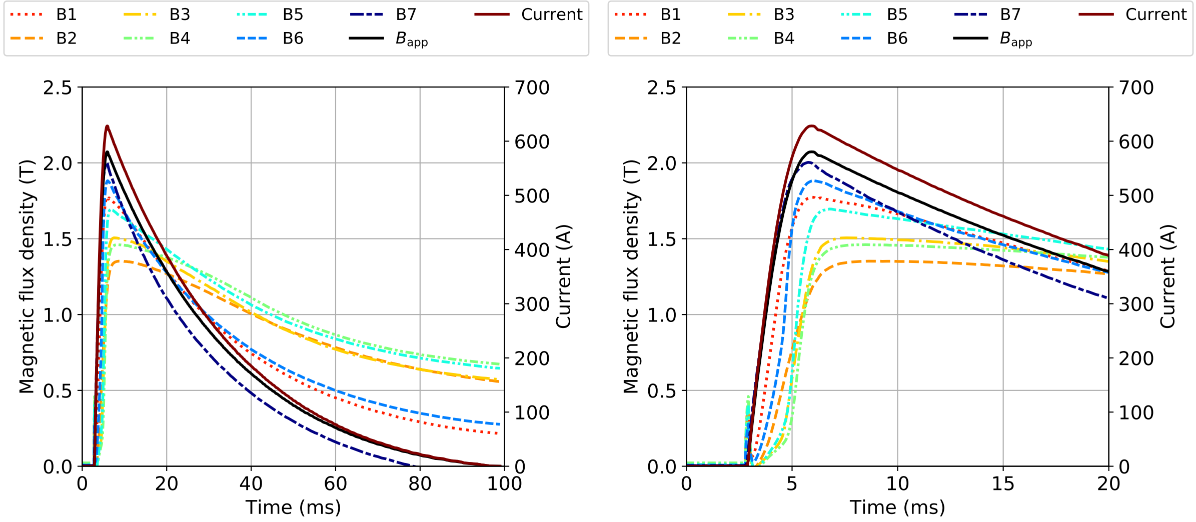

(e) $L_3/5$ mF/300 V **(f)** $L_3/5$ mF/300 V

Figure 5.6. Current and magnetic flux density waveforms during magnetisation in $C = 5$ mF system

5.2.2. Steady-state results - measurement at point

Due to the low number of measurement points on the surface of the HTS bulk, visualisation of data can be done in a limited fashion. For this purpose, the trapped magnetic field has been plotted along the radii of the bulk on GS and GSB as shown in Figures 5.7 and 5.8, where both start at the center (0 mm) and move towards the edge (12 mm) along the radius. The consecutive colors appearing on the legends in Figures 5.7 and 5.8 correspond with values of voltages $U_{C0} = 50 \dots 300$ V that were applied from the power supply. The voltages were increased incrementally every 50 V. The behaviour of GS and GSB regions is distinctive from one another. The system with lower energy, meaning $C = 2$ mF, results in lower trapped fields than the system with $C = 5$ mF. In the case of the former, the distribution of trapped field is M-shaped[1] as in Figure 2.16-4 along the diameter of the bulk on the GS, whereas on the GSB it is V-shaped[1] as in Figure 2.16-8. In the system with L_1 coil, the trapped field starts to slowly diffuse towards center of bulk at fields above 0.6 T, which is visible by the increase of field at the sensor located at 4 mm.

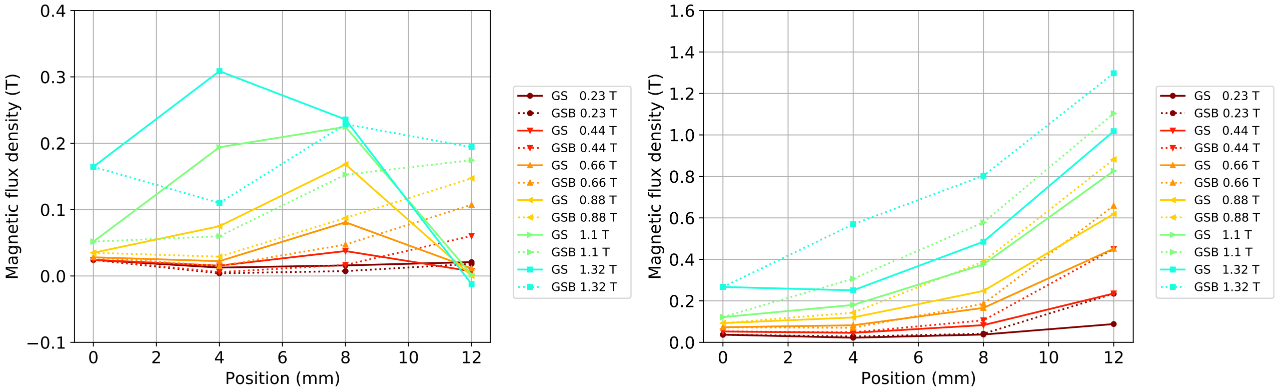

(a) $L_1/2$ mF Trapped field **(b)** $L_1/2$ mF Peak field

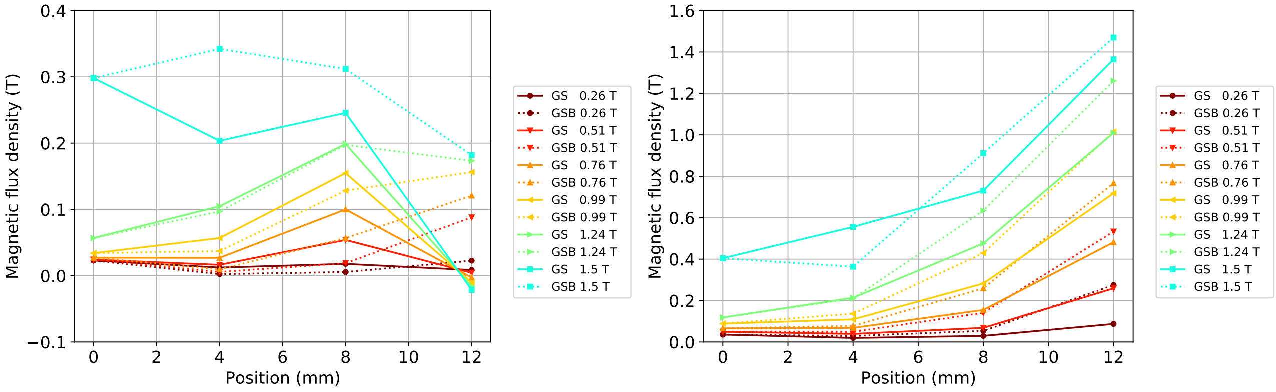

(c) $L_2/2$ mF Trapped field **(d)** $L_2/2$ mF Peak field

Figure 5.7. Distribution of trapped magnetic flux density on GS and GSB for different $\hat{B}_{\text{app}}$ in system with $C = 2$ mF

---

[1] Referring to shape of field distribution along the diameter is at the assumption of having similar distribution at all GS or GSB, at position 180° from the measurement, which is a mirror image.

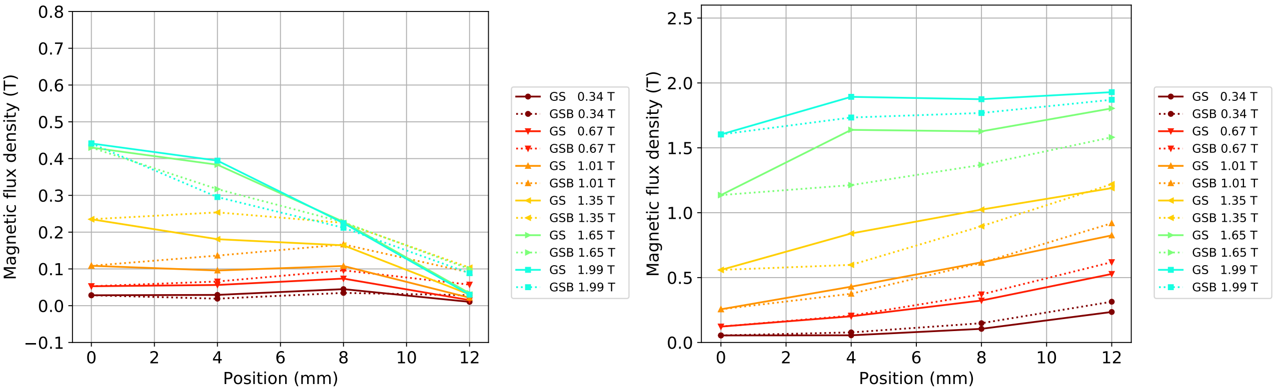

(a) $L_1/5$ mF Trapped field **(b)** $L_1/5$ mF Peak field

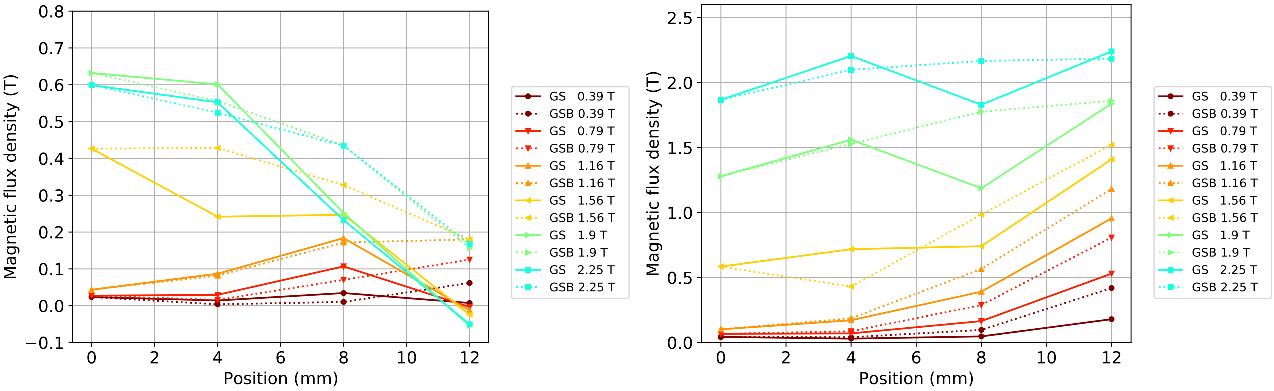

(c) $L_2/5$ mF Trapped field **(d)** $L_2/5$ mF Peak field

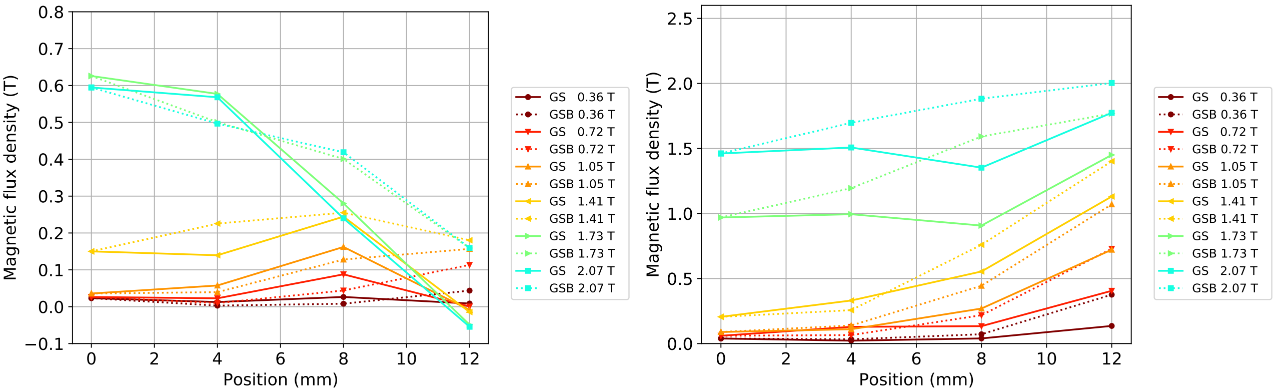

(e) $L_3/5$ mF Trapped field **(f)** $L_3/5$ mF Peak field

Figure 5.8. Distribution of trapped magnetic flux density on GS and GSB for different $\hat{B}_{\text{app}}$ in system with $C = 5$ mF

Nevertheless, the field cannot penetrate to the center even at 1.3 T (Figure 5.8a). The values shown in legend in Figures 5.7 and 5.8 are peak values of applied field $\hat{B}_{\mathrm{app}}$ measured at the spot and it was decided to ommit rounding numbers to get a clearer understanding of occuring values. In the system with L_2 coil, at higher applied magnetic field $\hat{B}_{\mathrm{app}} = 1.6$ T the diffusion towards center is visible through GS, and substantial values are reached on the GSB as well (Figure 5.8b). In system with higher energy $C = 5$ mF the field distribution changes it shape as higher fields are applied, and transitions from M-shaped (Figure 2.16-4), to inverse U-shape (or ∩-shape) on GS and from M-shaped to inverse V-shape (or Λ-shape) as in Figure 2.16-8 on the GSB in system with L_1 coil (Figure 5.8c). In system with L_1 coil the cases at fields $\hat{B}_{\mathrm{app}} = 1.6$ T and $\hat{B}_{\mathrm{app}} = 1.9$ T differ slightly, which means, that a plateau and optimum magnetic flux [91] has been reached for this particular system (solenoid coil with $L_1 = 9$ mH, $C = 5$ mF, $T = 77$ K) and this particular bulk. Increasing applied flux density any further might not increase the trapped field, but contrary - it can be decreased due to higher generated power losses in the bulk. Similarly, in system (solenoid coil with $L_2 = 3$ mH, $C = 5$ mF, $T = 77$ K) the trapped field decreases at higher applied fields $\hat{B}_{\mathrm{app}} = 2.3$ T compared to lower $\hat{B}_{\mathrm{app}} = 2.0$ T.

The distribution of trapped field in systems with L_2 (Figure 5.8c) and L_3 (Figure 5.8e) is quite similar at lower values of applied field and highest values. At the intermediate stage (yellow lines - $U_{\mathrm{C0}} = 200$ V), the values of peak applied field (shown in legend) differ, which might explain the difference in obtained values.

Comparing results presented in Figures 5.8b and 5.8d one can observe that the distribution of trapped field is similar (but has different values) for applied fields $\hat{B}_{\mathrm{app}} \leq 1.6$ T. The field distribution has similar features on both GS and GSB. This indicates that higher ${}^{\mathrm{d}B}\!/_{\mathrm{d}t}$ plays an important role in trapped magnetic field distribution and its values. The same can not be said in the case of the system with L_1 coil. Also, L_2 coils allowed for higher peak applied fields and consequently higher trapped fields using the same power source in both cases ($C = 2$ mF and 5 mF).

If the applied field has a low amplitude ≤ 1.3 T, in all cases, it results in the highest value at the position 8 mm. This is due to two counter-currents induced inside the bulk. Firstly, when the current was ascending, a current in one direction was induced, whereas a counter-current was induced during the descending phase. However, the duration and field strength was such that it could not be induced in the opposite direction on the whole cross-section of the bulk resulting in inverted M-shape field distribution (Figure 2.16-4). As a result, the magnetic field measured at the edge of the bulk has a different direction than at the other locations as it has the same similar to what has been shown previously in Figure 2.16-8.

Analysis of the peak measured flux density on the surface of the HTS bulk shows that the highest values occur on the edges of the bulk in all cases. This is due to the proximity of the bulk and the coil, where the magnetic field has the highest values. In both systems with $C = 2$ mF the peak field at the center generally stays at the lowest level (Figures 5.7b and 5.7d), whereas in systems with $C = 5$ mF the peak field gradient becomes more uniform as higher fields are applied (Figures 5.8b, 5.8d and 5.8f). At sufficiently high field values $\hat{B}_{\mathrm{app}} \geq 2.0$ T and both coils with higher current rate-of-change (L_2 in Figure 5.8d and L_3 in Figure 5.8f) there is a visible dip in the measured peak field at position 8 mm. This might indicate that the current density diffuses towards the center and consequently increases field closer to the center (points 0 mm and 4 mm), which results in a visible dip in position 8 mm or might be due to temperature increase at the center, allowing for more field to pass through the bulk resulting in higher readings at the center.

5.2.3. Steady-state results - influence of peak applied field

To visualise the influence of peak applied magnetic flux density $\hat{B}_{\text{app}}$ on value of trapped field a set of characteristics has been created and shown in Figures 5.9 and 5.10. Systems with $C = 2$ mF (Figures 5.9a and 5.9c) show that trapped field at the center of the bulk (B4) does not rise until reaching at least $\hat{B}_{\text{app}} > 1$ T. Both systems are far from reaching saturation of trapped magnetic field, thus applied field can be further increased by increasing capacitance to $C = 5$ mF (Figure 5.10). Much higher peak values are achieved in the system with $C = 5$ mF (Figures 5.10b, 5.10d and 5.10f) due to higher total charge stored in capacitors. This results in higher trapped field, especially at the center of the bulk in all system at sufficiently high applied fields (Figures 5.10a, 5.10c and 5.10e) above 1.5 T.

The coil with higher inductance (L_1) seems to penetrate further into the center of the bulk, compared to other coils (L_2 and L_3) for the same values of the applied field below 1 T. For fields above $\hat{B}_{\text{app}} > 1.5$ T the system with coil L_1 starts to reach saturation point (Figure 5.10a). Increasing applied field only slightly increases trapped field at the center (B4) of the bulk.

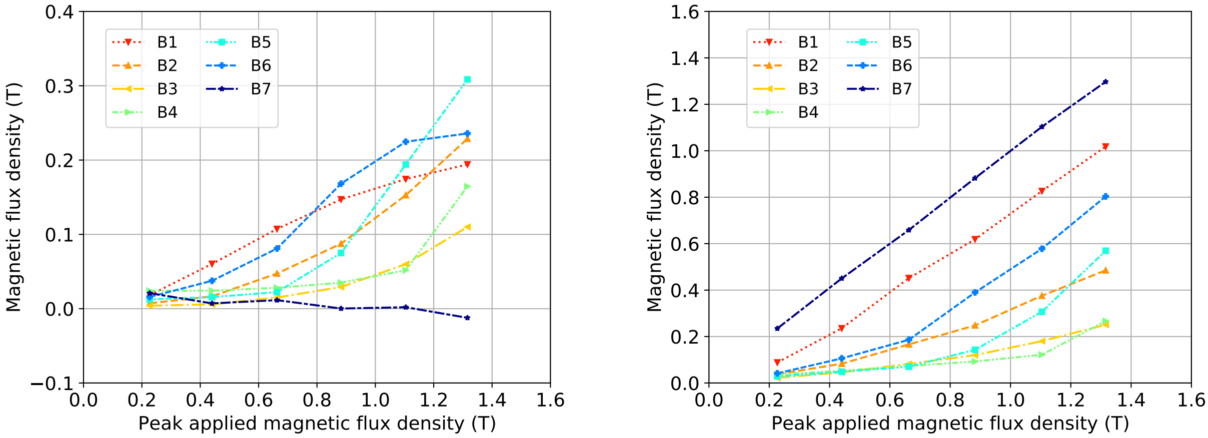

(a) $L_1/2$ mF Trapped field **(b)** $L_1/2$ mF Peak field

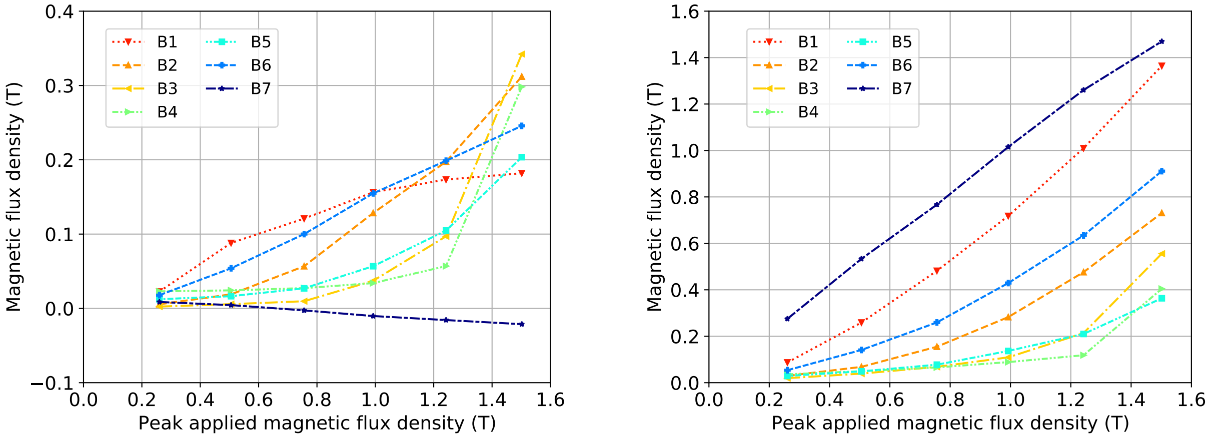

(c) $L_2/2$ mF Trapped field **(d)** $L_2/2$ mF Peak field

Figure 5.9. Influence of peak applied magnetic flux density on the magnetic field on the surface of the bulk in system with $C = 2$ mF

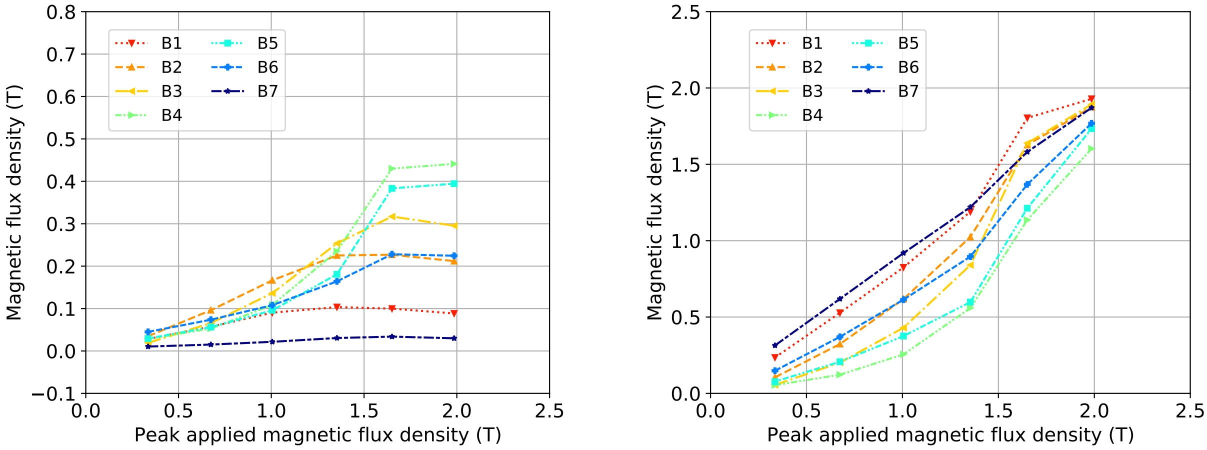

(a) L_1/5 mF Trapped field **(b)** L_1/5 mF Peak field

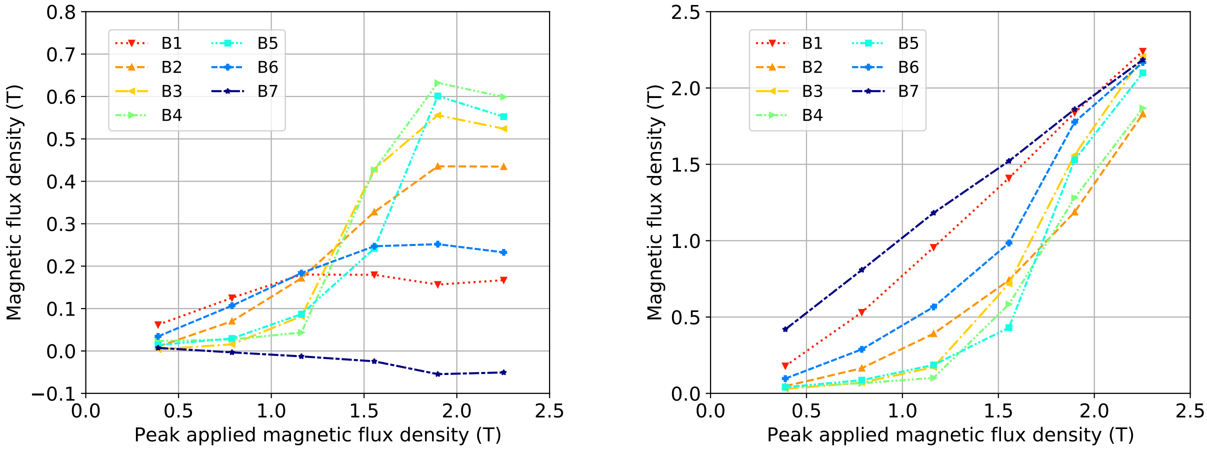

(c) L_2/5 mF Trapped field **(d)** L_2/5 mF Peak field

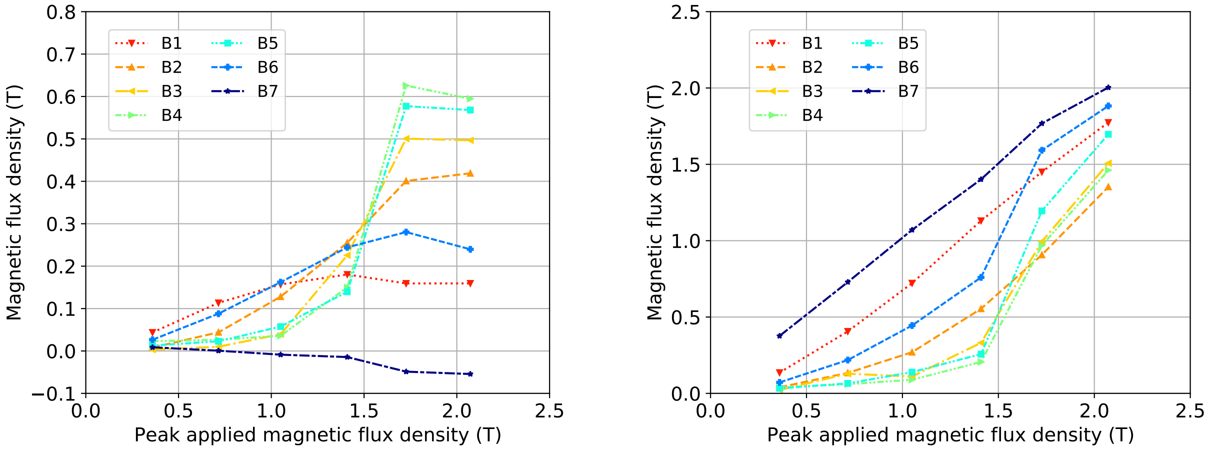

(e) L_3/5 mF Trapped field **(f)** L_3/5 mF Peak field

Figure 5.10. Influence of peak applied magnetic flux density on the magnetic field on the surface of the bulk in system with $C = 5$ mF

In other cases (L_2 and L_3), after reaching a certain peak magnetic flux density, the bulk's center becomes saturated, and further increase of applied field > 2 T results in a drop of the trapped field as shown in Figures 5.10c and 5.10e. This is probably due to excessive power losses being induced in the bulk. The system with coil L_2 results in a much higher trapped field (≈ 2.4 T), which can be possibly attributed to higher ${}^{\mathrm{d}B}/_{\mathrm{d}t}$ and higher peak field $\hat{B}$ at the same time. Higher applied peak fields $\hat{B}$ are reached due to a more compact design, compared to L_3 coil made of wire with a bigger diameter. The more tightly coil is wounded, the stronger field can be generated at a given distance from the winding.

However, the coil L_2 reaches optimum trapped field [91] of approximately 0.6 T at the applied field of $\hat{B}_{\mathrm{app}} \approx 2$ T, the coil L_3 reaches it at $\hat{B}_{\mathrm{app}} \approx 1.6$ T. This shows, the significance of achieving higher current rate-of-change. The same values in systems with both coils was achieved at $U_{\mathrm{C0}} = 250$ V, but at a cost of much higher current in system with L_3 coil reaching $\hat{I} = 500$ A, compared to system with L_2 where peak measured current was at 300 A.

The peak magnetic flux density measured by each sensor and corresponding peak applied flux density shown in both Figures 5.9, and 5.10 indicate that if values differ significantly, the trapped field will be lower. If increasing $\hat{B}_{\mathrm{app}}$ causes a significant increase in measured peak field, and values are converging, this might indicate good effectiveness of PFM. Nevertheless, a too high value of an applied field might result in a lower trapped field.

The highest values occur at the edges of the bulk, which is to be expected due to the proximity of coil turns, although this value seems to drop as the peak applied field increases. This might be due to a significant eddy current being induced in the bulk, which counteracts the applied field.

5.3. Summary

The designed coils perform as intended, and current waveforms are congruent to what simulations have estimated. The measurements have shown that increasing capacitance and voltage positively influence peak current value, resulting in higher peak fields. The coil labelled as L_2 had the best highest peak-ampere turns per volt unit value $N\hat{I}/\hat{U_{\text{C0}}} > 500$ A/V which can be attributed to the lower diameter of the wire compared to L_3 coil, thus allowing for tighter loops, even a higher number of turns, which resulted in the highest peak fields $\hat{B}_{\text{app}} > 2$ T. Nevertheless, such high values negatively affect trapped magnetic fields inside the HTS bulk, probably due to higher overall losses. In this particular system - solenoid coil magnetising HTS bulk $D_{\text{HTS}} = 28$ mm and $H_{\text{HTS}} = 10$ mm cooled by LN2 at 77 K; the limit seems to be at around $\hat{B}_{\text{trap}} \approx 0.6$ T of trapped field, regardless of the coil inductance.

Increasing capacitance does result in higher currents as predicted, but since it is a nonlinear dependence, there is a diminishing return from increasing it. On the other hand, the benefit is dividing the current per connected capacitor and consequently lowering losses and thermal stress within, which might result in damaging capacitors. Therefore, most benefits are seen from increasing the voltage that proportionally influences the value of the magnetic flux density, although an optimum value has to be chosen since too high applied fields result in a decrease of trapped fields.

The measurements have shown that decreasing inductance of the coil allowed for reaching $\hat{B}_{\text{trap}}$ at lower applied fields $\hat{B}_{\text{app}} \approx 1.7$ T; thus at lower voltages. So the coil with lower inductance could be smaller overall, but the disadvantage of using a coil with lower inductance is the higher peak current that components have to conduct and dissipate - mostly parallel diode D_2.

During the measurements, flux jumps have not been observed in the magnetic field waveforms, although on static measurements, the trapped field suddenly increases at the center (sensor B4) after exceeding the threshold value of the applied field at around $\hat{B}_{\text{app}} \approx 1.4$ T. The measurements are consistent in that regard for every coil; therefore, it seems to be a feature of the HTS bulk magnetised with the RLC flux pump operating at given conditions.

6

Electromagnetic modelling

In this chapter, the numerical approach to electromagnetic modelling of superconducting materials is presented. The first Section 6.1 focuses on the description of electromagnetic problems using partial-differential equations and has been divided into four subsections. The Subsection 6.1.1 presents and describes Maxwell's equations of classical electromagnetics with corresponding interface conditions between subdomains of different material properties in next Subsection 6.1.2. The third Subsection 6.1.3 specifies different PDE formulations based on field potentials used for modelling slow-changing electromagnetic problems related to superconductivity. The last Subsection 6.1.4 characterises different models of nonlinear resistivity of superconducting materials. The second Section 6.2 briefly describes the finite-element method used for finding the solution of electromagnetic problems. The third Section 6.3 presents the FEM model setup used for modelling the pulsed-field magnetisation of superconducting bulks. The model is calibrated by comparing numerical solutions to data obtained experimentally by adjusting the material properties of the HTS bulk. Next, Section 6.4 presents the numerical results of the calibrated model. The FEM model is used to estimate quantities that are difficult or unmeasurable experimentally, i.e. current density or losses during transient state inside the magnetised bulk. The last Section 6.5 summarises the numerical investigation presented in the chapter and concludes obtained results.

6.1. Partial-differential equations

6.1.1. Maxwell's equations

Superconductivity can be analysed on the level of individual quantum vortices by solving Ginzburg-Landau equation [226], which shows the movement of fluxons through the superconductor under various conditions [227]. On the other hand, in applications, such a fine of resolution is not needed, but superconductors can be analysed with Maxwell's equations instead [159, 228]. In classical electromagnetism the Maxwell's equations are set of four differential equations including: Gauss's law (6.1), Gauss's law for magnetism (6.2), Faraday's law (6.3), and Ampere's law (6.4) [229]. These equations can also be given as a set of integral equations [230]. The Maxwell's equations allow for solution of a general case of electromagnetic problem, although depending on the type of problem some simplifications are possible.

$$\boldsymbol{\nabla} \cdot \mathbf{D} = \varrho \tag{6.1}$$

$$\boldsymbol{\nabla} \cdot \mathbf{B} = 0 \tag{6.2}$$

$$\boldsymbol{\nabla} \times \mathbf{E} = -\frac{\partial \mathbf{B}}{\partial t} \tag{6.3}$$

$$\boldsymbol{\nabla} \times \mathbf{H} = \mathbf{J} + \frac{\partial \mathbf{D}}{\partial t} \tag{6.4}$$

where: $\nabla = \left[\frac{\partial}{\partial x}; \frac{\partial}{\partial y}; \frac{\partial}{\partial z}\right]$ - differential operator; $\mathbf{D}$ - electric displacement field (electric induction); $\mathbf{E}$ - electric field; ϱ - charge density; $\mathbf{B}$ - magnetic flux density; $\mathbf{H}$ - magnetic field strength; $\mathbf{J}$ - current density;
The electric induction and magnetic flux density can be nonlinear and depend on other fields: $\mathbf{D} = \mathbf{D}(\mathbf{E})$ and $\mathbf{B} = \mathbf{B}(\mathbf{H})$, which can be described as constitutive relations as in (6.5) and (6.6) respectively.

$$\mathbf{D} = \varepsilon \mathbf{E} = \varepsilon_0 \varepsilon_{\mathrm{r}} \mathbf{E} \tag{6.5}$$

$$\mathbf{B} = \mu \mathbf{H} = \mu_0 \mu_{\mathrm{r}} \mathbf{H} \tag{6.6}$$

where: $\mu_0 = 4\pi 10^{-7}$ H/m - magnetic permeability of free space; ε_0 - electric permittivity of free space; ε_{r} - relative permittivity of medium; μ_{r} - relative permeability of a medium.
Another constitutive relation is the electromagnetic Ohm's law given by the (6.7).

$$\mathbf{E} = \rho \mathbf{J} = \frac{1}{\sigma} \mathbf{J} \tag{6.7}$$

where: ρ - resistivity of a medium; σ - conductivity of a medium;

In all equations mentioned above, the material properties ε_{r}, μ_{r}, ρ generally are nonlinear and depend on various fields acting on the medium, i.e., magnetic flux density, electric field, temperature, strain or stress. Since different fields can influence the material properties, other differential equations are necessary to describe the behaviour of the system. However, if the field values change within known limits, an appropriate constant value can be given, at least for preliminary simulations. The nonlinear material properties result in much accurate solution, and for slow-changing magnetic field problems typically the magnetic permeability given as $\mu_{\mathrm{r}} = f(\mathbf{B})$ or $\mu_{\mathrm{r}} = f(\mathbf{H})$ is used to describe B-H curve of ferromagnetic materials.

In order to find a solution of the electromagnetic problem, it is convenient to describe it in terms of potentials - vector or scalar, rather than a set of equations, like Maxwell's equations (6.1-6.4). The classical examples are: the magnetic vector potential $\mathbf{A}$ and electric scalar potential φ [231]. From the set of Maxwell's equations and vector calculus, the magnetic flux density can be related to magnetic vector potential as shown in (6.8), which also satisfies (6.2).

$$\mathbf{B} = \boldsymbol{\nabla} \times \mathbf{A} \tag{6.8}$$

For magnetic fields varying in time the (6.3) combined with (6.8) results in (6.9).

$$\boldsymbol{\nabla} \times \mathbf{E} = -\frac{\partial \mathbf{B}}{\partial t} = -\frac{\partial}{\partial t}(\boldsymbol{\nabla} \times \mathbf{A}) = -\boldsymbol{\nabla} \times \left(\frac{\partial \mathbf{A}}{\partial t}\right) \tag{6.9}$$

By bringing all components to left-hand side the (6.10) is obtained.

$$\boldsymbol{\nabla} \times \mathbf{E} + \boldsymbol{\nabla} \times \left(\frac{\partial \mathbf{A}}{\partial t}\right) = \boldsymbol{\nabla} \times \left(\mathbf{E} + \frac{\partial \mathbf{A}}{\partial t}\right) = 0 \tag{6.10}$$

From the vector calculus, the curl of field is zero if that field is a gradient of some potential φ, from which the (6.11) is derived.

$$\mathbf{E} = -\frac{\partial \mathbf{A}}{\partial t} - \boldsymbol{\nabla}\varphi \tag{6.11}$$

The abovementioned potentials are only classic examples, and it is possible to describe the problem in terms of other potentials, which will be further discussed in Section 6.1.3.

6.1.2. Interface conditions

The analysed domain usually is composed of different materials where each has different material properties, i.e. ferromagnetic core and air have different magnetic permeabilities. All four of the vector fields in Maxwell's equations are satisfying interface conditions on boundary between subdomains (materials) given by (6.12-6.15). The fields between two subdomains are presented in Figure 6.1 with corresponding normal ($\mathbf{n}$) and tangential $\mathbf{t}$ components.

$$\mathbf{n} \cdot (\mathbf{B}_2 - \mathbf{B}_1) = 0 \tag{6.12}$$

$$\mathbf{n} \times (\mathbf{H}_2 - \mathbf{H}_1) = \boldsymbol{\eta} \tag{6.13}$$

$$\mathbf{n} \cdot (\mathbf{D}_2 - \mathbf{D}_1) = \varrho_{\mathrm{S}} \tag{6.14}$$

$$\mathbf{n} \times (\mathbf{E}_2 - \mathbf{E}_1) = 0 \tag{6.15}$$

where: $\mathbf{n}$ - normal vector on interface boundary; $\mathbf{t}$ - tangential vector on interface boundary; $\boldsymbol{\eta}$ - surface current density on interface boundary; ϱ_{S} - surface charge density on interface boundary

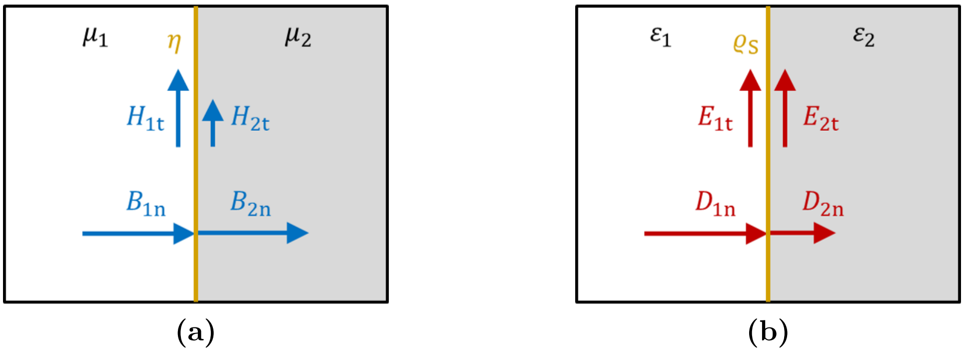

Figure 6.1. Visualisation of boundary conditions for electromagnetic field

6.1.3. Electromagnetic PDE formulations

The four partial differential equations (6.1-6.4) are expressed in terms of many different fields like **E**, **H**, **J**, **B**, **D**, which are connected via constitutive relations (6.5), (6.6) and (6.7), and finding the solution to all of these simultaniously is a difficult task due to number of degrees of freedom. As mentioned in Subsection 6.1.1 the PDEs should be expressed in terms of potentials, that allows for deriving magnetic and electric fields distribution. The problem of modelling pulsed-field magnetisation of superconducting bulks can be categorised as *low-frequency electromagnetic fields*, meaning that wavelength is much bigger than the dimensions of analysed objects. The electric charge density ϱ_V does not change in the whole domain. The assumption is net-zero charge density, which leads to charge conservation law in (6.16) [230].

$$\nabla \cdot \mathbf{J} = -\frac{\partial \varrho_V}{\partial t} = 0 \tag{6.16}$$

Thus, three out of four Maxwell's equations are used to describe the low-frequency electromagnetic problem, which are equations (6.17-6.19).

$$\nabla \cdot \mathbf{B} = 0 \tag{6.17}$$

$$\nabla \times \mathbf{E} = -\frac{\partial \mathbf{B}}{\partial t} \tag{6.18}$$

$$\nabla \times \mathbf{H} = \mathbf{J} \tag{6.19}$$

Constitutive relations (6.6) and (6.7) still holds, as well as equations (6.8) and (6.11). These equations consist of a basis for deriving partial-differential equations expressed in terms of potentials.

Calculating the distribution of magnetic field or current density generally requires solving single or set of partial differential equations. For simple geometries, the application of Biot-Savart or Ampere's law is sufficient to describe the distribution of these fields [144, 229]. In other cases where it is necessary to solve a PDE, the symmetry of the model can be exploited or other forms of simplification, i.e. constant material properties, removing nonlinearities the PDE solved analytically [144, 232]. However, in the case of superconducting materials and complex geometries, generally, the best approach is to solve it numerically [228].

The results of numerical calculations for flux pumps published so far show good convergence with measurements for each type of pump. Most of numerical solutions are obtained via finite-element method (FEM) [22, 128, 233, 234]. FEM based calculations allow for numerical analysis of complex geometries of bulk superconductors in the shape of pellets, cuboids, or HTS tape structures [235]. The PDE formulation can be described with magnetic vector potential **A**, but other state variables are also widely used: **H**, **E** and **T**. Selecting the appropriate state variable usually depends on the numerical description of the problem. For example, **A**−formulation suits well eddy-current problems, especially in 2D, where it can be reduced to only A_z component. This reduces the problem from vector-valued to scalar-valued problem because only the z-component of the field is calculated. This formulation is generally used for all sorts of electromagnetic problems since it is quite natural to define current density **J** as a source of a field, like a coil or electric potential φ. Solving a vector-valued problem requires solving a set of equations equal to the number of components of the vector.
In other cases like **H**−formulation and **E**−formulation, even in 2D, the problem stays vector-valued; thus, x and y components of vector fields have to be calculated. These formulations show their strengths in problems, where sources are given as magnetic or electric field intensities. In the case of superconductivity in **H**−formulation, it is easier to calculate nonlinear material properties. An example could be a domain where a coil produces a magnetic field of known value, which can be given on a boundary of the domain without explicitly modelling the coil itself. The huge popularity of **H**−formulation in modelling superconductivity can be attributed to using resistivity in (6.7) and Ampere's law (6.19) as $\mathbf{E} = \rho(\mathbf{J})\mathbf{J}$ instead of conductivity, thus simplifying numerical setup.

The **A**−formulation is mainly used in classical electrodynamics problems but also finds its place in modelling superconducting phenomenon [107–112]. This formulation is described by pair of potentials: magnetic vector potential **A** and scalar electric potential φ. The formulation is created by substituting current density in (6.19). Additionally, the magnetic field intensity **H** can be substituted by transforming (6.6), thus resulting in (6.20).

$$\boldsymbol{\nabla} \times \frac{1}{\mu}\mathbf{B} = \mathbf{J}_\mathrm{s} - \sigma\frac{\partial \mathbf{A}}{\partial t} - \sigma\boldsymbol{\nabla}\varphi \tag{6.20}$$

Since the magnetic field **B** is described in terms of magnetic vector potential **A** (6.8), therefore by applying it to (6.20), the final formulation is given as in (6.21) below.

$$\boldsymbol{\nabla} \times \frac{1}{\mu}\boldsymbol{\nabla} \times \mathbf{A} = \mathbf{J}_\mathrm{s} - \sigma\frac{\partial \mathbf{A}}{\partial t} - \sigma\boldsymbol{\nabla}\varphi \tag{6.21}$$

The magnetic vector potential **A** is an unknown value, except for the Dirichlet boundary conditions and the current density $\mathbf{J}_\mathrm{s}$ and electric scalar potential φ are given as sources. In all materials where eddy currents are induced, the conductivity of the material has to be defined. The conductivity for superconducting materials is a nonlinear function of electric field intensity $\sigma = \sigma(\mathbf{E})$ or other value depending on material properties. If eddy currents are not induced the conductivity $\sigma = 0$, thus removing the term $\sigma\frac{\partial \mathbf{A}}{\partial t}$. For superconductivity-related problems, this formulation requires the defining conductivity in terms of the electric field $\mathbf{E} = -\frac{\partial \mathbf{A}}{\partial t}$, which, although possible, does not perform very well for high values of n in the E-J power-law (6.38).

The scalar electric potential φ is used when the source is given as electric potential, whereas current density $\mathbf{J}$ for the current sources. The former is used when circuit equivalent parameters (resistance, inductance or capacitance) are known and can be fed into the model or result from FEM simulation, but that comes at the cost of computational resources. The (6.21) can also be derived by applying Coulomb gauge (6.22) [236].

$$A \rightarrow A + \boldsymbol{\nabla}\varphi \tag{6.22}$$

So far, the $\mathbf{H}-$formulation (6.23) is the most popular of all formulations in modelling superconducting phenomenon [122–133, 237]. The formulation arises from problems that require solving Faraday's law (6.3), and ease of numerical implementation of nonlinear resistivity of superconductors (6.35). The formulation requires more computational resources since it is a vector-valued problem and also a special type of finite elements to be used in the FEM method, which are curl-conforming elements - Nedelec 1st-kind ($\mathrm{N1}^e$) or 2nd-kind ($\mathrm{N2}^e$) elements in 3D space or Raviart-Thomas elements RT^e in 2D space [238]. The full overview of H-formulation in superconductivity, its benefits and uses have been presented in [237].

$$\boldsymbol{\nabla} \times \rho \boldsymbol{\nabla} \times \mathbf{H} = -\mu \frac{\partial \mathbf{H}}{\partial t} - \mu \frac{\partial \mathbf{H}_\mathrm{s}}{\partial t} \tag{6.23}$$

The $\mathbf{T}-$formulation, similarly to $\mathbf{A}-$formulation used in classical electromagnetism of eddy current problems, but also found its way in simulations of superconductivity problems [113–117]. The formulation is described by $\mathbf{T}$ - a vector current potential and scalar magnetic potential $\varPhi$. In some regions, the current density is source-less, meaning that divergence of current density is also equal to zero in those regions (6.24).

$$\boldsymbol{\nabla} \cdot \mathbf{J} = 0 \tag{6.24}$$

It means that the current density can be defined with a vector current potential $\mathbf{T}$ as shown in (6.25) and does not affect the (6.24).

$$\mathbf{J} = \boldsymbol{\nabla} \times \mathbf{T} \tag{6.25}$$

The similarity between equations (6.25) and (6.19) can be seen. Additionally, introducing magnetic scalar potential $\varPhi$ as in (6.26), does not affect abovementioned equations, and satifies (6.17).

$$\mathbf{H} = \mathbf{T} - \boldsymbol{\nabla}\varPhi \tag{6.26}$$

This results in (6.27).

$$\boldsymbol{\nabla} \times \rho \boldsymbol{\nabla} \times \mathbf{T} = -\mu \frac{\partial \left(\mathbf{T} - \boldsymbol{\nabla}\varPhi\right)}{\partial t} - \frac{\partial \mathbf{B}_\mathrm{s}}{\partial t} \tag{6.27}$$

Depending on the gauge fixing, the (6.27) with (6.17) can form two different set of PDEs. As an example, the $\mathbf{T}-$formulation will be used to present derivation for different gauges, however the same applies to $\mathbf{H}-$formulation and other formulations. For the Coulomb gauge [236] the condition is (6.28) that results in set of two PDEs (6.29).

$$\boldsymbol{\nabla} \cdot \mathbf{T} = 0 \tag{6.28}$$

$$\begin{cases} \boldsymbol{\nabla} \times \rho \boldsymbol{\nabla} \times \mathbf{T} = -\mu \frac{\partial (\mathbf{T}-)}{\partial t} - \frac{\partial \mathbf{B}_\mathrm{s}}{\partial t} \\ \nabla^2 \mathit{\Phi} = 0 \end{cases} \tag{6.29}$$

Whereas for the Lorentz gauge [236] (6.30) leads to different set of (6.31).

$$\boldsymbol{\nabla} \cdot \mathbf{T} = -\frac{\mu}{\rho} \frac{\partial \mathit{\Phi}}{\partial t} \tag{6.30}$$

$$\begin{cases} \boldsymbol{\nabla} \times \rho \boldsymbol{\nabla} \times \mathbf{T} = -\mu \frac{\partial \mathbf{T}}{\partial t} - \frac{\partial \mathbf{B}_\mathrm{s}}{\partial t} \\ \boldsymbol{\nabla} \cdot \rho \boldsymbol{\nabla} \mathit{\Phi} = -\mu \frac{\partial \mathit{\Phi}}{\partial t} \end{cases} \tag{6.31}$$

The PDE defined in terms of electric field intensity **E**, also known as **E**−formulation has been used to solve superconducting problems [118–121] and is given by the (6.32). Similarly to **A**−formulation, the formulation requires the definition of conductivity in terms of the electric field, instead of current density (6.38).

$$\boldsymbol{\nabla} \times \frac{1}{\mu} \boldsymbol{\nabla} \times \mathbf{E} = -\sigma \frac{\partial \mathbf{E}}{\partial t} \tag{6.32}$$

In recent years more widely used become a **T** − **A** - formulation which combines both **T**−formulation and **A**−formulation [239–242]. The formulation takes benefits from the **A**−formulation, which are the definition of current sources **J** and application of nonlinear resistivity from **T**−formulation. The formulation is defined as a set of three equations (6.33).

$$\begin{cases} \boldsymbol{\nabla} \times \frac{1}{\mu} \boldsymbol{\nabla} \times \mathbf{A} = \mathbf{J}_s \\ \mathbf{B} = \boldsymbol{\nabla} \times \mathbf{A} \\ \boldsymbol{\nabla} \times \rho \boldsymbol{\nabla} \times \mathbf{T} = -\frac{\partial \mathbf{B}}{\partial t} \end{cases} \tag{6.33}$$

Recently the **A** − **H** - formulation has been proposed to solve a superconducting problem [243], which combines both **A**−formulation and **H**−formulation.

Lastly, it is worth mentioning the approach developed by A. M. Campbell [244], which has been derived from **A**−formulation and is given as (6.34). The equation solves directly for the critical state where magnetic flux penetrates the sample. The implementation is as straightforward as **A**−formulation, and current sources $\mathbf{J}_\mathrm{s}$ can be used, thus making it relatively easy to implement in existing software. The equation has been used in a couple of studies [46, 245] so far.

$$\boldsymbol{\nabla} \times \frac{1}{\mu} \boldsymbol{\nabla} \times \mathbf{A} = \mathbf{J}_\mathrm{s} + \mathbf{J}_\mathrm{p} - \frac{1}{\rho} \frac{\partial \mathbf{A}}{\partial t} - \mathbf{k} \left[1 - \exp\left(-\frac{(A - A_\mathrm{p}) \mu_0 J_\mathrm{c}}{k A_\mathrm{r}} \right) \right] \tag{6.34}$$

where: $\mathbf{k} = \mathbf{J}_\mathrm{c} \cdot \mathrm{sgn}(A_\mathrm{p} - A) - \mathbf{J}_\mathrm{p}$
In this formulation in case of superconducting materials, the value of resistivity ρ is treated as parameter, which can be adjusted based on experimental studies [245].

6.1.4. Nonlinear resistivity of superconductors

As in classical electromagnetism, the electromagnetic Ohm's law (6.7) is a basis for establishing material resistivity, which in many cases does not depend on the value of current density or electric field but rather on temperature. Thus, it requires coupled modelling with a heat equation to obtain the temperature iteratively. If the temperature is known, it is more preferable to input a constant value at a fixed temperature for simplicity. On the other hand, the resistivity of superconducting materials depends on the current value at any given point. Therefore, by combining Ohm's law (6.7) and E-J power law, the resistivity can be derived as (6.35).

$$\rho = \frac{E_{\mathrm{c}}}{J_{\mathrm{c}}}\left(\frac{|\mathbf{J}|}{J_{\mathrm{c}}}\right)^{n-1} \tag{6.35}$$

Equation (6.35) describes the behaviour of superconductors resistivity; it is not well suited for numerical simulations due to poor stability if the value is equal to zero. The introduction of a bias value ρ_0 as in (6.36) improves the numerical stability of the solution. The value of $\rho_0 \leq 10^{-2}\frac{E_{\mathrm{c}}}{J_{\mathrm{c}}}$ was pointed out to work the best. The value itself could be interpreted as resistivity due to thermal activation [109, 246, 247].

$$\rho = \frac{E_{\mathrm{c}}}{J_{\mathrm{c}}}\left(\frac{|\mathbf{J}|}{J_{\mathrm{c}}}\right)^{n-1} + \rho_0 \tag{6.36}$$

There have been attempts of modelling resistivity (6.37) and conductivity (6.38) as a function of electric field for purpose of modelling with $\mathbf{A}-$formulation and $\mathbf{E}-$formulation. As mentioned previously, those relations does not performs well for high values of n, since the power $\frac{(n-1)}{n} \to 1$, and the resistivity behaves linearly.

$$\rho = \frac{E_{\mathrm{c}}}{J_{\mathrm{c}}}\left(\frac{|\mathbf{E}|}{E_{\mathrm{c}}}\right)^{\frac{n-1}{n}} \tag{6.37}$$

$$\sigma = \frac{J_{\mathrm{c}}}{E_{\mathrm{c}}}\left(\frac{E_{\mathrm{c}}}{|\mathbf{E}|}\right)^{\frac{n-1}{n}} \tag{6.38}$$

The superconducting materials are generally not good conductors or even behave as insulators in the normal state ($T > T_{\mathrm{c}}$), and the resistivity is much higher than in the superconducting state ($\rho_{\mathrm{n}} \gg \rho_{\mathrm{SC}}$). The model proposed in [124] introduces saturation point of resistivity and treats superconducting material as a parallel connection of resistances - one being a superconductor described by E-J power law (2.6) given as ρ_{SC}, and the second one in normal (resistive) state ρ_{n}. A similar description is popular in modelling superconducting tapes, cables or coils where the substrate takes over current conduction when the resistivity of the superconducting layer becomes significantly high [246, 247].

$$\rho = \frac{\rho_{\mathrm{SC}}\rho_{\mathrm{n}}}{\rho_{\mathrm{SC}} + \rho_{\mathrm{n}}} \tag{6.39}$$

where ρ_{SC} is equal to the resistivity modeled using (6.35) or (6.36) and the ρ_{n} is the resistivity of superconductor in normal state.

The importance of introducing saturation as in (6.39) is highlighted the most in the case of solving **H**−formulation and **T**−formulation in the whole domain. To successfully solve these PDEs, the resistivity of all subdomains in the model has to be given, including free space, similarly to magnetic permeability in **A**−formulation. The procedure of assigning resistivity to free space $\rho = 1$ is typical, which is much greater than the resistivity of any conducting subdomains where eddy currents will be induced. This approach does not interfere with the results but is necessary for the conformity of the solution. The comparison between resistivities given derived from E-J power law (6.35) and with a saturation (6.39) as a function of current density has been shown in Figure 6.2.

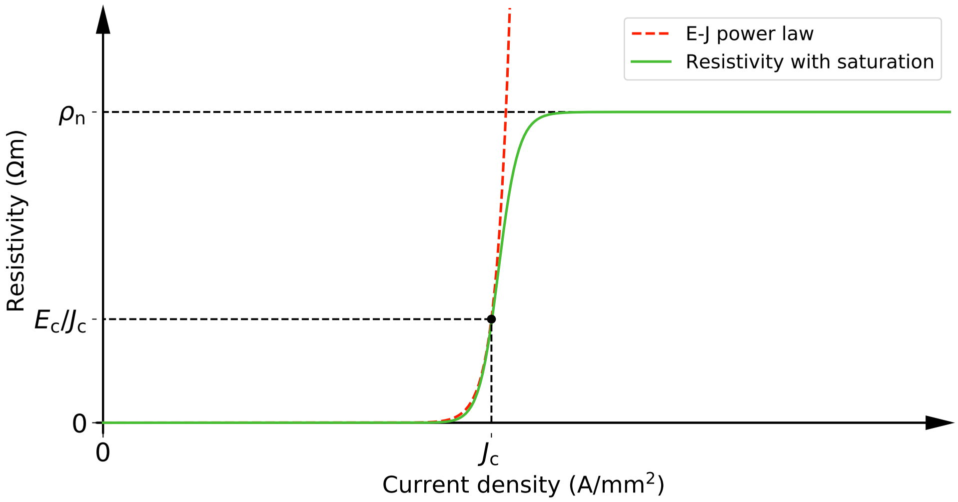

Figure 6.2. Nonlinear resistivity of superconducting materials

6.2. Finite element method

The solution to a partial differential equation can be obtained analytically for cases with multiple simplifying assumptions, including geometry simplification or exploiting axisymmetry, and constant material properties, which usually are also isotropic. Although an analytical solution gives a glimpse into the relationship between variables and field distribution, it is not well suited for generalized cases with complex geometries and nonlinear material properties. One of the ways to obtain the field distribution resulting from the solution of a given PDE is by finite-element method (FEM), which will be presented briefly in the following section. The finite-element method has been extensively discussed in the literature, including the underlying mathematics, accuracy and stability of different PDE equations, stepping methods or finite elements [248–250]. Therefore, only key steps in formulating a PDE problem using a FEM solver will be discussed further.

Finite-element method is a generalisation of the classical variational (Ritz) method and weighted-residual (Galerkin) method [251–253]. It is mostly used to numerically solve problems that have complex geometries and problems that may have multiple different boundary conditions on different parts of the model, which will be hard or even impossible to solve analytically. The solution is obtained by solving a weighted-integral (weak formulation) of the partial-differential equation by finding the weights associated with every element. The weights are calculated as a solution to a set of algebraic equations that has been assembled from the connections between neighbouring elements of discretised domain and set boundary conditions [251].

6.2.1. Defining a problem

The solver used for FEM simulations in the analysed problems is an open-source software called FEniCS [254] Although FEniCS provides a rich application programming interface (API) to interact with, only selected features will be used; thus, only those will be discussed in the following section to describe the process of formulating a PDE problem. The general approach stays the same, regardless of used software, where some may require setting up the simulation in greater detail, i.e. Deal.II [255], and some provide easy out-of-the-box experience, like Agros 2D [256], whereas somewhere in-between is COMSOL Multiphysics [257] and Ansys [258] allowing for limited but in-depth access to the algorithms via API. Those will include steps required for preparing the model - geometry, meshing, selecting element types, weak formulation of PDE and solving nonlinear PDE equations, without diving too much into mathematics underlying finite elements, basis function, weighted residual method or matrix operations, including matrix preconditioners or types of solvers, which are beyond the scope of this thesis.

There are three main steps in defining a PDE problem in any software [251–253]:

1. **Preprocessing** is a stage at which the preparation of simulation domain begins and consists of two steps:
   (a) **Geometry building** - at this point, the geometry could either be created from scratch according to the datasheet or imported from a CAD file. Nevertheless, in many cases, the geometry of the model requires some processing for numerical calculations. It is important to determine which parts of the model are important and which are not, or some parts may require special treatment. This might include removing some elements of the model entirely that are not important, like finer details, or even changing its shape to a simpler (i.e. round object replaced with

polygons). Elements like winding consisting of multiple strands can be replaced with a single homogenized block with appropriate material properties. At this point, the dimensionality of the model is determined. Whether the model will be calculated as 3D, 2D (on cross-section) or perhaps even in 1D (i.e. along the cable's length). In some cases, the model's symmetry can be exploited since not always a full geometry has to be used, but only selected part with symmetry boundary conditions, i.e. one-quarter of the model. A simple 2D geometry created in Gmsh [259] has been presented in Figure 6.3a.

(b) **Meshing** - at this stage, the domain is divided (discretised) into finite elements of a particular type. The initial mesh is generally of poor quality and requires some treatment. The mesh could have a fixed size or can change iteratively during simulation. The software user can select a setting to adjust mesh size and behaviour in certain regions to better fit the needs and achieve sufficient accuracy. The input values of settings can be determined on some characteristic length at given subdomains, i.e. skin depth δ in eddy current problems or $y+$ value in computational fluid dynamics (CFD) simulation for flow close to the wall where sheer stress occurs. The quality of mesh strictly determines the accuracy of the solution - if the mesh is too coarse, the solution accuracy will be poor, or the solver might not even converge at all. On the other hand, a fine mesh may result in better accuracy, but too fine a mesh leads to a high number of degrees of freedom (DOF) which increases the computational cost, and the solution may never arise. To determine at which point the size of the mesh becomes acceptable, a mesh dependency study has to be conducted. In such a study, the mesh is refined, and the simulation parameters are monitored to determine a point of diminishing returns, where solution values are not changing significantly. In time-dependent problems, the mesh could be generated from scratch at every time step or fixed during all time-steps. The type and order of elements are chosen at this point. The geometry presented in Figure 6.3a has been meshed and shown in Figure 6.3b.

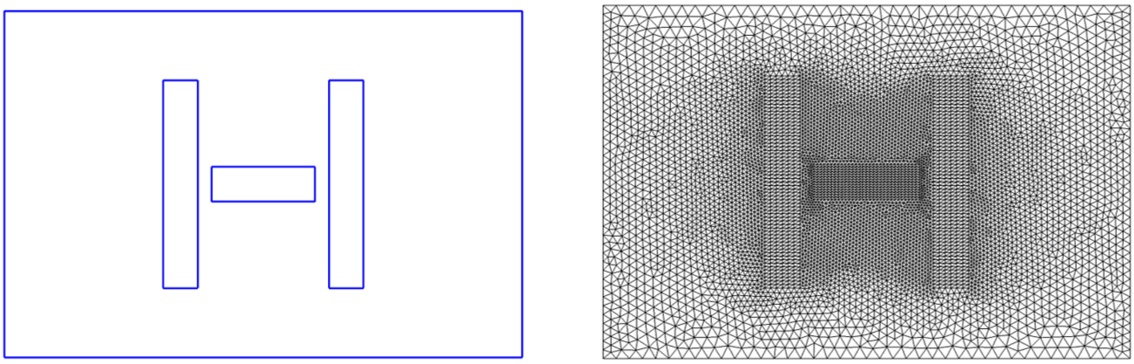

(a) Geometry **(b)** Meshing

Figure 6.3. Visualisation of created: (a) geometry and (b) meshing

To decide whether the mesh quality is good enough, there are indicators that are worth looking up during the meshing like aspect ratio, skewness, Jacobian, distortion and stretch [260]. The exact definition of these quality indicators might change depending on the software. One of the basic and most often used metric is the *aspect ratio* which is defined as a ratio between the maximum and minimum edge length of the element. It is recommended to have elements of ratio at most 1.6 or lower closer to 1.0. Elements with symmetrical shapes are rather desired than elements with a high aspect ratio. The meshing is done to conform elements perfectly to the geometry. Also, some compromise is required to reduce computational cost. For example, besides filling the whole space, if the mesh is constructed out for two or more submeshes, those can not overlap, and there can not be any hanging nodes, which implies that the mesh is conforming between neighbouring subdomains.

(c) **Problem and boundary conditions setup** - the problem has to be defined on the given geometry. The type of simulation, thus governing PDE which will be solved, has to be defined on the meshed domain. Depending on the interface of the FEM solver, a limited number of choices might be presented to the user, i.e. Ansys Electronics [258], where the type of simulation is selected, and the equations and matrices are assembled in the background. On the other side of the spectrum is FEniCS [254], which requires a manual definition of PDE in weak form, and the user can control the software behaviour at every step. If the partial-differential equation or set of PDEs is chosen, material properties are selected for the subdomains. The next major step is to impose boundary and initial conditions. These are necessary to obtain a valid solution. An example setup for geometry (Figure 6.3a) is shown in Figure 6.4 for simulating the superconductor as nearly perfect diamagnetic ($\mu_\mathrm{r} = 0.001$) with a surrounding coil using $\mathbf{A}-$formulation.

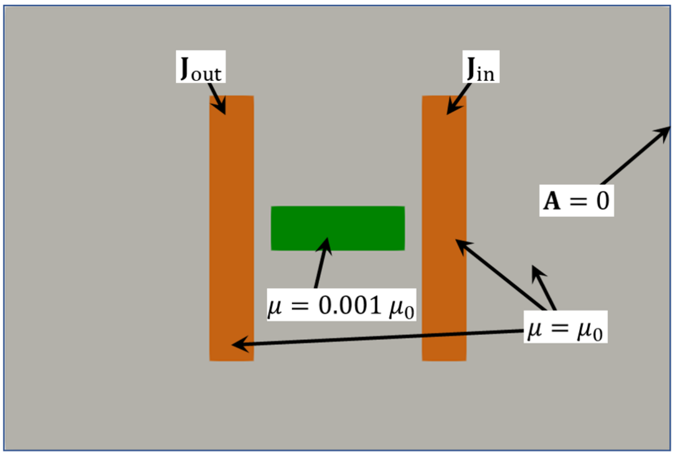

Figure 6.4. Visualisation of model definition for solving $\mathbf{A}-$formulation with superconducting bulk as nearly perfect diamagnetic

2. **Computation** is finding the solution to the problem that has been set up during *preprocessing* step. A set of linear equations is solved either directly if the system is linear or interactively if the system is nonlinear. Additional mesh refinement can be performed between iterations. The desired parameters are followed, and their change with every iteration is observed to confirm the convergence of the solution, i.e. relative error at each iteration (Figure 6.5). The solution can be obtained for different parameters, i.e. values of current density or dimensions.

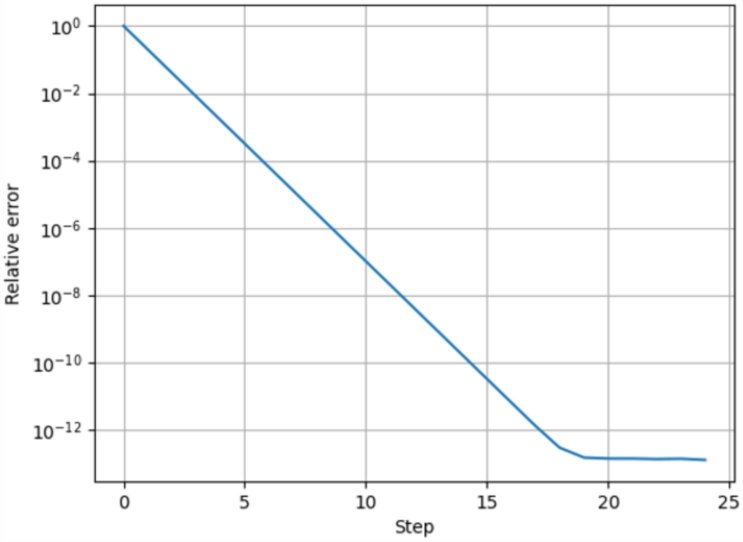

Figure 6.5. Convergence of FEM solution relative error

3. **Postprocessing** - after performed calculations, the collected data has to be examined and presented in some way. This may be in the form of extracting data at a single point, a couple of points over the curve or visualising the solution in the whole domain. Besides solution convergence, it is important to determine solution conformity. In special cases, the obtained result can be compared to the known analytical solution. Generally, such a thing can not be done. Proper visualisation of results allows for better judgment of model conformity, deriving proper conclusions and easier communicating the results to other people. The solution over the mesh can be visualised as is or can be further processed to highlight some aspects of the field. The software could use provided visualisation toolbox, or the data can be exported and viewed in external tools, i.e. ParaView [260]. The solution of the described above problem is obtained as the distribution of magnetic vector potential **A** (Figure 6.6a), which allows for a calculation of other quantities, i.e. distribution of magnetic flux density (Figure 6.6b).

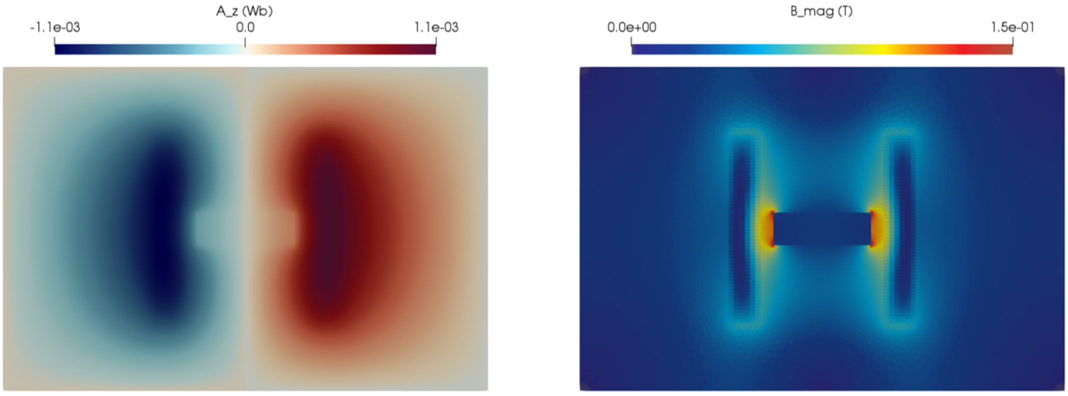

(a) A_z field distribution

(b) $|\mathbf{B}|$ field distribution

Figure 6.6. (a) Solution of 2D $\mathbf{A}-$formulation for state variable A_z; (b) and magnitude of **B** field calculated using (6.8)

6.3. Numerical model setup

The numerical model has been developed using a finite-element method solver FEniCS 2019.1.0 [254]. It has been decided to create a 2D axisymmetric model of the PFM system since both solenoid and bulk have axial symmetry. Although the 2D simulation can not include effects on both GS and GSB, the model should act as a sufficient approximation of magnetisation on the growth sectors that consist of the majority of the bulk's surface compared to growth sector boundaries. The geometry and mesh for the simulation were created using Gmsh [259]. The dimensions of coils have been taken from Table 4.1, and windings have been modelled as homogenised structures with a rectangular cross-section instead of simulating every single wire. Due to the axial symmetry of the model, only half of the domain cross-section has been created (Figure 6.7a). The whole domain Ω has been divided into three subdomains - HTS bulk (Ω_{HTS}), coil and surrounding free space. The boundary $\partial\Omega$ was given the Dirichlet boundary condition $\mathbf{A} = 0$ to the axis of symmetry of the model, whereas the mixed boundary condition $\partial\mathbf{A}/\partial\mathbf{n} = -\mathbf{A}/R_{\partial\Omega}$ was given to the outer (rounded) edge of radius $R_{\partial\Omega}$ of the free space [261] that results in magnetic field not being restricted by the domain.

The whole domain has been meshed using triangular elements (Figures 6.7b and 6.7c), which are structured in the HTS bulk's subdomain (Figure 6.7c), and unstructured in the rest of the domain (Figure 6.7b). The finest mesh was created in the bulk's subdomain to minimise the numerical error of the eddy currents being induced inside the bulk, especially due to the nonlinear behaviour of its resistivity. The mesh dependency study has been conducted, which resulted in 14400 cells inside the bulk and a total number of 64132 cells in the whole domain. The Lagrange elements of the 1st-order P_1 were used to discretise the domain [261, 262].

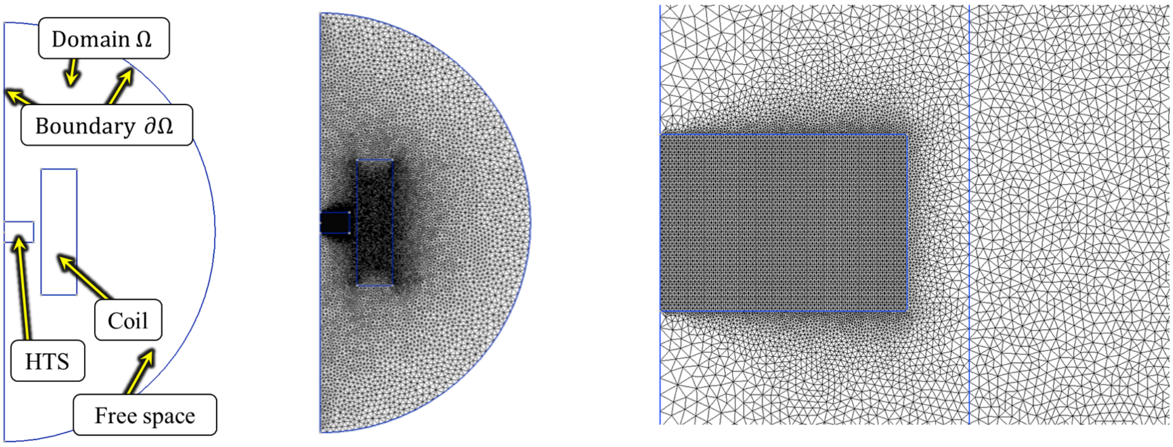

(a) geometry **(b)** meshed domain **(c)** close-up of the meshed bulk

Figure 6.7. Geometry and mesh of the analysed domain for pulsed-field magnetisation of the HTS bulk

The magnetic field created by the flux pump was obtained by solving the $\mathbf{A}-$formulation on the whole domain, including eddy currents in the HTS bulk. The current density source $\mathbf{J}_{\mathrm{s}}(t)$ is calculated using equations describing current generated by the flux pump system (4.25) and evaluated as current density in tangential direction $J_\theta(t)$ of the coil (6.41).

$$\nabla \times \frac{1}{\mu_0} \nabla \times \mathbf{A} = \mathbf{J}_{\mathrm{s}}(t) - \sigma \frac{\partial \mathbf{A}}{\partial t} \tag{6.40}$$

$$J_{\theta}(t) = \frac{Ni(t)}{WH} \tag{6.41}$$

To perform a simulation in FEniCS software, the weak formulation of the PDE has to be derived and implemented. The weak formulation is obtained by taking an inner product of the PDE (6.40) and test function $\mathbf{w}$ [261, 262]. Since the problem is solved using axial symmetry, the magnetic vector potential $\mathbf{A}$ is considered to have only tangential component A_{θ} (perpendicular to the geometry), therefore $\mathbf{A} = [0; A_{\theta}; 0]$.

$$-\frac{1}{\mu_0}\int_{\Omega}(\boldsymbol{\nabla}\times\mathbf{A})\cdot(\boldsymbol{\nabla}\times\mathbf{w})\,\mathrm{d}V = \int_{\Omega_{\mathrm{HTS}}}\mathbf{J}_{\mathrm{s}}\cdot\mathbf{w}\,\mathrm{d}V - \sigma\int_{\Omega_{\mathrm{HTS}}}\frac{\partial\mathbf{A}}{\partial t}\cdot\mathbf{w}\,\mathrm{d}V \tag{6.42}$$

For the modelling, the derivative of magnetic vector potential over time needs to be expressed as a difference between values obtained at time steps h apart (6.43); therefore, by assuming a finite step of Δt the backward Euler finite stepping scheme can be applied (6.44), that calculates difference between current solution $\mathbf{A}_{\mathrm{n}}$ and previous solution $\mathbf{A}_{\mathrm{n-1}}$ at every point [261, 262]. For the simulation the time step of $\Delta t = 250$ µs was used with total simulation time of $T_{\mathrm{end}} = 400$ ms.

$$\frac{\partial\mathbf{A}(t)}{\partial t} = \lim_{h\to\infty}\frac{\mathbf{A}(t)-\mathbf{A}(t-h)}{h} \tag{6.43}$$

$$\lim_{h\to\infty}\frac{\mathbf{A}(t)-\mathbf{A}(t-h)}{h} \approx \frac{\mathbf{A}_{\mathrm{n}}(t)-\mathbf{A}_{\mathrm{n-1}}(t)}{\Delta t} \tag{6.44}$$

The resistivity of superconducting material can be expressed in terms of electric field $\mathbf{E}$ as previously shown (6.37), whereas $|\mathbf{E}| = \left|\frac{\partial\mathbf{A}}{\partial t}\right|$. Additionally, the resistivity $\rho_0 = E_{\mathrm{c}}/J_{\mathrm{c0}}$ responsible for the flux flow losses can be added, that will improve numerical stability (6.45). The conductivity of the superconductor to be used in solving PDE (6.40) is calculated as the inverse of the resistivity (6.46). The eddy currents are considered only in the HTS bulk.

$$\rho_{\mathrm{HTS}} = \frac{E_{\mathrm{c}}}{J_{\mathrm{c}}(\mathbf{B})}\left(\frac{|\mathbf{E}|}{E_{\mathrm{c}}}\right)^{\frac{n-1}{n}} + \rho_0 \tag{6.45}$$

$$\sigma_{\mathrm{HTS}} = \frac{1}{\rho_{\mathrm{HTS}}} \tag{6.46}$$

The critical current is considered to be field-dependent value $J_{\mathrm{c}}(\mathbf{B})$ according to the (2.10), due to lack of data regarding J_{c} in parallel and perpendicular direction of the a-b plane of the HTS material. The eddy current flowing through the superconducting material is calculated using (6.47), and the magnetic flux density vector $\mathbf{B}$ (6.48), which has vertical component B_{z} and radial component B_{r}. The visualisation of field distribution was done in ParaView [260].

$$\mathbf{J}_{\mathrm{HTS}} = \sigma_{\mathrm{HTS}}\frac{\partial\mathbf{A}}{\partial t} \tag{6.47}$$

$$\mathbf{B} = \boldsymbol{\nabla}\times\mathbf{A} \tag{6.48}$$

6.4. Results

6.4.1. Transient analysis

The numerical model has to be calibrated before performing the analysis. A multiple model variants have been analysed to set parameters required for the numerical simulations. As a result, the values have been defined: $n = 13$, $J_\mathrm{c} = 1.6 \cdot 10^8$ A/m^2, $B_\mathrm{c} = 0.25$ T, $E_\mathrm{c} = 10^{-4}$ V/m. Other parameters required for generating current pulse are based on the derived model in Section 4.4, including coil and HTS bulk geometries. Since the most interesting behaviour has been observed for higher capacitance ($C = 5$ mF), the simulations were performed for only this case at different voltages U_C0. An example simulation results are shown in Figure 6.8 of vertical components B_z of magnetic flux density $\mathbf{B}$ on the bulk's surface from four points where sensors would be located.

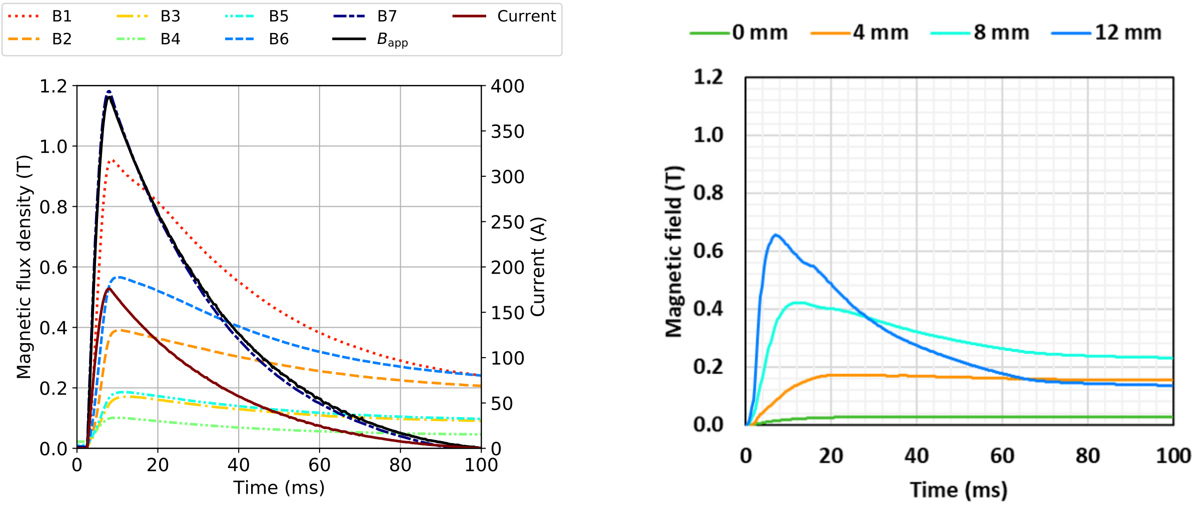

(a) Measurement **(b)** Simulation

Figure 6.8. Magnetic flux density waveforms for system L_3/5 mF/150 V

The relative critical current density J/J_c distribution inside the HTS bulk on the half cross-section during magnetisation has been presented in Figures 6.9 and 6.10 for coil L_3 with an inductance of 1 mH in a system with $C = 5$ mF and charged up to $U_\mathrm{C0} = 300$ V. The fields distribution were chosen for selected time steps to visualise the magnetisation process. In the beginning, with a low value of applied field (Figures 6.9a/b), the magnetic field is not present in the bulk's structure. As the applied field increases to the peak value at around $t = 3.5$ ms (Figures 6.9c/d) the eddy current inside the bulk is induced in such a direction that opposes the applied field. Next (Figures 6.9e/f), the applied magnetic flux density starts decreasing, but the magnetic field penetrates further into the bulk's structure. At this point, the majority of current density should flow in the same direction. After that, the current is being induced in the opposite direction (Figures 6.10a/b) when the applied field starts descending. It can be seen that critical current starts to be induced from the edge of the bulk. As the applied field decreases, the induced counter-current penetrates further at a value of around J_c (Figures 6.10c/d). The dynamics of the current induction decreases as time passes since the field rate-of-change is also lower. Finally, current density flows in the opposite direction to the primarily induced current through the whole structure (Figures 6.10e/f), which in some cases might fall even further over time due to flux creep losses. Depending on the applied field, the total current on the cross-section of the bulk might be lower, and the current might flow in opposite directions or partially through the bulk.

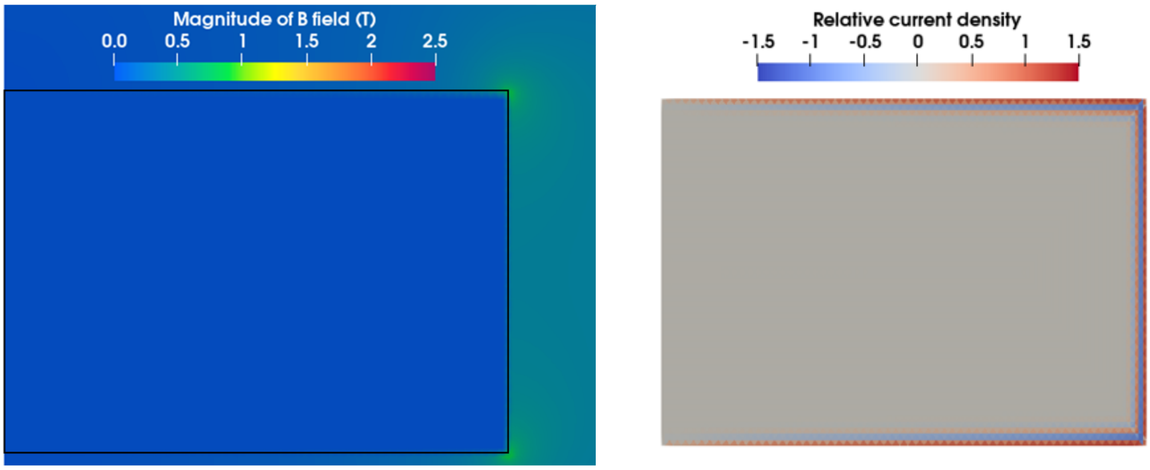

(a) $t = 0.1$ ms **(b)** $t = 0.1$ ms

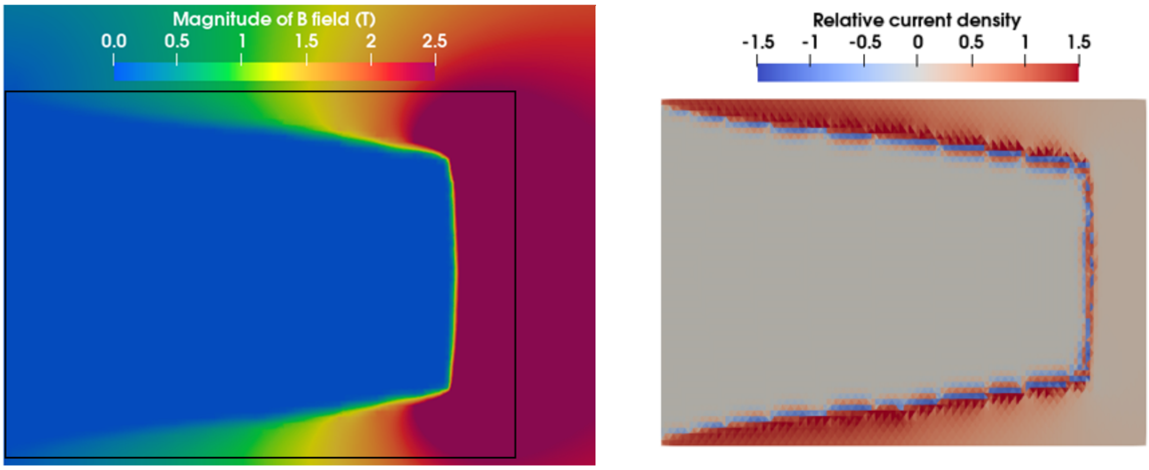

(c) $t = 2$ ms **(d)** $t = 2$ ms

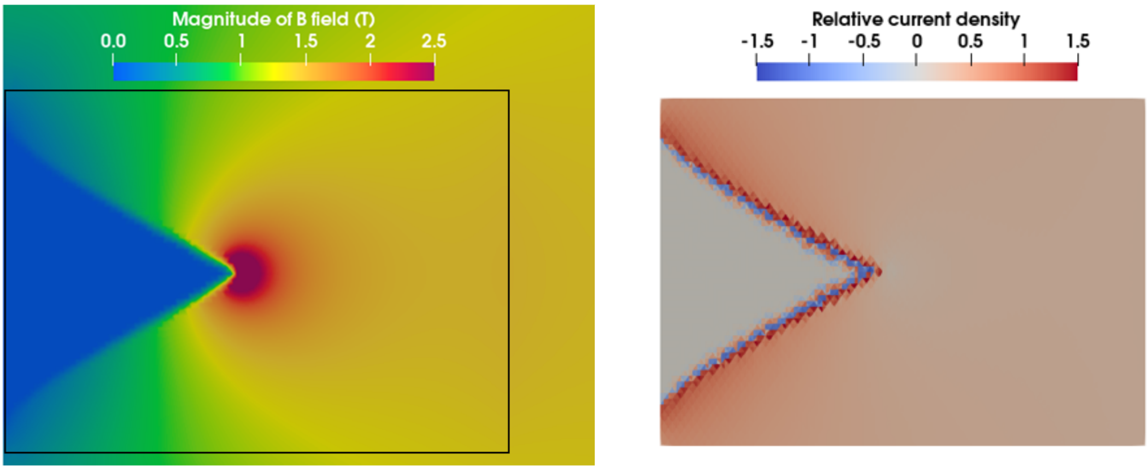

(e) $t = 10$ ms **(f)** $t = 10$ ms

Figure 6.9. Distribution of magnetic flux density and relative value of J_c during pulsed-field magnetisation at different time steps in system with L_3 coil, $C = 5$ mF and $U_{C0} = 300$ V

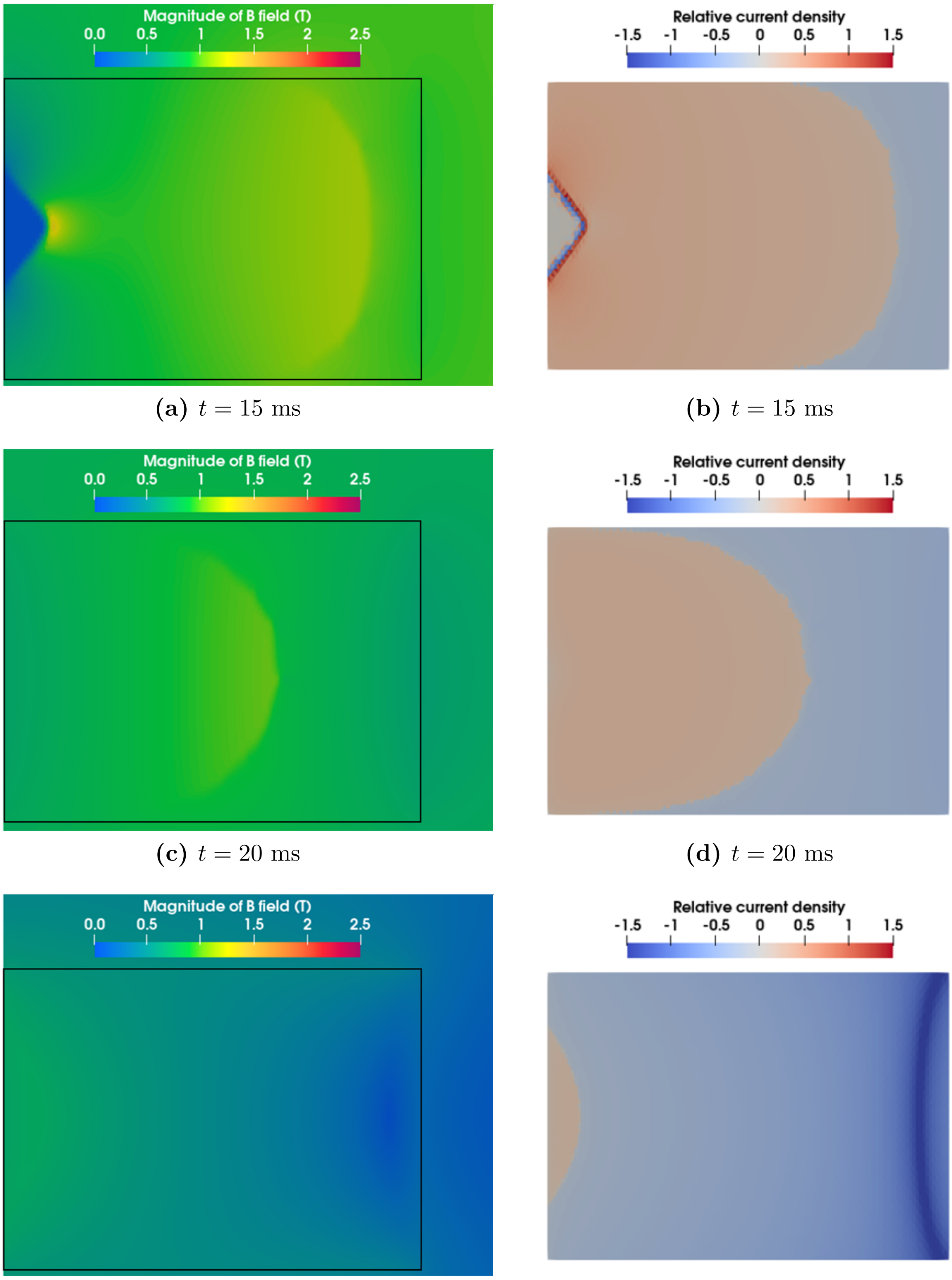

(a) $t = 15$ ms

(b) $t = 15$ ms

(c) $t = 20$ ms

(d) $t = 20$ ms

(e) $t = 50$ ms

(f) $t = 50$ ms

Figure 6.10. Distribution of magnetic flux density and relative value of J_c during pulsed-field magnetisation at different time steps in system with L_3 coil, $C = 5$ mF and $U_{C0} = 300$ V

The final values of current density obtained after pulsed-field magnetisation are presented in Figures 6.11a/b. If, however, the applied field would have a lower value, it will result in a different field and current density distribution (Figures 6.12a/b), where current flows in both directions inside the bulk and can not penetrate through the whole cross-section. The current density inside the bulk has lower value than J_c due to influence of the magnetic field (2.10).

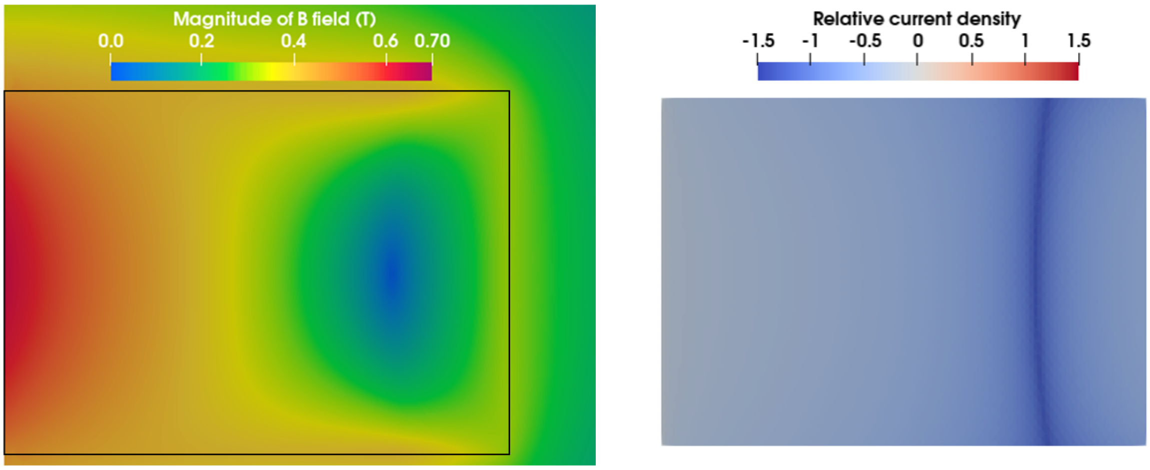

(a) $t = 400$ ms

(b) $t = 400$ ms

Figure 6.11. Distribution of magnetic flux density and relative value of critical current density during pulsed-field magnetisation at different time steps in system with L_3 coil, $C = 5$ mF and $U_{C0} = 300$ V

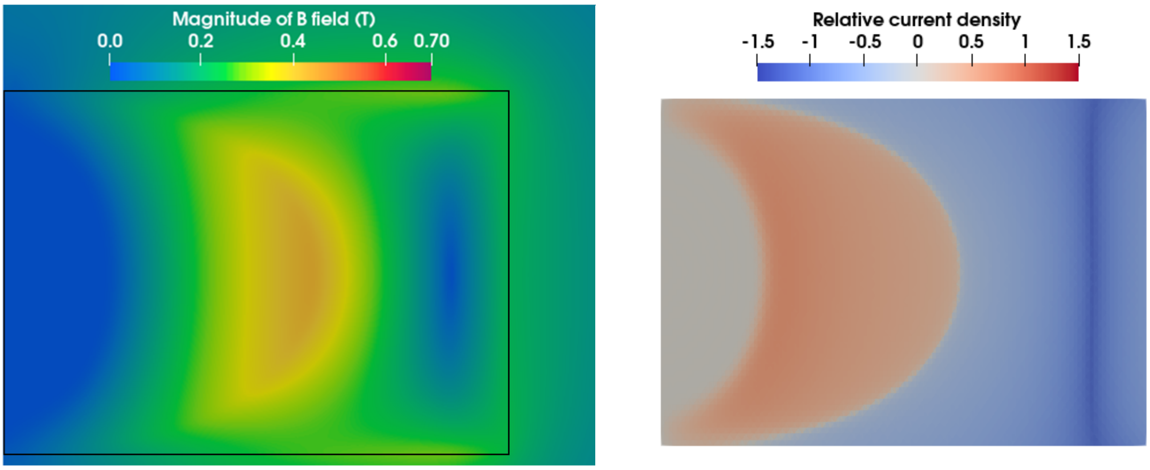

(a) $t = 400$ ms

(b) $t = 400$ ms

Figure 6.12. Distribution of magnetic flux density and relative value of critical current density during pulsed-field magnetisation at different time steps in system with L_3 coil, $C = 5$ mF and $U_{C0} = 150$ V

6.4.2. Steady-state analysis

The results of the magnetic flux distribution on the bulk's surface have been compared with the experimental results in Figure 6.13. As voltage increases and consequently applied field, the trapped field on the surface of the HTS bulk increases towards the center.

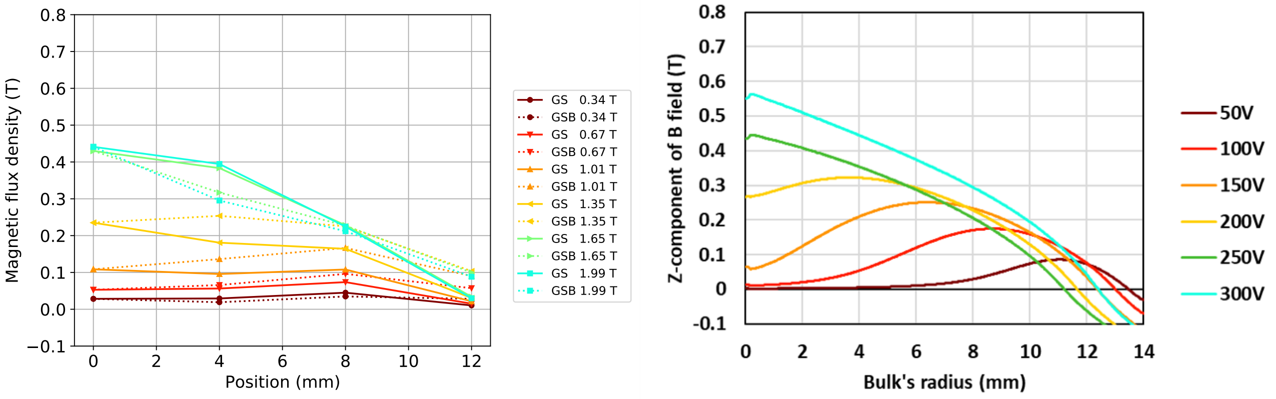

(a) L_1/5 mF Trapped field **(b)** L_1/5 mF Trapped field

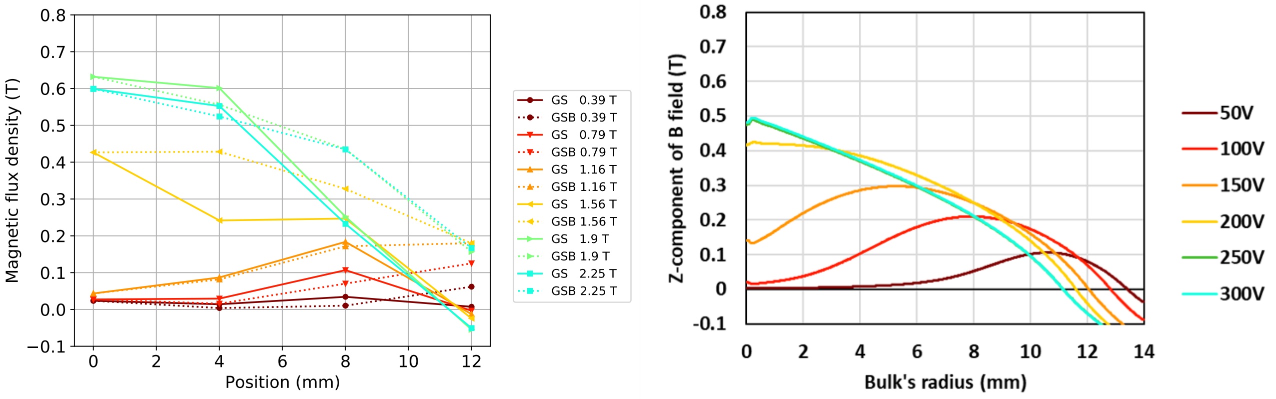

(c) L_2/5 mF Trapped field **(d)** L_2/5 mF Trapped field

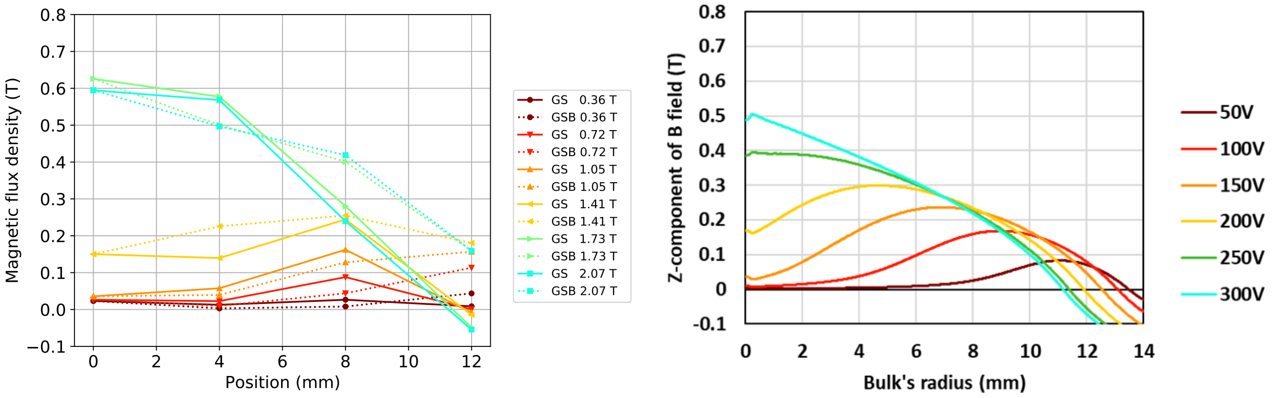

(e) L_3/5 mF Trapped field **(f)** L_3/5 mF Trapped field

Figure 6.13. Distribution of trapped magnetic flux density on GS and GSB for different $\hat{B}_{\text{app}}$ in system with $C = 5$ mF compared with simulation results

The data presented in Figure 6.13 for the same cases (applied voltages) were coloured the same. However, to highlight the differences due to simplification of the 2D axisymmetric model, the voltages were used as labels (Figures 6.13b/d/f) and peak applied fields $\hat{B}_{\mathrm{app}}$ as in Figures 6.13a/c/e. Another difference is the number of measuring points in the experimental investigation, where a total of seven sensors has been located - four along the radii of GS and GSB regions spaced 4 mm apart. In the case of the simulation, the vertical magnetic flux component (perpendicular to the bulk's top surface) B_{z} has been shown on the plots along the whole radius of the bulk's surface.

Comparing the data obtained for all coils presented in Figure 6.13, the simulation deviates slightly from the experimental data, especially for the case of L_1 coil (Figures 6.13a/b), where a higher peak value of the trapped field was obtained computationally. The lowest values of the trapped field were obtained for the L_3, contrary to what also has been measured. This is possibly due to the oversimplification of the axisymmetric model and not taking into account, for example, power losses and resulting temperature field. However, the results match close to the bulk's edges (12 mm), where the magnetic flux is oriented in the opposite direction (Figures 6.13b/d/f). An additional error can be attributed possibly due to the coil's geometry simplification. In L_1 and L_2 coils, the wire diameter is lower compared to L_3 coil. In the first two coils, the turns are compacted closer together. However, in the case of L_3 coil, the larger wire diameter results in more free space between turns, meaning that the fill factor (ratio of the area occupied by conductors to the coil's cross-sectional area) is lower compared to the first two coils. A certain error can be attributed to the assumption of the uniform current density distribution $\mathbf{J}_{\mathrm{s}}$ within the coil. Especially at the beginning of pulsed-field magnetisation, when the magnetic field is expulsed from the bulk and distorted in the surrounding free space.

As mentioned in the introductory chapter (1), the pinning on the GS and GSB differ, including the very center of the bulk, where the seed was located. Such difference might explain the different behaviour of the numerical model compared to the experimental results. Additionally, the whole structure of the bulk has different properties inside, which results from the manufacturing process. The exact material properties of the bulks inside were estimated by comparing waveforms of the magnetic field on its surface, thus limiting the predicting values. The values of trapped field obtained for flux pump system operating below 250 V match experimental results, both in terms of values and field distribution.

Another source of error might be due to an insufficient number of iterations during the calibration of the models. The total number of performed measurements taken in during experimental research was 30. The simulation requires fine stepping time for the whole pulse duration and beyond to obtain the data in the steady-state. This results in a significant computational time of each case to achieve sufficient numerical accuracy, and therefore numerical results were compared with the small number of cases for the limited number of iterations.

6.5. Summary

The numerical simulations of the pulsed-field magnetisation of the HTS bulk were calibrated by comparing magnetic flux waveforms measured by the hall sensors located at the surface of the bulk. The computations were based on the finite-element method used to solve the $\mathbf{A}-$formulation in the domain. The current waveforms have been generated using derived equations (4.25) of the flux pump system. A simplified 2D axisymmetric model was used.

The numerical analysis has allowed for computing current density inside the superconducting bulk during the transient state of the PFM, which otherwise can not be measured directly. The analysis has shown that during the current pulse ascending phase, the eddy current inside the bulk is induced, which instantaneously reaches the value of $\approx J_\mathrm{c}$ due to the low resistivity of the material. The counter-current starts being induced in the opposite direction during the descending phase of the current pulse waveform. The process continues as long as the applied pulse is sufficiently high and the current decays long enough. The higher the capacitor bank voltage U_C0 is, the higher is the peak current $\hat{I}$ and corresponding peak applied field $\hat{B}_\mathrm{app}$. This also results in a longer pulse duration since the whole energy stored in the capacitor bank must be depleted. The counter-current induced inside the bulk continues to be induced inside to the point of occupying the whole cross-section. This results in achieving the highest magnetic flux density at the center of the bulk.

If the applied field has a lower peak value, the amount of induced counter-current is lower, and two currents flowing in opposite directions are present on the cross-section of the bulk. This results in achieving a peak field somewhere in-between the bulk's center and its edge along the radius. The trapped field also reaches lower peak values than in a system with much stronger applied fields.

The results obtained numerically differ from the measured values since the simulated model was heavily simplified to the simulation of the 2D cross-section of the system. The simplifications were also made regarding the temperature inside the bulk, which was not considered. The power losses and the temperature might play an essential role in the pulsed-field magnetisation since the HTS bulk operates close to its critical temperature.

7

Summary & Conclusions

7.1. Summary

The aim of the thesis was to examine the influence of flux pump circuit parameters on waveforms of the current and the applied magnetic field, and consequently, on the effectiveness of the pulsed-field magnetisation.

The dissertation began with an introductory Chapter 1 where key points related to pulsed-field magnetisation are presented from the engineering point of view. Next, an extensive literature review has been presented on subjects describing the current state of the art on the PFM: flux pump systems, measuring equipment, phenomena arising during pulsed-field magnetisation (influence of peak applied field or flux jumps), types of coils, cooling systems, types of superconductors, multi-pulse methods of magnetisation and applications. As a result, a hypothesis has been formulated to extend simplifications and fill in the absence of a particular description of flux pump systems for pulsed-field magnetisation.

To give a background to a potential reader about the superconductivity phenomena, the second Chapter 2 presents the fundamentals of superconductivity briefly. The focus of that chapter is to present electromagnetic formulas describing superconductors under the influence of the magnetic field, current and temperature used in the engineering practice of designing superconducting devices and their applications.
Next Chapter 3 has been dedicated strictly to pulsed-field magnetisation, where the aspects of that process are described in greater detail, backed with a literature review. The chapter highlights features of pulsed-field magnetisation with comparison to other methods (FC and ZFC) and different types of PFM systems. From the variety of structures, an RLC circuit has been chosen as one for investigation with a solenoid coil.

The in-depth study of a flux pump circuit for PFM has been presented in Chapter 4 divided into two main parts focused on the flux pump circuit and magnetising coil design. The analysis was done to describe a current waveform generated by the circuit, emphasising the influence of the circuit components. The derived formulas for the current waveform are applicable to the multi-pulse operation of the circuit, including those with controllable

electronic switches (i.e. transistors). However, the research has been focused on single-pulse magnetisation to reduce the number of potential variables.
A methodology for designing a solenoid coil dedicated for pulsed-field magnetisation was introduced. The described design procedure has been developed to achieve particular parameters of the coil - gain and field rate-of-change.

The designed coil and system were built and examined experimentally in Chapter 5 operating on the YBCO bulk cooled with liquid nitrogen (77 K) at atmospheric pressure. Primarily, two coils ($L_1 = 9$ mH and $L_2 = 3$ mH) were designed using the procedure presented in Chapter 4 to examine the influence of current and field rate-of-change on the trapped field. Both coils were used in the system with two capacitance values ($C = 2$ mF and $C = 5$ mF) to explore the influence of the capacitance on current and magnetic field waveforms. As a consequence of measurements, the third coil ($L_3 = 1$ mF) has been designed and tested only in a system with $C = 5$ mF, since only the system with this capacitance had a substantial effect on the trapped field. The effect of a peak field has been explored by applying a range of voltages, from 50 V to 300 V in the flux pump to magnetise the HTS bulk. The trapped field measurements were done using off-the-shelf components, including seven linear hall sensors (CYSJ362A) located near the surface along the growth-sector boundary and on the growth sector. The use of readily available components has proven to be a cost-effective and reliable solution in the range of measured fields. The measurement of the magnetic field had been done in seven points in total where sensors were located. However, the advantage of such a measurement are field waveforms obtained in the transient state during magnetisation. Nevertheless, gathered data does not give a complete picture of the processes inside the superconducting bulk.

A separate Chapter 6 has been dedicated to the modelling of superconductors, focusing on the electromagnetic aspect of pulsed-field magnetisation. At the beginning of the chapter, an overview of partial-differential formulations is presented, used to approximate phenomena arising inside the superconductor during PFM. To evaluate mathematical model of the superconductor, a finite-element method has been used. The results obtained numerically and experimentally overlap at low and high applied fields, with a deviation in intermediate states. The inconsistency might be due to simplifications implemented in the model. The simulations can be treated as an extension of the measurements, allowing for obtaining unmeasurable quantities such as current density distribution inside the superconductor or power losses and consequently temperature field distribution inside.

7.2. Final conclusions

The presented study was focused on the pulsed-field magnetisation of HTS bulks. It has been shown that coil inductance has a beneficial effect on the trapped field inside the bulk. This conclusion favours using smaller coils with lower inductance instead of larger systems. However, this comes with a drawback in the form of higher currents required to generate sufficiently high fields, thus forcing the use of proper components suited for the application. More compact coils can be used inside devices to magnetise bulks. The solenoid coil does not interfere with a magnetic field produced by the bulk since it could be wrapped around it.

The pulsed-field magnetisation effectiveness can be judged by the magnitude of the trapped field and its distribution at a given applied field. It has been shown, that coil with the lowest inductance value (1 mH) resulted in trapped field of $B_{\text{trap}} = 0.6$ T at approximately 1.6 T of applied field at the center, where comparable value has been achieved at $\hat{B}_{\text{app}} \approx 2$ T for 3 mH coil. The 9 mH coil was not able to reach a trapped field of that magnitude. The capacitance value C plays a vital role in achieving high trapped fields since it is the only source of energy in the RLC flux pump. Increasing capacitance results in significantly longer pulses, allowing for current to be induced inside the bulk. The limitation of achievable high trapped field B_{trap} in the analysed system could be related to: type of the system (RLC) imposing current waveform, coil type directly dictating field distribution, and limited cooling capabilities of the bulk.

The equations describing the current waveform account for R, L and C parameters of the flux pump have been derived. The procedure developed for designing solenoid coils for PFM systems accounts for desired output parameters and coil geometry. The feature of low coil inductance can be further explored to maximise the trapped field. In conducted study applying a single pulse of high magnitude $\hat{B}_{\mathrm{app}} > 2$ T resulted in a decrease of trapped field, possibly due to higher losses generated in the bulk and poor heat dissipation.

Finite-element method simulation for an electromagnetic simulation has been implemented and evaluated in open-source solver FEniCS. The equations describing the current waveform were used as the current density source in the FEM model. This allows for the association of the flux pump circuit with exact waveforms arising in the analysed system. The results obtained numerically are congruent with experimental results at low and high applied fields. For low applied fields (< 0.5 T), the magnetic field on the surface forms a ring shape. For higher applied fields, the trapped field in the center of bulk rises significantly. The intermediate values differ, possibly due to limitations of a 2D model, compared to a 3D model. One of the results of FEM analysis is the current distribution inside the bulk, which shows that the current responsible for the generated field inside the bulk is induced when the current waveform declines.

The abovementioned conclusions confirm the stated hypothesis at the beginning of this dissertation.

7.3. Key achievements

As the most important original, to the Author's knowledge, achievements contributing to the field of electrical engineering, the following can be appointed:

- developed methodology of designing coils for pulsed-field magnetisation in RLC flux pump taking into account desired parameters, such as gain ($\hat{B}/\hat{I}$), current and field rate-of-change, and coil dimensions;
- derived equation describing capacitor's voltage and coil's current waveforms for an RLC flux pump system;
- designed and constructed of flux pump dedicated for PFM of superconductors;
- performed measurements of the trapped field in HTS bulk achieved by pulsed-field magnetisation;
- verified by experimental validation developed models of the flux pump;
- implemented and evaluated numerical models utilising finite-element method describing PFM of superconductors in open-source software;

7.4. Potential future research

The conducted study focused on a single-pulse PFM system utilising a solenoid coil. Therefore, the research on the influence of applied magnetic field's gradient over time on the trapped field was limited and could be extended to split and CMDC coil systems, although the methodology for designing coil ought to be modified.

The analysed RLC flux pump system did not allow for active current waveform control, unlike in a system with electronic switches, i.e. transistors. Such systems allow for pulse width modulation of a signal, thus shaping the current waveform. The multi-pulse PFM method could be explored, emphasising the already mentioned field rate-of-change, which could potentially result in higher trapped fields.

Setting up FEM simulation and computing results for problems such as pulsed-field magnetisation is a tedious task, requiring significant computational resources due to the multitude of coupled fields. A potential solution to decrease computational time and cost is to utilise a neural network to predict field distribution inside the bulk at given conditions. However, the neural network would still require training data to be obtained either experimentally or computationally. The advantage of neural nets lies in problem generalisation capability; therefore, not many data points would be required.

Bibliography

[1] R. Flükiger, “Overview of superconductivity and challenges in applications,” *Reviews of Accelerator Science and Technology*, vol. 05, pp. 1–23, 01 2012, doi: 10.1142/S1793626812300010.

[2] D. Castelvecchi, “First room-temperature superconductor excites — and baffles — scientists,” *Nature*, vol. 586, pp. 349–349, 10 2020, doi: 10.1038/d41586-020-02895-0.

[3] E. Snider, N. Dasenbrock-Gammon, R. McBride, M. Debessai, H. Pasan, K. Vencatasamy, K. Lawler, A. Salamat, and R. Dias, “Room-temperature superconductivity in a carbonaceous sulfur hydride,” *Nature*, vol. 586, p. 373–377, 10 2020, doi: 10.1038/s41586-020-2801-z.

[4] A. Narlikar, *High Temperature Superconductivity 2: Engineering Applications.* Engineering online library, Springer, 2004.

[5] C. Rey, *Superconductors in the Power Grid: Materials and Applications.* Woodhead Publishing Series in Energy, Elsevier Science, 2015.

[6] J. Wang, S. Wang, and P. Press, *High Temperature Superconducting Magnetic Levitation.* De Gruyter, 2017.

[7] L. Rossi, “The lhc superconducting magnets,” vol. 1, pp. 141 – 145 Vol.1, 06 2003.

[8] F. Lackner, M. Duret, T. Jean-Philippe, H. Prin, F. Savary, L. Clement, A. Verweij, S. Triquet, and C. Scheuerlein, “Consolidation of the 13 ka superconducting magnet circuits of the lhc at cern,” *IEEE Transactions on Applied Superconductivity*, vol. 25, pp. 1–1, 01 2014, doi: 10.1109/TASC.2014.2382879.

[9] **Lasek, Pawel and Michalak, Jaroslaw and Stepien, Mariusz**, “**Critical current of HTS 2G tape operating under high-frequency triangular wave current with DC bias**,” pp. 1–4, 2019, doi: 10.1109/PEE.2019.8923527.

[10] M. Tomita and M. Murakami, “High-temperature superconductor bulk magnets that can trap magnetic fields of over 17 tesla at 29 k,” *Nature*, vol. 421, pp. 517–20, 02 2003, doi: 10.1038/nature01350.

[11] J. H. Durrell, A. R. Dennis, J. Jaroszynski, M. D. Ainslie, K. G. B. Palmer, Y.-H. Shi, A. M. Campbell, J. Hull, M. Strasik, E. E. Hellstrom, and D. A. Cardwell, “A trapped field of 17.6 t in melt-processed, bulk gd-ba-cu-o reinforced with shrink-fit steel,” *Superconductor Science and Technology*, vol. 27, p. 082001, jun 2014, doi: 10.1088/0953-2048/27/8/082001, [Online] https://doi.org/10.1088/0953-2048/27/8/082001.

[12] J. Sim, K. Lee, G. Cha, and J.-K. Lee, "Development of a hts squirrel cage induction motor with hts rotor bars," *Applied Superconductivity, IEEE Transactions on*, vol. 14, pp. 916 – 919, 07 2004, doi: 10.1109/TASC.2004.830317.

[13] J.-H. Lee, H.-S. Choi, W. Nah, I. H. Park, J. Kang, J. Joo, J.-K. Byun, Y.-K. Kwon, M.-H. Sohn, and S. Kim, "Maximization of flux-linkage in hts motors using shape design sensitivity analysis with critical current constraint," *Applied Superconductivity, IEEE Transactions on*, vol. 14, pp. 1906 – 1909, 07 2004, doi: 10.1109/TASC.2004.830926.

[14] F. Werfel, U. Floegel-Delor, R. Rothfeld, T. Riedel, B. Goebel, D. Wippich, P. Schirrmeister, and R. Koenig, "Next generation of hts magnetic application: Hts bulk and coil interaction," *Journal of Physics: Conference Series*, vol. 507, p. 032055, 05 2014, doi: 10.1088/1742-6596/507/3/032055.

[15] F. Weng, M. Zhang, T. Lan, Y. Wang, and W. Yuan, "Fully superconducting machine for electric aircraft propulsion: study of AC loss for HTS stator," *Superconductor Science and Technology*, vol. 33, p. 104002, aug 2020, doi: 10.1088/1361-6668/ab9687, [Online] https://doi.org/10.1088/1361-6668/ab9687.

[16] Y. Iwasa, "Hts and nmr/mri magnets: Unique features, opportunities, and challenges," *Physica C: Superconductivity*, vol. 445-448, pp. 1088–1094, 10 2006, doi: 10.1016/j.physc.2006.05.040.

[17] B. Shen, Y. Öztürk, W. Wu, L. Lu, J. Sheng, Z. Huang, Y. Zhai, Y. Yuan, W. Wang, J. Yin, D. Menon, A. Ercole, A. Carpenter, T. Painter, C. Li, J. Gawith, J. Ma, J. Yang, M. Parizh, and T. Coombs, "Development of an hts magnet for ultra-compact mri system: Optimization using genetic algorithm (ga) method," *IEEE Transactions on Applied Superconductivity*, vol. PP, pp. 1–1, 02 2020, doi: 10.1109/TASC.2020.2974417.

[18] O. V. Vakaliuk, M. D. Ainslie, and B. Halbedel, "Lorentz force velocimetry using a bulk HTS magnet system: proof-of-concept," *Superconductor Science and Technology*, vol. 31, p. 084003, jun 2018, doi: 10.1088/1361-6668/aac949, [Online] https://doi.org/10.1088/1361-6668/aac949.

[19] L. Chen, Y. S. Cha, H. Claus, T. R. Askew, H. Zheng, B. W. Veal, and F. Z. Peng, "Demagnetization of trapped field in high t-c superconductors using pulsed field methods," *IEEE Transactions On Applied Superconductivity*, vol. 17, pp. 20–26, 03 2007, doi: 10.1109/TASC.2006.887543.

[20] L. Chen, Y. S. Cha, H. Claus, H. Zheng, B. W. Veal, and F. Z. Peng, "Optimization of pulsed-current profile for magnetizing high t-c bulk ybco superconductors," *IEEE Transactions On Plasma Science*, vol. 34, pp. 1702–1708, 10 2006, doi: 10.1109/TPS.2006.881890.

[21] J. Kapek, K. Berger, M. R. Koblischka, F. Trillaud, and J. Leveque, "2-d numerical modeling of a bulk hts magnetization based on h formulation coupled with electrical circuit," *IEEE Transactions On Applied Superconductivity*, vol. 29, 08 2019, doi: 10.1109/TASC.2019.2897331.

[22] J. Arnaud, J. F. P. Fernandes, and P. J. C. Branco, "Modifying the pulsed-field-magnetization technique for hts bulks in electrical machines without magnetic field sensors," *IEEE Transactions on Applied Superconductivity*, vol. 28, no. 4, pp. 1–4, 2018.

[23] T. Ida, H. Matsuzaki, E. Morita, H. Sakashita, T. Harada, H. Ogata, Y. Kimura, M. Miki, M. Kitano, and M. Izumi, “Pulsed field waveforms for magnetization of hts gd-ba-cu-o bulk magnets,” *7Th European Conference On Applied Superconductivity (Eucas’05)*, vol. 43, pp. 539–542, 2006, doi: 10.1088/1742-6596/43/1/133.

[24] T. Ida, Y. Kimura, T. Sano, K. Yamaguchi, M. Izumi, and M. Miki, “Trapped field measurements of gd-ba-cu-o bulk superconductor in controlled pulse field magnetizing,” *8Th European Conference On Applied Superconductivity (Eucas’07)*, vol. 97, 2008, doi: 10.1088/1742-6596/97/1/012292.

[25] T. Ida, M. Watasaki, Y. Kimura, M. Miki, and M. Izumi, “Trapped magnetic field measurements on hts bulk by peak controlled pulsed field magnetization,” *9Th European Conference On Applied Superconductivity (Eucas 09)*, vol. 234, 2010, doi: 10.1088/1742-6596/234/3/032023.

[26] J. Arnaud, J. F. P. Fernandes, and P. J. C. Branco, “Use of bulk superconductors in the excitation system of low-speed synchronous generators,” *IEEE Transactions On Applied Superconductivity*, vol. 31, 08 2021, doi: 10.1109/TASC.2021.3054721.

[27] A. Szalay, D. Horvath, I. Vajda, A. G. Mamalis, and C. Harnois, “Influence of some metallic additives on the flux trapping ability of high temperature superconducting ceramics,” *Journal Of Materials Processing Technology*, vol. 181, pp. 36–39, 01 2007, doi: 10.1016/j.jmatprotec.2006.03.050.

[28] H. Fujishiro, H. Mochizuki, M. D. Ainslie, and T. Naito, “Trapped field of 1.1t without flux jumps in an mgb2 bulk during pulsed field magnetization using a split coil with a soft iron yoke,” *Superconductor Science & Technology*, vol. 29, 08 2016, doi: 10.1088/0953-2048/29/8/084001.

[29] C. Yun, K. Ri, and K. Mun, “The study of trapped field, mechanical stress, and internal temperature distribution during pulsed field magnetization of the bulk superconductors with giant field leaps,” *Journal Of Superconductivity And Novel Magnetism*, vol. 33, pp. 3727–3734, 12 2020, doi: 10.1007/s10948-020-05664-2.

[30] T. Ida, Z. Li, M. Miki, M. Watasaki, and M. Izumi, “Waveform control pulse magnetization for hts bulk with flux jump,” *IEEE Transactions on Applied Superconductivity*, vol. PP, pp. 1–1, 03 2018, doi: 10.1109/TASC.2018.2816099.

[31] T. Hirano, Y. Takahashi, S. Namba, T. Naito, and H. Fujishiro, “A record-high trapped field of 1.61 t in mgb2 bulk comprised of copper plates and soft iron yoke cylinder using pulsed-field magnetization,” *Superconductor Science & Technology*, vol. 33, 08 2020, doi: 10.1088/1361-6668/ab9542.

[32] M. D. Ainslie, J. Srpcic, D. Zhou, H. Fujishiro, K. Takahashi, D. A. Cardwell, and J. H. Durrell, “Toward optimization of multi-pulse, pulsed field magnetization of bulk high-temperature superconductors,” *IEEE Transactions On Applied Superconductivity*, vol. 28, 06 2018, doi: 10.1109/TASC.2017.2788924.

[33] K. Yokoyama and T. Oka, “Improvement of trapped magnetic field of a rebco bulk magnet activated by pulsed field magnetization in a high-cooling power two-stage gm-type refrigerator,” *IEEE Transactions On Applied Superconductivity*, vol. 29, 08 2019, doi: 10.1109/TASC.2019.2897481.

[34] H. Fujishiro, T. Hiyama, T. Tateiwa, Y. Yanagi, and T. Oka, “Importance of initial m-shaped trapped field profile in a two-stage pulse field magnetization (mmpsc) method,” *Physica C-Superconductivity And Its Applications*, vol. 463, pp. 394–397, 10 2007, doi: 10.1016/j.physc.2007.03.440.

[35] H. Fujishiro, T. Hiyama, T. Naito, T. Tateiwa, and Y. Yanagi, “Possible explanation for trapped field enhancement on rebacuo bulk by modified multi-pulse technique with stepwise cooling (mmpsc),” *Materials Science And Engineering B-Advanced Functional Solid-State Materials*, vol. 151, pp. 95–100, 06 2008, doi: 10.1016/j.mseb.2008.03.010.

[36] H. Fujishiro, T. Tateiwa, and T. Hiyama, “Enhancement of trapped field and total trapped flux on high temperature bulk superconductor by a new pulse-field magnetization method,” *Japanese Journal Of Applied Physics Part 1-Regular Papers Brief Communications & Review Papers*, vol. 46, pp. 4108–4112, 07 2007, doi: 10.1143/JJAP.46.4108.

[37] H. Fujishiro, T. Tateiwa, K. Kakehata, T. Hiyama, and T. Naito, “Trapped field and temperature rise on a phi 65 mm gdbacuo bulk by pulse field magnetization,” *Superconductor Science & Technology*, vol. 20, pp. 1009–1014, 10 2007, doi: 10.1088/0953-2048/20/10/020.

[38] H. Fujishiro, T. Hiyama, T. Miura, T. Naito, S. Nariki, N. Sakai, and I. Hirabayashi, “Pulsed field magnetization for gdbacuo bulk with stronger pinning characteristics,” *IEEE Transactions On Applied Superconductivity*, vol. 19, pp. 3545–3548, 06 2009, doi: 10.1109/TASC.2009.2018081.

[39] E. Morita, H. Matsuzaki, Y. Kimura, I. Ohtani, H. Ogata, M. Izumi, Y. Nonaka, M. Murakami, T. Ida, H. Sugimoto, M. Miki, and M. Kitano, “Study of single pulsed-field magnetization of gd–ba–cu–o bulk high-temperature superconductor with a split type of armature coil for rotating machinery,” *Superconductor Science and Technology*, vol. 19, pp. S486–S490, apr 2006, doi: 10.1088/0953-2048/19/7/s12, [Online] https://doi.org/10.1088

[40] K. Takahashi, M. D. Ainslie, H. Fujishiro, and T. Naito, “Pulsed-field magnetizing characteristics of rectangular-shaped gd–ba–cu–o bulk using split- and solenoid-type coils,” *IEEE Transactions on Applied Superconductivity*, vol. 27, no. 4, pp. 1–5, 2017, doi: 10.1109/TASC.2016.2625764.

[41] K. Takahashi, M. D. Ainslie, H. Fujishiro, T. Naito, Y.-H. Shi, and D. A. Cardwell, “Trapped field properties of a y-ba-cu-o bulk by pulsed field magnetization using a split coil inserted by iron yokes with various geometries and electromagnetic properties,” *Physica C-Superconductivity And Its Applications*, vol. 536, pp. 1–10, 05 2017, doi: 10.1016/j.physc.2017.03.005.

[42] M. D. Ainslie, H. Fujishiro, H. Mochizuki, K. Takahashi, Y.-H. Shi, D. K. Namburi, J. Zou, D. Zhou, A. R. Dennis, and D. A. Cardwell, “Enhanced trapped field performance of bulk high-temperature superconductors using split coil, pulsed field magnetization with an iron yoke,” *Superconductor Science & Technology*, vol. 29, 07 2016, doi: 10.1088/0953-2048/29/7/074003.

[43] K. Yokoyama and T. Oka, “Influence of the shape of soft-iron yoke on trapped field performance of hts bulk,” *IEEE Transactions On Applied Superconductivity*, vol. 30, 06 2020, doi: 10.1109/TASC.2020.2976064.

[44] H. Fujishiro, T. Naito, and M. Oyama, “Size effect of magnetizing solenoid coil for pulsed field magnetization on the trapped field on superconducting bulk,” *IEEE Transactions On Applied Superconductivity*, vol. 22, 06 2012, doi: 10.1109/TASC.2011.2178381.

[45] E. Morita, H. Matsuzaki, Y. Kimura, I. Ohtani, M. Izumi, Y. Nonaka, M. Murakami, T. Ida, H. Sugimoto, M. Miki, and M. Kitano, “Single pulsed-field magnetization on gd-ba-cu-o bulk hts assembled for axial-gap type rotating machines,” *7Th European Conference On Applied Superconductivity (Eucas’05)*, vol. 43, pp. 796–799, 2006, doi: 10.1088/1742-6596/43/1/194.

[46] Z. Xu, R. Lewin, A. M. Campbell, D. A. Cardwell, and H. Jones, “Simulation studies on the magnetization of (re)bco bulk superconductors using various split-coil arrangements,” *Superconductor Science & Technology*, vol. 25, 02 2012, doi: 10.1088/0953-2048/25/2/025016.

[47] Y. Kimura, K. Yamaguchi, T. Sano, D. Sugyo, M. Izumi, T. Ida, S. Nariki, N. Sakai, I. Hirabayashi, and M. Miki, “Practical technique of pulsed field magnetization for bulk hts application,” *8Th European Conference On Applied Superconductivity (Eucas’07)*, vol. 97, 2008, doi: 10.1088/1742-6596/97/1/012295.

[48] E. Morita, H. Matsuzaki, Y. Kimura, I. Ohtani, H. Ogata, M. Izumi, Y. Nonaka, M. Murakami, T. Ida, H. Sugimoto, M. Miki, and M. Kitano, “Study of single pulsed-field magnetization of gd-ba-cu-o bulk high-temperature superconductor with a split type of armature coil for rotating machinery,” *Superconductor Science & Technology*, vol. 19, pp. S486–S490, 07 2006, doi: 10.1088/0953-2048/19/7/S12.

[49] Z. Deng, N. Shinohara, M. Miki, B. Felder, K. Tsuzuki, M. Watasaki, S. Kawabe, R. Taguchi, and M. Izumi, “Pulsed-field magnetization properties of bulk superconductors by employment of vortex-type coils,” *Superconductivity Centennial Conference 2011*, vol. 36, pp. 958–962, 2012, doi: 10.1016/j.phpro.2012.06.088.

[50] Y. Kimura, H. Matsumoto, H. Fukai, N. Sakai, I. Hirabayashi, M. Izumi, and M. Murakami, “Improvement of thermal stability with alloy impregnation in gd-ba-cu-o superconductors for pulsed field magnetization,” *7Th European Conference On Applied Superconductivity (Eucas’05)*, vol. 43, pp. 389–392, 2006, doi: 10.1088/1742-6596/43/1/097.

[51] E. Morita, H. Matsuzaki, Y. Kimura, H. Ogata, M. Izumi, T. Ida, M. Murakami, H. Sugimoto, and M. Miki, “Study of a new split-type magnetizing coil and pulsed field magnetization of gd-ba-cu-o high-temperature superconducting bulk for rotating machinery application,” *Superconductor Science & Technology*, vol. 19, pp. 1259–1263, 12 2006, doi: 10.1088/0953-2048/19/12/006.

[52] H. Fujishiro, T. Tateiwa, K. Kakehata, T. Hiyama, T. Naito, and Y. Yanagi, “Trapped field characteristics on phi 65 mm gdbacuo bulk by modified multi-pulse technique with stepwise cooling (mmpsc),” *Physica C-Superconductivity And Its Applications*, vol. 468, pp. 1477–1480, 09 2008, doi: 10.1016/j.physc.2008.05.142.

[53] R. Taguchi, K. Yamaguchi, Y. Kimura, M. Miki, K. Tsuzuki, T. Ida, and M. Izumi, "Characterization of pinning stability of hts gd123 bulks by using a pulsed-field magnetization," *9Th European Conference On Applied Superconductivity (Eucas 09)*, vol. 234, 2010, doi: 10.1088/1742-6596/234/1/012042.

[54] H. Fujishiro, T. Arayashiki, T. Tamura, T. Naito, H. Teshima, and M. Morita, "Trapped field profiles on square gdbacuo bulks with different arrangement of growth sector boundaries," *Japanese Journal Of Applied Physics*, vol. 51, 09 2012, doi: 10.1143/JJAP.51.093005.

[55] M. L. Khene, L. Alloui, F. Bouillault, A. K. Ntichi, S. M. Mimoune, and M. Feliachi, "3-d numerical evaluation of trapped magnetic field and temperature of a rectangular gdbacuo bulk magnetized by mmpsc method," *IEEE Transactions On Magnetics*, vol. 51, 03 2015, doi: 10.1109/TMAG.2014.2360839.

[56] K. Takahashi, M. D. Ainslie, H. Fujishiro, and T. Naito, "Pulsed-field magnetizing characteristics of rectangular-shaped gd-ba-cu-o bulk using split-and solenoid-type coils," *IEEE Transactions On Applied Superconductivity*, vol. 27, 06 2017, doi: 10.1109/TASC.2016.2625764.

[57] Y. Ru, H. Yong, and Y. Zhou, "Numerical simulation of dynamic fracture behavior in bulk superconductors with an electromagnetic-thermal model," *Superconductor Science & Technology*, vol. 32, 07 2019, doi: 10.1088/1361-6668/ab0e93.

[58] T. Hirano, H. Fujishiro, T. Naito, M. D. Ainslie, and Y.-H. Shi, "Flux dynamics and thermal behavior of a gdbacuo bulk magnetized by single- and double-pulse techniques using a split-type coil," *IEEE Transactions On Applied Superconductivity*, vol. 29, 08 2019, doi: 10.1109/TASC.2019.2900979.

[59] F. Shimoyashiki, H. Fujishiro, T. Naito, and M. D. Ainslie, "Trapped field properties of gdbacuo bulk superconductors of various diameters magnetized by pulsed fields using an identical split coil," *IEEE Transactions On Applied Superconductivity*, vol. 29, 08 2019, doi: 10.1109/TASC.2019.2901349.

[60] G. Giunchi, E. Perini, T. Cavallin, R. Quarantiello, V. Cavaliere, and A. Matrone, "Persistent magnetization of mgb2 cylinders induced by a pulsed field," *Advances In Cryogenic Engineering, Vols 53A And 53B*, vol. 985, pp. 1007–+, 2008.

[61] H. Fujishiro, T. Tamura, T. Arayashiki, M. Oyama, T. Sasaki, T. Naito, G. Giunchi, and A. F. Albisetti, "Pulsed field magnetization of large mgb2 bulk fabricated by reactive liquid mg infiltration," *Japanese Journal Of Applied Physics*, vol. 51, 10 2012, doi: 10.1143/JJAP.51.103005.

[62] A. Patel, S. C. Hopkins, G. Giunchi, A. F. Albisetti, Y. Shi, R. Palka, D. A. Cardwell, and B. A. Glowacki, "The use of an mgb2 hollow cylinder and pulse magnetized (re)bco bulk for magnetic levitation applications," *IEEE Transactions On Applied Superconductivity*, vol. 23, 06 2013, doi: 10.1109/TASC.2012.2236143.

[63] H. Fujishiro, T. Naito, M. Oyama, T. Arayashiki, T. Tamura, T. Sasaki, and G. Giunchi, "Numerical simulation of trapped field and temperature rise in mgb2 bulks magnetized by pulsed field," *IEEE Transactions On Applied Superconductivity*, vol. 23, 06 2013, doi: 10.1109/TASC.2012.2237224.

[64] T. Ujiie, T. Naito, H. Fujishiro, A. F. Albisetti, and G. Giunchi, “Shielding and trapped field properties of large mgb2 bulk,” *Proceedings Of The 26Th International Symposium On Superconductivity (Iss 2013)*, vol. 58, pp. 306–309, 2014, doi: 10.1016/j.phpro.2014.09.076.

[65] H. Fujishiro, T. Naito, T. Ujiie, A. F. Albisetti, and G. Giunchi, “Trapped field and flux dynamics in mgb2 superconducting bulks magnetized by pulsed field,” *Proceedings Of The 26Th International Symposium On Superconductivity (Iss 2013)*, vol. 58, pp. 286–289, 2014, doi: 10.1016/j.phpro.2014.09.054.

[66] H. Fujishiro, T. Ujiie, T. Naito, A. F. Albisetti, and G. Giunchi, “Trapped magnetic field between double stacked mgb2 bulks magnetized by pulsed field,” *11Th European Conference On Applied Superconductivity (Eucas2013), Pts 1-4*, vol. 507, 2014, doi: 10.1088/1742-6596/507/3/032016.

[67] H. Fujishiro, T. Ujiie, H. Mochizuki, T. Yoshida, and T. Naito, “Recent progress of mgb2 bulk magnets magnetized by pulsed field,” *IEEE Transactions On Applied Superconductivity*, vol. 25, 06 2015, doi: 10.1109/TASC.2014.2359544.

[68] H. Mochizuki, H. Fujishiro, T. Naito, A. F. Albisetti, and G. Giunchi, “Trapped field properties of a concentric-circled mgb2 bulk composite magnetized by pulsed field and field cooling,” *Superconductor Science & Technology*, vol. 28, 10 2015, doi: 10.1088/0953-2048/28/10/105004.

[69] T. Naito, H. Mochizuki, H. Fujishiro, and H. Teshima, “Trapped magnetic-field properties of prototype for gd-ba-cu-o/mgb2 hybrid-type superconducting bulk magnet,” *Superconductor Science & Technology*, vol. 29, 03 2016, doi: 10.1088/0953-2048/29/3/034005.

[70] H. Fujishiro, H. Mochizuki, T. Naito, M. D. Ainslie, and G. Giunchi, “Flux jumps in high-j(c) mgb2 bulks during pulsed field magnetization,” *Superconductor Science & Technology*, vol. 29, 03 2016, doi: 10.1088/0953-2048/29/3/034006.

[71] T. Miyazaki, S. Fukui, J. Ogawa, T. Sato, T. Oka, J. Scheiter, W. Haessler, E. Kulawansha, Z. Yuanding, and K. Yokoyama, “Pulse-field magnetization for disc-shaped mgb2 bulk magnets,” *IEEE Transactions On Applied Superconductivity*, vol. 27, 06 2017, doi: 10.1109/TASC.2016.2639298.

[72] H. Fujishiro, K. Takahashi, M. D. Ainslie, H. Mochizuki, and T. Naito, “Trapped field enhancement of a thin, high-j(c) mgb2 bulk without flux jumps using pulsed field magnetization with a split-type coil with a soft iron yoke,” *IEEE Transactions On Applied Superconductivity*, vol. 27, 06 2017, doi: 10.1109/TASC.2016.2637363.

[73] T. Oka, A. Takeda, S. Sasaki, J. Ogawa, S. Fukui, T. Sato, J. Scheiter, W. Haessler, J. Katsuki, A. Miura, and K. Yokoyama, “Magnetic flux invasion and field-capturing in pulsed-field magnetization for layered mgb2 bulk magnets,” *IEEE Transactions On Applied Superconductivity*, vol. 28, 06 2018, doi: 10.1109/TASC.2018.2792530.

[74] K. Yokoyama, T. Oka, K. Berger, R. Dorget, M. Koblischka, M. Grigoroscuta, M. Burdusel, D. Batalu, G. Aldica, P. Badica, N. Sakai, M. Muralidhar, and M. Murakami, “Investigation of flux jumps during pulsed field magnetization in graphene-added mgb2 bulks,” *14Th European Conference On Applied Superconductivity (Eucas2019)*, vol. 1559, 2020, doi: 10.1088/1742-6596/1559/1/012080.

[75] N. Sakai, T. Oka, K. Yamanaka, L. Dadiel, H. Oki, J. Ogawa, S. Fukui, J. Scheiter, W. Haessler, K. Yokoyama, J. Noudem, M. Miryala, and M. Murakami, “Occurrence of flux jumps in mgb2 bulk magnets during pulse-field magnetization,” *14Th European Conference On Applied Superconductivity (Eucas2019)*, vol. 1559, 2020, doi: 10.1088/1742-6596/1559/1/012024.

[76] K. Berger, J. Leveque, D. Netter, B. Douine, and A. Rezzoug, “Influence of temperature and/or field dependences of the e-j power law on trapped magnetic field in bulk ybacuo,” *IEEE Transactions On Applied Superconductivity*, vol. 17, pp. 3028–3031, 06 2007, doi: 10.1109/TASC.2007.902095.

[77] X. Chaud, E. Haanappel, J. G. Noudem, and D. Horvath, “Trapped field of ybco single-domain samples using pulse magnetization from 77k to 20k,” *8Th European Conference On Applied Superconductivity (Eucas’07)*, vol. 97, 2008, doi: 10.1088/1742-6596/97/1/012047.

[78] A. A. Kartamyshev, E. P. Krasnoperov, Y. D. Kuroedov, O. L. Polushchenko, and N. A. Nizhelskiy, “Magnetic flux relaxation in a pulse-magnetized y-ba-cu-o superconductor,” *Technical Physics Letters*, vol. 35, pp. 796–799, 09 2009, doi: 10.1134/S1063785009090041.

[79] Z. Deng, M. Izumi, M. Miki, K. Tsuzuki, B. Felder, W. Liu, J. Zheng, S. Wang, J. Wang, U. Floegel-Delor, and F. N. Werfel, “Trapped flux and levitation properties of multiseeded ybco bulks for hts magnetic device applications-part ii: Practical and achievable performance,” *IEEE Transactions On Applied Superconductivity*, vol. 22, 04 2012, doi: 10.1109/TASC.2011.2172436.

[80] J. Zou, M. D. Ainslie, D. Hu, W. Zhai, N. D. Kumar, J. H. Durrell, Y.-H. Shi, and D. A. Cardwell, “Numerical simulation and analysis of single grain ybco processed from graded precursor powders,” *Superconductor Science & Technology*, vol. 28, 03 2015, doi: 10.1088/0953-2048/28/3/035016.

[81] D. K. Namburi, K. Takahashi, T. Hirano, T. Kamada, H. Fujishiro, Y.-H. Shi, D. A. Cardwell, J. H. Durrell, and M. D. Ainslie, “Pulsed-field magnetisation of y-ba-cu-o bulk superconductors fabricated by the infiltration growth technique,” *Superconductor Science & Technology*, vol. 33, 11 2020, doi: 10.1088/1361-6668/abb590.

[82] A. Baskys, A. Patel, S. C. Hopkins, V. Kalitka, A. Molodyk, and B. A. Glowacki, “Self-supporting stacks of commercial superconducting tape trapping fields up to 1.6 t using pulsed field magnetization,” *IEEE Transactions On Applied Superconductivity*, vol. 25, 06 2015, doi: 10.1109/TASC.2014.2360871.

[83] A. G. Page, A. Patel, A. Baskys, S. C. Hopkins, V. Kalitka, A. Molodyk, and B. A. Glowacki, “The effect of stabilizer on the trapped field of stacks of superconducting tape magnetized by a pulsed field,” *Superconductor Science & Technology*, vol. 28, 08 2015, doi: 10.1088/0953-2048/28/8/085009.

[84] S. Zou, V. M. R. Zermeño, and F. Grilli, “Simulation of stacks of high-temperature superconducting coated conductors magnetized by pulsed field magnetization using controlled magnetic density distribution coils,” *IEEE Transactions on Applied Superconductivity*, vol. 26, no. 3, pp. 1–5, 2016, doi: 10.1109/TASC.2016.2520210.

[85] S. Zou, V. M. R. Zermeno, A. Baskys, A. Patel, F. Grilli, and B. A. Glowacki, "Simulation and experiments of stacks of high temperature superconducting coated conductors magnetized by pulsed field magnetization with multi-pulse technique," *Superconductor Science & Technology*, vol. 30, 01 2017, doi: 10.1088/0953-2048/30/1/014010.

[86] L. Hao, Z. Huang, F. Dong, D. Qiu, and Z. Jin, "A novel hybrid magnet made of hts tape stacks and permanent magnets for motor applications," *IEEE Transactions On Applied Superconductivity*, vol. 29, 08 2019, doi: 10.1109/TASC.2019.2899151.

[87] I. M. Harca, K. Machaj, L. Tomkow, and B. A. Glowacki, "Magnetic flux in stacks of superconducting tapes of different architecture," *Superconductor Science & Technology*, vol. 33, 11 2020, doi: 10.1088/1361-6668/abb11c.

[88] B. Cohen, "The world's strongest permanent magnet (neodymium-iron-boron): A chemical perspective.," 10 2019.

[89] H. Ikuta, A. Mase, Y. Yanagi, M. Yoshikawa, Y. Itoh, T. Oka, and U. Mizutani, "Melt-processed sm - ba - cu - o superconductors trapping strong magnetic field," *Superconductor Science and Technology*, vol. 11, pp. 1345–1347, nov 1998, doi: 10.1088/0953-2048/11/11/001, [Online] https://doi.org/10.1088/0953-2048/11/11/001.

[90] H. Fujishiro, T. Tateiwa, A. Fujiwara, T. Oka, and H. Hayashi, "Higher trapped field over 5t on htsc bulk by modified pulse field magnetizing," *Physica C: Superconductivity*, vol. 445-448, pp. 334–338, 10 2006, doi: 10.1016/j.physc.2006.04.077.

[91] D. Zhou, M. D. Ainslie, Y. Shi, A. R. Dennis, K. Huang, J. R. Hull, D. A. Cardwell, and J. H. Durrell, "A portable magnetic field of >3 t generated by the flux jump assisted, pulsed field magnetization of bulk superconductors," *Applied Physics Letters*, vol. 110, no. 6, p. 062601, 2017, doi: 10.1063/1.4973991.

[92] A. Baskys, K. Filar, A. Patel, and B. Glowacki, "A trapped field of 13.4 t in a stack of hts tapes with 30 um substrate," *arXiv*, 2017.

[93] A. Patel, A. Baskys, T. Mitchell-Williams, A. McCaul, W. Coniglio, J. Hanisch, M. Lao, and B. A. Glowacki, "A trapped field of 17.7 t in a stack of high temperature superconducting tape," *Superconductor Science and Technology*, vol. 31, no. 9, p. 09LT01, 2018.

[94] D. Zhou, M. D. Ainslie, J. Srpcic, K. Huang, Y. Shi, A. R. Dennis, D. A. Cardwell, J. H. Durrell, M. Boll, and M. Filipenko, "Exploiting flux jumps for pulsed field magnetisation," *Superconductor Science & Technology*, vol. 31, 10 2018, doi: 10.1088/1361-6668/aad786.

[95] Z. Deng, M. Miki, K. Tsuzuki, B. Felder, R. Taguchi, N. Shinohara, and M. Izumi, "Pulsed field magnetization properties of bulk re-ba-cu-o as pole-field magnets for hts rotating machines," *IEEE Transactions On Applied Superconductivity*, vol. 21, pp. 1180–1184, 06 2011, doi: 10.1109/TASC.2010.2085071.

[96] M. D. Ainslie, J. Zou, H. Mochizuki, H. Fujishiro, Y.-H. Shi, A. R. Dennis, and D. A. Cardwell, "Pulsed field magnetization of 0 degrees-0 degrees and 45 degrees-45 degrees bridge-seeded y-ba-cu-o bulk superconductors," *Superconductor Science & Technology*, vol. 28, 12 2015, doi: 10.1088/0953-2048/28/12/125002.

[97] Y. Kimura, H. Matsuzaki, I. Ohtani, E. Morita, M. Izumi, N. Sakai, I. Hirabayashi, M. Miki, M. Kitano, and T. Ida, “Recovery of trapped field distribution around a growth sector in a gd-ba-cu-ohts bulk with pulsed-field magnetization,” *Superconductor Science & Technology*, vol. 19, pp. S466–S471, 07 2006, doi: 10.1088/0953-2048/19/7/S09.

[98] Y. Komi, M. Sekino, and H. Ohsaki, “Three-dimensional numerical analysis of magnetic and thermal fields during pulsed field magnetization of bulk superconductors with inhomogeneous superconducting properties,” *Physica C-Superconductivity And Its Applications*, vol. 469, pp. 1262–1265, 08 2009, doi: 10.1016/j.physc.2009.05.121.

[99] M. D. Ainslie, H. Fujishiro, T. Ujiie, J. Zou, A. R. Dennis, Y.-H. Shi, and D. A. Cardwell, “Modelling and comparison of trapped fields in (re)bco bulk superconductors for activation using pulsed field magnetization,” *Superconductor Science & Technology*, vol. 27, 06 2014, doi: 10.1088/0953-2048/27/6/065008.

[100] R. Weinstein, D. Parks, R.-P. Sawh, K. Carpenter, and K. Davey, “Anomalous results observed in magnetization of bulk high temperature superconductors-a windfall for applications,” *Journal Of Applied Physics*, vol. 119, 04 2016, doi: 10.1063/1.4945018.

[101] T. Oka, A. Takeda, H. Oki, K. Yamanaka, L. Dadiel, K. Yokoyama, W. Haessler, J. Scheiter, N. Sakai, and M. Murakami, “Magnetic flux trapping and flux jumps in pulsed field magnetizing processes in rebco and mg-b bulk magnets,” *32Nd International Symposium On Superconductivity (Iss2019)*, vol. 1590, 2020, doi: 10.1088/1742-6596/1590/1/012025.

[102] B. Felder, M. Miki, K. Tsuzuki, M. Izumi, and H. Hayakawa, “Optimization of a condensed-neon cooling system for a hts synchronous motor with gd-bulk hts field-pole magnets,” *9Th European Conference On Applied Superconductivity (Eucas 09)*, vol. 234, 2010, doi: 10.1088/1742-6596/234/3/032009.

[103] M. s. Kim, J. Jang, Y. J. Hwang, and Y. Choi, “Performance evaluation of current leads for a 5 tesla electromagnetic properties measurement system,” *Applied Sciences*, vol. 10, p. 6712, 09 2020, doi: 10.3390/app10196712.

[104] Y. Shirai, M. Shiotsu, H. Tatsumoto, H. Kobayashi, Y. Naruo, S. Nonaka, and Y. Inatani, “Critical current test of liquid hydrogen cooled htc superconductors under external magnetic field,” *Physics Procedia*, vol. 81, pp. 158–161, 12 2016, doi: 10.1016/j.phpro.2016.04.040.

[105] K. Yokoyama, A. Katsuki, A. Miura, and T. Oka, “Comparison of trapped field characteristic of bulk magnet system using various type refrigerators,” *30Th International Symposium On Superconductivity (Iss2017)*, vol. 1054, 2018, doi: 10.1088/1742-6596/1054/1/012072.

[106] K. Yokoyama, A. Katsuki, A. Miura, and T. Oka, “Comparison of magnetizing characteristics of superconducting bulk magnet cooled by stirling and gm refrigerators during pulsed field magnetization,” *IEEE Transactions On Applied Superconductivity*, vol. 28, 06 2018, doi: 10.1109/TASC.2018.2791993.

[107] L. Prigozhin, “Analysis of critical-state problems in type-ii superconductivity,” *IEEE Transactions on Applied Superconductivity*, vol. 7, no. 4, pp. 3866–3873, 1997, doi: 10.1109/77.659440.

[108] G. Barnes, M. McCulloch, and D. Dew-Hughes, “Computer modelling of type II superconductors in applications,” *Superconductor Science and Technology*, vol. 12, no. 8, pp. 518–522, 1999, doi: 10.1088/0953-2048/12/8/308.

[109] S. Stavrev, F. Grilli, B. Dutoit, N. Nibbio, E. Vinot, I. Klutsch, G. Meunier, P. Tixador, Yifeng Yang, and E. Martinez, “Comparison of numerical methods for modeling of superconductors,” *IEEE Transactions on Magnetics*, vol. 38, no. 2, pp. 849–852, 2002, doi: 10.1109/20.996219.

[110] A. M. Campbell, “A direct method for obtaining the critical state in two and three dimensions,” *Superconductor Science and Technology*, vol. 22, p. 034005, jan 2009, doi: 10.1088/0953-2048/22/3/034005, [Online] https://doi.org/10.1088

[111] L. Dupré and G. Crevecoeur, “A fast algorithm for calculating the critical state in superconductors,” *COMPEL - The International Journal for Computation and Mathematics in Electrical and Electronic Engineering*, vol. 33, no. 3, 2014, doi: 10.1108/COMPEL-10-2013-0333.

[112] M. D. Ainslie and H. Fujishiro, “Modelling of bulk superconductor magnetization,” *Superconductor Science and Technology*, vol. 28, p. 053002, mar 2015, doi: 10.1088/0953-2048/28/5/053002, [Online] https://doi.org/10.1088

[113] N. Amemiya, K. Miyamoto, N. Banno, and O. Tsukamoto, “Numerical analysis of ac losses in high t/sub c/ superconductors based on e-j characteristics represented with n-value,” *IEEE Transactions on Applied Superconductivity*, vol. 7, no. 2, pp. 2110–2113, 1997, doi: 10.1109/77.621008.

[114] N. Amemiya, K. Miyamoto, S. ichi Murasawa, H. Mukai, and K. Ohmatsu, “Finite element analysis of ac loss in non-twisted bi-2223 tape carrying ac transport current and/or exposed to dc or ac external magnetic field,” *Physica C: Superconductivity*, vol. 310, no. 1, pp. 30 – 35, 1998, doi: 10.1016/S0921-4534(98)00428-6.

[115] N. Amemiya, S. I. Murasawa, N. Banno, and K. Miyamoto, “Numerical modelings of superconducting wires for AC loss calculations,” *Physica C: Superconductivity and its Applications*, vol. 310, no. 1-4, pp. 16–29, 1998, doi: 10.1016/S0921-4534(98)00427-4.

[116] N. Banno and N. Amemiya, “Numerical analysis of ac loss in high t/sub c/ twisted tape carrying ac transport current in external ac magnetic field. effect of twisting on loss reduction,” *IEEE Transactions on Applied Superconductivity*, vol. 9, no. 2, pp. 2561–2564, 1999, doi: 10.1109/77.785009.

[117] G. Meunier, Y. Le Floch, and C. Guérin, “A nonlinear circuit coupled t - t0 - ϕ formulation for solid conductors,” *IEEE Transactions on Magnetics*, vol. 39, no. 3 I, pp. 1729–1732, 2003, doi: 10.1109/TMAG.2003.810200.

[118] J. K. Sykulski, R. L. Stoll, A. E. Mahdi, and C. P. Please, “Modelling htc superconductors for ac power loss estimation,” *IEEE Transactions on Magnetics*, vol. 33, no. 2, pp. 1568–1571, 1997, doi: 10.1109/20.582565.

[119] S. R. Sykulski J.K., Rotaru M., “Highly non-linear field diffusion in htc superconducting tapes,” *COMPEL - The international journal for computation and mathematics in electrical and electronic engineering*, vol. 18, no. 2, pp. 215–224, 1999, doi: 10.1108/03321649910264217.

[120] J. K. Sykulski, M. Rotaru, and R. L. Stoll, “2d modeling of field diffusion and ac losses in high temperature superconducting tapes,” *IEEE Transactions on Magnetics*, vol. 36, no. 4, pp. 1178–1182, 2000, doi: 10.1109/20.877650.

[121] E. Vinot, G. Meunier, and P. Tixador, “Different formulations to model superconductors,” *IEEE Transactions on Magnetics*, vol. 36, no. 4 PART 1, pp. 1222–1225, 2000, doi: 10.1109/20.877661.

[122] F. Grilli, V. Zermeno, M. Vojenciak, E. Pardo, A. Kario, and W. Goldacker, “AC losses of pancake coils made of roebel cable,” *IEEE Transactions on Applied Superconductivity*, vol. 23, no. 3, pp. 0–4, 2013, doi: 10.1109/TASC.2013.2238987.

[123] F. Sass, G. G. Sotelo, R. de Andrade Junior, and F. Sirois, “H-formulation for simulating levitation forces acting on HTS bulks and stacks of 2G coated conductors,” *Superconductor Science and Technology*, vol. 28, no. 12, 2015, doi: 10.1088/0953-2048/28/12/125012.

[124] J. Xia and Y. Zhou, “Numerical simulations of electromagnetic behavior and AC loss in rectangular bulk superconductor with an elliptical flaw under AC magnetic fields,” *Cryogenics*, vol. 69, pp. 1–9, 2015, doi: 10.1016/j.cryogenics.2015.02.003, [Online] http://dx.doi.org/10.1016/j.cryogenics.2015.02.003.

[125] M. Zhang, W. Yuan, J. Kvitkovic, and S. Pamidi, “Total AC loss study of 2G HTS coils for fully HTS machine applications,” *Superconductor Science and Technology*, vol. 28, no. 11, p. 115011, 2015, doi: 10.1088/0953-2048/28/11/115011, [Online] http://dx.doi.org/10.1088/0953-2048/28/11/115011.

[126] K. Ozturk, M. Kabaer, M. Abdioglu, A. Patel, and A. Cansiz, “Clarification of magnetic levitation force and stability property of multi-seeded YBCO in point of supercurrent coupling effect,” *Journal of Alloys and Compounds*, vol. 689, pp. 1076–1082, 2016, doi: 10.1016/j.jallcom.2016.08.069, [Online] http://dx.doi.org/10.1016/j.jallcom.2016.08.069.

[127] M. D. Ainslie, D. Zhou, H. Fujishiro, K. Takahashi, Y.-H. Shi, and J. H. Durrell, “Flux jump-assisted pulsed field magnetisation of high-jcbulk high-temperature superconductors,” *Superconductor Science and Technology*, vol. 29, p. 124004, oct 2016, doi: 10.1088/0953-2048/29/12/124004, [Online] https://doi.org/10.1088

[128] S. Zou, V. Zermeno, and F. Grilli, “Influence of parameters on the simulation of hts bulks magnetized by pulsed field magnetization,” *IEEE Transactions on Applied Superconductivity*, vol. 26, pp. 1–1, 06 2016, doi: 10.1109/TASC.2016.2535379.

[129] A. Patel, S. Hahn, J. Voccio, A. Baskys, S. C. Hopkins, and B. A. Glowacki, “Magnetic levitation using a stack of high temperature superconducting tape annuli,” *Superconductor Science and Technology*, vol. 30, no. 2, 2017, doi: 10.1088/1361-6668/30/2/024007.

[130] K. Hogan, J. F. Fagnard, L. Wéra, B. Vanderheyden, and P. Vanderbemden, “Bulk superconducting tube subjected to the stray magnetic field of a solenoid,” *Superconductor Science and Technology*, vol. 31, no. 1, 2018, doi: 10.1088/1361-6668/aa9651.

[131] R. Brambilla, F. Grilli, L. Martini, M. Bocchi, and G. Angeli, “A Finite-Element Method Framework for Modeling Rotating Machines with Superconducting Windings,” *IEEE Transactions on Applied Superconductivity*, vol. 28, no. 5, pp. 1–11, 2018, doi: 10.1109/TASC.2018.2812884.

[132] L. Quéval, K. Liu, W. Yang, V. M. Zermeño, and G. Ma, “Superconducting magnetic bearings simulation using an H-formulation finite element model,” *Superconductor Science and Technology*, vol. 31, no. 8, 2018, doi: 10.1088/1361-6668/aac55d.

[133] J. Geng and T. A. Coombs, “Modeling methodology for a HTS flux pump using a 2D H-formulation,” *Superconductor Science and Technology*, vol. 31, no. 12, 2018, doi: 10.1088/1361-6668/aae4bc.

[134] A. Patel and B. A. Glowacki, “Enhanced trapped field achieved in a superconducting bulk using high thermal conductivity structures following simulated pulsed field magnetization,” *Superconductor Science & Technology*, vol. 25, 12 2012, doi: 10.1088/0953-2048/25/12/125015.

[135] A. Baskys, A. Patel, S. Hopkins, D. Kenfaui, X. Chaud, M. Zhang, and B. A. Glowacki, “Composite superconducting bulks for efficient heat dissipation during pulse magnetization,” *11Th European Conference On Applied Superconductivity (Eucas2013), Pts 1-4*, vol. 507, 2014, doi: 10.1088/1742-6596/507/1/012003.

[136] W. J. Yang, Z. Y. Fu, L. Yu, M. Ye, H. B. Tang, and Y. Liu, “Simulation of pulse field magnetization of a bulk superconductor and its interaction with an electromagnet,” *IEEE Transactions on Applied Superconductivity*, vol. 25, no. 3, pp. 1–4, 2015, doi: 10.1109/TASC.2015.2391091.

[137] T. Hirano, K. Takahashi, F. Shimoyashiki, H. Fujishiro, T. Naito, and M. D. Ainslie, “Influence of j(c)(b, t) characteristics on the pulsed field magnetization of rebacuo disk bulks,” *IEEE Transactions On Applied Superconductivity*, vol. 29, 04 2019, doi: 10.1109/TASC.2018.2872819.

[138] H. Wu, H. Yong, and Y. Zhou, “Stress analysis in high-temperature superconductors under pulsed field magnetization,” *Superconductor Science & Technology*, vol. 31, 04 2018, doi: 10.1088/1361-6668/aaafaa.

[139] H. Wu, H. Yong, and Y. Zhou, “Analysis of mechanical behavior in inhomogeneous high-temperature superconductors under pulsed field magnetization,” *Superconductor Science & Technology*, vol. 33, 12 2020, doi: 10.1088/1361-6668/abb8ed.

[140] F. Shimoyashiki, H. Fujishiro, T. Hirano, T. Naito, and M. D. Ainslie, “Simulation of mechanical stresses in reinforced rebacuo disk bulks during pulsed-field magnetization,” *14Th European Conference On Applied Superconductivity (Eucas2019)*, vol. 1559, 2020, doi: 10.1088/1742-6596/1559/1/012029.

[141] T. Hirano, H. Fujishiro, T. Naito, and M. D. Ainslie, “Simulation of mechanical stresses in reinforced rebacuo ring bulks during pulsed-field magnetization,” *14Th European Conference On Applied Superconductivity (Eucas2019)*, vol. 1559, 2020, doi: 10.1088/1742-6596/1559/1/012027.

[142] Z. Huang, H. S. Ruiz, Y. Zhai, J. Geng, B. Shen, and T. A. Coombs, "Study of the pulsed field magnetization strategy for the superconducting rotor," *IEEE Transactions on Applied Superconductivity*, vol. 26, no. 4, pp. 1–5, 2016, doi: 10.1109/TASC.2016.2523059.

[143] K. Berger, J. Kapek, A. Colle, M. Stepien, B. Grzesik, T. Lubin, and J. Lévêque, "3-d modeling of coils for pulsed field magnetization of hts bulk pellets in an electrical machine," *IEEE Transactions on Applied Superconductivity*, vol. 28, no. 4, pp. 1–5, 2018, doi: 10.1109/TASC.2018.2804906.

[144] M. Elbaa, K. Berger, B. Douine, M. Halit, E. H. Ailam, and S. E. Bentridi, "Analytical modeling of an inductor in a magnetic circuit for pulsed field magnetization of hts bulks," *IEEE Transactions On Applied Superconductivity*, vol. 28, 06 2018, doi: 10.1109/TASC.2018.2809438.

[145] H. Fujishiro, T. Naito, and M. Oyama, "Mechanism of magnetic flux trapping on superconducting bulk magnetized by pulsed field using a vortex-type coil," *Superconductor Science & Technology*, vol. 24, 07 2011, doi: 10.1088/0953-2048/24/7/075015.

[146] H. Fujishiro and T. Naito, "Simulation of temperature and magnetic field distribution in superconducting bulk during pulsed field magnetization," *Superconductor Science & Technology*, vol. 23, 10 2010, doi: 10.1088/0953-2048/23/10/105021.

[147] M. L. Khene, L. Alloui, S. M. Mimoune, F. Bouillault, and M. Feliachi, "3d analysis of applied field effect on trapped magnetic field during pulsed field magnetization of bulk superconductor," *European Physical Journal-Applied Physics*, vol. 66, 04 2014, doi: 10.1051/epjap/2014130479.

[148] M. D. Ainslie, D. Zhou, H. Fujishiro, K. Takahashi, Y.-H. Shi, and J. H. Durrell, "Flux jump-assisted pulsed field magnetisation of high-j(c) bulk high-temperature superconductors," *Superconductor Science & Technology*, vol. 29, 12 2016, doi: 10.1088/0953-2048/29/12/124004.

[149] Z. Huang, H. S. Ruiz, and T. A. Coombs, "Pulsed field magnetization strategies and the field poles composition in a bulk-type superconducting motor," *Physica C-Superconductivity And Its Applications*, vol. 534, pp. 73–81, 03 2017, doi: 10.1016/j.physc.2017.01.004.

[150] F. London, *Superfluids: Macroscopic theory of superconductivity.* Structure of matter series, Wiley, 1950.

[151] K. Tang, K. Hoffmann, and Q. Tang, *Ginzburg-Landau Phase Transition Theory and Superconductivity.* International Series of Numerical Mathematics, Springer Basel AG, 2001.

[152] J. Schrieffer, *Theory Of Superconductivity.* Advanced Books Classics, Avalon Publishing, 1999.

[153] S. Chakravarty, "Quantum oscillations and key theoretical issues in high temperature superconductors from the perspective of density waves," *Reports on Progress in Physics*, vol. 74, p. 022501, Jan 2011, doi: 10.1088/0034-4885/74/2/022501, [Online] http://dx.doi.org/10.1088/0034-4885/74/2/022501.

[154] H. Onnes, *The Discovery of Superconductivity: 1910-1914*. 1911.

[155] P. Mangin and R. Kahn, *Superconductivity: An introduction*. Springer International Publishing, 2016.

[156] R. Kleiner, W. Buckel, and R. Huebener, *Superconductivity: An Introduction*. Wiley, 2016.

[157] S. Sarangi, S. Chockalingam, R. Mavinkurve, and S. Bhat, "Experimental evidence for zero dc resistance of superconductors," 07 2005.

[158] F. Mancini and R. Citro, *The Iron Pnictide Superconductors: An Introduction and Overview*. Springer Series in Solid-State Sciences, Springer International Publishing, 2017.

[159] Y. Iwasa, *Case Studies in Superconducting Magnets: Design and Operational Issues*. Springer US, 2009.

[160] A. Narlikar, *Frontiers in Superconducting Materials*. Springer Berlin Heidelberg, 2005.

[161] Y. Wang, *Fundamental Elements of Applied Superconductivity in Electrical Engineering*. Wiley, 2013.

[162] P. Seidel, *Applied Superconductivity: Handbook on Devices and Applications*. Encyclopedia of Applied Physics, Wiley, 2015.

[163] P. W. Anderson, "Theory of flux creep in hard superconductors," *Phys. Rev. Lett.*, vol. 9, pp. 309–311, Oct 1962, doi: 10.1103/PhysRevLett.9.309, [Online] https://link.aps.org/doi/10.1103/PhysRevLett.9.309.

[164] A. Patel, S. C. Hopkins, A. Baskys, V. Kalitka, A. Molodyk, and B. A. Glowacki, "Magnetic levitation using high temperature superconducting pancake coils as composite bulk cylinders," *Superconductor Science and Technology*, vol. 28, no. 11, 2015, doi: 10.1088/0953-2048/28/11/115007.

[165] K. Muller and J. Bednorz, "The discovery of high-temperature superconductivity (reprinted)," *La Recherche*, pp. 88–90, 05 2000.

[166] R. Hott and T. Wolf, "Cuprate high temperature superconductors," 02 2015, doi: 10.1002/3527600434.eap738.

[167] A. Narlikar, *Frontiers in Magnetic Materials*. Springer, 2005.

[168] **Habelok, Krzysztof and Lasek, Pawel and Stepien, Mariusz**, "**Characterization the critical current in HTS tape placed between Halbach arrays**," pp. 1–4, 2017, doi: 10.1109/ELMECO.2017.8267762.

[169] K. Zmorayova, S. Piovarci, M. Radušovská, V. Antal, and P. Diko, "Influence of baceo3 and bao2 addition on the microstructure of y-123/y-211 bulk supercondustors," *Materials Science Forum*, vol. 782, pp. 549–552, 04 2014, doi: 10.4028/www.scientific.net/MSF.782.549.

[170] B. Seeber, *Handbook of Applied Superconductivity, Volume 2*. CRC Press, 1998.

[171] M. Kapolka, V. M. R. Zermeño, S. Zou, A. Morandi, P. L. Ribani, E. Pardo, and F. Grilli, “Three-dimensional modeling of the magnetization of superconducting rectangular-based bulks and tape stacks,” *IEEE Transactions on Applied Superconductivity*, vol. 28, no. 4, pp. 1–6, 2018, doi: 10.1109/TASC.2018.2801322.

[172] R. Huebener, “The abrikosov vortex lattice: Its discovery and impact,” *Journal of Superconductivity and Novel Magnetism*, vol. 32, 03 2019, doi: 10.1007/s10948-018-4916-0.

[173] D. K. Namburi, Y. Shi, K. G. Palmer, A. R. Dennis, J. H. Durrell, and D. A. Cardwell, “Control of y-211 content in bulk YBCO superconductors fabricated by a buffer-aided, top seeded infiltration and growth melt process,” *Superconductor Science and Technology*, vol. 29, p. 034007, feb 2016, doi: 10.1088/0953-2048/29/3/034007, [Online] https://doi.org/10.1088/0953-2048/29/3/034007.

[174] E. Talantsev, N. Long, N. Strickland, and J. Tallon, “Pinning force anisotropy for hts wires,” *Materials Science Forum*, vol. 700, pp. 7–10, 09 2011, doi: 10.4028/www.scientific.net/MSF.700.7.

[175] A. Sotnikova and I. Rudnev, “The effect of temperature on pinning mechanisms in hts composites,” *Journal of Physics: Conference Series*, vol. 747, p. 012047, 09 2016, doi: 10.1088/1742-6596/747/1/012047.

[176] M. Kazimierczuk, *High-Frequency Magnetic Components.* Wiley, 2011.

[177] D. Parks, R. Weinstein, K. Davey, and R.-P. Sawh, “A study of pulsed activation of trapped field magnets-part 1: Effects of pulse height and creep,” *IEEE Transactions On Applied Superconductivity*, vol. 23, 06 2013, doi: 10.1109/TASC.2012.2231454.

[178] C. P. Bean, “Magnetization of hard superconductors,” *Phys. Rev. Lett.*, vol. 8, pp. 250–253, Mar 1962, doi: 10.1103/PhysRevLett.8.250, [Online] https://link.aps.org/doi/10.1103/PhysRevLett.8.250.

[179] C. P. BEAN, “Magnetization of high-field superconductors,” *Rev. Mod. Phys.*, vol. 36, pp. 31–39, Jan 1964, doi: 10.1103/RevModPhys.36.31, [Online] https://link.aps.org/doi/10.1103/RevModPhys.36.31.

[180] T. Miyazaki, T. Miyatake, H. Kato, K. Zaitsu, Y. Murakami, T. Hase, and M. Hamada, “Development of nb3sn superconducting wires for high field magnets at kobe steel and jastec,” *Cryogenics*, vol. 48, pp. 341–346, 07 2008, doi: 10.1016/j.cryogenics.2008.05.002.

[181] J. Ekin and O. U. Press, *Experimental Techniques for Low-Temperature Measurements: Cryostat Design, Material Properties and Superconductor Critical-Current Testing.* OUP Oxford, 2006.

[182] T. Janowski, B. Kondratowicz-Kucewicz, G. Wojtasiewicz, S. Kozak, J. Kozak, M. Majka, and L. Jaroszynski, “Superconducting devices for power engineering,” *Acta Physica Polonica A*, vol. 130, pp. 537–544, 08 2016, doi: 10.12693/APhysPolA.130.537.

[183] J. H. Kim, C. J. Hyeon, S. H. Chae, D. J. Kim, C.-J. Boo, Y.-S. Jo, Y. S. Yoon, S.-G. Kim, H. Lee, and H. M. Kim, “Design and analysis of cooling structure on advanced air-core stator for megawatt-class hts synchronous motor,” *IEEE Transactions on Applied Superconductivity*, vol. 27, no. 4, pp. 1–7, 2017, doi: 10.1109/TASC.2017.2669194.

[184] W. Nick, G. Nerowski, H.-W. Neumüller, M. Frank, P. Hasselt, J. Frauenhofer, and F. Steinmeyer, "380 kw synchronous machine with hts rotor windings - development at siemens and first test results," *Physica C: Superconductivity*, vol. 372, pp. 1506–1512, 08 2002, doi: 10.1016/S0921-4534(02)01069-9.

[185] K. Hamilton, A. Pantoja, Z. Jiang, J. Storey, R. Badcock, and C. Bumby, "Design and performance of a "squirrel-cage" dynamo-type hts flux pump," *IEEE Transactions on Applied Superconductivity*, vol. PP, pp. 1–1, 02 2018, doi: 10.1109/TASC.2018.2805161.

[186] **Lasek, Pawel and Habelok, Krzysztof and Stepien, Mariusz**, "**Armature Winding Analysis for High-temperature Superconducting PM-excited AC Machines**," *International Journal of Applied Electromagnetics and Mechanics*, vol. 64, 01 2020, doi: 10.3233/JAE-209523.

[187] **Habelok, Krzysztof and Lasek, Pawel and Stepien, Mariusz**, "**Analysis of magnetic field distribution in a transverse-flux linear motor with superconducting windings**," *International Journal of Applied Electromagnetics and Mechanics*, vol. 64, 01 2020, doi: 10.3233/JAE-209524.

[188] R. Weinstein, D. Parks, R. Sawh, K. Davey, and K. Carpenter, "Observation of a bean model limit—a large decrease in required applied activation field for tfms," *IEEE Transactions on Applied Superconductivity*, vol. 25, no. 3, pp. 1–6, 2015, doi: 10.1109/TASC.2014.2366722.

[189] H. Zhang, J. Geng, and T. A. Coombs, "Magnetizing high-tc superconducting coated conductor stacks using a transformer–rectifier flux pumping method," *Superconductor Science and Technology*, vol. 31, p. 105007, aug 2018, doi: 10.1088/1361-6668/aad78a, [Online] https://doi.org/10.1088

[190] M. D. Ainslie, H. Fujishiro, T. Ujiie, J. Zou, A. R. Dennis, Y.-H. Shi, and D. A. Cardwell, "Modelling and comparison of trapped fields in (RE)BCO bulk superconductors for activation using pulsed field magnetization," *Superconductor Science and Technology*, vol. 27, p. 065008, apr 2014, doi: 10.1088/0953-2048/27/6/065008, [Online] https://doi.org/10.1088

[191] R. Weinstein, D. Parks, R. P. Sawh, K. Carpenter, and K. Davey, "A significant advantage for trapped field magnet applications - A failure of the critical state model," *Applied Physics Letters*, vol. 107, no. 15, 2015, doi: 10.1063/1.4933313, [Online] http://dx.doi.org/10.1063/1.4933313.

[192] R. C. Mataira, M. D. Ainslie, R. A. Badcock, and C. W. Bumby, "Origin of the DC output voltage from a high- Tc superconducting dynamo," *Applied Physics Letters*, vol. 114, no. 16, 2019, doi: 10.1063/1.5085226.

[193] y. Yan, C. Hsu, Z. Hong, W. Xian, W. Yuan, and T. Coombs, "A novel design of thermally actuated magnetization flux pump for high temperature superconducting bulks," *Applied Superconductivity, IEEE Transactions on*, vol. 21, pp. 1568 – 1571, 07 2011, doi: 10.1109/TASC.2010.2087737.

[194] T. Coombs, Z. Hong, and X. Zhu, "A thermally actuated superconducting flux pump," *Physica C-superconductivity and Its Applications - PHYSICA C*, vol. 468, pp. 153–159, 02 2008, doi: 10.1016/j.physc.2007.11.003.

[195] T. Coombs, J. Geng, L. Fu, and K. Matsuda, “An overview of flux pumps for hts coils,” *IEEE Transactions on Applied Superconductivity*, vol. 27, pp. 1–1, 01 2016, doi: 10.1109/TASC.2016.2645130.

[196] H. L. Laquer, “An electrical flux pump for powering superconducting magnet coils,” *Cryogenics*, vol. 3, pp. 27–30, Jan. 1963, doi: 10.1016/0011-2275(63)90067-5.

[197] H. Zhang, J. Geng, B. Shen, L. Fu, X. Zhang, C. Li, J. Li, and T. A. Coombs, “Magnetization of coated conductor stacks using flux pumping,” *IEEE Transactions on Applied Superconductivity*, vol. 27, no. 4, pp. 1–5, 2017, doi: 10.1109/TASC.2017.2652544.

[198] L. Fu, K. Matsuda, T. Lecrevisse, Y. Iwasa, and T. Coombs, “A flux pumping method applied to the magnetization of ybco superconducting coils: Frequency, amplitude and waveform characteristics,” *Superconductor Science and Technology*, vol. 29, p. 04LT01, 04 2016, doi: 10.1088/0953-2048/29/4/04LT01.

[199] C. Hoffmann, R. Walsh, E. Karrer-Mueller, and D. Pooke, “Design parameters for an hts flux pump,” *Physics Procedia*, vol. 36, pp. 1324–1329, 12 2012, doi: 10.1016/j.phpro.2012.06.299.

[200] C. Hoffmann, D. Pooke, and A. D. Caplin, “Flux pump for hts magnets,” *IEEE Transactions on Applied Superconductivity*, vol. 21, no. 3, pp. 1628–1631, 2011, doi: 10.1109/TASC.2010.2093115.

[201] J. Storey, A. Pantoja, Z. Jiang, K. Hamilton, R. Badcock, and C. Bumby, “Impact of annular yoke geometry on performance of a dynamo-type hts flux pump,” *IEEE Transactions on Applied Superconductivity*, vol. PP, pp. 1–1, 01 2018, doi: 10.1109/TASC.2018.2797171.

[202] L. Fu, K. Matsuda, M. Baghdadi, and T. Coombs, “Linear flux pump device applied to high temperature superconducting (hts) magnets,” *IEEE Transactions on Applied Superconductivity*, vol. 25, no. 3, pp. 1–4, 2015.

[203] Y. Murata, Z. Hong, y. Yan, and T. Coombs, “Coupled thermal-magnetic analysis on thermally actuated superconducting flux pump,” *Applied Superconductivity, IEEE Transactions on*, vol. 21, pp. 2291 – 2294, 07 2011, doi: 10.1109/TASC.2010.2093555.

[204] K. Zmorayova, V. Antal, M. Radusovska, S. Piovarci, D. Volochova, and P. Diko, “Microstructure and Properties of Y-123 / Y-211 Bulk Superconductors with BaCeO 3 and BaO 2 Addition,” *ACTA Physica Polonica A*, vol. 126, no. 1, pp. 366–367, 2014, doi: 10.12693/APhysPolA.126.366.

[205] M. D. Ainslie, H. Fujishiro, K. Takahashi, Y.-H. Shi, and C. D. A., “Pulsed Field Magnetization of Bridge-Seeded Bulk YBCO Using Solenoid and Split Coils,” *IEEE Transactions on Appiled Superconductivity*, 2017, doi: 10.1109/TASC.2017.2667621.

[206] J. R. Hull and M. Strasik, “Concepts for using trapped-flux bulk high-temperature superconductor in motors and generators,” *Superconductor Science & Technology*, vol. 23, 12 2010, doi: 10.1088/0953-2048/23/12/124005.

[207] D. Zhou, Y. Shi, W. Zhao, A. R. Dennis, M. Beck, M. D. Ainslie, K. G. Palmer, D. A. Cardwell, and J. H. Durrell, "Full magnetization of bulk (RE) Ba2Cu3O7-δ magnets with various rare-earth elements using pulsed fields at 77 K," *IEEE Transactions on Applied Superconductivity*, vol. 27, no. 4, pp. 18–21, 2017, doi: 10.1109/TASC.2016.2638200.

[208] S. Zou, V. M. R. Zermeño, A. Baskys, A. Patel, F. Grilli, and B. A. Glowacki, "Simulation and experiments of stacks of high temperature superconducting coated conductors magnetized by pulsed field magnetization with multi-pulse technique," *Superconductor Science and Technology*, vol. 30, p. 014010, nov 2016, doi: 10.1088/0953-2048/30/1/014010, [Online] https://doi.org/10.1088

[209] T. B. Mitchell-Williams, A. Baskys, S. C. Hopkins, V. Kalitka, A. Molodyk, B. A. Glowacki, and A. Patel, "Uniform trapped fields produced by stacks of HTS coated conductor tape," *Superconductor Science and Technology*, vol. 29, no. 8, 2016, doi: 10.1088/0953-2048/29/8/085008.

[210] M. D. Ainslie, H. Fujishiro, H. Mochizuki, K. Takahashi, Y.-H. Shi, D. K. Namburi, J. Zou, D. Zhou, A. R. Dennis, and D. A. Cardwell, "Enhanced trapped field performance of bulk high-temperature superconductors using split coil, pulsed field magnetization with an iron yoke," *Superconductor Science and Technology*, vol. 29, p. 074003, may 2016, doi: 10.1088/0953-2048/29/7/074003.

[211] H. Matsuzaki, Y. Kimura, I. Ohtani, M. Izumi, T. Ida, Y. Akita, H. Sugimoto, M. Miki, and M. Kitano, "An axial gap-type hts bulk synchronous motor excited by pulsed-field magnetization with vortex-type armature copper windings," *IEEE Transactions on Applied Superconductivity*, vol. 15, no. 2, pp. 2222–2225, 2005, doi: 10.1109/TASC.2005.849617.

[212] S. Zou, V. M. R. Zermeño, and F. Grilli, "Simulation of high temperature superconducting bulks magnetized by pulsed field magnetization with an electromagnetic-thermal coupled model," *arXiv*, 2015.

[213] KEMET, *Screw Terminal Aluminum Electrolytic Capacitors ALS70/71, High CV, +85°C*, 2020. [Online]: https://content.kemet.com.

[214] D. Hanselman, *Brushless Permanent-magnet Motor Design.* New Horizons in Comparative Politics, McGraw-Hill, 1994.

[215] S. Muniz, V. Bagnato, and M. Bhattacharya, "Analysis of off-axis solenoid fields using the magnetic scalar potential: An application to a zeeman-slower for cold atoms," *American Journal of Physics*, 05 2015, doi: 10.1119/1.4906516.

[216] Vishay Semiconductors, *Thyristor/Diode and Thyristor/Thyristor, 135 A to 160 A (INT-A-PAK Power Modules)*, 2018. [Online]: https://docs.rs-online.com/.

[217] SEMIKRON, *SEMITRANS 3 IGBT Module SKM 200GB173D datasheet*, 2008. [Online]: https://www.semikron.com.

[218] CAN SUPERCONDUCTORS, *SUPERCONDUCTING YBCO LEVITATION BULK*, 2018. [Online]: https://www.can-superconductors.com.

[219] ChenYang Technologies GmbH & Co. KG, *CYSJ362A GaAs Hall Effect Element*, 2016. [Online]: http://www.hallsensors.de/.

[220] Keysight Technologies, *DSOX2004A Oscilloscope: 70 MHz, 4 Analog Channels.* [Online]: https://www.keysight.com.

[221] Agillent Technologies, *DSOX2014A Oscilloscope: 100 MHz, 4 Analog Channels.* [Online]: https://www.keysight.com.

[222] Rigol Technologies, Co. Ltd., *Rigol PVP2150 150MHz Passive Oscilloscope Probe.* [Online]: https://res.cloudinary.com.

[223] Aim TTi, *Bench/System DC Power Supply Dual Outputs, 2 x 80V/50A 600W, USB/RS232/LAN/GPIB Interfaces.* [Online]: https://resources.aimtti.com.

[224] Chauvin Arnoux, *Current clamps for AC/DC current - PAC series.* [Online]: https://www.elfadistrelec.pl/.

[225] TKD-Lambda Americas, *GENESYS Programmable DC power supply.* [Online]: https://product.tdk.com.

[226] A. Schmid, “A time dependent ginzburg-landau equation and its application to the problem of resistivity in the mixed state,” *Physik der kondensierten Materie*, vol. 5, no. 4, pp. 302–317, 1966.

[227] T. Matsuno, E. S. Otabe, and Y. Mawatari, “Explicit integrators based on a bipartite lattice and a pair of affine transformations to solve quantum equations with gauge fields,” *Journal of the Physical Society of Japan*, vol. 89, no. 5, p. 054006, 2020, doi: 10.7566/JPSJ.89.054006.

[228] T. Orlando and K. Delin, *Foundations of Applied Superconductivity.* Electrical Engineering Series, Addison-Wesley, 1991.

[229] H. H, W. Hayt, and J. Buck, *Engineering Electromagnetics.* Electrical engineering series, McGraw-Hill, 2001.

[230] M. Getzlaff, *Fundamentals of Magnetism.* Springer Berlin Heidelberg, 2007.

[231] M. Fujimoto, *Physics of Classical Electromagnetism.* IFIP International Federation for Information Proc, Springer New York, 2007.

[232] C. Balanis, *Advanced Engineering Electromagnetics, 2nd Edition.* Wiley, 2012.

[233] J. Ogawa, T. Oka, S. Fukui, T. Sato, N. Watanabe, and Z. Basir, “Numerical study of the influence of material properties on pulsed-field magnetization for hts bulk magnets,” *Applied Superconductivity, IEEE Transactions on*, vol. 24, pp. 1–4, 06 2014, doi: 10.1109/TASC.2013.2282174.

[234] T. Coombs, “A finite element model of magnetization of superconducting bulks using a solid-state flux pump,” *IEEE Transactions on Applied Superconductivity - IEEE TRANS APPL SUPERCONDUCT*, vol. 21, pp. 3581–3586, 12 2011, doi: 10.1109/TASC.2011.2163390.

[235] F. Werfel, U. Floegel-Delor, R. Rothfeld, T. Riedel, B. Goebel, D. Wippich, P. Schirrmeister, and R. Koenig, “Next generation of hts magnetic application: Hts bulk and coil interaction,” *Journal of Physics: Conference Series*, vol. 507, p. 032055, 05 2014, doi: 10.1088/1742-6596/507/3/032055.

[236] J. D. Jackson, *Classical electrodynamics; 2nd ed.* New York, NY: Wiley, 1975.

[237] B. Shen, F. Grilli, and T. Coombs, “Overview of h -formulation: A versatile tool for modeling electromagnetics in high-temperature superconductor applications,” *IEEE Access*, vol. PP, pp. 1–1, 05 2020, doi: 10.1109/ACCESS.2020.2996177.

[238] M. Rognes, R. Kirby, and A. Logg, “Efficient assembly of h(div) and h(curl) conforming finite elements,” 05 2012.

[239] H. Zhang, M. Zhang, and W. Yuan, “An efficient 3D finite element method model based on the T–A formulation for superconducting coated conductors,” *Superconductor Science and Technology*, 2017, doi: 10.1088/1361-6668/30/2/024005.

[240] Y. Wang, M. Zhang, F. Grilli, Z. Zhu, and W. Yuan, “Study of the magnetization loss of CORC® cables using a 3D T-A formulation,” *Superconductor Science and Technology*, vol. 32, no. 2, 2019, doi: 10.1088/1361-6668/aaf011.

[241] E. Berrospe-Juarez, V. M. Zermeño, F. Trillaud, and F. Grilli, “Real-time simulation of large-scale HTS systems: Multi-scale and homogeneous models using the T-A formulation,” *Superconductor Science and Technology*, vol. 32, no. 6, 2019, doi: 10.1088/1361-6668/ab0d66.

[242] T. Benkel, M. Lao, Y. Liu, E. Pardo, S. Wolfstadter, T. Reis, and F. Grilli, “T-A-Formulation to Model Electrical Machines with HTS Coated Conductor Coils,” *IEEE Transactions on Applied Superconductivity*, vol. 30, no. 6, pp. 1–8, 2020, doi: 10.1109/TASC.2020.2968950.

[243] L. Bortot, B. Auchmann, I. C. Garcia, H. D. Gersem, M. Maciejewski, M. Mentink, S. Schöps, J. V. Nugteren, and A. P. Verweij, “A coupled a–h formulation for magneto-thermal transients in high-temperature superconducting magnets,” *IEEE Transactions on Applied Superconductivity*, vol. 30, no. 5, pp. 1–11, 2020, doi: 10.1109/TASC.2020.2969476.

[244] A. M. Campbell, “A new method of determining the critical state in superconductors,” *Superconductor Science and Technology*, vol. 20, pp. 292–295, feb 2007, doi: 10.1088/0953-2048/20/3/031, [Online] https://doi.org/10.1088/0953-2048/20/3/031.

[245] Z. Xu, R. Lewin, A. M. Campbell, D. A. Cardwell, and H. Jones, “Theoretical simulation studies of pulsed field magnetisation of (re)bco bulk superconductors,” *9Th European Conference On Applied Superconductivity (Eucas 09)*, vol. 234, 2010, doi: 10.1088/1742-6596/234/1/012049.

[246] J. Duron, F. Grilli, B. Dutoit, and S. Stavrev, “Modelling the e-j relation of high-tc superconductors in an arbitrary current range,” *Physica C Superconductivity*, vol. 401, 01 2004, doi: 10.1016/j.physc.2003.09.044.

[247] J. Duron, F. Grilli, L. Antognazza, M. Decroux, B. Dutoit, and Ø. Fischer, “Finite-element modelling of YBCO fault current limiter with temperature dependent parameters,” *Superconductor Science and Technology*, vol. 20, pp. 338–344, mar 2007, doi: 10.1088/0953-2048/20/4/007, [Online] https://doi.org/10.1088

[248] D. Voltmer, *Fundamentals of Electromagnetics 1: Internal Behavior of Lumped Elements.* Fundamentals of Electromagnetics, Morgan & Claypool, 2007.

[249] A. Taflove and S. Hagness, *Computational Electrodynamics: The Finite-difference Time-domain Method.* Artech House antennas and propagation library, Artech House, 2005.

[250] A. Polycarpou, *Introduction to the Finite Element Method in Electromagnetics.* Synthesis Lectures on Computational Electromagnetics, Morgan & Claypool Publishers, 2006.

[251] O. Zienkiewicz, R. Taylor, and J. Zhu, *The Finite Element Method: Its Basis and Fundamentals.* Elsevier Science, 2005.

[252] R. Garg, *Analytical and Computational Methods in Electromagnetics.* Artech House electromagnetic analysis series, Artech House, 2008.

[253] V. Adams and A. Askenazi, *Building Better Products with Finite Element Analysis.* Building Better Products with Finite Element Analysis, OnWord Press, 1999.

[254] FEniCS Project. https://fenicsproject.org/.

[255] Deal.II. https://www.dealii.org/.

[256] Agrod Suite. http://www.agros2d.org/.

[257] COMSOL Multiphysics. https://www.comsol.com/.

[258] Ansys. https://www.ansys.com/.

[259] Gmsh. https://gmsh.info/.

[260] ParaView. https://www.paraview.org/.

[261] H. Langtangen and A. Logg, *Solving PDEs in Python: The FEniCS Tutorial I.* Simula SpringerBriefs on Computing, Springer International Publishing, 2017.

[262] A. Logg, K.-A. Mardal, G. N. Wells, *et al.*, *Automated Solution of Differential Equations by the Finite Element Method.* Springer, 2012.

[263] J. Gnilsen, A. Usoskin, M. Eisterer, U. Betz, and K. Schlenga, "Current–voltage characteristics of double disordered REBCO coated conductors exposed to magnetic fields with edge gradients," *Superconductor Science and Technology*, vol. 32, p. 104002, sep 2019, doi: 10.1088/1361-6668/ab3c09, [Online] https://doi.org/10.1088/1361-6668/ab3c09.

[264] Lake Shore, *F71 and F41 Teslameters/technical-specifications*, 2019. [Online]: https://www.lakeshore.com.

[265] SANWA ELECTRIC INSTRUMENT CO., LTD., *DIGITAL MULTIMETER PC7000.* [Online]: https://ndn.com.pl.

[266] L. Kirkup and R. B. Frenkel, *An Introduction to Uncertainty in Measurement: Using the GUM (Guide to the Expression of Uncertainty in Measurement).* Cambridge University Press, 2006.

[267] Tektronix, Inc., *AC/DC Current Measurement Systems - TCPA300, TCP312A, TCP305A, TCP303, TCPA400, TCP404XL Datasheet.* [Online]: https://download.tek.com/.

[268] Tektronix, Inc., *Mixed Signal Oscilloscopes - MSO3000 Series, DPO3000 Series Datasheet*. [Online]: https://download.tek.com/.

[269] J. Conway, "Exact solutions for the magnetic fields of axisymmetric solenoids and current distributions," *IEEE Transactions on Magnetics*, vol. 37, no. 4, pp. 2977–2988, 2001, doi: 10.1109/20.947050.

[270] V. Labinac, N. Erceg, and D. Kotnik-Karuza, "Magnetic field of a cylindrical coil," *American Journal of Physics - AMER J PHYS*, vol. 74, pp. 621–627, 07 2006, doi: 10.1119/1.2198885.

[271] S. Babic and C. Akyel, "An improvement in the calculation of the magnetic field for an arbitrary geometry coil with rectangular cross section (vol 18, pg 493, 2005)," *International Journal of Numerical Modelling-electronic Networks Devices and Fields - INT J NUMER MODEL ELECTRON N*, vol. 21, pp. 220–221, 05 2008, doi: 10.1002/jnm.675.

[272] Bahco, *Bahco 1150D electronic calipers*. [Online]: https://www.bahco.com.

Appendices

A

Magnetic field sensors

A.1. Hall sensor calibration

To measure the magnetic flux density, a set of seven CYSJ362A [219] hall sensors have been used, which have already been used in measurements related to superconductivity [263]. To properly perform the measurement of magnetic flux density, the sensors have to be calibrated individually to obtain voltage-magnetic flux density characteristics. The magnetic flux density values expected to occur in the system are above 2 T; thus, sensors have to calibrated in that range. On top of that, the applied magnetic field does change over time since the current is a pulse wave with a short rising time and long falling time.

The calibration of the sensors has been done with a solenoid coil $L_2 = 3$ mH, without the presence of any ferromagnetic materials. The coil L_2 was chosen since it results in the highest peak magnetic flux density generated by the flux pump. The procedure of calibration was done in two steps. Firstly, a relationship between the value of current and magnetic flux density of each coil has was established at the center of the solenoid. Secondly, the relationship between voltage reading and magnetic flux density for every sensor was found. Both measurements combined allows for evaluating the $B(U)$ function of the sensors.

The testing setup composed of a 3D printed guide and coil is presented in Figure A.1. The 3D printed guide has been printed on a 3D printer with a PLA material, an organic and non-magnetic material, and does not change its dimensions significantly when exposed to liquid nitrogen. The sensors were located at the very center of the coil, where magnetic field is the most uniform and has an axial component. The spot where sensors were located has additional radial channels to provide liquid nitrogen for cooling (Figure A.1b). The guide also has multiple openings in the axial direction to reduce temperature gradient and provide paths for placing a reference hall probe (F71 Teslameter by Lake Shore Cryotronics [264]) and wiring of the sensors. The sensors were secured in place with Kapton tape and pressed from top and bottom with two pieces of the guide to reduce the possibility of any movement during measurement (Figure A.1a).

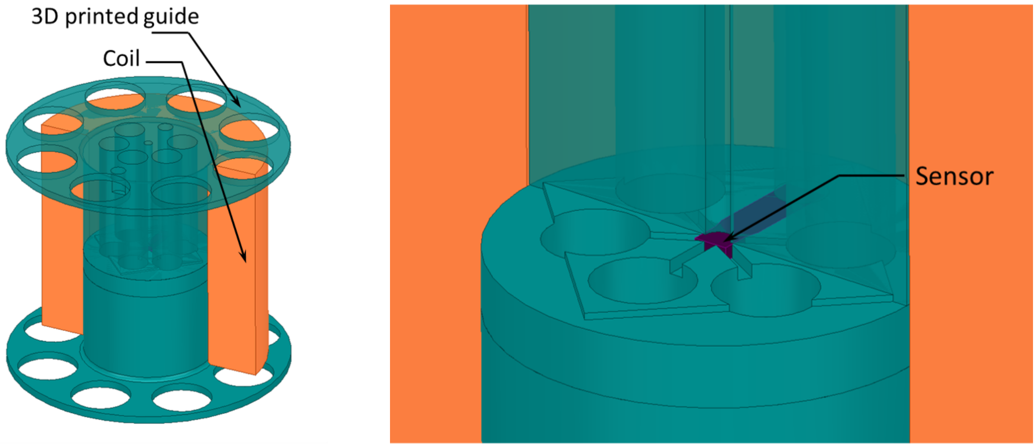

(a) (b)

Figure A.1. Visualisation of the hall sensor calibration setup: (a) view through coil cross-section; (b) close view at the sensor location

A.1.1. Coil characteristics

The measurements were done at room temperature by passing DC current through the coil to verify the current-magnetic flux density relationship of all designed coils. The system was powered by a DC power supply with a current of up to 10 A. For measurement of the current, the Sanwa PC7000 multimeter [265] has been used. The value of magnetic flux density has been measured using teslameter F71 Teslameter by Lake Shore Cryotronics [264] at the place where the sensor was located through the opening at the center of the 3D printed guide. The readings from the teslameter were obtained in the 10 s averaging window. The measurements were done at a steady-state of current at room temperature, which limited the value of maximum current flowing through the coil due to power supply maximum current since the coil has a relatively high resistance. Unfortunately, it was impossible to achieve DC currents of values comparable with peak currents generated by the flux pump due to the amount of power required to produce such high currents in the range of hundreds of amperes.

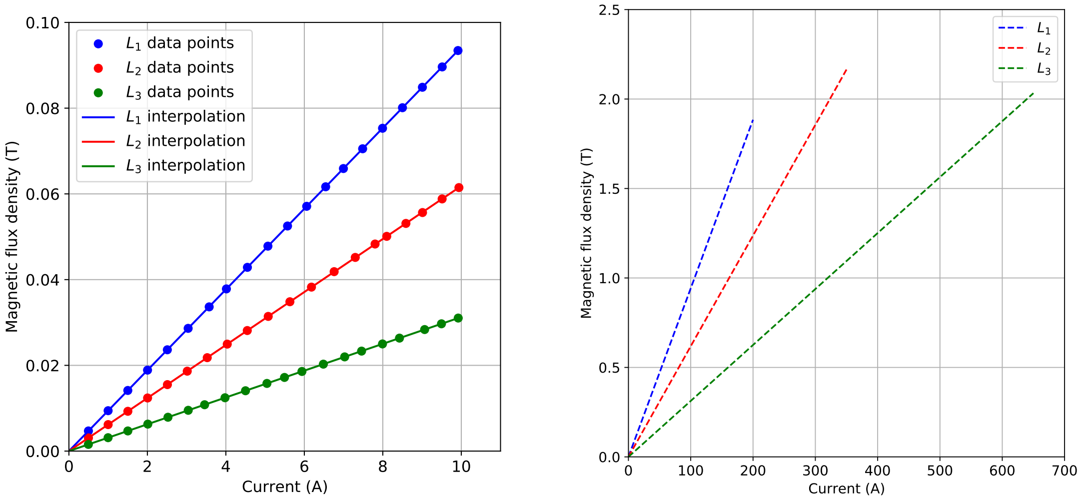

(a) Measurement **(b)** Extraplation

Figure A.2. The current - magnetic flux density characteristics of the coils

Figure A.2a shows the current-magnetic flux density characteristics of each coil, which have been interpolated using linear regression (A.1) on the measured data points. The interpolation was then used to extrapolate values expected to occur in the flux pump system when pulse currents are generated of much higher values (Figure A.2b). The uncertainty of regression coefficients has been calculated [266].

$$\begin{cases} B_{\mathrm{L1}}(I) = 9.4213(11) \cdot 10^{-3} \cdot I + 0.0053(67) \cdot 10^{-3} & \text{for } L_1 \\ B_{\mathrm{L2}}(I) = 6.185(23) \cdot 10^{-3} \cdot I - 0.010(14) \cdot 10^{-3} & \text{for } L_2 \\ B_{\mathrm{L3}}(I) = 3.12727(21) \cdot 10^{-3} \cdot I + 0.0016(13) \cdot 10^{-3} & \text{for } L_3 \end{cases} \tag{A.1}$$

A.1.2. Characteristic of the sensors

In the next step, the relation between measured magnetic flux density and voltage reading of the hall sensors is analysed. The sensors terminals were connected via ϕ100 µm wires, which were twisted to minimise mutual inductance and reduce the influence of noise and other external sources. The hall sensors operate as voltage dividers and were powered from controlled power supply AIM-TTI QPX600DP [223] at 10 V with the additional output capacitance of 4.7 µF and 100 nF connected in parallel to the supply bus. The voltage readings were obtained with seven passive oscilloscope probes Rigol PVP2150 [222], each connected to every sensor output. For calibration purposes, the current was measured using Tektronix TCP404XL [267] current probe connected via Tektronix TCPA400 [267] amplifier to Tektronix MSO 3014 Mixed Signal Oscilloscope [268].

During the measurements, the sensors were located at the center of the 3D printed guide (Figure A.1), where the distribution of field is the most homogeneous and magnetic field has mainly axial component. The whole setup (coil, sensors and guide) was submerged in liquid nitrogen. By applying pulsed current waveform and measuring the response allowed for reaching values of sufficiently high magnetic fields that reflect operating conditions of the sensors during pulsed-field magnetisation of the superconducting bulk. Fifteen consecutive field pulses have been applied to each sensor; all generated using the designed flux pump system with $C = 5$ mF and coil $L_2 = 3$ mH, which has shown to achieve the highest peak applied field (Figure A.2b).

The Figure A.3a shows an average of fifteen current pulses with corresponding average voltage reading in Figure A.3b. The averages were calculated at each discrete point in time captured by the oscilloscope. From the series of fifteen readings, the standard deviation of the obtained data at each point in time for current (Figure A.3c) and voltage (Figure A.3d) have been calculated. The standard deviation gives a value of type A uncertainty of both waveforms. Both plots of standard deviation in Figures A.3c and A.3d show relatively high standard deviation at $t = 0$ s. This is due to oscilloscope triggering at that point in time, resulting in slight variation at each applied pulse. However, the standard deviation at other discrete time steps is much smaller, which hints at good repeatability of applied pulses and measurements.

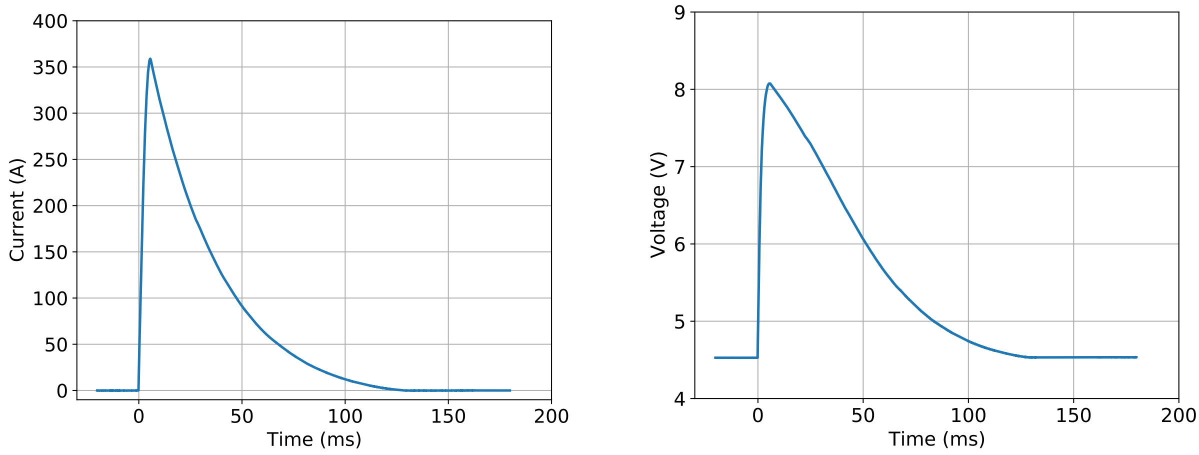

(a) average current

(b) average voltage (sensor B1)

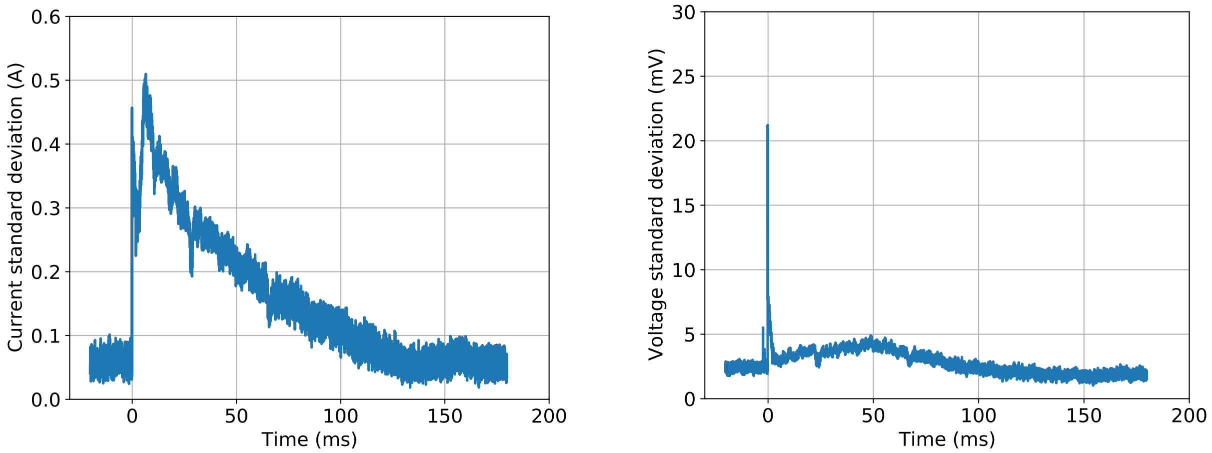

(c) standard deviation of the current waveform

(d) standard deviation of the voltage reading (sensor B1)

Figure A.3. Statistical analysis of current and voltage waveforms: (a) average current; (b) average voltage (sensor B1); (c) standard deviation of the current waveform; (d) standard deviation of the voltage from the hall sensor B1

The data on the oscilloscope has been registered simultaneously on all channels; therefore, the current and voltage waveforms occur at the same discrete time steps. From the obtained data (Figure A.3a and A.3b), the voltage-current curve been plotted (Figure A.4a). The magnetic flux density and current relation of the coil used for calibration (L_2) can then be used (A.1) to evaluate magnetic flux density acting on the sensor for a given current flowing through the coil (Figure A.4b). It can be seen that sensors have a nonlinear characteristic.

To obtain the readings of the magnetic flux density from the measured voltage on the output of the hall sensor, the characteristic on the Figure A.4b needs to be inverted and then interpolated. Due to nonlinearity of the sensor, a polynomial of 5^{th} – degree (A.2) has been used for all sensors, and plotted in Figure A.5.

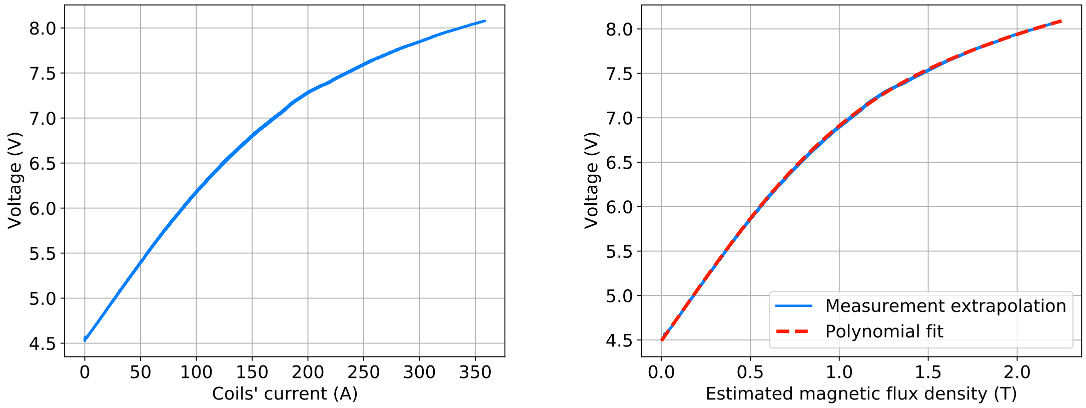

(a) **(b)**

Figure A.4. (a) Dependence between voltage reading from hall sensor B1 and current applied to the coil; (b) dependence between voltage reading from hall sensor B1 and estimated magnetic flux density acting on the sensor B1

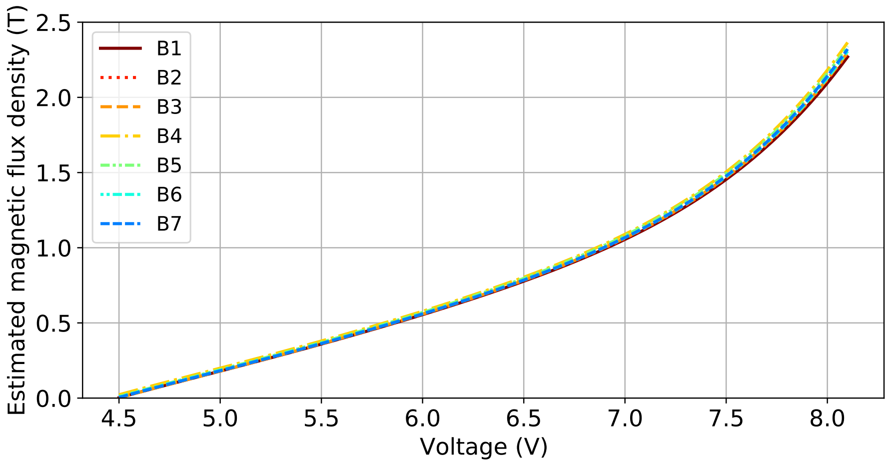

Figure A.5. Estimated magnetic flux acting on the sensor at certain measured voltage on the output

$$B(U) = b_5U^5 + b_4U^4 + b_3U^3 + b_2U^2 + b_1U + b_0 \tag{A.2}$$

Table A.1. Polynomial coefficients of $B(U)$ characteristics of sensors

Sensor	b_5 (T/V^5)	b_4 (T/V^4)	b_3 (T/V^3)	b_2 (T/V^2)	b_1 (T/V)	b_0 (T)
B1	0.005182072	-0.143760372	1.60458443	-8.97273473	25.4197588	-29.5177764
B2	0.005356595	-0.148703169	1.66052674	-9.28839505	26.3077311	-30.5140564
B3	0.005337621	-0.148228498	1.65599813	-9.26818656	26.2692351	-30.4985592
B4	0.005663087	-0.157259221	1.75633426	-9.82416477	27.7996206	-32.1465271
B5	0.005382361	-0.149075019	1.66111044	-9.27252894	26.2130990	-30.3498843
B6	0.005232156	-0.144834273	1.61323303	-9.00310364	25.4561030	-29.5021564
B7	0.005450233	-0.151133583	1.68583811	-9.42032687	26.6519664	-30.8727187

The polynomial (A.2) coefficients have been listed in Table A.1 for every sensor. The uncertainty of the voltage measurement influences the readings of the magnetic flux density. Using the law of propagation of uncertainty [266] (A.3).

$$u_{c1}\left(B(U)\right) = \sqrt{\left(\frac{\partial B(U)}{\partial U}\right)^2 u_c^2(U)} \tag{A.3}$$

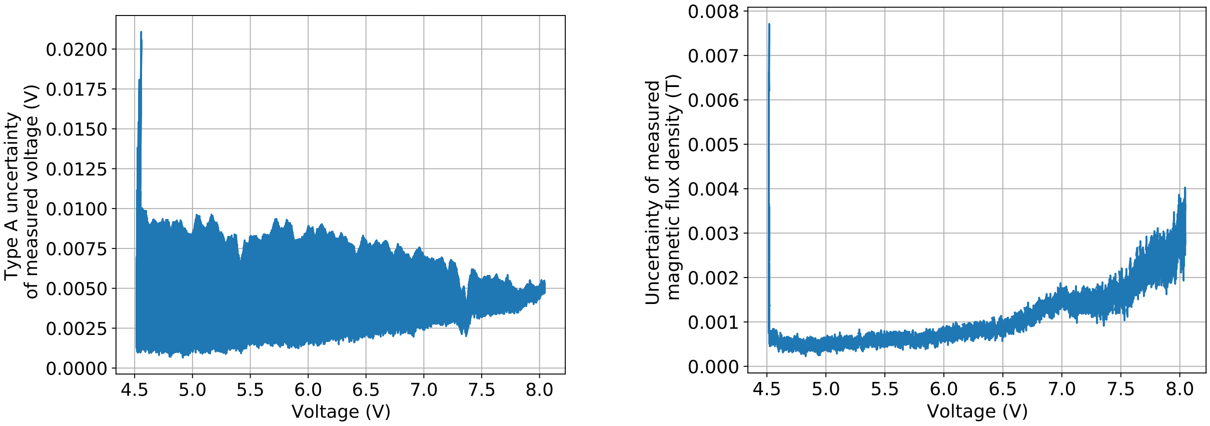

(a) **(b)**

Figure A.6. Uncertainty of measured magnetic flux density based on voltage measurement of the sensor

A.1.3. Monte Carlo simulation of magnetic field uncertainty

The relationship between magnetic flux density produced by the current flowing through the solenoid coil is described by a linear function, both in air and liquid nitrogen. Both media does not have magnetic properties (contrary to the liquid oxygen, which is dielectric). The magnetic flux density - current dependence has been estimated for all coils (A.1). However, the position of the calibrated sensors and coil dimensions have uncertainty. The basis for calculating a magnetic flux density d**B** at any given point in space at a distance **r** from a wire piece d**l** with current I is given by the Biot-Savart law (A.4) [236].

$$\mathrm{d}\mathbf{B} = \frac{\mu_0 I}{4\pi} \frac{\mathrm{d}\mathbf{l} \times \hat{\mathbf{r}}}{|\mathbf{r}|^2} \tag{A.4}$$

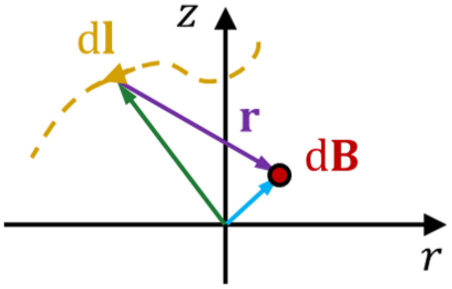

Figure A.7. Visualisation of the Biot-Savart law

Integrating the (A.4) along the wire length gives a magnetic flux density at given point. Despite simple description, the magnetic flux density is known for particular setups like magnetic field distribution along the axis of symmetry (z-axis) for a single current loop of radius R (A.5) [236].

$$B_{\mathrm{z}}(z) = \frac{\mu_0 I}{2} \frac{R^2}{\left(R^2 + z^2\right)^{3/2}} \tag{A.5}$$

Equation (A.5) is only valid for calculating flux along z-axis. To obtain a magnetic flux density at any point in space, or even at least on the plane encapsulated by the current loop, the problem becomes non-trivial. The problem becomes even more complicated when considering a coil of given dimensions - height and thickness with a current density distribution.

One of the ways to obtain the magnetic field distribution is to solve a PDE expressed in terms of magnetic vector potential $\mathbf{A}$ (A.6). Assuming that the analysed coil is a solenoid, the PDE can be expressed in a cylindrical coordinate system (A.7).

$$\boldsymbol{\nabla} \times \boldsymbol{\nabla} \times \mathbf{A} = -\mu \mathbf{J} \tag{A.6}$$

$$\frac{1}{r}\frac{\partial}{\partial r}\left(r\frac{\partial A\theta}{\partial r}\right) - \frac{A\theta}{r^2} + \frac{\partial^2 A\theta}{\partial z^2} = -\mu J\theta \tag{A.7}$$

Equation (A.7) can be solved by using method of separation of variables i.e. $A_\theta(r,z) = R(r)S(z)$, resulting in set of two PDEs. A method of variable separation can be applied to relationship $\mathbf{B} = \boldsymbol{\nabla} \times \mathbf{A}$ as described in [269], which results in set of equations (A.8).

$$\begin{cases} B_{\mathrm{z}}(r,z) = \dfrac{1}{r}\dfrac{\partial}{\partial r}\left[rA_\theta(r,z)\right] \\ B_{\mathrm{r}}(r,z) = -\dfrac{\partial A_\theta(r,z)}{\partial z} \end{cases} \tag{A.8}$$

The solutions derived by authors in [269] are expressed in terms of elliptic integrals derived from standard Bessel function identities. The magnetic field density distribution from a solenoid coil obtained via analytical solution described with Bessel functions, and experimental results have been compared in [270], which shows a slight deviation of both sets from one another. The comparison between different models for calculating magnetic flux density has been presented in [271] for a coil with a rectangular cross-section. The authors provide an efficient algorithm for calculating magnetic flux density with similar accuracy to more complex models.

Another way of obtaining magnetic flux density is by describing the problem using (A.6) or (A.7) and solving it using a finite-element method or finite-difference method or some derivative of those. Since the source of the magnetic field is the solenoid, the latter description (A.7) is preferable, allowing for solving an axisymmetric 2D problem, significantly reducing computational cost and time compared to 3D.

Lastly, the magnetic flux density can be calculated by numerically integrating over each wire in the solenoid and obtaining the solution by rewriting Biot-Savart law in the discrete form (A.9). Using this method, the magnetic flux density can be calculated one point at a time; sufficient accuracy can be achieved by dividing the coil into small enough fragments of finite length. This approach allows for calculating magnetic flux density produced by the coil or single wire of any shape and dimensions. However, the simplification used in the analysed case assumes that each turn has an infinitely small diameter. Such assumption can be done, if the distance from the wire where calibrated sensor was located ($D_{\mathrm{in}}/2 = 17.5$ mm) is much higher than wire diameter ($D_{\mathrm{w1}} = 1.445$ mm in L_1 and L_2 coils and $D_{\mathrm{w1}} = 2$ mm in L_3 coil), thus not influencing the magnetic field value substantially.

$$\Delta\mathbf{B} = \frac{\mu_0 I}{4\pi}\frac{\Delta\mathbf{l} \times \hat{\mathbf{r}}}{|\mathbf{r}|^2} \tag{A.9}$$

The total magnetic flux density produced by each j-th segment of every i-th turn can be calculated using (A.10).

$$\mathbf{B} = \sum_{i=1}^{N}\sum_{j=1}^{M}\Delta\mathbf{B}_{\mathrm{ij}} = \sum_{i=1}^{N}\sum_{j=1}^{M}\frac{\mu_0 I}{4\pi}\frac{\Delta\mathbf{l}_{\mathrm{ij}} \times \hat{\mathbf{r}}_{\mathrm{ij}}}{|\mathbf{r}_{\mathrm{ij}}|^2} \tag{A.10}$$

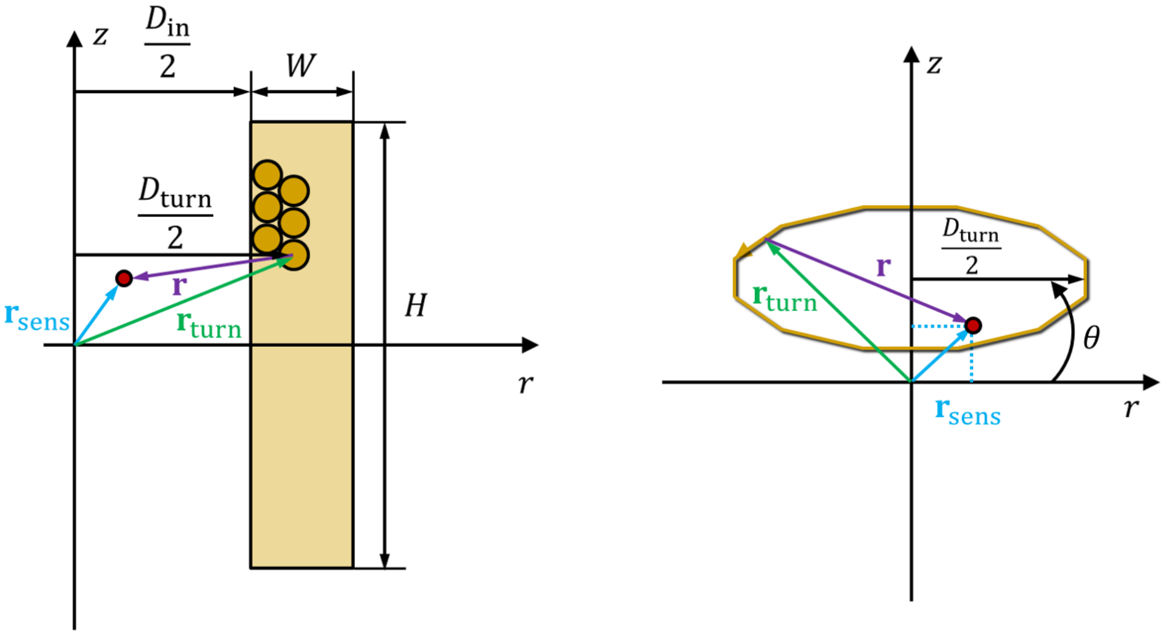

(a) **(b)**

Figure A.8. (a) Biot-Savart law applied to the i-th turn; (b) Biot-Savart law applied to the j-th segment of the i-th turn

Due to the multitude of variables and their nature (electromagnetic and geometric), it has been decided to estimate the uncertainty of the magnetic flux density using Monte Carlo simulation, which has been calculated using (A.10). To the uncertainty of the measured magnetic flux density contributes geometrical and electrical factors such as:

- **Current** flowing through the coil I that has been measured, therefore having average value (Figure A.3a), type A uncertainty given as standard deviation (Figure A.3c) and type B uncertainty attached to the used equipment [267, 268];

- **Coil dimensions, including position of each turn** - the coil L_2 used for calibration is composed of $N = 421$ turns in total, with a height $H = 60$ mm, inner radius $R_{\text{in}} = D_{\text{in}}/2 = 17.5$ mm and the thickness of $W = 13.5$ mm. The exact poistion of each turn is unknown and its uncertainty, however knowing that coil has been wounded with a crossed pattern (Figure 4.10) and the number of wires in each layer can be calculated (4.52), thus estimating position of each wire with diameter D_{w1}. The coil dimensions (H, W and D_{in}) were measured using Bahco 1150D electronic calipers [272] to obtain average value and type A uncertainty by performing series of measurements. Fifteen measurements were taken for each of the dimensions.
- **Sensor position** - The position has been estimated by measuring the dimensions of the 3D printed components (Figure A.1) locating it at the center of the coil on the axis of symmetry. The diameter, height and depth of sensor indentation were measured using Bahco 1150D electronic calipers [272] in series to estimate average value and its standard deviation. One of the components of the uncertainty contributing to the sensors placement is the location of the hall sensor itself shown in the datasheet [219]. Using the law of propagation of uncertainty, the uncertainty of the sensors position in both directions along r-axis for component r_{sens} and position along z-axis for component z_{sens} of the vector $\mathbf{r}_{\text{sens}}$ (Figure A.8). Fifteen measurements were taken for each of the dimensions.

All turns are considered as circle loops divided into segments with infinitesimal wire diameter. Such simplification can be done due to the significant value of inner diameter D_{in} and consequently calibrated sensor, compared to the wire diameter. It is also assumed that sensor position changes only on the two-dimensional plane along the radius and z-axis since the system is axisymmetric.

All hall sensors were calibrated individually, and the uncertainty has been evaluated for all of them since the measurement is conducted in an environment beyond the temperature range specified in the datasheet. The values specified above (D_{in}, W and H) are measured multiple times to evaluate average value and standard deviation of the measurement. Additionally, the wire diameter D_{w1} measurements are conducted. These measurements combined with coil dimensions result in the uncertainty of the parameters of each turn - radius and position along z-axis. Since it is impossible to view the position of each turn within the coil, it is assumed that the position of each turn is equally uncertain and is calculated individually for each turn.

Name	**Value**	**Average**	**Std Dev.**	u_{A}	u_{B}	u_{c}
Coil inner diameter	D_{in}	34.54 mm	0.38 mm	0.38 mm	0.03 mm	0.38 mm
Coil thickness	W	13.66 mm	0.47 mm	0.47 mm	0.03 mm	0.47 mm
Coil height	H	60.06 mm	0.04 mm	0.04 mm	0.03 mm	0.05 mm

The position of each i-th turn in the coil depends on the given coil inner diameter D_{in} and coil width W for both which the combined standard uncertainty u_{c} is known. Therefore the uncertainty of the diameter D_{turn} i-th turn has been calculated as combined uncertainties of inner diameter D_{in} and coil thickness W (A.11).

$$u_{\text{c}}(D_{\text{turn}}) = \sqrt{u_{\text{c}}^2(D_{\text{in}}) + u_{\text{c}}^2(W)} \tag{A.11}$$

The sensor is positioned within the coil at an average measured distance of 30.13 mm with a standard deviation of 0.04 mm from the coil's top based on fifteen consecutive measurements. The accuracy of the manufactured hall sensor is within ±0.1 mm [219]. The combined standard uncertainty of the sensor position in z-axis $u_{\mathrm{c}} = 0.11$ mm. Similarly, the diameter of the stand used for calibration (Figure A.1) has an average measured diameter of 34.35 mm with a standard deviation of 0.03 mm. The stand diameter is 0.19 mm smaller than the average coil inner diameter (34.54 mm); thus, the stand movement is restricted by half of that value in the radial direction equal to 0.10 mm. Therefore, the combined standard uncertainty of the sensor position in the radial direction is estimated as 0.15 mm. However, it has been assumed that the confidence interval of sensor position is at the level of 99%, resulting in k_α factor of 2.576 [266].

Name	**Parameter**	$k_\alpha u_{\mathrm{c}}$
Sensor position in z-axis	z_{sens}	0.28 mm
Sensor position in r-axis	r_{sens}	0.39 mm

The type A uncertainty of current was read from the plot for a corresponding current value in Figure A.3c, which has been plotted as a function of applied current in Figure A.9a and type B uncertainty from the datasheet of the probe [267] as ±3% of the reading. Both were combined to calculate the combined standard uncertainty of the measurement shown in Figure A.9b. It can be seen that type B uncertainty is the dominating factor at currents above 10 A; however, at lower values, the type A uncertainty is higher due to scope triggering time delay.

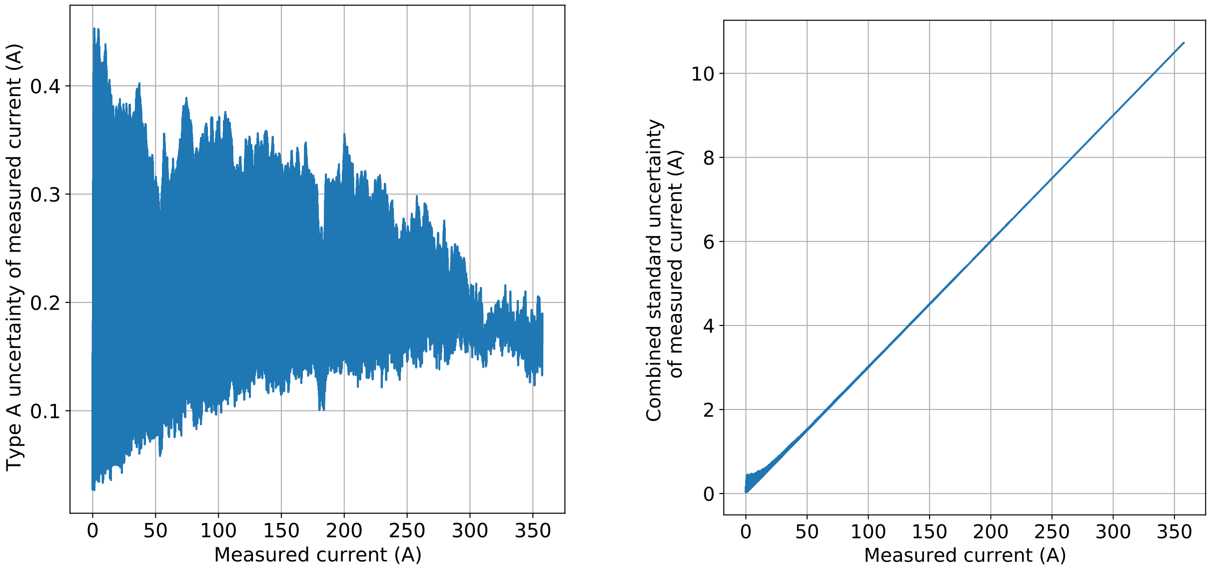

(a) **(b)**

Figure A.9. (a) Type A uncertainty of measured current; (b) Combined standard uncertainty of the current measurement

The simulation was repeated for values of current $\hat{I} = 50 \ldots 350$ A every 50 A and additional value of $\hat{I} = 10$ A being at the lower end of the spectrum. The simulation has been conducted for 10^6 random values generated using the normal distribution for each selected current value. The accuracy of the current measurement is given in the datasheet as ±3% of the measured value of current [267]. The obtained normal distribution of the magnetic flux density for current value of $\hat{I} = 100$ A is shown in Figure A.10. The uncertainty of the magnetic flux density resulting from the Monte Carlo simulation $u_{\mathrm{c2}}\left(B(I)\right)$ is given as a standard deviation of the data for each simulated current value.

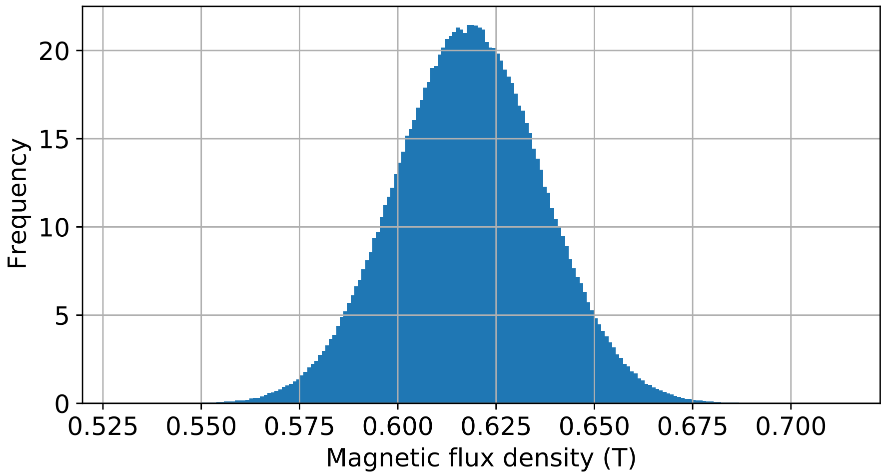

Figure A.10. Histogram of measured magnetic flux density for applied current of $\hat{I} = 100$ A

The final value of combined standard uncertainty of the magnetic flux density $u_\mathrm{c}(B)$ is a combination of uncertainty evaluated from the voltage reading $u_{\mathrm{c}1}\left(B(U)\right)$ calculated using Monte Carlo simulation $u_{\mathrm{c}2}\left(B(I)\right)$ as in (A.12). For the selected current values, a corresponding voltage readings (Figure A.3) and combined standard uncertainties $u_\mathrm{c}(U)$ have been calculated. The error bars for simulated values of current resulting in expected values of magnetic flux density acting on the sensor and voltages are shown in Figure A.11.

$$u_\mathrm{c}(B) = \sqrt{u_{\mathrm{c}1}^2\left(B(U)\right) + u_{\mathrm{c}2}^2\left(B(I)\right)} \tag{A.12}$$

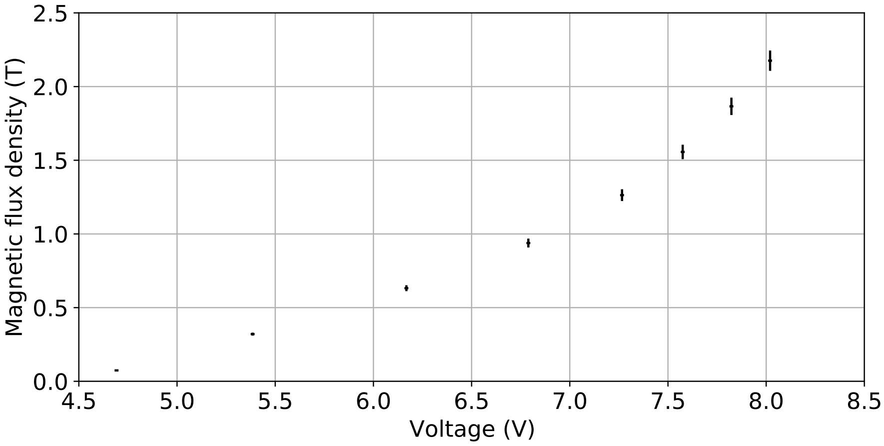

Figure A.11. Magnetic flux density - voltage dependence of the sensor B1 with marked error bars for values of current obtained via Monte Carlo simulation